VOJTĚCH KRČMARSKÝ

A TRAPPED-ION QUANTUM NETWORK OVER 230 M

A TRAPPED-ION QUANTUM NETWORK OVER 230 M

VOJTĚCH KRČMARSKÝ

Thesis submitted to the
Faculty of Mathematics, Computer Science and Physics
of the Leopold-Franzenz University of Innsbruck
in partial fulfilment of the requirements for the degree of

Doctor of philosophy
(Physics)

Carried out under supervision of
o. Univ.-Prof. Dr. Rainer Blatt
and
Asst. Prof. Dr. Ben Lanyon
2023

ABSTRACT

The field of quantum information science and technology brings completely new ways of working with information using the laws of quantum physics. These promise improvements in computing capabilities, simulations of quantum systems, sensing, and communication. Connecting several quantum devices into a quantum network would provide a powerful platform for distributed quantum computing, remote quantum sensing and communication. The envisioned quantum networks consist of a matter-based nodes, for storing and processing of quantum information, which are connected by photonic channels. The resource that is being distributed in such networks is quantum entanglement which can then be used for the aforementioned applications. A challenge today is to develop and demonstrate the basic building blocks and functionalities of quantum networks in the lab.

Trapped ions are considered a promising candidate platform with which to enable quantum networks thanks to their capability to process and store quantum information as well as to interface with optical photons. Despite being one of the first systems to be entangled over distance using photons, trapped ions have never been entangled over a distance beyond several meters.

This thesis presents a two-node quantum network of trapped ions separated by 230 m over the university campus in Innsbruck. The trapped-ion network nodes are placed in two buildings and do not share any common resources, such as lasers, or control systems. At the core of each node is a linear Paul ion trap, surrounded by an optical cavity to enhance the collection of photons generated by the ions.

Three main results are presented in this thesis. First, the design and construction of one of the network nodes is presented. The ion-trap vacuum chamber assembly and steps towards reaching ultra-high vacuum are described. Second, the observation of indistinguishable photons from two independent trapped-ion network nodes is presented. Indistinguishability is characterized via the Hong-Ou-Mandel interference experiment and its theoretical description is provided. Finally, heralded entanglement between an ion in each node by means of the detection of photons is experimentally established and supported by theoretical models.

ZUSAMMENFASSUNG

Quanteninformationswissenschaft und -technologie bringen neue Möglichkeiten Information unter Verwendung der Gesetze der Quantenphysik zu verarbeiten. Dies verspricht Verbesserungen in den Bereichen Rechenleistung, Simulation von Quantensystemen, Sensorik und Kommunikation. Die Verbindung mehrerer Quantengeräte zu einem Quantennetzwerk ist für verteiltes Quantenrechnen, entfernte Quantensensorik sowie Kommunikation notwendig. Die in dieser Arbeit vorgestellten Quantennetzwerke bestehen aus materiebasierten Netzwerkknoten zur Speicherung und Verarbeitung von Quanteninformation. Die Knoten sind wiederum durch photonische Kanäle zum Austausch von Information miteinander verbunden. Das Ziel bei diesen Netzwerken ist die Verteilung von Quantenverschränkung, welche als Ressource für die oben genannten Anwendungen dient.

Dank ihrer Fähigkeit Quanteninformation zu verarbeiten und zu speichern sowie mit optischen Photonen zu interagieren, gelten gefangene Ionen als vielversprechende Plattform zur Realisierung von Quantennetzwerkknoten. Obwohl sie zu den ersten Quantensystemen gehören, die in räumlich getrennten Fallen mithilfe von Photonen verschränkt wurden konnte bisher noch keine erfolgreiche Verschränkung über eine Entfernung von mehreren Metern bei gefangenen Ionen nachgewiesen werden.

Diese Arbeit präsentiert ein Quantennetzwerk, bestehend aus zwei Knoten mit gefangenen Ionen die über eine Distanz von 230 m auf dem Universitätscampus in Innsbruck verteilt sind. Die materiebasierten Netzwerkknoten befinden sich in zwei separaten Gebäuden und teilen keine gemeinsame Hardware wie Laser oder Steuerungssysteme. Im Kern jedes Knotens befindet sich eine Ionenfalle, welche von einem optischen Resonator umgeben ist um die Effizienz der Erzeugung einzelner Photonen durch die Ionen zu verbessern.

Diese Arbeit präsentiert drei wesentliche Ergebnisse. Zunächst wird der Aufbau von einem der beiden Netzwerkknoten detailliert vorgestellt. Der Knoten besteht aus einer linearen Paul-Falle, die sich in einer Vakuumkammer befindet und von einem optischen Resonator umgeben ist. Die Montage der Ionenfalle und der Vakuumkammer sowie die Schritte zur Erreichung eines Ultrahochvakuums werden ausführlich beschrieben. Das zweite Hauptergebnis dieser Arbeit ist die Beobachtung von ununterscheidbaren Photonen, die aus zwei unabhängigen Netzwerkknoten mit gefangenen Ionen stammen. Die Ununterscheidbarkeit wird durch ein Hong-Ou-Mandel-Interferenzexperiment charakterisiert und durch eine theoretische Beschreibung untermauert. Schließlich wird durch den experimentellen Nachweis von Photonen-

koinzidenzen die angekündigte Verschränkung zwischen einem Ion in jedem Knoten realisiert.

PUBLICATIONS

The work presented in this thesis culminated in the following journal publications:

- V. Krutyanskiy, M.Galli, V. Krcmarsky, S. Baier, D. A. Fioretto, Y. Pu, A. Mazloom, P. Sekatski, M. Canteri, M. Teller, J. Schupp, J. Bate, M. Meraner, N. Sangouard, B. P. Lanyon, and T. E. Northup. "Entanglement of Trapped-Ion Qubits Separated by 230 Meters" In: *Phys. Rev. Lett. 130, 050803 (2023)*, DOI: 10.1103/PhysRevLett.130.050803.

- J.Schupp, V. Krcmarsky, V. Krutyanskiy, M. Meraner, T. E. Northup, and B. P. Lanyon. "Interface between Trapped-Ion Qubits and Traveling Photons with Close-to-Optimal Efficiency" In: *PRX Quantum 2, 020331 (2021)*, DOI: 10.1103/PRXQuantum.2.020331

Additional papers have been published in the framework of this thesis but are not presented within it:

- V. Krutyanskiy, M. Meraner, J. Schupp, V. Krcmarsky, H. Hainzer, and B. P. Lanyon. "Light-matter entanglement over 50 km of optical fibre." In: *npj Quantum Information 5.1 (2019), p.72.* DOI: 10.1038/s41534-019-0186-3.

- M. Meraner, A. Mazloom, V. Krutyanskiy, V. Krcmarsky, J. Schupp, D. A. Fioretto, P. Sekatski, T. E. Northup, N. Sangouard, and B. P. Lanyon. "Indistinguishable photons from a trapped-ion quantum network node." In: *Physical Review A 102.5 (2020), p. 052614*. DOI: 10.1103/PhysRevA.102.052614.

- V. Krutyanskiy, M. Canteri, M. Meraner, J. Bate, V. Krcmarsky, J. Schupp, N. Sangouard, and B. P. Lanyon. "Telecom-Wavelength Quantum Repeater Node Based on a Trapped-Ion Processor." In: *Phys. Rev. Lett. 130, 213601 (2023)*. DOI: 10.1103/PhysRevLett.130.213601.

ACKNOWLEDGMENTS

The successful completion of this thesis would not have been possible without help and support of countless people. Firstly, I want to thank Rainer for giving me the opportunity to do the PhD in his group and Ben who put his trust in me and let me be part of his team. I am grateful to all the members of the group for sharing their knowledge and experience. Your insights and suggestions have been invaluable, and I am immensely grateful for your support.

I want to thank Josef Schupp, Helene Hainzer, Viktor Krutianskiy and Martin Meraner for creating a great and friendly environment not only in the lab. I want to thank my colleagues and friends from the cavity teams who participated on the networking experiments: Maria Galli, Dario Fioretto, Yunfei Pu, Simon Baier, Konstantin Friebe, Klemens Schuppert, and Markus Teller for their commitment, hard work, and cooperation.

I want to thank people from the mechanical and electronics workshop at IQOQI, where our experimental apparatus was created. Namely Stefan Haslwanter for building most of the parts of our trap, Andreas Stasser, and Bernhard Öttl for support and always finding a time to create things for me, and Gerhard Hendl for helping with electronical circuits.

The work wouldn't have been possible without administrative support. I would like to thank Elisabeth Huck, Nikolaus Falschlunger for providing the support not only with all the orders I had to place. I want to thank Patricia Moser and Claudia Mevenkamp for administrative support.

The past years I spent in Innsbruck were not only about physics. I had the opportunity to explore the beauty of the Alps. I want to thank Matthis Bock and everyone who accompanied me on my mountain adventures. I want to thank Viktor Krutyanskiy and Martin Meraner for teaching me how to ski.

I am grateful to my friends who supported me throughout the good and the bad times - Zuzana, Petr and Samuel Kelnar, Pavel Zoufaly, Jan Janus, Zdenka Janusova and friends I found at Thermo Fisher Scientific Brno.

Last but not least I want to thank my family - my parents Lucie and Vladimir, my sister Alzbeta and her husband Petr for their unwavering support and understanding throughout the duration of my studies. Special thanks goes to my two nieces Emilie and Josefina who charge me with their infinite energy and bring out the child in me.

Thank you all.

CONTENTS

LIST OF FIGURES

LIST OF TABLES

1 INTRODUCTION

Since the beginning of the human race, communication has been a crucial part of human interaction. Even before language or writing was used, people were sharing information necessary for their survival. The primitive methods for sending messages such as signal fires or drums were used in many places around the world. Famous examples are native Americans or ancient Chinese protecting the Great Wall. In Homer's Iliad, the fall of the city Troy is announced with fire signals. Sailors used semaphores, hand signals, and flags for sharing information. Such "primitive" means of communication are still used in the modern times, though with more advanced technology. For example, light signals are used in airports to provide crucial instructions for pilots [1].

Information has always been an invaluable resource. With the invention of computers, it became more accessible and empowered people to harness its full potential. Rapid development of computational power boosted progress in every aspect of human exploration. The best computers in the world help in drug design, improving the safety of new vehicles, or studying the climate. The invention of the internet in the 1960s, and especially the world wide web in 1989, enabled fast exchange of information across the globe which changed our everyday lives. Our lives happen also on the internet, where we share knowledge, interact with friends and perform financial transactions. Whilest performing these tasks we rely on security provided by classical communication encryption[1]. Breaking this encryption is beyond the capabilities of even the most powerful computers[2].

Advances in understanding quantum physics brought major achievements in the 20th century including the transistor [3] and laser [4]: powering the computer revolution and opening new possibilities in studying quantum phenomena. In the past decades, a completely new approach to store, process and share information has emerged and the associated research field is known as *quantum information science*. Here, information is encoded in degrees of freedom of quantum systems and both encoding and manipulation of that information can exploit all the weird and counter-intuitive properties of quantum physics, such as *superposition* or *entanglement*. The field advertises new possibilities and advances in computing [5] and simulations [6] as well as improvements in time keeping [7] and sensing [8]. In the field of

1 Currently, the most advanced encryption standard is the AES-256 [2]

2 Computational time required to break the encryption using brutal force approach exceeds the current age of the universe by many orders of magnitude

communication, quantum information offers fundamentally secure communication through quantum cryptography [9].

The rapid development of quantum information science and technology in the last 30 years can be attributed to the development of laboratory techniques that enable the manipulation of single quanta. The Penning trap [10] and Paul trap [11] are notable advances since they enabled storage and manipulation of single atomic ions. Quantum information experiments utilize not only single trapped ions [12, 13], but also many other quantum systems, such as neutral atoms [14], solid state systems based on color centers in diamond [15], quantum dots [16], superconducting circuits [17] and other systems. The first quantum technologies are commercially available. In 2007, the state elections in Geneva, Switzerland, were secured by quantum cryptography [18]. The first small-scale quantum computers, based on superconducting technology[3], NV centers[4] or trapped ions[5] are available for customers.

Today, the internet involves a network of billions of classical technological devices, such as PCs, mobile phones or tablets. In the envisioned *quantum internet* [23, 24], quantum devices will be connected together in a network for scalable quantum computing, worldwide communication, or distributed sensing. The envisioned quantum network consists of matter-based nodes in which quantum information is stored and processed. Those nodes are connected together by photonic channels in which photons distribute quantum information and entanglement between the nodes [23].

Some of the fundamental building blocks of future quantum networks have been demonstrated using a range of different physical systems including, including trapped ions [25–28], neutral atoms [29], and color centers in diamond [30]. In those works entanglement of remote quantum matter is established via traveling photons. The most advanced realization of a quantum network to date is a three-node system of color centers in diamond [31].

Trapped ions are, together with superconducting circuits, a highly promising platform for quantum information processing [32, 33]. Trapped ions are well controlled and manipulated using laser pulses and have been proven able to store quantum information over time scales on the order of minutes [34]. Trapped ions are used as quantum simulators [35] and quantum computers [32], in which quantum algorithms such as the Shor algorithm have been demonstrated [36]. They are used for precise time keeping [37], even in space [38]. The capability to establish ion-photon entanglement [39] and use that to entangle ions in remote traps has been achieved [25, 40]. Those results, in combination with the established ability to perform quantum

3 e.g. IBM Quantum System One [19]
4 e.g. XEEDQ [20]
5 e.g. Alpine Quantum Technologies [21], IonQ [22]

processing on multiple ion-qubits in same trap, makes the trapped ion platform highly promising for realizing future quantum network nodes. However, trapped ions have not yet been entangled over distances greater than a few meters [25, 40] and have employed common resources, such as lasers, to achieve those short quantum links.

The aim of this thesis is to establish a two-node quantum network of trapped ions that are placed in remote buildings and don't share any common resources. Our approach is to couple the ions to an optical cavity to increase the photon collection probability and enable the generation of indistinguishable photons at near infrared wavelength.

The last chapter of this thesis presents the entanglement of two ions across that network. The rest of the thesis presents two key steps towards that final result. First, the construction of one of the two ion-trap nodes. The other node already existed prior to the beginning of this PhD project [41] and consists of a linear Paul ion trap with an integrated optical cavity for collecting 854 nm photons from a trapped calcium ion. That system was the first, and at the time of the beginning of this thesis, the only ion-cavity system to have successfully generated ion-photon entanglement. The first milestone of this thesis was, therefore, to build another ion-cavity system with at least equal capabilities. The second key step is the observation and modeling of two-photon interference between photons generated by two remote ion-trap network nodes. The visibility of two-photon interference sets the maximum achievable quality of remote ion entanglement in our experiments and had not previously been observed for photons produced by ions in cavities. An outline of the structure of this thesis is now provided.

Chapter 2 begins by briefly introducing the basic unit of quantum information — the qubit — as well as the basic terminology necessary for the thesis. Next, two-photon interference on a beamsplitter is introduced and described mathematically. The chapter ends with a description of how two-photon interference can be used to establish entanglement between two remote systems by the process known as entanglement swapping.

The first part of Chapter 3 introduces key components of our ion trap network. First, the calcium ion confined in a trap is introduced. The level structure of the ion and implementation of a qubit is presented. Operations that prepare the ion in a specific electronic state are described in the section. Furthermore, the process that generates single photons out of the trapped ion coupled with an optical cavity is described. The second part of the chapter is dedicated to presenting a theoretical model for the two-photon interference experiment. The model is used to simulate the wavepacket shape of photons from the two participating network nodes and the interference visibility of these two photons. The model accounts for distinguishability arising

from spontaneous scattering during the photon generation process as well as more technical imperfections encountered in the experiment.

Chapter 4 presents the construction of one of the network nodes. The design of a vacuum chamber and its components is described in detail. A special focus is put on presenting the methods used for assembling the vacuum system, establishing ultra high vacuum and designing the helical resonator required for high-voltage supply of the ion trap.

Chapter 5 describes the two-photon interference experiment, in which the photons originated from the separate network nodes. First, the experimental apparatus is presented, followed by the executed experimental sequence. The next part is dedicated to the pre-requisites necessary for performing the experiment, including remote synchronization, frequency matching of the remote cavities and independent calibrations of key experimental parameters. Section 5.5 presents the results of two-photon interference, otherwise known as a Hong-Ou-Mandel experiment. The measurement outcomes are compared to predictions of theoretical model presented in the previous chapter and are used for predictions for further experiments.

Chapter 6 presents the entanglement of two remote ions in our network. The chapter begins with a short introduction, followed by the subsequent research paper and supplementary material in their published forms.

Chapter 7 concludes the results presented in this thesis and presents an outlook to further steps for building quantum networks with trapped ions.

2

BACKGROUND CONCEPTS

The basic unit of quantum information is the *qubit* and one of the main functions of envisioned quantum network is to establish *entanglement* between qubits in remote nodes. The first part of this chapter introduces the qubit and its realizations. The concept of a qubit is then used to introduce entanglement. The second part of this chapter describes the concept of photon indistinguishability and means of its measurement. Specifically, the experiment of two-photon interference on a beamsplitter is described and different photon input states are discussed. Finally, the process of entanglement swapping is described, which is used in Chapter 6 to establish entanglement across our network.

2.1 QUANTUM INFORMATION, ENTANGLEMENT, AND QUBIT

2.1.1 *Qubit*

Classical computers process information in form of binary digits, or *bits*. One bit is the smallest unit of classical information. In a binary system a bit can be in only one of two possible states: 0 or 1. These states describe two discrete values e.g., true or false, on or off. In classical computers, bits can be realized by two discrete voltage levels or a charged and uncharged capacitor. The quantum analogy of a classical bit is a two-level quantum system, or quantum bit, with states $|\downarrow\rangle$ and $|\uparrow\rangle$. In contrast to a classical bit, a *qubit* can exist in any linear combination of the two states. We can write an arbitrary superposition state of a qubit as

$$|\psi\rangle = \alpha\,|\downarrow\rangle + \beta\,|\uparrow\rangle\,, \tag{2.1}$$

where α, β are complex coefficients satisfying $|\alpha|^2 + |\beta|^2 = 1$. The qubit can be visualized on a unit sphere by a vector pointing from the center towards the surface of the sphere. In spherical coordinates the vector is given by two angles φ and ϑ

$$|\psi\rangle = \cos(\vartheta/2)\,|\downarrow\rangle + e^{i\varphi}\sin(\vartheta/2)\,|\uparrow\rangle\,. \tag{2.2}$$

A qubit can be and has been realized in a broad range of two-level quantum systems. Electron spin [42] or nuclear spin [43], collective excitation in atomic ensembles [44], or transmons in superconducting circuits [45] are just a few examples of physical implementation of a qubit in a stationary system. A qubit can be also realized using various degrees of freedom of single quanta of light: photons [46]. For

example, the number of photons in a given mode, the arrival time of photons or the polarization can all be used to realize a two level quantum system.

In this thesis, mainly two different implementations of a qubit will be used. First, a qubit is encoded into two states of the single outer valence electron in a trapped calcium ion. There are many possibilities for different qubit encoding with the ion's electronic structure and we use several of them in the results in Chapter 6. All employed encodings have an energy splitting and the lower of the two is referred to as the ground state and the upper is referred to as the excited state. The second qubit implementation used is the polarization of a single photon. Two levels of a polarization qubit are e.g., horizontal linear polarization $|H\rangle$ and vertical linear polarization $|V\rangle$ of the photon.

2.1.2 *Multiple qubits and entanglement*

In certain cases, the state of a system consisting of N qubits can be described as a tensor product of each individual qubit state vector ψ_i

$$|\Psi\rangle = |\psi_1\rangle \otimes |\psi_2\rangle \otimes \ldots \otimes |\psi_N\rangle \,. \tag{2.3}$$

However, not every state can be written in this form. The commonly used definition of entanglement is: *If a state $|\Psi\rangle$ cannot be written as a product state of its constituents in the form of Equation 2.3, it is entangled* [47]. An example of such a state is

$$|\Psi\rangle = \frac{1}{\sqrt{2}} \left(|\downarrow\rangle |\uparrow\rangle - |\uparrow\rangle |\downarrow\rangle \right), \tag{2.4}$$

which is known as Bell state, named after the physicist John Bell. The amount of entanglement in a two-qubit state can be quantified by a range of measures, including concurrance [48], negativity [49] and entanglement of formation [50]. Equation 2.4 is an example of a maximally entangled two-qubit state.

2.2 PHOTON INDISTINGUISHABILITY

One of the main goals of this thesis is to establish entanglement between ions trapped in remote network nodes. To establish entanglement we use photons emitted by different nodes and a process known as *entanglement swapping* [51]. For ideal operation of the entanglement swapping process, the photons emitted by the remote nodes must be indistinguishable: that is, it must not be possible to identify which node emitted a given photon.

The extent to which a quantum emitter produces indistinguishable photons can be assessed by performing a two-photon interference experiment. Here, two photons impinge on opposite input ports of a beamsplitter. If the two photons are perfectly indistinguishable, they

bunch into a single output port of the beamsplitter. The purely quantum phenomenon of two-photon interference was first studied already in the 1980s [52]. Theoretical works of beamsplitter transformations were published in a close chronological order by Prasad, Scully, and Martiensen who first derived the unitary transformation of a lossless beamsplitter [53] and Ou, Hong, and Mandel [54] who expressed the transformation of a beamsplitter for a linear superposition of coherent states. Fearn and Loudon studied the lossless beamsplitter with a focus on quantization of the input and output modes [55]. Experimental realizations of two-photon interference followed shortly after the theoretical studies. The famous paper by Hong, Ou, and Mandel [52] presents the interference of two photons produced by parametric down-conversion on a beamsplitter in which the famous "coincidence dip" was observed.

Today, the two-photon interference visibility is generally regarded as a key performance metric for quantum emitters, in which a maximum visibility of 1 corresponds to photons that are completely indistinguishable. Indistinguishability of photons originating from a variety of different physical systems have been studied. Quantum interference of single photons from solid state systems based on color centers in diamond, such as Nitrogen-Vacancy (NV) centers [56–58] and Silicon-Vacancy (SiV) centers [59] was observed. Two-photon interference has been studied with quantum dots [60–63]. The phenomenon was also observed with single photons from atomic ensembles [64, 65], as well as with neutral atoms coupled to optical cavity [66]. Indistinguishability of photons collected in free-space from trapped ions was also studied [67–69]. More recently, the interference of photons originating from two different systems — trapped Ba^+ ion and Rb atomic ensemble — was observed [70]. At the beginning of my PhD studies, two-photon interference had not been observed for photons emitted by trapped ions into optical cavities.

2.2.1 *A simple model of two-photon interference*

This subsection presents a simple model of two-photon interference. Consider an experimental setup involving a beamsplitter with two input ports labeled as a and b, and two output ports labeled a' and b', as sketched in Figure 2.1(a). Each output port is monitored by a single photon detector, labeled $D_{a'}$ and $D_{b'}$. The four modes a, b, a', and b' are each associated with bosonic annihilation operators $\hat{a}, \hat{b}, \hat{a}'$, and $\hat{b}'$, respectively. In the case of a lossless beamsplitter, a photon entering the beamsplitter through one of the input ports is either reflected with probability $|r|^2$ or transmitted with probability $|t|^2$, satisfying $|r|^2 + |t|^2 = 1$, where r and t are reflection and transmission probability amplitudes, respectively.

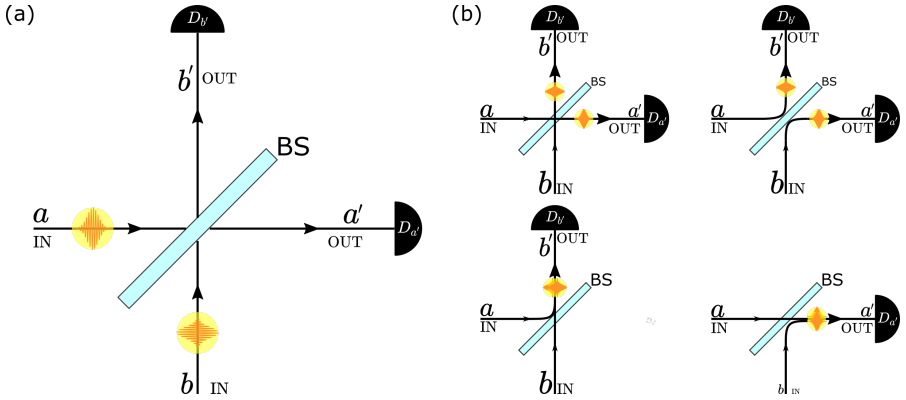

Figure 2.1: **Setup to measure two-photon interference on a beamsplitter.** (a) Two photons enter a beamsplitter from two input ports a and b. The two output ports a', b' are monitored by single photon detectors $D_{a'}$ and $D_{b'}$. (b) Four possible scenarios can occur. Both photons can be transmitted or reflected by the beamsplitter, resulting in them leaving in different output ports, or one photon is reflected and the other transmitted leading to bunching into a single output port. If the two photons are perfectly indistinguishable, they will always bunch and leave the beamsplitter together through one of the output ports a' or b'.

INDISTINGUISHABLE PHOTONS

Consider two *indistinguishable* photons entering the beamsplitter through input ports a and b. By indistinguishable it is meant here that the photons are identical in every way except that they are injected into different input ports. The expression

$$|\Psi_{In}\rangle = |1,1\rangle_{a,b} = \hat{a}^\dagger \hat{b}^\dagger |0,0\rangle_{a,b} \tag{2.5}$$

describes the quantum state of the photons in front of the beamsplitter in the Fock basis where the operators are bosonic creation operators for the photons in the corresponding modes. The beamsplitter changes the input state according to the following transformations

$$\hat{a}^\dagger \xrightarrow{\hat{U}_{BS}} t\hat{a'}^\dagger - ir\hat{b'}^\dagger \tag{2.6a}$$

$$\hat{b}^\dagger \xrightarrow{\hat{U}_{BS}} t\hat{b'}^\dagger - ir\hat{a'}^\dagger \tag{2.6b}$$

Intuitively, four output scenarios are possible, as can be seen in Figure 2.1(b). The two photons can both be transmitted or reflected by the beamsplitter. In these cases, both photons leave in different output ports, resulting in simultaneous detection events at both detectors $D_{a'}$ and $D_{b'}$, so called coincidence events. In the other two cases, one photon is reflected and one is transmitted by the beamsplitter. In those cases, both photons will leave together in one output port and only

one detector will register a detection event (click). The output state after the beamsplitter, calculated using Equation 2.5 together with Equation 2.6a and Equation 2.6b, is given by

$$\begin{aligned} |\Psi_{out}\rangle &= \hat{U}_{BS}\,|\Psi_{In}\rangle = \hat{U}_{BS}(\hat{a}^\dagger \hat{b}^\dagger\,|0,0\rangle_{a,b}) = \\ &= (t\hat{a'}^\dagger - ir\hat{b'}^\dagger)(t\hat{b'}^\dagger - ir\hat{a'}^\dagger)\,|0,0\rangle_{a',b'} = \\ &= \left[(t^2 - r^2)\hat{a'}^\dagger \hat{b'}^\dagger - irt(\hat{a'}^\dagger \hat{a'}^\dagger + \hat{b'}^\dagger \hat{b'}^\dagger)\right]|0,0\rangle_{a',b'}\,. \end{aligned} \tag{2.7}$$

In the last equation, the first term with $\hat{a'}^\dagger \hat{b'}^\dagger$ corresponds to the cases in which the two photons leave the beamsplitter in different output ports, while the second term corresponds to the cases in which the photons bunch into the same output port.

In the case where $r^2 = t^2 = 1/2$ (a *balanced beamsplitter*), the first term in Equation 2.7 vanishes and the output state is given by

$$|\Psi_{out}^{50:50}\rangle = -\frac{i}{2}\left(\hat{a'}^\dagger \hat{a'}^\dagger + \hat{b'}^\dagger \hat{b'}^\dagger\right)|0,0\rangle_{a',b'}\,. \tag{2.8}$$

In this case, the photons will always bunch into a single output port of the beamsplitter, as the other cases destructively interfere. The above result, that the photons always bunch together in the beamsplitter output ports, is in general only valid under the initial assumption that the photons are indistinguishable in all degrees of freedom (e.g., their frequency, polarization, spatial mode, temporal mode etc.).

DISTINGUISHABLE PHOTONS

Two distinguishable photons arriving on the beamsplitter are now considered. For that, a new degree of freedom to the input modes a and b that makes the two photons fully distinguishable is introduced. By 'fully' distinguishable it is meant that the two different photon states are orthogonal. Two orthogonal linear polarizations: horizontal (labeled "H") and vertical (labeled "V") and corresponding subscripts for the bosonic operators are used. The input state is thus given by

$$|\Psi_{In}\rangle = |H,V\rangle_{a,b} = \hat{a_H}^\dagger \hat{b_V}^\dagger\,|0,0\rangle_{a,b}\,. \tag{2.9}$$

By applying the transformation of Equation 2.6a and Equation 2.6b for a balanced beamsplitter ($r^2 = t^2 = 1/2$), the following output state is obtained

$$|\Psi_{out}\rangle = \frac{1}{2}\left(\hat{a'_H}^\dagger \hat{b'_V}^\dagger - \hat{a'_V}^\dagger \hat{b'_H}^\dagger - i\hat{a'_H}^\dagger \hat{a'_V}^\dagger - i\hat{b'_H}^\dagger \hat{b'_V}^\dagger\right)|0,0\rangle_{a,b}\,. \tag{2.10}$$

One sees that the probability that both detectors fire (a coincidence detection event) is 50%.

The two-photon interference experiment provides a means to measure the extent to which two photons can be made indistinguishable.

First, in an experiment one lets two fully distinguishable photons arrive on a beamsplitter and estimates the coincidence probability $C^{\perp}$. For that, the photons are made orthogonal in a chosen degree of freedom, e.g., by displacing their temporal arrival time or rotating their relative polarization. Then the intentional distinguishability is removed and the new coincidence probability $C^{\parallel}$ is estimated. The ratio

$$V = 1 - \frac{C^{\parallel}}{C^{\perp}} \tag{2.11}$$

is known as the two-photon interference visibility. Fully indistinguishable photons yield $V = 1$, while fully distinguishable photons yield $V = 0$. Intermediate values refer to partially indistinguishable photons. This two-photon interference experiment was first performed by Hong, Ou, and Mandel in 1987 [52], and often is called *Hong-Ou-Mandel interference*, or shortly HOM interference.

2.2.2 *Bell states on a beamsplitter*

In the previous subsection, beamsplitter input states consisting of photons in a product state were considered. Let's have a look now at what happens if photons in an entangled state are sent onto the balanced beamsplitter ($r^2 = t^2 = 1/2$). Specifically, consider injecting two photons, one in each input port, that are prepared into any one of the four Bell states:

$$\left|\Phi^{\pm}\right\rangle = \frac{1}{\sqrt{2}}\left(\left|H,H\right\rangle_{a,b} \pm \left|V,V\right\rangle_{a,b}\right) \tag{2.12a}$$

and

$$\left|\Psi^{\pm}\right\rangle = \frac{1}{\sqrt{2}}\left(\left|H,V\right\rangle_{a,b} \pm \left|V,H\right\rangle_{a,b}\right). \tag{2.12b}$$

The Bell states form an orthonormal basis for the Hilbert space of two-qubit states. Therefore, any pure two-photon state can be expressed as a linear superposition of the four Bell states. Consequently, once the transformation of Bell states by the beamsplitter is known, transformation of any two-photon input state by a beamsplitter can be worked out. In the following, the transformation of each Bell state is presented.

$\left|\Phi^{\pm}\right\rangle$ arriving on a beamsplitter

The input Bell states $\left|\Phi^{\pm}\right\rangle$ can be written using creation operators as

$$\left|\Phi^{\pm}\right\rangle_{a,b} = \frac{1}{\sqrt{2}}\left(\hat{a_H}^{\dagger}\hat{b_H}^{\dagger} \pm \hat{a_V}^{\dagger}\hat{b_V}^{\dagger}\right)\left|0,0\right\rangle_{a,b}. \tag{2.13}$$

By applying the beamsplitter transformations of Equation 2.6a and Equation 2.6b, the output state is given by

$$|\Phi^{\pm}\rangle_{a,b} \xrightarrow{\hat{U}_{BS}} \frac{1}{\sqrt{2}}\left[\frac{1}{2}\left(\hat{a_H'}^{\dagger} - i\hat{b_H'}^{\dagger}\right)\left(\hat{b_H'}^{\dagger} - i\hat{a_H'}^{\dagger}\right) \pm \frac{1}{2}\left(\hat{a_V'}^{\dagger} - i\hat{b_V'}^{\dagger}\right)\left(\hat{b_V'}^{\dagger} - i\hat{a_V'}^{\dagger}\right)\right]|0,0\rangle_{a',b'}\,, \tag{2.14}$$

which simplifies to

$$\begin{aligned}&\frac{-i}{2\sqrt{2}}\left[\left(\hat{a_H'}^{\dagger}\hat{a_H'}^{\dagger} + \hat{b_H'}^{\dagger}\hat{b_H'}^{\dagger}\right) \pm \left(\hat{a_V'}^{\dagger}\hat{a_V'}^{\dagger} + \hat{b_V'}^{\dagger}\hat{b_V'}^{\dagger}\right)\right]|0,0\rangle_{a',b'} = \\ &= \frac{-i}{2\sqrt{2}}\left(|HH,0\rangle_{a',b'} + |0,HH\rangle_{a',b'} \pm |VV,0\rangle_{a',b'} \pm |0,VV\rangle_{a',b'}\right),\end{aligned} \tag{2.15}$$

where e.g., $|HH,0\rangle_{a',b'}$ represents two horizontal photons in mode a' and no photon in the mode b'. The last equation shows that if two photons arrive on a beamsplitter in Bell state $|\Phi^+\rangle$ or $|\Phi^-\rangle$, the two photons will always bunch and leave through the same output port. This is a direct consequence of the Hong-Ou-Mandel effect described earlier.

$|\Psi^+\rangle$ ARRIVING ON A BEAMSPLITTER

The Bell state $|\Psi^+\rangle$ from Equation 2.12b can be re-written using creation operators as

$$|\Psi^+\rangle_{a,b} = \frac{1}{\sqrt{2}}\left(\hat{a_H}^{\dagger}\hat{b_V}^{\dagger} + \hat{a_V}^{\dagger}\hat{b_H}^{\dagger}\right)|0,0\rangle_{a,b}\,. \tag{2.16}$$

By applying the beamsplitter transformation, the following state is obtained at the output

$$|\Psi^+\rangle_{a,b} \xrightarrow{\hat{U}_{BS}} \frac{1}{\sqrt{2}}\left[\frac{1}{2}\left(\hat{a_H'}^{\dagger} - i\hat{b_H'}^{\dagger}\right)\left(\hat{b_V'}^{\dagger} - i\hat{a_V'}^{\dagger}\right) + \frac{1}{2}\left(\hat{a_V'}^{\dagger} - i\hat{b_V'}^{\dagger}\right)\left(\hat{b_H'}^{\dagger} - i\hat{a_H'}^{\dagger}\right)\right]|0,0\rangle_{a',b'}\,, \tag{2.17}$$

which simplifies to

$$-\frac{i}{\sqrt{2}}\left(\hat{a_H'}^{\dagger}\hat{a_V'}^{\dagger} + \hat{b_H'}^{\dagger}\hat{b_V'}^{\dagger}\right)|0,0\rangle_{a',b'} = -\frac{i}{2}\left(|HV,0\rangle_{a',b'} + |0,HV\rangle_{a',b'}\right). \tag{2.18}$$

In this case, the two photons also bunch into the same output port of the beamsplitter, however the photons are orthogonally polarized.

$|\Psi^-\rangle$ ARRIVING ON A BEAMSPLITTER

First, the $|\Psi^-\rangle$ state is re-written using the creation operators as

$$|\Psi^-\rangle_{a,b} = \frac{1}{\sqrt{2}}\left(\hat{a_H}^{\dagger}\hat{b_V}^{\dagger} - \hat{a_V}^{\dagger}\hat{b_H}^{\dagger}\right)|0,0\rangle_{a,b}\,. \tag{2.19}$$

By applying the beamsplitter transformation, the following state at the output is obtained

$$\begin{aligned}|\Psi^-\rangle_{a,b} \xrightarrow{\hat{U}_{BS}} \frac{1}{\sqrt{2}}\Bigg[&\frac{1}{2}\left(\hat{a_H'}^\dagger - i\hat{b_H'}^\dagger\right)\left(\hat{b_V'}^\dagger - i\hat{a_V'}^\dagger\right) - \\ &\frac{1}{2}\left(\hat{a_V'}^\dagger - i\hat{b_V'}^\dagger\right)\left(\hat{b_H'}^\dagger - i\hat{a_H'}^\dagger\right)\Bigg]|0,0\rangle_{a',b'},\end{aligned} \tag{2.20}$$

which simplifies to

$$\frac{1}{\sqrt{2}}\left(\hat{a_H'}^\dagger\hat{b_V'}^\dagger - \hat{a_V'}^\dagger\hat{b_H'}^\dagger\right)|0,0\rangle_{a',b'} = \frac{1}{2}\left(|H,V\rangle_{a',b'} - |V,H\rangle_{a',b'}\right). \tag{2.21}$$

One sees that photons arriving on a beamsplitter in $|\Psi^-\rangle$ will always exit in opposite output ports: they antibunch. Overall, the calculation shows that the only input Bell state that leads to photons exiting in two different ports is the $|\Psi^-\rangle$ and can lead to simultaneous (coincident) detector events of detectors $D_{a'}$ and $D_{b'}$.

2.3 ENTANGLEMENT SWAPPING

Establishing an entangled pair of qubits between remote network nodes is one of the principal goals of this thesis. The interaction of two photons on a beamsplitter was studied in the previous section. In this subsection, the use of such an interaction for generating entanglement between two network nodes is studied.

Different methods can be used to achieve entanglement between two remote quantum systems using traveling photons. In the DLCZ protocol [71], the detection of a single photon is used to entangle two systems. The protocol was experimentally realized with ensembles of trapped neutral atoms [72–74]. Entanglement of remote NV centers using the single photon detection scheme was also performed by Bernien *et.al.* [58] and Hensen *et.al.* [30]. With yet another method, Ritter *et al.* [75] used direct photon transmission and absorption to entangle two single rubidium atoms in optical cavities.

In the experiments presented in this thesis, we use the two-photon method to establish entanglement between our remote ions. The method was first presented by Zukovski *et al.* in [76], based on work of Yurke and Stoler [77]. Here, entanglement of two independent systems may be established in the cases in which two photons are detected and exploits the two-photon interference effect of the previous subsection. The method was carried out experimentally with atomic ensembles [73] and with two trapped ytterbium ions a few meters apart [25]. The principle of entanglement swapping based on two-photon interference is described in the following subsection.

2.3.1 *Entanglement swapping based on two-photon interference*

Let the goal be to maximally entangle two remote stationary qubits A and B, one in each node. Those qubits are referred to as "memories" for convenience. Each quantum memory has two states $|\uparrow\rangle$ or $|\downarrow\rangle$. Each memory is first entangled with a traveling photon via e.g., direct emission. For the photon, the polarization degree of freedom is chosen to carry the quantum information. Two orthogonal polarization states $|H\rangle$ and $|V\rangle$ are used in the following paragraphs. The fully entangled pairs, consisting of one quantum memory and a separate photon can be written as

$$\begin{aligned} |\Psi\rangle_A &= \frac{1}{\sqrt{2}} \left(|\downarrow\rangle_A |H\rangle_A + |\uparrow\rangle_A |V\rangle_A\right) \\ |\Psi\rangle_B &= \frac{1}{\sqrt{2}} \left(|\downarrow\rangle_B |H\rangle_B + |\uparrow\rangle_B |V\rangle_B\right). \end{aligned} \tag{2.22}$$

Here, the left ket vector denotes state of the quantum memory, while the right vector describes state of the photon. The input state of the experiment can be described as

$$|\Psi\rangle_{In} = |\Psi\rangle_A \otimes |\Psi\rangle_B, \tag{2.23}$$

which can be re-written as

$$\begin{aligned} |\Psi\rangle_{In} = \frac{1}{2} \left(|\downarrow\rangle_A |\downarrow\rangle_B |H\rangle_A |H\rangle_B + |\uparrow\rangle_A |\downarrow\rangle_B |V\rangle_A |H\rangle_B + \right. \\ \left. + |\downarrow\rangle_A |\uparrow\rangle_B |H\rangle_A |V\rangle_B + |\uparrow\rangle_A |\uparrow\rangle_B |V\rangle_A |V\rangle_B\right). \end{aligned} \tag{2.24}$$

This state can now be re-written in the Bell state basis for the photonic part of the state using the following identities:

$$|H\rangle_A |H\rangle_B = \frac{1}{\sqrt{2}} \left(\left|\Phi^+\right\rangle_{AB} + \left|\Phi^-\right\rangle_{AB}\right) \tag{2.25a}$$

$$|H\rangle_A |V\rangle_B = \frac{1}{\sqrt{2}} \left(\left|\Psi^+\right\rangle_{AB} + \left|\Psi^-\right\rangle_{AB}\right) \tag{2.25b}$$

$$|V\rangle_A |H\rangle_B = \frac{1}{\sqrt{2}} \left(\left|\Psi^+\right\rangle_{AB} - \left|\Psi^-\right\rangle_{AB}\right) \tag{2.25c}$$

$$|V\rangle_A |V\rangle_B = \frac{1}{\sqrt{2}} \left(\left|\Phi^+\right\rangle_{AB} - \left|\Phi^-\right\rangle_{AB}\right), \tag{2.25d}$$

where $|\Phi^\pm\rangle$ and $|\Psi^\pm\rangle$ are defined in Equation 2.12a and Equation 2.12b, respectively. One obtains

$$\begin{aligned} |\Psi\rangle_{In} = \frac{1}{2\sqrt{2}} \left[\left(|\downarrow\rangle_A |\downarrow\rangle_B + |\uparrow\rangle_A |\uparrow\rangle_B\right) \left|\Phi^+\right\rangle_{AB} + \right. \\ + \left(|\downarrow\rangle_A |\downarrow\rangle_B - |\uparrow\rangle_A |\uparrow\rangle_B\right) \left|\Phi^-\right\rangle_{AB} + \\ + \left(|\uparrow\rangle_A |\downarrow\rangle_B + |\downarrow\rangle_A |\uparrow\rangle_B\right) \left|\Psi^+\right\rangle_{AB} + \\ \left. + \left(|\uparrow\rangle_A |\downarrow\rangle_B - |\downarrow\rangle_A |\uparrow\rangle_B\right) \left|\Psi^-\right\rangle_{AB}\right]. \end{aligned} \tag{2.26}$$

Those two photons are sent into separate input ports of the experimental setup shown in Figure 2.1(a) for the case of a balanced beamsplitter. In Section 2.2.2 we already calculated the beamsplitter transformation for input Bell states and determined that only $|\Psi^-\rangle$ can lead to a coincident detection event in the output ports. That is, in the case of a coincident detection event, two photons in Equation 2.26 are destroyed but the full state collapses into the two atom entangled state.

$$|\Psi\rangle_{Coin.} = \frac{1}{\sqrt{2}} \left(|\uparrow\rangle_A |\downarrow\rangle_B - |\downarrow\rangle_A |\uparrow\rangle_B \right). \tag{2.27}$$

This non-deterministic measurement is equal to projecting the two photon input state via the operator $M = \mathcal{I} \otimes |\Psi^-\rangle \langle\Psi^-|$, where $\mathcal{I}$ is the one qubit identity operator followed by tracing out the photon state. In the absence of any losses the probability of this projection occurring is

$$p_{swap} = \langle \Psi_{In} \left| M^\dagger M \right| \Psi_{In} \rangle = \frac{1}{4}. \tag{2.28}$$

One sees that the heralded interaction of two halves of an entangled memory-photon pairs (the two photons) can result in *swapping* the quantum entanglement to two previously independent systems that do not share a common past (the atoms).

3

KEY COMPONENTS OF THE INNSBRUCK ION TRAP NETWORK AND MODEL

The first part of this chapter focuses on briefly summarizing established techniques that we use for manipulating the trapped ion and for producing single photons from the ion via an optical cavity. The second part of this chapter is dedicated to the theoretical model used for modeling the two-photon interference experiments presented in Chapter 5.

3.1 CALCIUM ION IN A LINEAR PAUL TRAP

The two nodes of our quantum network are called the "IQOQI node" and the "UIBK node". Both nodes of our quantum network use single trapped calcium ions, specifically $^{40}Ca^{+}$. This isotope of calcium is the most naturally abundant (96.941% natural occurance fraction [78]) and has no nuclear spin. Both nodes ionize neutral calcium using an isotope-selective two-photon process [79]. In this process, one of the two outer valence electrons are removed. Specifically, we use a diode laser tuned to 422 nm that excites the valence electron from the ground state $4s\,^1S_0$ to the excited state $4p\,^1P_1$. This first step selects the isotope that will be ionized and trapped. In the second step the excited electron receives enough energy to be transferred to the continuum [80]. Sufficient energy corresponds to a photon wavelength of 390 nm, however we use laser light at 375 nm.

The ion is trapped in each node using a 3D radio frequency linear Paul trap. Details on the IQOQI trap are presented in Chapter 4. Details on the UIBK trap can be found in [41, 81, 82]. The single trapped calcium ion has three orthogonal harmonic modes of motion in the trap. To give an example, the modes in the IQOQI trap used in the experiment presented in Chapter 5 are $\omega_x \approx \omega_y = 2\pi \times 2.0\,\text{MHz}$ in the radial direction, and $\omega_z = 2\pi \times 0.927\,\text{kHz}$ in the axial direction. A static magnetic field of approximately 4 Gauss is applied in the trapping regime to define the quantization axis. Figure 3.1 shows an energy diagram of the single outer valence electron in $^{40}Ca^{+}$, revealing the relevant energy levels used in our experiments as well as the transition wavelengths and excited state lifetimes.

The motional state of the ion is prepared via Doppler cooling using two laser fields. Laser light at 397 nm drives the $4^2S_{1/2} \rightarrow 4^2P_{1/2}$ transition with excited state lifetime 7.1 ns. The second laser field at 866 nm drives the transition $3^2D_{3/2} \rightarrow 4^2P_{1/2}$. This repumps the cases when the electron decays from $4^2P_{1/2}$ to $3^2D_{3/2}$. A more de-

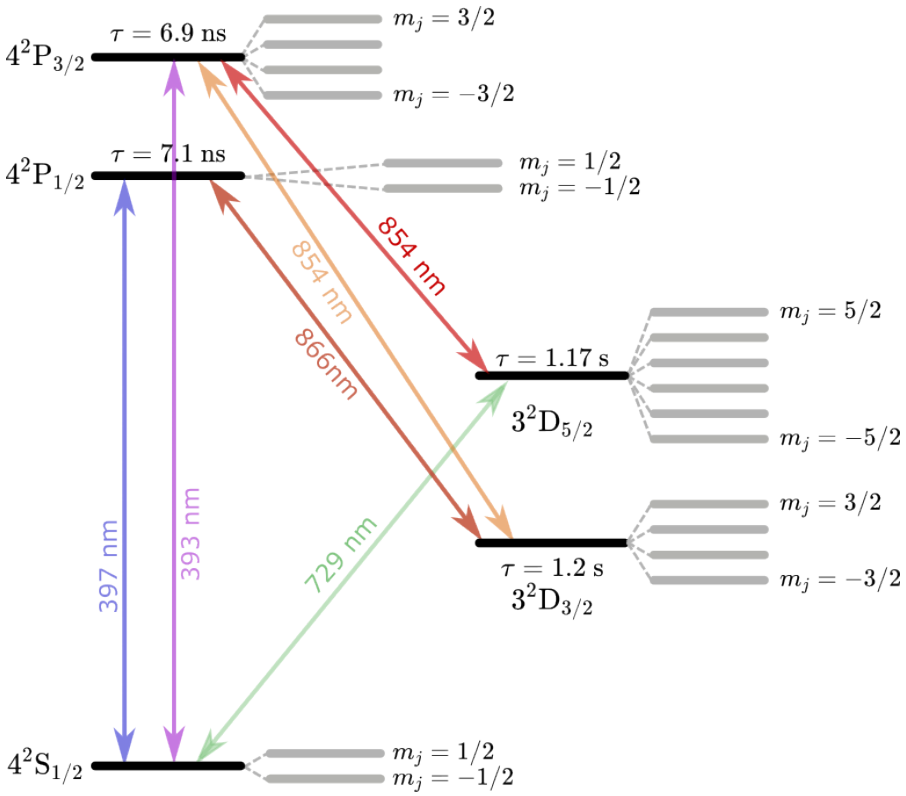

Figure 3.1: **Energy level scheme of the $^{40}Ca^+$ ion.** Each energy level is split in the presence of a magnetic field of a few Gauss as a consequence of Zeeman effect. Colored arrows represent transitions between levels and their wavelengths are labeled. The lifetime τ of each excited state is shown.

tailed description of Doppler cooling in a similar system to ours is described for example in Section 4.2 of Cornelius Hempel's thesis [47]. After Doppler cooling in the IQOQI trap during the experiments presented in Chapter 5, the expectation value of the number of motional quanta in the lowest frequency axial mode of $\omega_z/2\pi = 0.92\,\text{MHz}$ was measured to be 11 ± 2 [83].

There are methods to further decrease the ion temperature below the values achieved by Doppler cooling. Techniques of Electromagnetically-induced-transparency (EIT) cooling [84], resolved sideband cooling [85], Raman sideband cooling [86], or polarization gradient cooling [87] are commonly used to reach sub-Doppler temperatures or even motional ground state of trapped ions. In the work presented here we do not employ any of these.

After Doppler cooling, the electronic state of the ion is prepared via optical pumping. At IQOQI this is done via circularly polarized laser light at 397 nm. The UIBK node uses a different method of preparing the electronic state of the ion using a 729 nm laser. Details of both methods can be found in e. g., Section 4.3 of [47]. As a result, both systems are initialized in one of the Zeeman sub-levels of the electronic state $4^2S_{1/2}$. The probability of finding the electron in the target state is typically on the order 99% or higher.

Two states connected by the 729 nm electric quadrupole transition are used for encoding a qubit. The ground state is chosen in the $4^2S_{1/2}$ manifold and the excited state is chosen in the $3^2D_{5/2}$ manifold. The excited state lifetime $\tau = 1.17\,\text{s}$ [88] is far longer than the times required to implement single and two-qubit operations, which are on the order of microseconds [89]. This optical qubit implementation is used in state-of-the art experiments with trapped ions, including quantum simulators with 10 [90], 20 [91], or even 51 ions [92]. It has been also used in quantum processors [93] demonstrating fault-tolerant gate operations [94].

A 397 nm laser driving the $S_{1/2} \rightarrow P_{1/2}$ transition is used in combination with an 866 nm repumper laser driving the $D_{3/2} \rightarrow P_{1/2}$ transition to perform Doppler cooling and to determine the state of the qubit. If the electron is in the $S_{1/2}$ manifold, it will be driven by the lasers and scatter many 397 nm photons per second into free space. A fraction of those 397 nm photons are collected by detectors (Photomultiplier tube and EMCCD camera) such that the ion appears as bright. When the electron is in the $D_{5/2}$ manifold, it does not undergo the laser driven transitions and thus no photons are generated. The ion then appears dark on the detectors. This method provides state readout with nearly unit fidelity [95]. The method is used in the presented experiments to determine the presence of an ion in the trap after Doppler cooling and to detect the state of the ion in experiments presented in Chapter 6.

3.2 PHOTON GENERATION PROCESS

The two ion-trap nodes in this thesis are each equipped with an in-vacuum optical cavity to collect single 854 nm photons, which are emitted near-resonantly with the $P_{3/2} \rightarrow D_{5/2}$ transition. The ion in each system is confined in the center of the ion-trap and is placed simultaneously at the position of the waist of the cavity. The cavities are constructed in a *near concentric* geometry such that the waist of the cavity mode lies in the center of the cavity. More details on the cavity systems can be found in the PhD thesis of Josef Schupp (IQOQI node) [83] and of Konstantin Friebe (UIBK node) [82]. What follows now is a condensed summary of the photon generation process used in both network nodes.

A cavity mediated Raman transition (CMRT) is utilized to generate a single 854 nm photon from a trapped ion. The scheme was theoretically proposed by Law and Kimble in [96] and experimentally demonstrated with trapped ions by Keller *et al.* [97]. In the following paragraphs, the concept of the CMRT process will be introduced using a model of a three-level atom coupled to a cavity and driven by a laser. Detailed studies of the process can be found in PhD thesis of Carlos Russo [41] and of Josef Schupp [83].

Three levels, creating a $\Lambda-$ type configuration with two ground states $|s\rangle$ and $|d\rangle$ and one excited state $|p\rangle$, are used in the process. The $|d\rangle \leftrightarrow |p\rangle$ transition is coupled by a longitudinal vacuum mode of the cavity. The $|s\rangle \leftrightarrow |p\rangle$ transition is driven by a laser field with Rabi frequency Ω_{drive}. The atom is located in the waist w_0 of the optical cavity, which itself consists of mirrors T_1 and T_2. The situation is depicted in Figure 3.2. The state $|p\rangle$ spontaneously decays to the $|d\rangle$ state or the $|s\rangle$ state with decay rates γ_{pd} and γ_{ps}, respectively. Both the cavity and the driving laser are detuned from nearby atomic transitions by Δ_{cavity} and Δ_{drive}, respectively. The vacuum cavity mode is coupled to the atomic dipole moment with coupling strength g given by [83]

$$g = \sqrt{\frac{c\gamma r_{D5/2}}{2l\tilde{A}_{eff}}}\mathcal{G}_m\zeta = g_0\mathcal{G}_m\zeta, \tag{3.1}$$

where ζ accounts for the projection of the cavity polarization onto the atomic dipole moment, $\mathcal{G}_m = \sqrt{10/15}$ is the Clebsch-Gordan coefficient describing the transition amplitude between the state $|p\rangle$ and $|d\rangle$, $r_{D5/2}$ is a branching ratio, γ is total spontaneous emission rate of the excited state $P_{3/2}$, l is the cavity length and $\tilde{A}_{eff} = A_{eff}/\sigma$ is effective mode area, with σ being the absorption cross-section and $A_{eff} = \pi w_0^2/4$, where w_0 is the cavity waist.

When both the drive laser and the cavity are detuned by the same amount ($\Delta = \Delta_{drive} = \Delta_{cavity}$) from the excited state $|p\rangle$, the system finds itself in *Raman resonance* between the states $|s\rangle$ and $|d\rangle$.

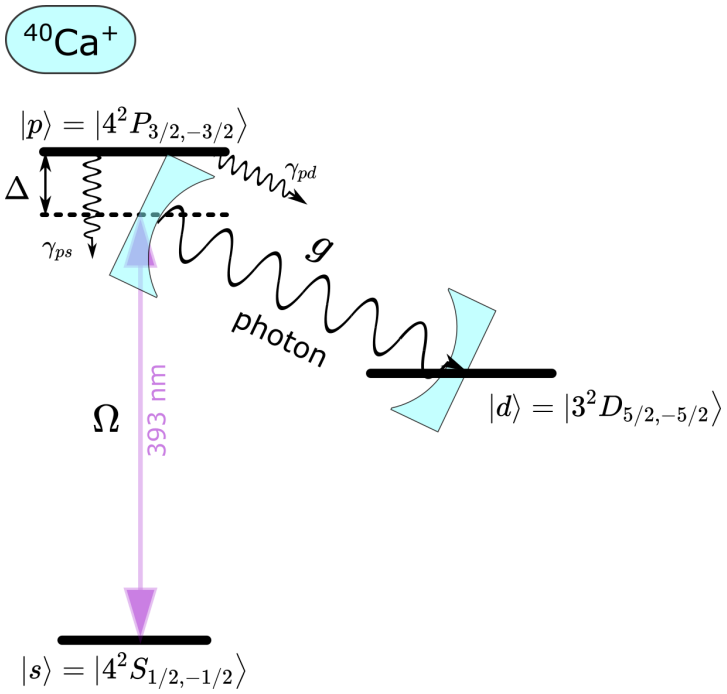

Figure 3.2: **Cavity-mediated Raman photon generation process in a three-level model of $^{40}Ca^+$ ion.** Ground state $|s\rangle$; metastable state $|d\rangle$, and excited state $|p\rangle$. The detuning $\Delta = \Delta_{drive} = \Delta_{cavity}$. The cavity-photon generation competes with spontaneous emission from the short-lived $|p\rangle$ state (decay rates γ_{ps} and γ_{pd}).

In the ideal case, the single photon generation process goes as follows. In the beginning, the ion is prepared in a ground state $|s\rangle$, see Figure 3.2. A drive laser pulse applied to the ion transfers the electron from $|s\rangle$ to $|d\rangle$ and a single 854 nm photon is emitted into the vacuum mode of the cavity.

The CMRT competes with spontaneous decay. During the process, the electron can be off-resonantly excited to the $|p\rangle$ state. From there it can spontaneously decay back to the $|s\rangle$ state by emitting a 393 nm photon into free space. In that case, the drive laser has another chance to generate a cavity photon via the CMRT. Alternatively the $|p\rangle$ state can decay to the $|d\rangle$ state. Once in the $|d\rangle$ state, the drive laser cannot re-excite the electron and the Raman process fails. In the ideal case, a generated cavity photon will exit the cavity via the designated output mirror, whose transmission is carefully chosen. Unwanted losses in the cavity mirrors and substrates can cause the cavity photon to be lost. In our network nodes, the atomic decay rate γ dominates over the cavity decay rate κ and the ion-cavity coupling rate g: That is $\gamma \gg \kappa, g$. To reduce the probability of spontaneous scattering occurring during the Raman process, the detuning Δ of the drive laser and of the cavity from the $|p\rangle$ state is chosen to be much larger than both the drive strength Ω_{drive} and the decay rate γ: $\Delta \gg \Omega_{drive}, \gamma$. Under this

condition the excited state can be adiabatically eliminated and the system treated as having effectively two levels: $|s\rangle$ and $|d\rangle$ [98–100][1]. The effective coupling rate of the Raman process is given by [41]

$$\Omega_{eff} = \frac{g\Omega_{drive}}{|2\Delta|}. \tag{3.2}$$

Furthermore, the spontaneous decay rate is reduced to the effective value

$$\gamma_{eff} = \left(\frac{\Omega}{2\Delta}\right)^2 \gamma, \tag{3.3}$$

where γ is the total decay rate of the excited state $|p\rangle$.

The CMRT process used in the experiments of Chapter 5 uses the specific transitions depicted in Figure 3.2. The 854 nm cavity photon generated on the employed σ^- transition is projected onto the plane given by the cavity axis and magnetic field. As a result, in our experimental setup, the photon leaving the cavity is vertically polarized.

The CMRT can be extended to produce photons entangled in their polarization with the electronic state of the ion [39, 81]. Here, a second Raman transition is driven simultaneously which leads to the generation of a horizontally polarized photon and leaves the electron in a second ($3^2D_{5/2,-3/2}$) Zeeman sub-level. When driven simultaneously with balanced coupling strengths, this bichromatic CMRT process implements the transformation

$$|s\rangle \rightarrow \frac{1}{\sqrt{2}}\left(|d\rangle\,|V\rangle + |d'\rangle\,|H\rangle\right), \tag{3.4}$$

where $|d\rangle$ and $|d'\rangle$ are the Zeeman sub-levels $D_{5/2,-5/2}$ and $D_{5/2,-3/2}$, respectively, and $|H(V)\rangle$ represents a single photon with horizontal (vertical) polarization. This bichromatic CMRT was first presented in [39] and became a standard tool for generating ion-photon entanglement in Innsbruck [101, 102].

3.3 3-LEVEL MODEL OF PHOTON DISTINGUISHABILITY IN OUR SYSTEM

This subsection presents a model for the distinguishability of photons produced via the cavity-mediated Raman photon generation process, for two independant network nodes. The development of the model was led by members of the group of Prof. Nicolas Sangouard, in collaboration with our teams in Innsbruck. The model is an extension of a previous one developed for a single ion-cavity node, in which the interference of two sequentially-produced photons was considered

1 However, as will be shown, finite population of the excited state during our experiments remains a limiting factor.

[69]. In summary, the photon generation process is modeled using a three level approximation for the internal electronic states of the ion with independently tunable parameters for each node. In case of matching parameters for both nodes, the only imperfection considered in the model that limits the predicted two-photon interference visibility is the spontaneous emission of photons from the excited electronic state of each atom. As will be shown in the experiments presented in Chapter 5, the limiting factor on the interference visibility in our ion-cavity systems is unwanted spontaneous emission from the ion during the cavity-mediated photon generation process. During the photon generation process, spontaneous decay events from the short-lived excited state ($|p\rangle$) onto the final state manifold ($|d\rangle$) act only as losses—no cavity photon is emitted through the Raman process if such an event occurs. In contrast, following any number of spontaneous decay events from $|p\rangle$ back to the initial state ($|s\rangle$) during the Raman laser pulse, a cavity photon can still be subsequently generated while the Raman laser remains on. Every spontaneously scattered photon carries away the information that the cavity photon has not yet been emitted. Consequently, the cavity photons impinging on the beamsplitter are each in a (temporally) mixed state and therefore they do not bunch perfectly when interfered at a beamsplitter.

3.3.1 *The Master equation*

The atomic model is restricted to a Λ-system formed by three levels $|s\rangle, |p\rangle$ and $|d\rangle$ (see Figure 3.3) corresponding to sublevels of $S_{J=1/2,m_j-1/2}$, $P_{J=3/2,m_j=-3/2}$ and $D_{J=5/2,m_j=-5/2}$ (or $D_{J=5/2,m_j=-3/2}$) that are of direct importance for the experiment, respectively. The model is valid for any three-level atom. The atom is initially prepared in the state $|s\rangle$. The $|s\rangle \rightarrow |p\rangle$ transition is off-resonantly driven by a laser with frequency $\omega_L = \omega_{ps} + \Delta - \delta_s$, where both Δ and δ_s are negative. The frequency $\delta_s = \Omega^2/4\Delta$, is the AC Stark-shift of the $|s\rangle$ state due to the laser field with Rabi frequency Ω. Let a and $a^\dagger$ be the bosonic annihilation and creation of the cavity field, respectively, whose frequency is given by $\omega_C = \omega_{pd} + \Delta$. The Hamiltonian of the laser-atom-cavity system is given by

$$\begin{aligned} H = {} & \omega_C a^\dagger a + \omega_{ps} |p\rangle\langle p| + \omega_{ds} |d\rangle\langle d| \\ & + \frac{1}{2}(e^{i\omega_L t} + e^{-i\omega_L t})(\Omega_t |s\rangle\langle p| + \Omega_t |p\rangle\langle s|) \\ & + g(|d\rangle\langle p| + |p\rangle\langle d|)(a^\dagger + a), \end{aligned} \tag{3.5}$$

where $\hbar$ is set to one and g is the ion-cavity coupling strength discussed in Section 3.2 and further in Section 5.4. The Hamiltonian can be simplified by noting that the cavity mode is initially empty $|0\rangle$. Therefore, the system remains in the three level manifold $\{|s,0\rangle, |d,1\rangle, |p,0\rangle\}$, where the last ket element describes the cavity photon number. Under

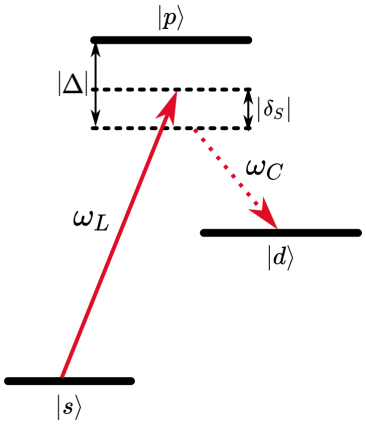

Figure 3.3: **Scheme of the Λ system relevant for the theoretical model and the experiment.** The transition between $|s\rangle$ and $|p\rangle$ is off-resonantly driven by a laser with frequency ω_L, detuned from the $|s\rangle$ to $|p\rangle$ transition by $|\Delta|$. The laser field induces AC Stark Shift $|\delta_S|$. States $|p\rangle$ and $|d\rangle$ are coupled by the field of a cavity with frequency ω_C. Note that in Figure 3.2, the AC-Stark shift δ_S is set to zero for simplicity.

the rotating wave approximation, the Hamiltonian in this subspace is thus given by

$$H_t = \begin{pmatrix} 0 & 0 & \Omega_t/2 \\ 0 & \delta_s & g \\ \Omega_t/2 & g & -\Delta + \delta_s \end{pmatrix}, \tag{3.6}$$

All cavity loss processes are captured by the rate κ, which includes e.g., transmission through the cavity mirrors, as well as any scattering and absorption losses in the mirror and mirror substrates. For the atom-cavity system, this process corresponds to a loss term $L_1 = \sqrt{2\kappa}\,|d,0\rangle\langle d,1|$. Finally, there are two scattering terms $L_2 = \sqrt{2\gamma_{sp}}\,|s,0\rangle\langle p,0|$ and $L_3 = \sqrt{2\gamma_{dp}}\,|d,0\rangle\langle p,0|$ corresponding to the two spontaneous decay paths from the $|p\rangle$ state. With this in hand, we can write down the master equation for the atom-cavity system

$$\dot{\varrho}_t = -\mathrm{i}\,[H_t, \varrho_t] + \sum_{i=1}^{3}\left(L_i \varrho_t L_i^\dagger - \frac{1}{2}\{L_i^\dagger L_i, \varrho_t\}\right), \tag{3.7}$$

where ϱ_t now is defined on a four level manifold including $|d,0\rangle$. H_t is extended trivially on the added level via $H_t\,|d,0\rangle = \delta_s\,|d,0\rangle$, that is, $|d,0\rangle$ is not coupled to the other three levels. Hence, the atom-cavity system evolves in the $\{|s,0\rangle, |d,1\rangle, |p,0\rangle\}$-manifold until it is brought to the state $|d,0\rangle$ either by the scattering term L_3 or via the cavity loss process L_1.

3.3.2 *Emitted photon*

The state of the photon emitted from the cavity into the desired mode is now studied. In the following, the photon state is computed in two steps. First, the sub-normalized wave-function of a photon conditioned on the atom-cavity system being in the state $|s,0\rangle$ at time s and no scattering events L_2 and L_3 happening at later times is obtained. Second, the full master equation is solved to compute the probability of scattering via L_2 happening at time s. Such a scattering event projects the system back onto $|s,0\rangle$.

3.3.2.1 *Conditional pure photon wave-function*

Let us start by addressing the wave-function of a photon conditioned on the atom-cavity system being in the state $|s,0\rangle$ at time s and no scattering events L_2 and L_3 happening at later times. To do so, the evolution of the atom-cavity system conditioned to the case with no scattering needs to be solved. The Lindbladian part of the master equation (Equation 3.7) describes random noise processes affecting the system. In particular, the terms $L_i\varrho_t L_i^\dagger dt$ corresponds to a scattering happening during an infinitesimal time interval dt. In contrast, the conjugate term $-\frac{1}{2}\{L_i^\dagger L_i,\varrho_t\}dt$ corresponds to no scattering happening during dt. Its role can be thought of as reducing the probability to find the system in the pre-scattered state $\varrho_{t+dt}\to\varrho_t-\frac{1}{2}\{L_i^\dagger L_i,\varrho_t\}dt$. Hence, to describe the evolution of the system conditioned on no scattering, all the terms $L_i\varrho_t L_i^\dagger$ are dropped and their conjugate terms $-\frac{1}{2}\{L_i^\dagger L_i,\varrho_t\}$ in the master equation (Equation 3.7) are kept. Such an evolution preserves the purity of a state, which can be written in the form of the Schrödinger equation with a non-Hermitian Hamiltonian

$$|\dot{\Phi}_t\rangle=\left(-\mathrm{i}H_t-\frac{1}{2}\sum_i L_i^\dagger L_i\right)|\Phi_t\rangle\,. \tag{3.8}$$

With the initial condition $|\Phi_s\rangle=|s,0\rangle$, this equation can be solved to give the system state $|\Phi_{t|s}\rangle$ conditioned on the event corresponding to no scattering at time $t\geq s$. In particular, for a (piece-wise) constant Rabi frequency, the solution reads $|\Phi_{t|s}\rangle=e^{\left(-\mathrm{i}H-\frac{1}{2}\sum_i L_i^\dagger L_i\right)(t-s)}|s,0\rangle$ which can be computed numerically. To obtain the amplitude of the photon emitted from the cavity at a given time we project the atom-cavity state at that time into $\sqrt{2\kappa}\,\langle d,1|$. In the laboratory frame, this gives

$$\begin{aligned}|\psi_s\rangle&=\int_s^\infty \psi_s(t)\,a_t^\dagger\,|0\rangle\,dt,\\ \psi_s(t)&=\sqrt{2\kappa}\,e^{-\mathrm{i}\omega_C t}\,\langle d,1|\Phi_{t|s}\rangle.\end{aligned} \tag{3.9}$$

The photonic state $|\psi_s\rangle$ is sub-normalized. Its norm

$$p_{pure}(s)=\langle\psi_s|\psi_s\rangle \tag{3.10}$$

is the probability that no scattering event happens after time s (given the initial condition). The normalized conditional state thus reads $|\psi_s\rangle / \sqrt{p_{pure}(s)}$. Note that $p_{pure}(0)$ is the probability that a photon is emitted without a single scattering during the evolution and the corresponding state is labeled $|\Psi_0\rangle = |\Psi_s\rangle / p_{pure}(0)$.

3.3.2.2 *Scattering probability*

The full master equation (Equation 3.7) is now solved and the atom-cavity density matrix ϱ_t for all times is obtained. For a (piecewise) constant Rabi frequency, the solution can be obtained analytically by vectorizing the master equation and the density matrix. The probability of scattering back to $|s, 0\rangle$ at time s is computed from this state as

$$P(s) = \mathrm{Tr}\left(\varrho_s L_2^\dagger L_2\right). \tag{3.11}$$

Note that the average number of L_2 scattering events per experimental run is simply given by the time integral of the scattering rate

$$\int_0^\infty P(s)ds, \tag{3.12}$$

and equals the expected number of laser photons scattered on the $|p\rangle \to |s\rangle$ transition. In our experiments, these are the ultraviolet photons emitted on spontaneous decay from $|p\rangle$ state back to initial $|s\rangle$ state. After such a scattering event the system is brought back to the initial state.

3.3.2.3 *The photon state*

The normalized state of the emitted photon that leaves the cavity at rate κ is given by

$$\rho = |\psi_0\rangle\langle\psi_0| + \int_0^\infty P(s)\,|\psi_s\rangle\langle\psi_s|\,ds + P_0\,|0\rangle\langle 0|\,, \tag{3.13}$$

where $|\psi_s\rangle$ is given in Equation 3.9 and $P(s)$ in Equation 3.11. The first term $|\psi_0\rangle\langle\psi_0|$ describes a pure cavity photon emitted without a single scattering event occur (L_2, L_3). This happens with probability $p_{pure}(0)$. The integral collects all the possibilities where the last $|p\rangle \to |s\rangle$ scattering process occurs at time s and no scattering events happen at later times. Any such history happens with probability $P(s)p_{pure}(s)$ and yields a photon in the state $|\psi_s\rangle / \sqrt{p_{pure}(s)}$. Finally, the last term $P_0\,|0\rangle\langle 0|$ with

$$\begin{aligned} P_0 &= 1 - \mathrm{Tr}\left(|\psi_0\rangle\langle\psi_0| + \textstyle\int_0^\infty P(s)\,|\psi_s\rangle\langle\psi_s|\,ds\right) \\ &= 1 - p_{pure}(0) - \int P(s)p_{pure}(s)ds \end{aligned} \tag{3.14}$$

collects the cases where no photon is emitted into the cavity. If the laser pulse is not turned off, this term can be alternatively computed as the overall probability of the $|p\rangle \rightarrow |d\rangle$ scattering

$$P_0 = \int_0^\infty \mathrm{Tr}(L_3^\dagger L_3 \rho_t). \tag{3.15}$$

The first two contributions of Equation 3.13 can be combined together by defining

$$\bar{P}(s) = P(s) + 2\delta(s), \tag{3.16}$$

where $\delta(s)$ is the delta-function with $2\int_0^\infty \delta(s)ds = 1$. The photon state ρ in Equation 3.13 then reads

$$\rho = \int_0^\infty \bar{P}(s)\,|\psi_s\rangle\langle\psi_s|\,ds + P_0\,|0\rangle\langle 0|\,. \tag{3.17}$$

3.3.3 *Effect of non-zero laser linewidth*

The effect of non-zero laser linewidth on our model is now described. The laser frequency linewidth, taken as half-width at half maximum, denoted as γ_{laser} introduces a phase noise which creates an additional loss term in the master equation (Equation 3.7) and changes it to

$$\dot{\varrho}_t = -\mathrm{i}\,[H_t, \varrho_t] + \sum_{i=1}^{4}\left(L_i \varrho_t L_i^\dagger - \frac{1}{2}\{L_i^\dagger L_i, \varrho_t\}\right), \tag{3.18}$$

where $L_4 = \sqrt{2\gamma_{laser}}\,|s,0\rangle\,\langle s,0|$ is a collapse operator corresponding to dephasing due to the non-zero laser linewidth. This dephasing term also alters the scattering probability in Equation 3.11 to

$$P(s) = \mathrm{Tr}\left(\varrho_s\, L_2^\dagger L_2\right) + \mathrm{Tr}\left(\varrho_s\, L_4^\dagger L_4\right). \tag{3.19}$$

The rest of the model remains unchanged.

3.3.4 *Photon statistics*

Now the Hong-Ou-Mandel (HOM) interference of two photons described by Equation 3.17 is modeled. Specifically, each photon enters into a different input port of a 50/50 beamsplitter. In the following the input and output modes of the beamsplitter are the same as in Section 2.2. Output port detectors $D_{a'}$ and $D_{b'}$ as shown in Figure 2.1(a) are considered with unit efficiency.

3.3.4.1 *Single click rates*

First, the case of a single photons injected into one of the ports is considered. This serves to provide an expression of the single photon detection probability from a single photon source (up to a factor

1/2 due to the beamsplitter). The probability density that a photon in the state ρ (Equation 3.17) triggers a click on the detector $D_{a'}$ at time t is given by $p_s(t) = \frac{1}{2}\mathrm{Tr}\left(\rho\, a_t^\dagger\, |0\rangle\langle 0|\, a_t\right)$. The 1/2 factor comes from the 50/50 beamsplitter. Direct application of Equation 3.17 and Equation 3.9 gives

$$p_s(t) = \epsilon \frac{1}{2} \int_0^\infty \bar{P}(s) |\psi_s(t)|^2 ds, \tag{3.20}$$

where $0 \leq \epsilon \leq 1$ is a factor that describes the total efficiency of the path, beginning after the cavity output mirror. The same result is obtained for the detector $D_{b'}$.

3.3.4.2 *Coincidence rates*

The twofold coincidence rate when one photon is sent into each input of the beamsplitter can now be computed. For two photons with orthogonal polarization, corresponding to states ρ_a and $\rho_{b_\perp}$, the probability to get a click at time t_1 in the detector $D_{a'}$ and a click at time t_2 in the detector $D_{b'}$ is given by

$$p_{C\perp}(t_1, t_2) = p_S^{(a)}(t_1) p_S^{(b_\perp)}(t_2) + p_S^{(a)}(t_2) p_S^{(b_\perp)}(t_1) \tag{3.21}$$

simply because there is no interference.

Next, two input photons with the same polarization ρ_a and ρ_b are considered. They are respectively characterized by $\bar{P}_a(s_a)$ with $\psi_{s_a}^{(a)}$ and $\bar{P}_b(s_b)$ with $\psi_{s_b}^{(b)}$ accordingly to Equation 3.17. The twofold coincidence probability with detector $D_{a'}$ clicking at time t_1 and detector $D_{b'}$ clicking at t_2 is computed as $p_{C\|}(t_1, t_2) = \mathrm{Tr}\left(\rho_a \otimes \rho_b\, \Pi_{t_1,t_2}\right)$ where Π_{t_1,t_2} is the projector onto the state

$$\frac{1}{2}(a_{t_1}^\dagger + b_{t_1}^\dagger)(a_{t_2}^\dagger - b_{t_2}^\dagger)\, |00\rangle \tag{3.22}$$

and e.g., $a_{t_1}^\dagger$ is the bosonic creation operator for the input mode a at time t_1, as in Equation 3.9. From Equation 3.17 and Equation 3.9 we find

$$\begin{aligned} p_{C\|}(t_1, t_2) = \frac{1}{4} \int_0^\infty & \bar{P}_a(s_a) \bar{P}_b(s_b) \times \\ & |\psi_{s_a}^{(a)}(t_1) \psi_{s_b}^{(b)}(t_2) - \psi_{s_a}^{(a)}(t_2) \psi_{s_b}^{(b)}(t_1)|^2 ds_a ds_b, \end{aligned} \tag{3.23}$$

where the term under the integral reads

$$\begin{aligned} & |\psi_{s_a}^{(a)}(t_1) \psi_{s_b}^{(b)}(t_2) - \psi_{s_a}^{(a)}(t_2) \psi_{s_b}^{(b)}(t_1)|^2 = \\ & |\psi_{s_a}^{(a)}(t_1)|^2 |\psi_{s_b}^{(b)}(t_2)|^2 + |\psi_{s_a}^{(a)}(t_2)|^2 |\psi_{s_b}^{(b)}(t_1)|^2 \\ & - \psi_{s_a}^{(a)}(t_1) \psi_{s_a}^{(a)*}(t_2)\, \psi_{s_b}^{(b)*}(t_1) \psi_{s_b}^{(b)}(t_2) \\ & - \psi_{s_a}^{(a)*}(t_1) \psi_{s_a}^{(a)}(t_2)\, \psi_{s_b}^{(b)}(t_1) \psi_{s_b}^{(b)*}(t_2). \end{aligned} \tag{3.24}$$

The last two terms are responsible for a destructive interference and bunching of the incident photons, which reduces the coincidence rate as compared to the orthogonal case.

3.3.4.3 *Visibility of the Hong-Ou-Mandel pattern*

The absolute detection times t_1 and t_2 are not relevant for computing the visibility of the Hong-Ou-Mandel (HOM) interference pattern. What matters is the difference between the detection times

$$\tau = t_1 - t_2. \tag{3.25}$$

We define the coincidence rate as a function of this delay between the clicks

$$p_{C\|(\perp)}(\tau) = \int p_{C\|(\perp)}(t_2 + \tau, t_2)\, dt_2. \tag{3.26}$$

Furthermore, detection window T is defined, by accepting only the coincidence events with a delay $|\tau| \leq T$ falling inside this window. For a fixed window T the HOM interference visibility is defined as

$$V(T) = 1 - R(T) \tag{3.27}$$

where $R(T)$ is the ratio between the coincidence probabilities for parallel and orthogonal photons (polarizations) with a bounded delay $|\tau| < T$

$$R(T) = \frac{\int_{-T}^{T} p_{C\|}(\tau) d\tau}{\int_{-T}^{T} p_{C\perp}(\tau) d\tau}. \tag{3.28}$$

3.3.5 *Constant frequency offset of two photons*

Here, a fixed frequency offset between the two interfering photons is considered. The frequency difference affects the phase of the photonic wavefunction as the phase is proportional to its frequency. This effect is modeled by modifying the wavefunction of one of the participating photons $\psi_s(t)$ in Equation 3.9. Specifically, the factor ω_C is replaced with $\omega_C + 2\pi\delta_f$, where δ_f is a constant offset of the photon's frequency. As a result the last two terms in Equation 3.24, which are responsible for interference in the coincidence probabilities, each pick up a phase. Let the photon wavefunctions of the photons at times t_1 and t_2 be written using

$$\begin{aligned}
\psi_{s_a}^{(a)}(t_1) &= a(t_1) e^{i\omega_a t_1} \\
\psi_{s_a}^{(a)}(t_2) &= a(t_2) e^{i\omega_a t_2} \\
\psi_{s_b}^{(b)}(t_1) &= b(t_1) e^{i\omega_b t_1} \\
\psi_{s_b}^{(b)}(t_2) &= b(t_2) e^{i\omega_b t_2},
\end{aligned} \tag{3.29}$$

where $a(t)$ and $b(t)$ are amplitudes and ω_a and ω_b are frequencies of the photons a and b, respectively. When substituted into Equation 3.24, the last two terms will each pick a phase. One term picks a phase

$$e^{i(\phi_a(t_1) - \phi_a(t_2) - \phi_b(t_2) + \phi_b(t_1))} \tag{3.30}$$

and the other picks phase

$$e^{-i(\phi_a(t_1)-\phi_a(t_2)-\phi_b(t_2)+\phi_b(t_1))}. \tag{3.31}$$

Here, $\phi_k(t_j)$ is a phase of a photon k at time j. By substituting $\omega_f = \omega_a - \omega_b$, an oscillation term $\cos(\omega_f(t_2 - t_1))$ appears in Equation 3.24, where $\omega_f = 2\pi\delta_f$ is the frequency difference. Then the coincidence rate is calculated.

Modifying the model in a described way, by replacing $\omega_C \to \omega_C + \delta_f$ is equivalent to adding a constant frequency offset to one of the photons once it leaves the cavity. This is not a process that we expect to be happening during our experiments. However, as will be shown in Chapter 5, it provides a useful simplified model for describing the results of our experiments.

4

DEVELOPMENT OF THE "IQOQI" ION-CAVITY NETWORK NODE

At the heart of each of our network nodes is an ion trap with an integrated optical cavity. The system is operated under vacuum to minimize interactions between the ion and background gas molecules. This chapter presents the construction of the IQOQI node of our quantum network. The structure of the chapter is now briefly described. First the design and components of the vacuum vessel are presented. Second, the top flange assembly, which carries the ion trap, and the bottom flange assembly, carrying the optical cavity setup and an atomic oven, are described. Third, the process used to achieve ultra-high vacuum (UHV) are described, necessary for operating the trap. The last part of this chapter is dedicated to the design and construction of a helical resonator which delivers radio-frequency voltage to the ion trap.

4.1 VACUUM VESSEL

A 3D drawing of our vacuum system is depicted in Figure 4.1. The vacuum vessel, inside which our ion-trap and optical cavity are placed, has been designed such that sufficient optical access is provided for bringing necessary laser light for manipulating the ion's electronic state, stabilizing the length of the cavity and collecting photons emitted into the optical cavity. To keep the pressure of the system in the UHV regime, we attach an ion pump and a non-evaporable getter to our chamber, as described in a later subsection. The vacuum chamber consists of two parts. The main part, custom made by the Kimball company is based on the MCF600-sphcube model, contains the ion trap and the cavity. The second part, referred to as "the cross", has an ion pump, a valve and one viewport. The "cross" was made by the company VACOM and has part number X63RS-304.

All items of the vacuum chamber are attached using con-flat (CF) flanges of various standardized sizes ranging from DN16 up to DN100. The CF attachment enables reaching UHV or even XHV conditions.

Standard viewports

Optical access to the trap is achieved by attaching glass viewports to the vacuum chamber. These viewports are made of 316LN stainless steel with quartz glass which is anti-reflection coated at wavelengths necessary for operating experiments with $^{40}Ca^{+}$ ions, as described

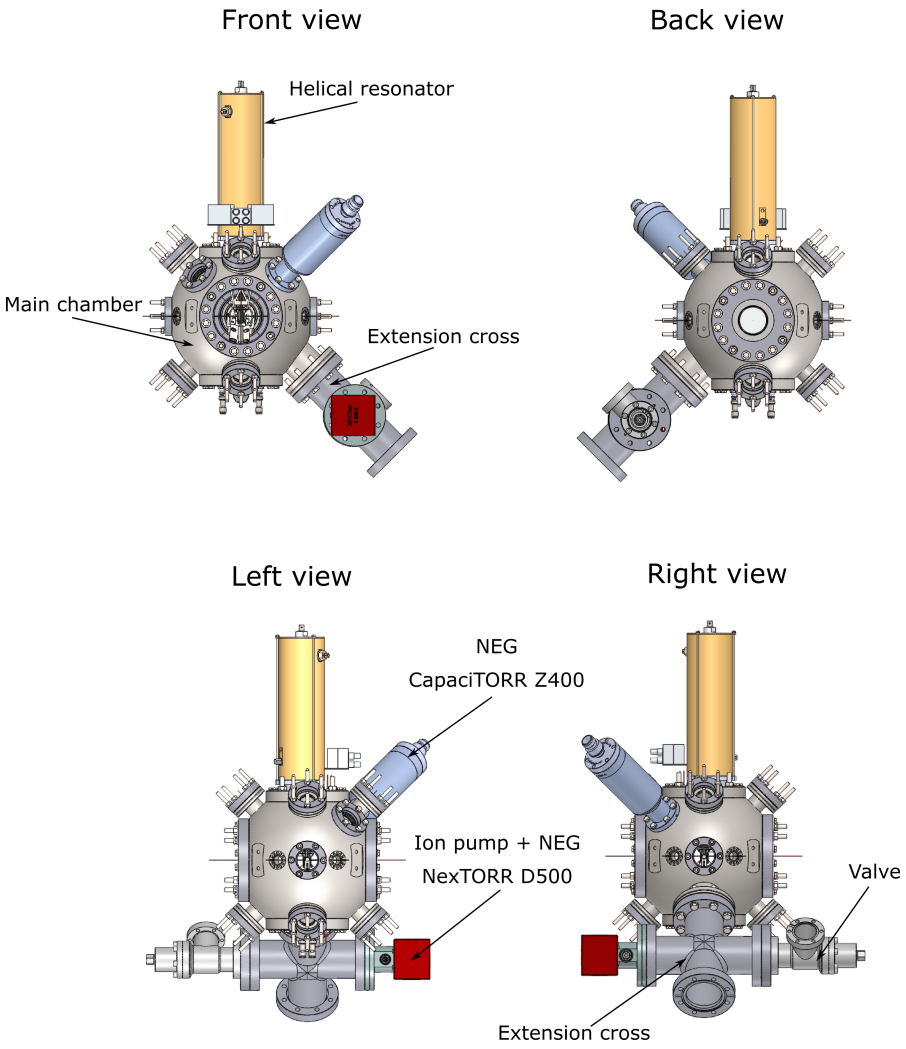

Figure 4.1: **A 3D drawing of the IQOQI node vacuum system.** The vacuum setup, containing the ion trap and optical cavity, is shown from four perspectives. To get a scale, the golden helical resonator on top of the chamber is 259.9 mm tall and the front flange in the top left figure is size DN100. NEG - Non Evaporable Getter. The CapaciTORR Z400 NEG has not been fully activated (as of February 2023).

below. In total 16 viewports are attached to the vacuum chamber. Fourteen of our viewports were made by the company VACOM and are specified to withstand a baking temperature of up to 200°C. Four viewports are on DN16 flanges and have glass diameter 16 mm. Eight viewports are mounted on DN40 with glass diameter 35 mm. One of these viewports, located on the top left side from DN100 viewport (see "Front view" in Figure 4.1), is not anti-reflection coated. One viewport has the size DN100 with glass diameter 98 mm. All the aforementioned viewports are attached to the main part of our vacuum chamber. One viewport of size DN63 with glass size of 68 mm is placed on the cross. The quoted parameters of reflections by VACOM are:

- $R < 1\%$ at wavelengths range $393 - 398$ nm
- $R < 0.3\%$ at 729 nm
- $R < 0.1\%$ at 780 nm
- $R < 0.2\%$ at 851 nm
- $R < 0.5\%$ at 866 nm

These parameters apply to both surfaces of the viewports. The calculated reflection curves provided by the manufacturer are shown in Figure A.1 of Appendix A.

Two viewports of the size DN40 that are placed in the direction of the optical cavity were made and anti-reflection coated by the company UKAEA. These optical viewports have been selected for their high optical quality as desired for transmitting single photons collected from the optical cavity out of the vacuum chamber. The result of the anti-reflection coating of these two viewports is reported in Figure A.2 of Appendix A

Inverted viewport

The inverted viewport is an element that enables an objective with high numerical aperture (NA) to be placed as close to the ion as possible without the need for it to be placed under vacuum. Our objective (Silloptics GmbH[1]) is designed for a working distance (ion-objective distance) of 59 mm. To achieve such a small distance, a viewport that recesses into the chamber is attached to the chamber. The viewport is welded into the center of a DN100 flange, but the glass itself corresponds to the DN40 size. A tube of diameter 54.5 mm recesses into the chamber. While the last glass surface of the objective

1 The objective was manufactured many years before my PhD for the 'quantum simulation' team at IQOQI and was ordered by Jan Benhelm. It is a five lens objective allowing both imaging of collected 397 nm photons as well as single-ion focusing of 729 nm laser light.

is 59 mm from the ion, the last glass surface of the inverted viewport is only 39.2 mm away from the ion.

The main purpose of the objective is to collect 397 nm photons emitted by the ion. The anti-reflection coating of the inverted viewport has therefore been designed for this wavelength. Additionally, the objective is also used for 729 nm laser light and thus the viewport is also antireflection coated for this wavelength. The production and antireflection coating of the inverted viewport was done by the company UKAEA. The result of the antireflection coating is shown in Figure A.2 in Appendix A.

Combined ion pump and NEG

While with externally attached turbomolecular pumps, pressures on the order 10^{-9} mbar can be reached, achieving and maintaining UHV conditions is possible by employing ion pumps and getters after separating the vacuum chamber from the outer environment. Ion pumps use electric and magnetic fields to ionize the background gas and trap the positively charged ions, as well as negative electrons, inside. The action of the ion pump generates a measurable current across the device, which can be used to estimate the pressure inside the vacuum chamber.

Getter pumps use reactive alloys, typically made of titanium or zirconium, to dissociate active gases, like O_2, N_2, CO, CO_2, H_2O, or even H_2. The particles are then permanently trapped in the structure of the getter in the form of a stable compound.

Both types of pumps are used in our setup. First, the SAES NexTORR D500 combined ion pump with non-evaporable getter (NEG) is mounted on a DN60 flange made of 304 grade stainless steel and attached to one port of an extension cross of our vacuum chamber (Figure 4.1). The D500 is equipped with two magnets which limit the maximum bake-out temperature to 150°C. If the magnets are removed, as was done in our case, the maximum bake-out temperature increases to 250°C. The pump is connected and operated using a controller (NIOPS-04) via cables designed for a maximum temperature of 200°C. The combined ion pump and NEG is specified to reach a pumping speed for hydrogen of 500 l/s if the NEG is properly activated.

Additionally, another NEG (SAES CapaciTorr Z-400) was attached to the chamber to further improve the vacuum in our chamber. This additional getter pump is placed into an extension tube to increase the distance to the optical cavity, in order to protect it from heat generated during NEG activation, where it can reach temperatures of up to 550°C. This Z-400 is mounted on a DN40 flange made of 316 LN stainless steel and can be baked at temperatures up to 400°C. When properly activated, this getter is specified to reach pumping speeds

greater then 530 l/s. Its activation is controlled by a special controller (CAPACITORR CF 35 D 400/B 200).

Both the ion pump and the NEG need to be activated during the bake-out process in order to reach their maximum pumping speed. The activation procedure for NEGs requires heating up the element up to 500°C and above, and keeping it at this temperature for approximately an hour. The activation of the ion pump and NEGs attached to our chamber was performed during the bake-out of the chamber described later in Section 4.4.

The pumping capabilities of any NEG deteriorates over time as the active area saturates. If the pumping speed is not sufficient anymore, a reactivation of this element by heating it up again is necessary, and can be carried out via the controller box. Under certain circumstances this can be done even without opening the vacuum chamber.

Valve

The vacuum chamber is isolated from the outer environment using a mechanical valve (VAT 54132-GE02-0001). This valve is made of 316L steel with CF flanges of size DN40 and is attached to our cross with a DN63 flange via a reducer flange (VACOM ZL063040-316). The valve was closed on January 16th 2018 and has not been opened since (as of February 2023).

4.2 TOP FLANGE ASSEMBLY AND THE ION TRAP

Our ion trap is based on a well established design of a radio frequency (RF) linear Paul three-dimensional blade trap, used in Innsbruck and elsewhere, which enables trapping multiple ions in a string along the trap axis. The distance of over 1 mm in all directions between blade electrodes enables optical access for all lasers necessary for manipulating the ion, while keeping scattered light low. Most importantly for cavity QED experiments it allows for the mode of the cavity to clear the trap without clipping.

The ion trap is attached to a DN100 flange and is inserted into the vacuum chamber from the top port. The ion-trap assembly is depicted in Figure 4.2 and we refer to it as the "Top Flange" assembly. A detailed schematic of the trap is shown in Figure 4.3. The trap consists of four blade electrodes aligned around the radial direction of the trap where RF field is applied to two opposing blades to create a confining potential in the radial direction of the trap. Two other blades are connected to a DC field, provided by a single 1.5 V AA battery to break the radial symmetry of the trapping potential. In the axial direction, the ions are trapped using positive DC fields applied to endcap electrodes. Any stray fields that would cause the ion to be pushed out of the RF zero potential in the radial direction can be

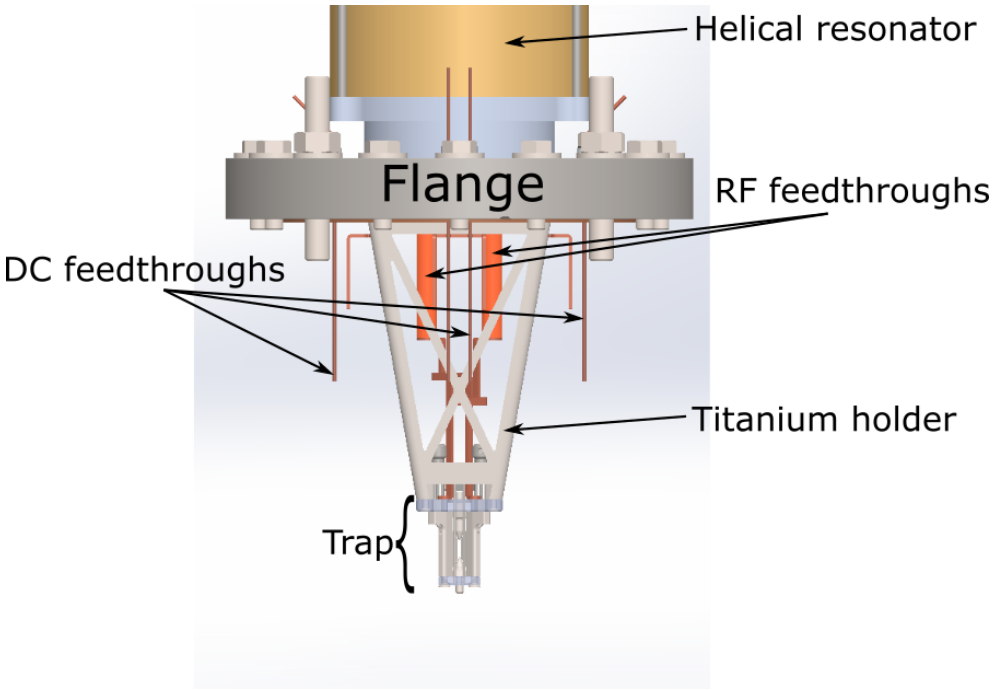

Figure 4.2: **A drawing of the top flange (size DN100) assembly carrying the ion trap.**

compensated by a set of double-rod electrodes in two perpendicular planes of the trap. Each DC electrode is controlled separately using a high voltage power supply.

Previous experience with traps made of stainless steel electrodes and ceramic (Macor) holders showed high temperatures during their operations, reaching up to 150°C [103]. In contrast, our trap is made out of gold-coated titanium blades and end cap electrodes, and sapphire holders, which have proven to achieve close to room temperature operation [104]. Those materials were used for the trap in the "precision" ion-trapping group formerly in Lab 2 at IQOQI, in which mixed species of trapped aluminum and calcium ions were used for precise frequency measurements [105] and implementation of ultra fast quantum gates [106].

As shown in Figure 4.3, the ion trap assembly has a height 80.28 mm. This includes also the length of copper electrodes that bring the RF field onto the blades. The ion trap itself has height of 27.85 mm and a maximum width 28.00 mm, given by the bigger of the two sapphire holders. The distance between the two endcap electrodes is 5.00 mm. In the radial direction, the distance between two opposing RF blades is 1.60 mm. Copper RF electrodes are attached to feedthroughs that are welded into the flange. The DC potential is brought to the endcap and compensation electrodes using Kapton® insulated single-core coax cable (LewVac KAPWC1X025). The core of the cable is made of silver-plated copper wire of diameter 0.25 mm. The wire is shielded by a braided tube against noise and the braid is grounded

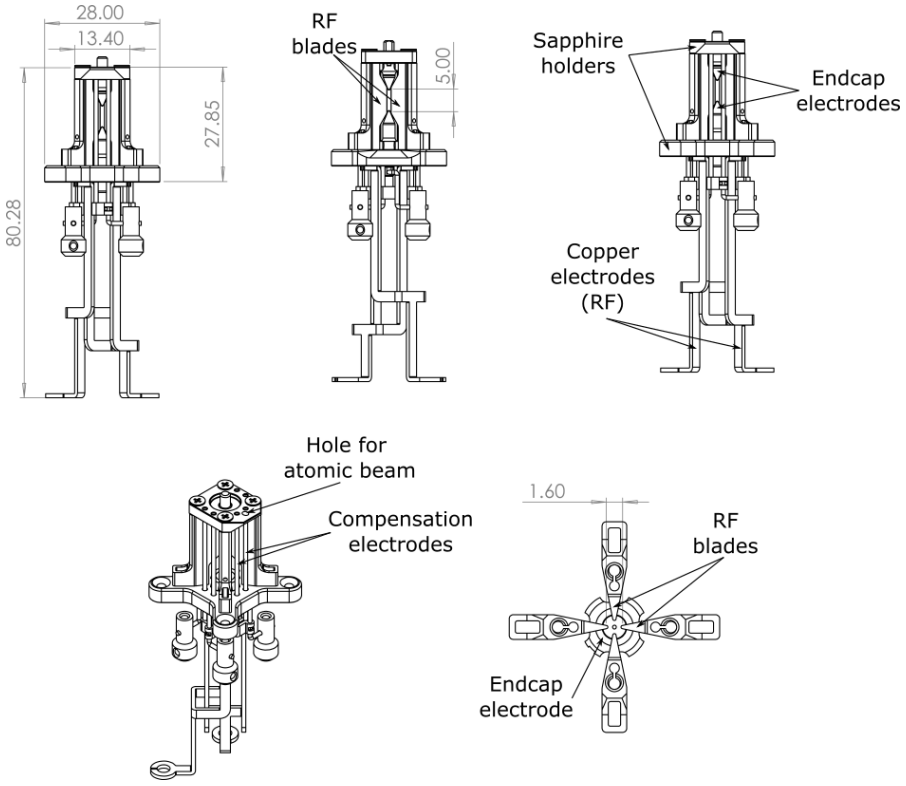

Figure 4.3: **Different views of the ion trap assembly.** The top three panels show the trap in an axial view (vertical direction) with significant dimensions labeled in mm. The bottom right panel shows a cut of the trap in the radial plane.

through the titanium holder to the main chamber (Figure 4.2). These cables are suitable for use in UHV conditions and have maximum bake-out temperature of 260°C. The Kapton wires can bring DC voltages up to 2 kV, or AC voltages with 600 V_{rms}, to the trap. Their maximum current rating is 2 A. The wires are attached to the top endcap electrode, as well as to compensation electrodes, using barrel-type clamps. The attachment to the bottom endcap electrode is done by winding the wire around the the outer side of the bottom endcap electrode and clamping it with a washer and a nut. Attachement to the copper feedthroughs is done using barrel type connectors. Each DC potential is brought through a separate copper feedthrough enabling independent control of each potential[2]. The connection of each trap electrode to its feedthrough is schematically depicted in Figure 4.4.

The trap is attached to a titanium holder which is then fixed to the top CF100 flange. The design and dimensions of this holder are shown in Figure 4.5. A target for producing neutral Ca atoms is attached to that holder for possible ablation loading of ions into the trap (not shown in Figure 4.5). A photograph in Figure 4.6 shows the assembled

2 DC feedthroughs depicted in Figure 4.2 were later trimmed to minimize any electronic noise that they might pick up.

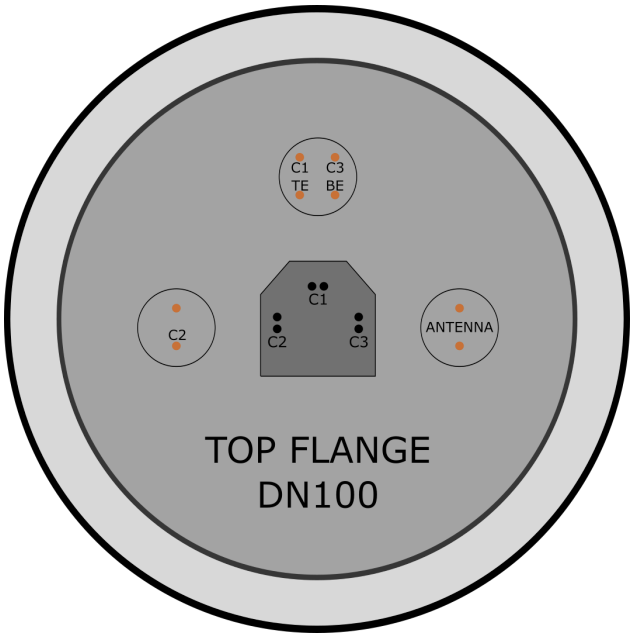

Figure 4.4: **A schematical drawing of connection of each electrode of the trap to a feedthrough.** C1, C2, and C3 mark the compensation electrodes, TE is top endcap electrode, BE is bottom endcap electrode. View is from the inside of the chamber looking out.

top flange before it was inserted into the vacuum chamber. Before the second bake-out, unused copper feedthroughs were trimmed.

4.3 BOTTOM FLANGE ASSEMBLY AND THE OPTICAL CAVITY

The second crucial part of our vacuum system is the optical cavity assembly which is attached to a DN100 flange and is inserted into the vacuum chamber from the bottom port. This flange contains the cavity and the atomic oven and we refer to it as the "bottom flange". Its assembly is depicted in Figure 4.7.

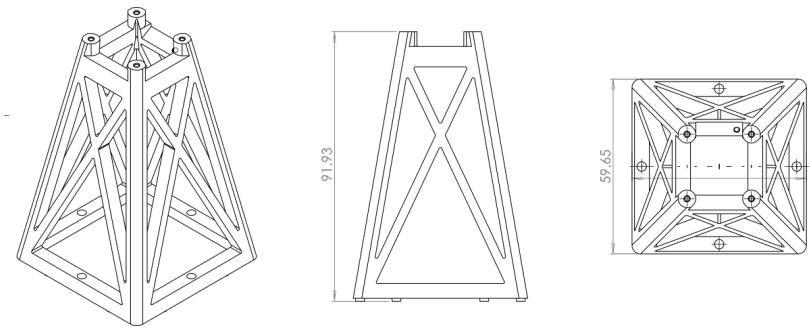

Figure 4.5: **A drawing of the Titanium trap holder.** This holder connects the ion trap assembly of Figure 4.3 to the top flange ofthe vacuum chamber, as shown in Figure 4.2. All dimensions are in mm.

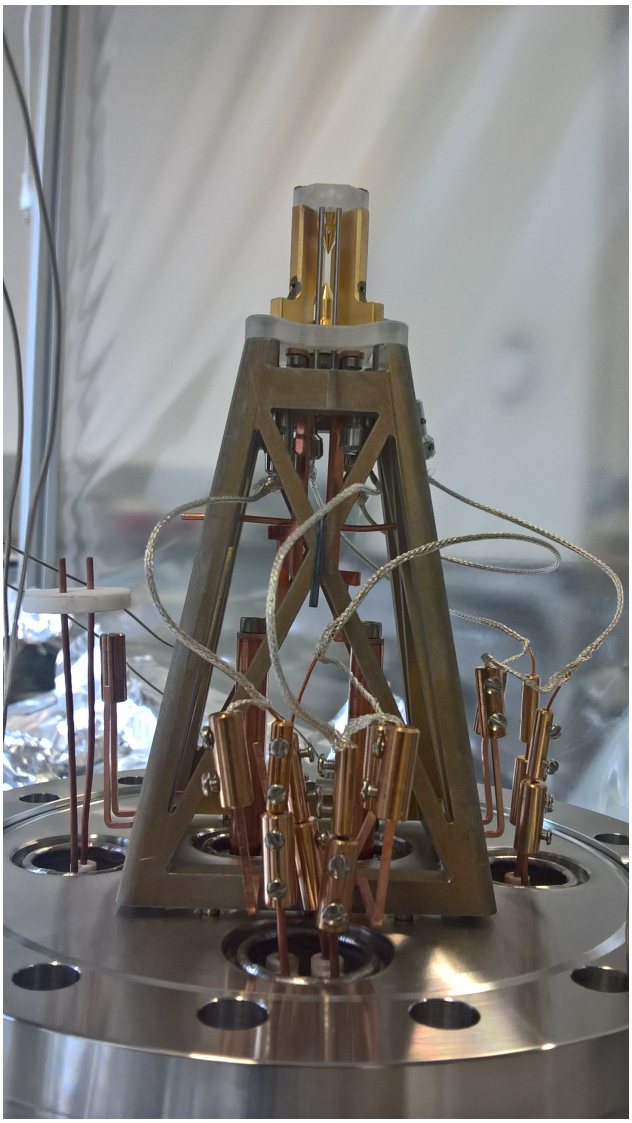

Figure 4.6: **A photograph of the top flange assembly with the ion trap attached to a titanium holder.** Endcap electrodes and compensation electrodes are connected to feedthroughs using Kapton insulated braided wires and barrel connectors. Radio frequency signals are brought in via two thick copper wires, hidden from view in the middle of the central titanium tower structure. Unused copper feedthroughs were trimmed before the second bake-out.

Atomic oven

Neutral calcium atoms are loaded into our trap using a resistively-heated atomic oven, generating a stream of neutral atoms. The atomic oven in our system contains two elements: calcium and barium. The

oven was made by the company AlfaVakuo e.U.[3] and contains 30 mg of barium with purity 99.9% and 40 mg of calcium with purity 99.98%.

The "oven launching" system that attaches the atomic oven to the bottom flange, and aligns the oven with the trapping region, is shown schematically in Figure 4.7. The atomic oven is surrounded by a titanium shield to protect the optical cavity from radiated heat generated while the oven is being heated during ion loading and from deposition of atoms on the cavity. A small aperture is drilled into the titanium shield and it is aligned with a hole in the bottom sapphire holder of the trap to enable the neutral atoms to enter the trapping region. The oven is attached to a Macor piece which is attached to two pillars that bring the setup to the correct height[4]. The ends of the oven are then attached to copper feedthroughs.

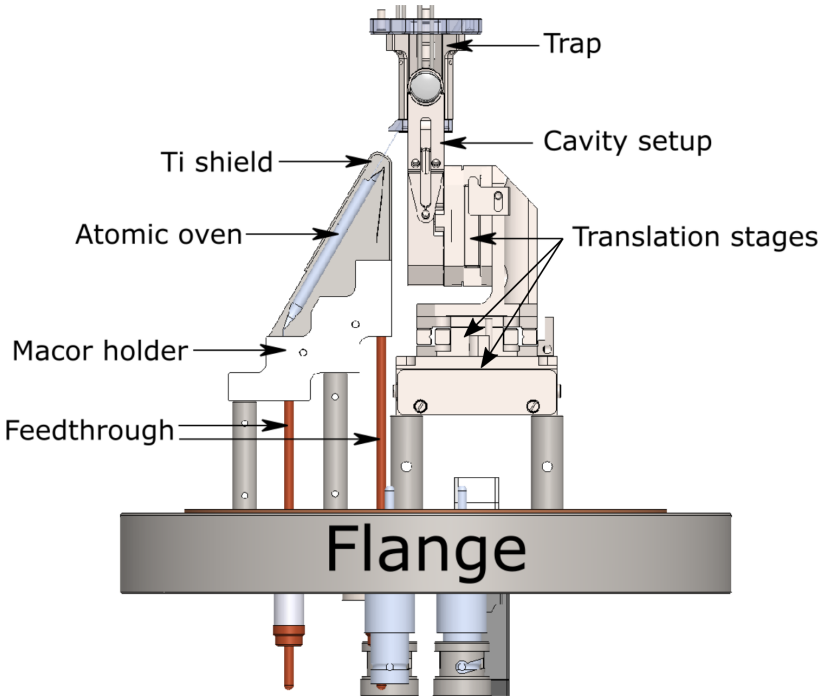

Figure 4.7: **A drawing of the bottom flange assembly with atomic oven and optical cavity assembly.** The atomic oven (AlfaVakuo) is attached to copper feedthroughs using grub screws. The height of the oven is given by two stainless steel pillars and a Macor holder. The atomic oven is covered with a Titanium shield with a small aperture and is aligned with an aperture in the lower sapphire trap holder to allow for a stream of neutral atoms to enter the trap. The trap is not attached to the bottom flange and is here shown for clarity. The optical cavity setup is attached to 3 nanopositioning translation stages (Attocube), as further described in Figure 4.8

3 Manufacturer part number: AS-Ba30/Ca40-3C

4 While assembling the setup, we found that the setup needs to be lifted, which we achieved by inserting several washers between the pillars and the Macor holder.

Optical cavity

The collection efficiency of single photons emitted by the ion is enhanced using cavity quantum electrodynamics (CQED) effects by coupling the trapped ion into a vacuum field of an optical resonator. The full description of the construction and development of our optical cavity is presented in PhD thesis of Josef Schupp [83] and a detailed study of the ion-cavity setup as a single photon source was presented in our paper [102]. A short summary of the optical cavity parameters and construction is now presented.
The optical cavity was designed and constructed with a focus on achieving the best possible extraction efficiency of photons out of the cavity. Our Faby-Perot cavity consists of two mirrors and is in the near-concentric regime. The following mirror and cavity parameters are taken from [83]. The details on measurement of these properties can be found in Chapter 4 and Appendix A of [83]. The mirrors are coated for reflection at 854 nm, which is the transition wavelength between the $3D_{5/2}$ and $4P_{3/2}$ levels of the $^{40}Ca^{+}$ ion at 854 nm. The two coated fused silica spherical mirrors have a radius of curvature $R_C = 9.984(7)$ mm. The total length of the cavity is $19.906(3)$ mm. The waist of the cavity field is $12.31(8)$ μm and is in the center of the cavity.

The main parameters determining the probability of a photon, which has already been emitted into the cavity, leaving through a preferred mirror are the transmissions of each mirror and unwanted scattering and absorption losses. The transmission of each mirror at 854 nm of $T_1 = 2.9(4)$ ppm and $T_2 = 90(4)$ ppm, where the subscript denotes the two different mirrors, were measured at the time of assembly. The total internal losses of the cavity are $L = 23(4)$ ppm.

Each mirror is glued to a homemade piezo stack which allows for fine length adjustment and stabilization of the cavity. These piezos are glued to a rigid titanium U-shaped holder. Two collimation lenses are mounted to the same U-shaped holder for collimating the outgoing photons and mode-matching of incoming laser beams. The U-shaped mount allows for a small tilt of the cavity axis up to $\pm 5^\circ$ with respect to the trap (ion string) axis. The final setup has a measured tilt of $4.1(1)^\circ$, see Section 4.1.2 of [83].

The rigid mount carrying the optical cavity is attached to three piezo stages ($2\times$ Attocube ANPx311/RES/UHV and $1\times$ Attocube ANPx321/RES/UHV) enabling nano-scale positioning of the cavity waist with respect to the position of an ion, in all three dimensions. These translation stages, made of titanium, are non-magnetic and suitable for operations under UHV conditions. The stages can be baked at temperature up to 150°C. The translation stage ANPx321 moves the cavity in a horizontal plane in a direction perpendicular to the cavity axis. One of the two ANPx311 stages moves the cavity in a

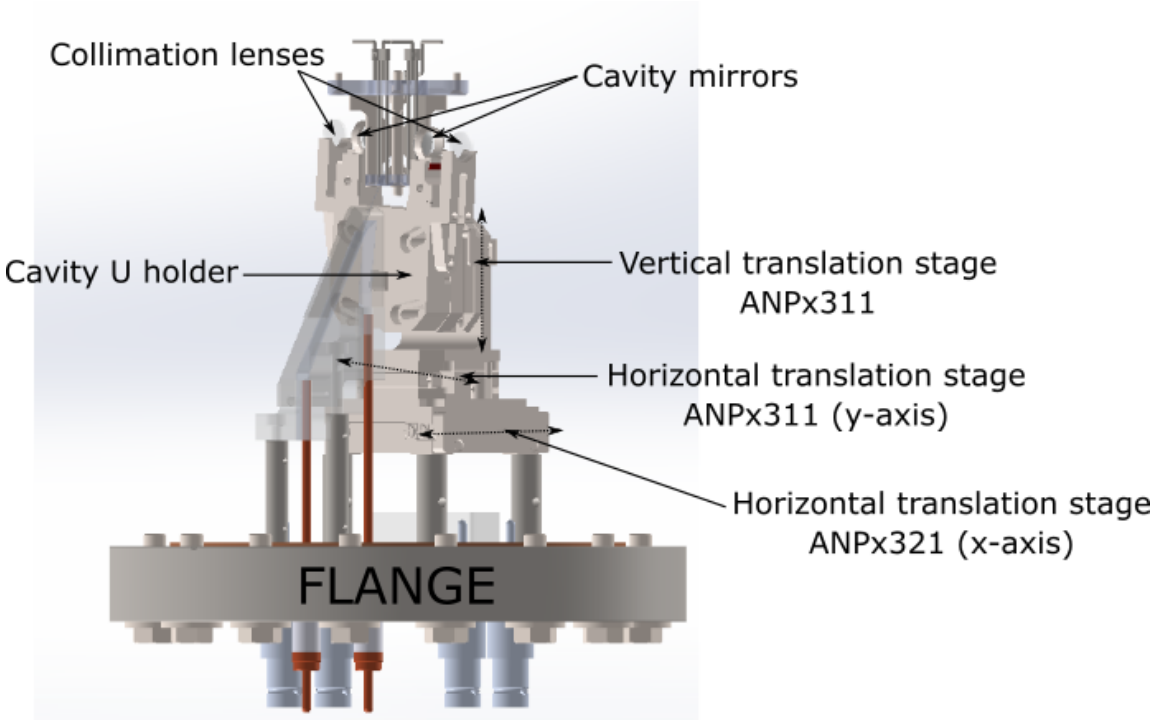

Figure 4.8: **A drawing of the bottom flange assembly with the cavity setup.** The two cavity mirrors are glued to piezos and to the U-shaped holder which is attached to a vertical translation stage. An L-shaped titanium piece attaches that upper assembly to a stack of two translation stages for positioning in the x-y plane. The whole assembly is placed on 4 pillars attached to a DN100 flange. Two collimation lenses are attached to the cavity U holder. The trap is not attached to the bottom flange and is here shown for clarity.

horizontal plane along an axis approximately parallel with the cavity axis, while the other one is mounted vertically via an L-shaped piece and translates the cavity in a vertical direction. Figure 4.8 illustrates the cavity setup.

The three translation stages are connected to a D-Sub type feedthrough in the bottom flange via a Kapton insulated cable provided by the company Attocube. The piezos for fine length control of the cavity are connected to copper feedthroughs using Kapton insulated braided wire and fixed to a barrel type connector. A photograph of the assembled bottom flange is shown in Figure 4.9. The Attocube translation stages are controlled using ANC350/RES controller and can be positioned with sub-nanometer precision. Voltage to the piezos for fine length adjustment are provided from a battery box and from a length stabilization PID circuit.

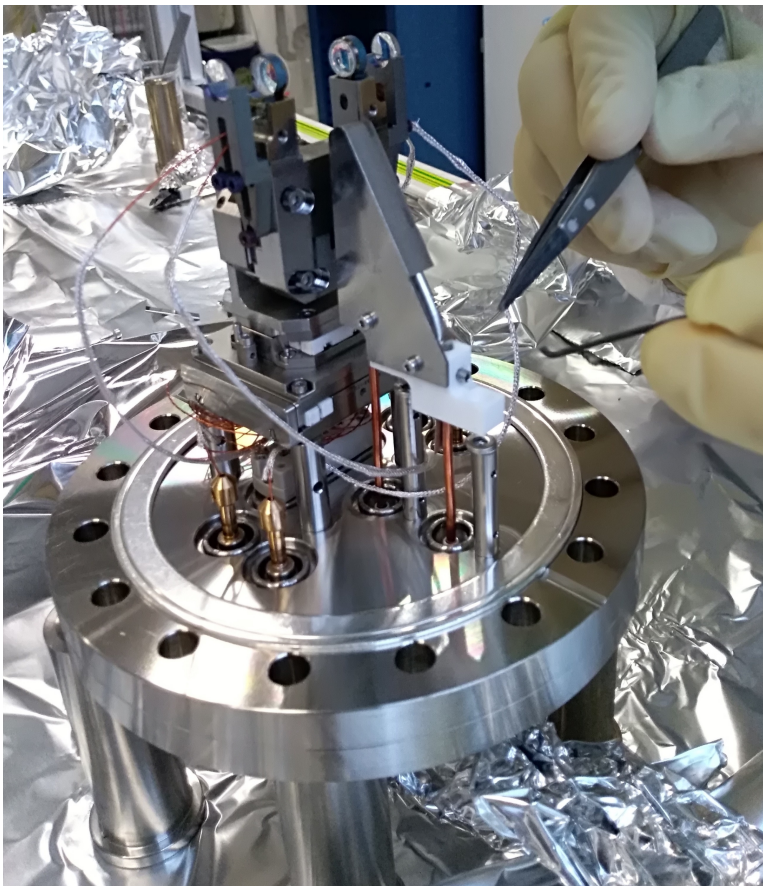

Figure 4.9: **A photograph of assembled bottom flange system with the optical cavity and atomic oven.**

4.4 CREATING ULTRA HIGH VACUUM

One of a big challenges when working with trapped ions is to keep them isolated from their environment. For example, a collision with a background gas molecule with enough energy can cause ion crystals to break apart, chemical reactions, or even ejection of an ion from the trapping potential. We therefore operate ion traps under ultra-high vacuum, meaning pressures below 10^{-9} mbar. At such pressures, the mean free path of the residual gas particles, which are predominantly hydrogen, reaches hundreds of kilometers. The quality of a vacuum is a crucial parameter, directly affecting the performance of the experimental setup. When preparing parts which were put into the vacuum chamber I largely followed the procedures described in document the "LIGO Vacuum Compatibility, Cleaning Methods and Qualification Procedures" [107]. I also benefited from discussions with P. Obšil who built an ion-trap setup himself, reaching pressures below 10^{-11} mbar and reaching one of the best conditions for room-temperature trapped-ion experiments [108]. Reaching UHV conditions is a demanding task

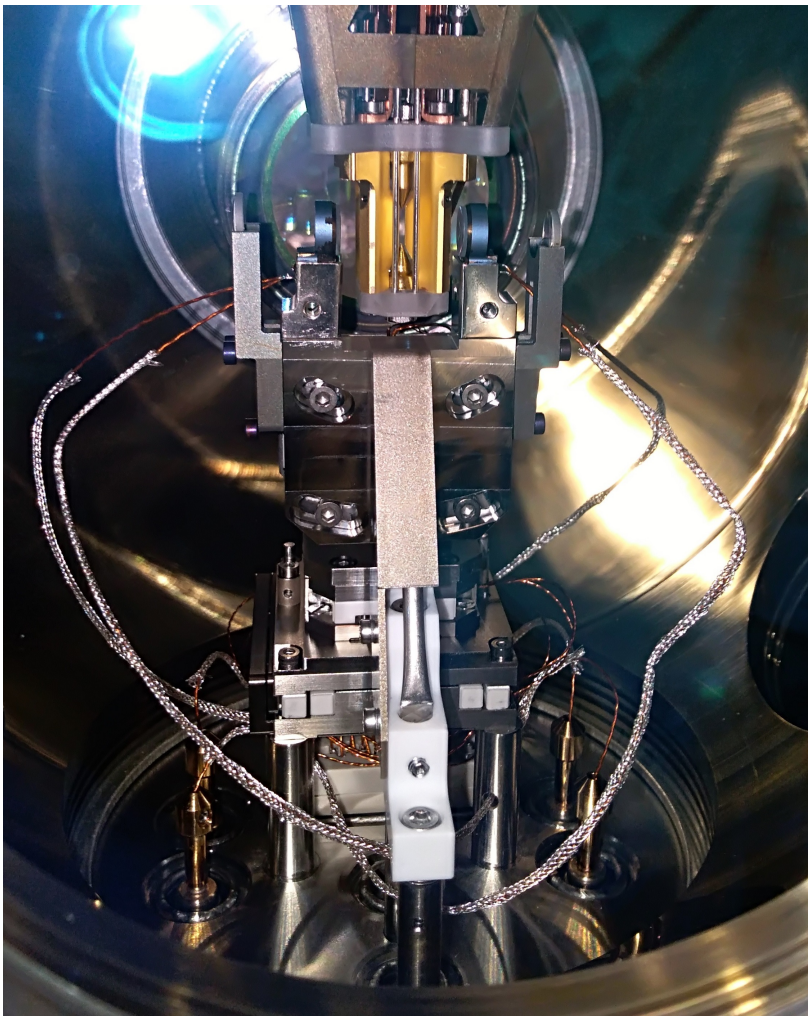

Figure 4.10: **Mating top and bottom flange assembly inside the vacuum vessel.** The optical cavity on the bottom flange surrounds the trap. The cavity is placed on three translation stages enabling precise positioning.

that requires precise work. Ideally, one would work in clean room environment when preparing a UHV system. Such a room was not available, therefore a small working area was thoroughly cleaned and equipped with a HEPA filtering system. The assembly of all vacuum parts happened in this area. Only parts and tools that were cleaned as described further in this chapter were allowed to be brought into this area.

Before any item is placed into our vacuum chamber, it has to be thoroughly cleaned to remove any grease, oil residuum from manufacturing, or other dirt. These contamination can lead to out-gassing, compromising the ability to reach UHV. The procedure of cleaning of in-vacuum parts is described in detail in Appendix B.

When attaching a viewport or any flange, a silver-plated copper gasket was used and the bolts were tightened to a desired torque using a specific pattern given by the size of the flange. The tightening pattern differs for different flange sizes. Silver-plated stainless steel screws were used to enclose our chamber. This silver layer on top of stainless steel is intended to make it easier to re-open the chamber if necessary. We have however noticed that the silver layer started falling off the screws, and the small silver dust contaminated our vacuum chamber. As the chamber was evacuated for a leak check purposes, the small particles, while traveling at high speed, scratched some of the viewports, leaving traces on the coating, as well as staying on the surface of the viewports. The debris was removed by carefully picking it with cotton sticks with methanol. Afterwards, the surface of each viewport was checked and if necessary, cleaned with methanol, or replaced.

To evacuate the vacuum chamber we employed several external pumping stations. First the system was evacuated with a Pfeiffer Vacuum pump station, consisting of an oil-sealed two-stage rotary vacuum pump (Pfeiffer Vacuum DUO 2.5) for generating coarse and medium vacuum and a turbo-molecular drag pump (TMU 071 P). The turbo-molecular pump is connected to the vacuum chamber using a bellows with DN40 flanges. To decrease the gas flow in the initial stage of pumping, a solid gasket with a 0.5 mm diameter hole in the middle was placed between the pump bellows and the vacuum chamber. During bake-outs the bellows was baked at 180°C using a heat tape, while carefully monitoring the temperature of the turbo-molecular pump to check that it did not exceed 90°C.

Before each bake-out, the chamber was pumped down to a pressure below 5×10^{-6} mbar and a leak check was performed by spraying helium into all joints and monitoring the presence of helium inside the vacuum system using a Residual Gas Analyzer (RGA, SRS RGA100) attached to the pump station. No leak could be found.

The baking process was performed twice. First the system was baked without the optical cavity and the performance of our trap was tested. This allowed to bake the chamber at 190°C, limited by the viewports and the ion pump. The timeline for this bake-out is shown in Figure 4.11. The temperature was slowly ramped up to 190°C. After three days of baking the NEG of the combined ion pump was put into conditioning mode, heating it up to 250°C. This local heat source did not cause the temperature of the rest of the setup to exceed 200°C as measured by the thermostat of the oven containing the chamber. This second phase of baking lasted for 3 days, taking the total baking time to 6 days. Then the apparatus was cooled down to room temperature. At this point we re-assembled magnets onto the ion pump and ramped the temperature to 150°C. The system was kept at this temperature for approximately 1 hour and during that time the degassing process

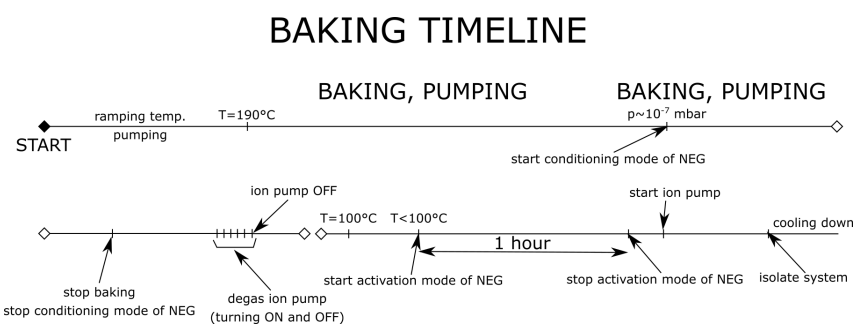

Figure 4.11: **Order of events during the first bake-out without the optical cavity.** Hollow diamonds represent a break in the timeline. The timeline is not to scale and key time periods are described in the main text.

of the ion pump was performed, by turning it on and off several times. When the temperature of the chamber dropped to 90°C, the NEG was put into activation mode, heating it up to 550°C within 30 min and kept at this temperature for 1 hour. During this process mainly hydrogen was released into the chamber, as observed on the RGA. After the NEG activation was finished, the vacuum chamber was separated from the outer environment by closing the valve attached to our cross. Then the ion pump was started. The indicated current initially dropped to 3 nA and within the next 12 hours dropped down to 0 nA, indicating that the pressure inside the vacuum chamber was below 4×10^{-10} mbar.

The second bake-out, with ion cavity in place, was carried out following the same scheme, only the maximum temperature of the system was set to 80°C. During the second bake-out it was decided that the second NEG (CapaciTorr Z-400) would not be activated, however the baking process itself lead to partial activation of the element.

4.5 HELICAL RESONATOR

Trapping ions in a linear Paul trap requires applying radio frequency (RF) voltage to the electrodes that create confinement in the radial direction, perpendicular to the ion string. A resonating circuit is used to enhance the amplitude of the RF voltage across the blades of the trap. Such a resonating circuit consists of the trap itself as the dominating capacitive element and a metal coil as an inductive element, creating together a quarter wave resonator. A typical helical resonator in Innsbruck has the coil placed inside a conductive cylindrical shield that is connected to a DC ground. One end of the coil is firmly attached to the shield while the other end is connected to a pair of blades in the ion trap. There is a gap between the top lid of the shield and the coil to prevent voltage flash-overs, while a gap between the coil and the bottom of the resonator allows for magnetic field passage

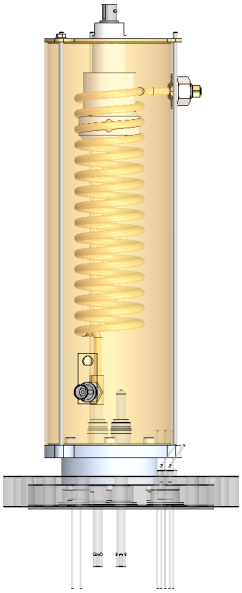

Figure 4.12: **Schematic of the helical resonator attached to our vacuum chamber.** Image produced by Solidworks. Radio Frequency is brought into the top BNC connector. The bottom two feedthroughs go to opposite blade pairs of the ion-vacuum ion trap. The unconnected feedthrough is in fact connected to a battery that lies outside of the cylindrical shield, which raises its voltage 1.5 V above DC ground.

reducing losses in the conductor [109]. The coil itself is a thick copper wire wound into a helix. The total length of the wire corresponds to a quarter of the resonance wavelength. When searching for optimal parameters for the resonator, a detailed analysis presented by Siverns *et. al.* [110] was used, in which the authors provide a semi-empirical model for calculating parameters of such a helical resonator.

Our helical resonator is placed on the top flange of the vacuum chamber (see Figure 4.1 for reference). The helical coil is placed inside a grounded cylindrical copper shield. The top end of the coil is fixed and electrically connected to the shield, while the bottom end of the coil is attached to a feed-through bringing the signal to a pair of blade electrodes in the ion trap. The RF signal, provided by a signal generator[5] and amplified by 40 dB with an amplifier[6], is brought to the coil via a slider with pin-point contact. This way we can optimize the impedance matching by changing the length of the coil on the grounded side. A schematic of our resonator can be seen in Figure 4.12.

5 Rohde&Schwarz SMA100A
6 MiniCircuits type LZY-22+

The main unknown parameter in our helical resonator system was the total capacitance of the setup consisting of the trap, connecting wires and even the coil itself. The capacitance of our trap assembly with wiring was measured to be 5 pF in air. This value was obtained using an LCR meter[7] connected to two opposing blades of the trap assembly. For our first trapping attempts we used a helical resonator which had the parameters presented in the first column of Table 4.1. The resonance frequency predicted by the model in [110] was 43.6 MHz, while the experimentally measured resonance frequency was 35 MHz. The difference is consistent with a total capacitance for the resonator-trap system of $C_{\text{total}} \approx 12$ pF.

A new helical resonator with lower resonance was designed to obtain higher radial motional frequency of ions (as $\omega_{rad} \propto \frac{V_{RF}}{\Omega}$, where V_{RF} is the amplitude of the applied RF field and Ω is the frequency of the oscillating RF field). Given geometrical constraints on the top vacuum flange that fix the diameter of the resonator shield, and the desire to use the existing slider with fixed coil pitch and diameter, the only free parameter left was the height of the coil (number of turns). Using the estimated total capacitance of the system ($C_{\text{total}} \approx 12$ pF) 15 turns was calculated to achieve resonance frequency of 25 MHz. Thanks to the presence of the slider, the number of turns can be slightly changed, whilst slightly changing also the resonance frequency. The calculated range of frequencies achievable with this new resonator is plotted in Figure 4.14. This plot shows that the resonance frequencies lie between 22 MHz and 25 MHz, depending on the position of the slider. After attaching the new resonator to the trap, an optimal point at 23 MHz was found. Consequently, for approximately the same RF power sent to the resonator, the radial secular frequency of ions in the trap increased from $\omega_{\text{rad}} = 2\pi \times 1$ MHz with the old resonator to $\omega_{\text{rad}} = 2\pi \times 2$ MHz with the new one. The parameters of our new helical resonator are summarized in Table 4.1. A schematic of the new resonator is depicted in Figure 4.13

Since copper readily oxidizes, the resonator was coated with 35.5 μm film of silver, topped by 0.5 μm of gold[8]. The silver plating has been shown to improve the quality factor by up to 3% [109] but we did not verify this in our system.

7 ISO-TECH LCR Meter LCR819

8 Both coatings done by the company Ögussa

Dimension	Old resonator Size [mm]	New resonator Size [mm]
Shield outer diameter D	84	84
Shield height B	182	255
Coil diameter d	40.4	40.4
Coil height b	76.5	155
Coil wire diameter d_0	5	5
Pitch τ	10	10
Resonance frequency f [MHz]	35	23

Table 4.1: **Comparison of the physical properties of the old and new helical resonators used to bring RF voltage to the ion-trap.** The resonance frequency is calculated from model from [110]. For the old resonator we used capacitance 5 pF measured by LCR meter, while the new resonator calculation uses capacitance of 12 pF based on estimations from measured resonance frequency of the old resonator.

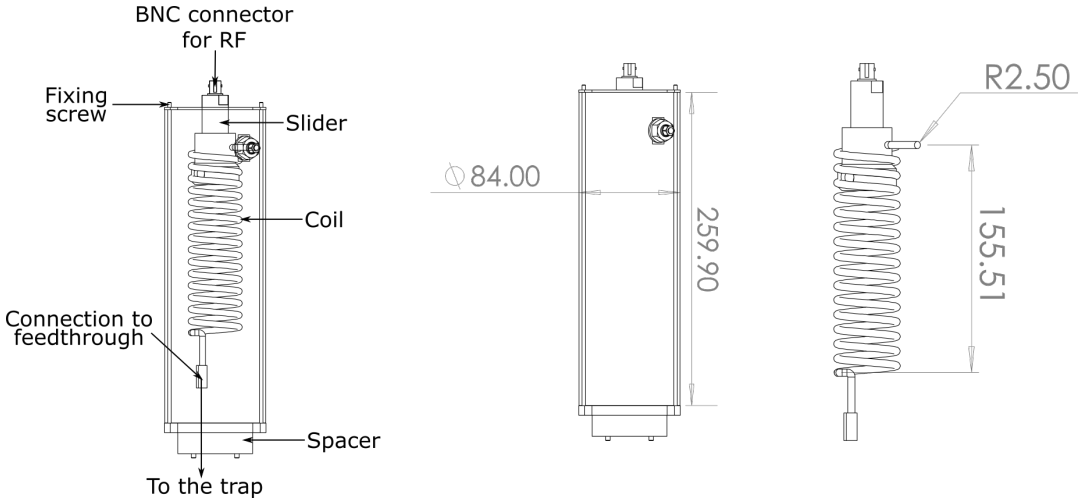

Figure 4.13: **A schematic drawing of the new helical resonator.** The resonator consists of a coil made of 5 mm thick copper wire. There are 15 turns of this coil with a pitch of 10 mm. The coil is placed inside a copper shield. On top, the whole system is closed with a cap with BNC connector. There is an aluminum spacer between the CF100 flange and the resonator setup to ensure physical access to other feedthroughs on the flange. The RF signal is brought to the coil via a BNC connector and plastic slider with a copper contact point which serves for fine tuning of the resonance frequency and optimizing the Q factor. The whole setup is fixed with 3 M3 grub screws to the spacer, while the spacer is attached with additional screws to the CF100 flange. All dimensions are in mm.

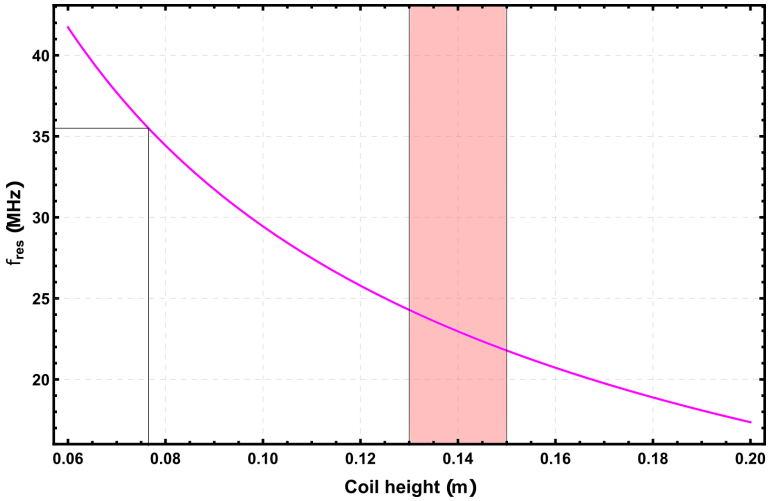

Figure 4.14: **Calculated resonance frequency of the new helical resonator.** The resonance frequency was calculated as a function of the total coil height. The calculation uses the model of [110] and the parameters of the second column in Table 4.1. The red colored area shows the tuning range of the designed resonator. Black lines show the central resonance frequency of the first resonator that we built.

5

INDISTINGUISHABLE PHOTONS FROM REMOTE NETWORK NODES

During my PhD we established a two-node quantum network where each node consisted of an ion trap with an integrated optical cavity. Chapter 4 presented the construction of one of those ion-trap nodes, known as the "IQOQI node". The second participating node of the network, known as the "UIBK node", is located in a remote building within the same "Technik" campus of the University Innsbruck. The two buildings are connected via several hundred meters of optical fiber.

Chapter 6 presents the entanglement of ions in the remote traps using the two-photon detection method described in Section 2.3. The quality of that entanglement is dependent on the degree to which the photons produced by each node are indistinguishable [70]. The first major experimental goal involving our two remote network nodes was to observe and understand the two-photon interference contrast, which serves as a measure of photon indistinguishability. As described in Section 2.2.1, the two-photon interference contrast can be measured by performing a "Hong-Ou-Mandel" (HOM) experiment.

This chapter reports the results of a HOM experiment between photons produced by our two remote nodes and is structured as follows. In Section 5.1, an overview of the entire experiment is presented. Details on the participating trapped-ion network nodes and the experimental setup used for the two-photon interference are presented. The optical fibers connecting the two remote nodes and classical communication channels between the two nodes are described in this section too. In Section 5.2, the procedure of running the HOM experiment, including the experimental sequence run by each node, is presented. Section 5.3 presents pre-requisites and calibrations necessary for running the experiment, the frequency matching of ion cavities, temporal wavepacket synchronization, transmissions of the optical fibers connecting the two nodes and a frequency beat between two remote lasers. Section 5.4 presents experimental parameters used for simulations of the two-photon interference contrast. Section Section 5.5 presents the experimental results and comparison to the theoretical simulation.

5.1 EXPERIMENTAL SETUP

5.1.1 *Overview*

An overview of our two-node quantum network is shown in Figure 5.1 as well as details on the key pieces of equipment and information channels. The two participating nodes are in two buildings at the Campus Technik in the western part of Innsbruck. One node, run by the team of Prof. Tracy Northup is in the Viktor-Franz-Hess Haus of the University of Innsbruck. This node is called the "UIBK node". The IQOQI node, run by Asst. Prof. Ben Lanyon is in a lab located in the ICT building, where the Institute of Quantum Optics and Quantum Information of the Austrian academy of Science, is located. Two optical fiber bundles, each of length 510(2) m, are laid across the campus connecting the two nodes.

Both nodes use atomic ions that are held in a macroscopic linear Paul trap, with an integrated optical cavity to enhance the collection of single 854 nm photons from the ion. Each node uses their own set of lasers to control the state of the ion and to trigger the emission of photons via the cavity mediated Raman transition (CMRT) described in Chapter 3. Single photons generated by the UIBK node are sent across to IQOQI through one of the optical fibers inside one of the two fiber bundles.

Each node has its own independent homemade central piece of classical computing hardware for experimental control, known as a Pulsebox [111], which executes the local sequence of operations (mainly laser pulses). To achieve synchronization, the UIBK node's Pulsebox triggers execution of the experimental sequence of laser operations at IQOQI by sending an electronic TTL pulse. The electronic pulse is translated into an optical signal using an optocoupler and is transmitted through one of the other fibers of the bundles to the IQOQI lab where it is translated back into an electronic TTL signal using a complementary optocoupler.

Ideally, each node produces a single-mode and fiber-coupled single photon which is then guided to a small breadboard with an optical setup known as the coincidence board (or "HOM board"). The coincidence board is located in the IQOQI lab that also contains the IQOQI node. The spatial modes of the two photons are overlapped on a beamsplitter on the HOM board and subsequently detected by one single photon detector in each output port of the beamsplitter. If the two single photon wavepackets arriving on the balanced beamsplitter from two nodes are overlapped in time, and all other degrees of freedom are the same, they should bunch into a single output port of the beamsplitter and no simultaneous clicks of the two detectors are detected. The following subsections present the key elements of our network in more detail.

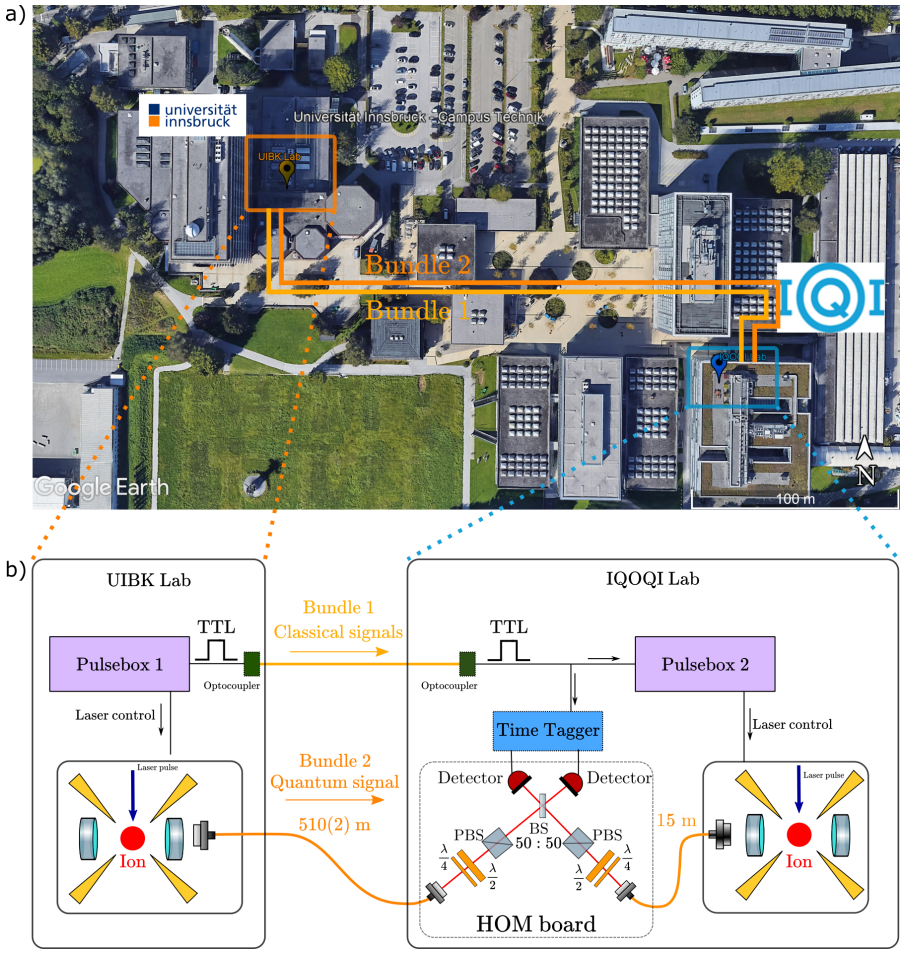

Figure 5.1: **An overview of the two-node quantum network.** a) Satellite image of the campus Technik (Google Earth. Image Landsat/-Copernicus). Bundle 1 and 2 are optical fiber bundles connecting labs in each building. b) *The UIBK lab*: Calcium ion (red ball), trapped in a macroscopic linear Paul trap (golden blade electrodes) and at the position of the waist of an optical cavity (two mirrors). Laser pulses, controlled via Pulsebox 1, control the generation of photons into the cavity. The photon is guided through a 510(2) m long single mode optical fiber to IQOQI. Pulsebox 1 sends a TTL pulse to IQOQI via optical fiber using an optocoupler. *The IQOQI lab*: Laser pulses, controlled via Pulsebox 2, trigger generation of a photon into the cavity. The photon is coupled into a 15 m long single mode optical fiber. Sequence execution of Pulsebox 2 is triggered by the TTL pulse arriving from the UIBK lab. Photons from both nodes are guided to an optical setup for Hong-Ou-Mandel interference (HOM board). Photon polarization is matched using a polarizing beamsplitter (PBS) and the detection rate from each side is optimized using a set of $\lambda/2$ and $\lambda/4$ waveplates. The two photons are brought onto a balanced beamsplitter BS (ThorLabs BS011). Each output port of the BS is monitored by a detector (SNSPD, Scontel FCOPRS-CCR-2TW+2SW85) and the photon detection events are counted by a Time Tagger (Swabian TimeTagger 20).

5.1.2 *The ion-trap network nodes*

Each ion-trap network node is in a room temperature vacuum chamber and employs the same basic design. A macroscopic linear Paul blade ion-trap is attached to the top flange of the vacuum chamber, hanging down via a rigid attachment. The ion trap is oriented such that the ion's principle axial motional mode is in the vertical direction. An optical cavity, placed inside the vacuum chamber, surrounds the ion trap and is oriented such that its axis is a few degrees away from horizontal and therefore close to perpendicular to the ion string, should more than one ion be loaded. The optical cavity is attached to the bottom flange of the vacuum chamber via piezo nano-positioning stages, enabling translation in all 3 spatial axes.

Both cavities are 20 mm long and in the near-concentric regime, resulting in a microscopic waist at the position of the ion[1]. Both nodes use a resistively-heated oven to produce neutral calcium atoms that are isotope-selectively ionized using a two-photon ionisation process involving lasers at 422 nm and 375 nm. The selected isotope is $^{40}Ca^{+}$.

In the following I will use a Cartesian coordinate system with three orthogonal directions x, y, and z. The vertical z direction in both nodes points along the axial centre of mass motion of the ion, defined by the line connecting the DC endcap electrodes of the ion trap. The cavity axis in each node is tilted a few degrees from the direction of the x axis in the $x-z$ plane. The tilt at the UIBK node is 4°[113] and $4.1(1)^\circ$ at the IQOQI node [102]. At each node, the atomic quantization axis is set to be parallel to the direction of an applied static magnetic field. The magnetic field is perpendicular to the x axis and points in a direction 45° to the z axis and in the y/z plane. At the UIBK node, a magnetic field of 4.17 G is created by DC currents in coils attached to the outside of the vacuum chamber. At the IQOQI node, a magnetic field of 4.22 G is created by rings of permanent magnets attached to the outside of the vacuum chamber. Figure 5.2 shows a conceptual schematic of the ion-cavity nodes, focusing on relative geometries of their principle components. At each node, the 393 nm Raman laser is parallel to the magnetic field axis. It is circularly polarized to maximize coupling strength on the $|s\rangle = |4^2S_{1/2}, m_j = -1/2\rangle$ to $|p\rangle = |4^2P_{3/2}, m_j = -3/2\rangle$ transition.

At the UIBK node, Doppler cooling of the ion is performed using 397 nm laser beams from two directions (Figure 5.2), combined with an 866 nm beam from a single direction. Optical pumping of the ion is performed involving a 729 nm laser beam at a 45 degree angle to the z axis.

1 For the details on the cavity length and waists, see the supplementary material of our paper [112], the thesis of Josef Schupp [83] (IQOQI) and the thesis of Konstantin Friebe (UIBK) [82].

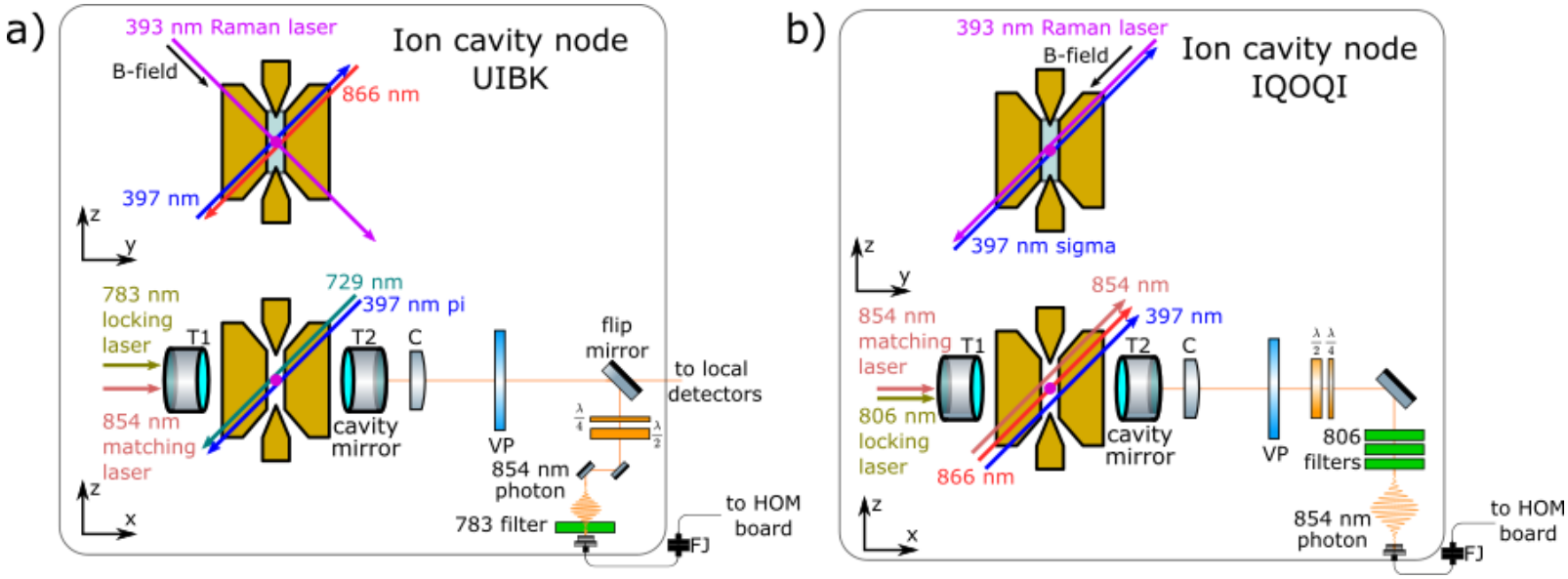

Figure 5.2: **Geometry and optical layout of the participating ion-cavity nodes.** Trapped ion (purple ball) confined in a linear Paul trap (golden electrodes), coupled to an optical cavity consisting of mirrors with transmissions T1 and T2. Photons emerging through mirror T2 are collimated by a lens C and leaves the vacuum chamber through viewport VP where they are guided via mirrors until it is coupled into single mode optical fiber and guided further to the HOM board (see Figure 5.3). Optical fibers are joined together using fiber joiners (FJ). **a)** *The UIBK node with laser beams and magnetic field directions.* The cavity is made resonant to both the 783 nm locking laser as well as to the shared 854 nm matching laser. The 729 nm laser is used for optical pumping and two 397 nm beams are used for Doppler cooling. An emitted 854 nm photon is guided into a local detection setup or is reflected by flip mirror and is guided into single mode fiber via a set of $\lambda/4$ and $\lambda/2$ waveplates and two additional mirrors. A 783 nm bandpass filter is placed in the path to remove any locking light. **b)** *The IQOQI node with laser beams and magnetic field directions.* The 397 nm sigma beam is used for optical pumping. The length of the cavity is stabilized to an 806 nm laser. An emitted 854 nm photon is guided into a SM fiber via a set of $\lambda/2$ and $\lambda/4$ waveplate and a mirror. A set of 806 nm filters removes any locking light.

At the IQOQI node, Doppler cooling is performed using a single beam path at 45 degrees to the z axis and in the x/z plane, in which both 397 nm and 866 nm laser light are sent. Optical pumping is done using circularly-polarized 397 nm light propagating in a direction parallel to the magnetic field axis.

5.1.3 *The coincidence board (HOM board)*

For interference of the two remotely-generated photons, an optical setup was built on an optical breadboard of dimensions 45×45 cm in the IQOQI lab. A schematic of this board is presented in Figure 5.3. Single photons from the IQOQI node are guided to the input port "IN IQOQI" via a single-mode (SM) optical fiber, where they are outcoupled into free space and collimated (Schäfter+Kirchhoff 60FC-4-M8-10). Photons are then reflected on a mirror (ThorLabs BB1-E03), pass a quarter waveplate (QWP, CeNing) then a half waveplate (HWP, CeNing) in manual rotation mounts. Those waveplates allow optimization of the polarization to maximize transmission through a subsequent polarizing beamsplitter (PBS, CeNing). An identical setup was built for the second input path "IN UIBK" of the board. Afterwards, the spatial modes of photons from both input ports are overlapped on a balanced beamsplitter (ThorLabs BS011)[2]. After reflecting off its own mirror (ThorLabs BB1-E03) each output mode then passes a bandpass filter before being coupled into a single mode optical fiber (Schäfter+Kirchhoff 60FC-4-M8-10). Photons are guided in single mode output fibers to superconducting nanowire single photon detectors (SNSPDs, Scontel FCOPRS-CCR-2TW75+2SW85). The detector efficiencies and dark count rate (DCR) are presented in Table 5.1. Because the detectors are polarization sensitive, a mechanical polarization controller (ThorLabs FPC560) is placed into each fiber path to optimize the detection efficiency. The SNSPDs are placed in

2 The transmission of the beamsplitter cube at 854 nm is, according to specification 51.4% for the S-polarization, and 52.5% for the P-polarization. The reflectance is 41.3% for the S-polarization, and 39.6% for the P-polarization. The values were not measured in the setup. The propagating light was set to be P-polarized.

	SNSPD1	SNSPD2
Efficiency (%)	87	88
DCR (1/s)	0.3(1)	0.5(1)

Table 5.1: **Efficiency and free-running dark count rate (DCR) of the 854 nm detectors.** The detectors are superconducting nanowire single photon detectors (SNSPD, Scontel FCOPRS-CCR-2TW75+2SW85). Presented values were obtained by Scontel's field service engineer during installation using a calibrated single photon source.

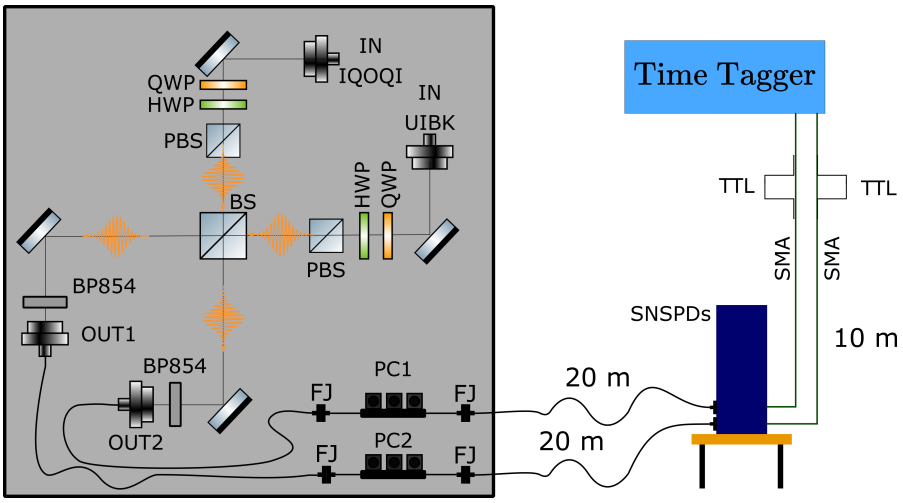

Figure 5.3: **A schematic drawing of the coincidence board (HOM board).** A photon from each node is brought to the setup via an optical fiber. The photons are first launched into free space using a beam collimator. Before the photons are overlapped on a beamsplitter (BS), each passes through a set of waveplates (QWP, HWP) and a polarizing beamsplitter (PBS) to ensure parallel polarization. Each output of the BS is coupled to a single mode fiber that carries the photons to an SNSPD detector. A bandpass filter at 854 nm is placed in front of each fiber coupler to reduce background. The SNSPDs are in a cryostat located in the basement of the IQOQI building, below the experimental setup. Because the detectors are polarization sensitive, polarization modulators PC1 and PC2 are used in each path to maximize the detection efficiency. The photons are guided to the detectors through 20 m shielded single mode fibers. The detected photons are converted into a TTL signal, brought from the detectors to a Time Tagger using SMA cables.

the basement of the ICT building, below the IQOQI lab. Two 20 m-long shielded optical fibers (ThorLabs 780HP) are used between the laboratory and the detectors. Connections between these fibers and output fibers of the coincidence board are made through fiber mating sleeves (ThorLabs ADAFCPM1). Signals produced by the SNSPDs are TTL pulses which are brought back into the laboratory using two 10 m SMA cables. The detection events are logged by a Time Tagger (Swabian TimeTagger 20) with a resolution of 1 ps.

5.1.4 *The fiber bundle*

The transfer of optical signals between the two participating nodes of our quantum network is done using two optical fiber bundles laid across the campus. Each bundle consists of 7 optical fibers with make and model numbers presented in Table 5.2. Each fiber is physically labeled with a color. The individual fibers were made by StockerYale

Label	Type	Wavelength(nm)
White (Weiss)	SMF 28	1330, 1550
Yellow (Gelb)	SMF 28	1330, 1550
Orange	S&Y-SCSM-780-HP1	780-970
Green (Grün)	S&Y-SCSM-780-HP1	780-970
Blue (Blau)	S&Y-SCSM-633-HP1	600-760
Black (Schwarz)	S&Y-PMF-820-B1	800-980
Red (Rot)	S&Y-PMF-633-B1	630-780

Table 5.2: Table of optical fibers in each of the two fiber bundles connecting the UIBK laboratory and the ICT building containing the IQOQI node.

and the whole system was sold by company Laser2000. The specification sheet of the used optical fibers are in Appendix C. The fiber bundles have one end in the basement of the ICT building. Additional 20 m long optical fibers are needed to connect the IQOQI node with the fiber bundles. The other end of the fiber bundles terminate directly in the UIBK node laboratory, thus only a few meter fibers are used to connect the node with the bundles. We use the fiber bundles for the following signals:

1. Single photons (Bundle 2, Orange)
2. Laser light at 786 nm for frequency beat (Bundle 1, Green)
3. Cavity length reference 854 nm laser light (Bundle 2, Green)
4. TTL signals encoded into 1330 nm light using an optocoupler (Bundle 1, White)

5.1.5 *Classical communication*

In the HOM experiment, a TTL pulse is used to synchronize experimental sequences run in the two participating nodes. While the UIBK node is running freely, constantly repeating the programmed experimental sequence, the execution of a sequence at IQOQI is triggered upon detection of an electronic TTL pulse sent by the UIBK Pulsebox. That TTL signal is sent between the nodes using the optical fiber link. Two optocoupler boxes (Terahertz Technologies TTI LTX-7215) are placed at each end of the fiber link. The device translates the electronic signal into an optical signal at 1330 nm wavelength on one side of the fiber link (Bundle 1, fiber "White"). When the optical signal reaches the second optocoupler unit on the other side of the fiber, it is translated back to an electronic signal. The TTL pulse is then brought into the Pulsebox at IQOQI using a 20 m BNC cable. The pulse is

split into two arms, one goes to the Pulsebox and one into the Time Tagger where the incoming pulse is registered for further evaluation. The IQOQI Pulsebox waits until the trigger pulse is received and only then begins the sequence execution, as described in more detail in Section 5.2. This approach ensures that if the IQOQI node executes its sequence, the UIBK node executes one as well.

5.2 EXPERIMENTAL DETAILS AND PULSE SEQUENCE

The experimental sequence for the Hong-Ou-Mandel experiment is described here. First, both nodes prepare their ion in the ground state $|s\rangle = \left|4S^2_{1/2}, m_j = -1/2\right\rangle$ via Doppler cooling and optical pumping. When the ion is in that state, it is ready for photon generation. Each node then attempts to produce one photon using the CMRT (see Section 3.2), realized using a 393 nm laser photon generation pulse. The timing of the first photon generation pulse at each node is chosen such that the temporal wavepackets of the photons arrive on a beamsplitter synchronously. This first pair of photons are henceforth referred to as the "synchronous pair". Both nodes then re-initialize the ion to the ground state and generate another photon. This time, the timing is chosen such that the temporal wavepackets of the photons are displaced in time on the beamsplitter such that they do not overlap at all. This second pair of photons are henceforth referred to as the "asynchronous pair". The exact laser pulse sequences at each node are not the same and are now described separately. A graphical interpretation of the experimental sequence is depicted in Figure 5.4.

The IQOQI node sequence. Each execution of a sequence begins with initialization. At the very beginning of the initialization phase, a 40 μs pulse of the Raman laser is generated, measured and stabilized to set the power of the Raman pulse such that the driving strength is constant throughout the duration of the experiment. Then, a 20 μs pulse of 854 nm light empties the $D_{5/2}$ state. Next, the ion is Doppler cooled for 2 ms, using 397 nm and 866 nm laser light. At this point, the IQOQI node waits until the TTL trigger pulse from UIBK node arrives. While the system is waiting, the Doppler cooling beams are kept on. Once the TTL pulse is received in this time window, the Doppler cooling lasers are switched off and photon generation begins.

During the photon generation phase, first, the ion is re-pumped by 20 μs of 854 nm and 866 nm laser light, followed by a Doppler cooling stage of duration 20 μs. Next, the ion is pumped into ground state $|s\rangle = \left|4S^2_{1/2}, m_j = -1/2\right\rangle$ using a 130 μs long pulse of σ-polarized 397 nm laser light, together with 866 nm laser light. Then the first photon (synchronous photon) is generated by a 20 μs Raman pulse at 393 nm. Simultaneously a TTL signal is raised, collected by a Time Tagger, marking the photon generation pulse in the collected data. Next, the ion is Doppler cooled for 50 μs and pumped back to the

ground state for 130 μs. Next, a second Raman pulse of duration 20 μs is applied to generate the second, asynchronous photon. This entire photon generation phase is repeated 15 times before another initialization and synchronization is performed. The sequence at IQOQI is now complete. The sequence at IQOQI is repeated 160,000 times, attempting to produce 2,400,000 pairs of photons.

The UIBK node sequence. The sequence running at UIBK node is very similar to the one executed at IQOQI. Each sequence execution at UIBK begins with Doppler cooling of the ion. When the ion is cooled, a TTL pulse of duration 5 μs is sent to IQOQI to trigger the sequence execution. The UIBK sequence then waits for the pulse to propagate to IQOQI and trigger the sequence execution. Next, the sequence continues with the photon generation phase. This consists of 30 μs of Doppler cooling and re-pumping from the $D_{5/2}$ state using 854 nm laser light and 866 nm laser light. Optical pumping, involving five 729 nm laser pulses each 5 μs long, then prepares the ion in the electronic ground state. Next, the first (synchronous) photon is generated by applying a 20 μs Raman pulse to the ion. The arrival time of the UIBK photon wavepacket at the HOM board is set by a wait time before this pulse. Next, the ion is shortly Doppler cooled for 30 μs and repumped from the $D_{5/2}$ state and optically pumped to the electronic ground state using 729 nm pulses. The sequence then waits for 50 μs before the second (asynchronous) photon is generated by applying a second Raman pulse of 20 μs duration. This photon generation phase is repeated 15 times and only then the sequence starts over. Simultaneously with each UIBK Raman pulse, a TTL pulse is sent to the Time Tagger, marking each photon generation attempt.

The photon detection events, along with other pulses marking specific events in the sequence, are recorded by the Time Tagger. The channel assignments are presented in Table 5.3

Channel	Event
0	Start of IQOQI sequence
2	SNSPD1 detection event
3	IQOQI Raman pulse marker
5	UIBK Raman pulse marker
6	SNSPD2 detection event

Table 5.3: Events collected during the sequence execution and their assignments to channels of the Time Tagger.

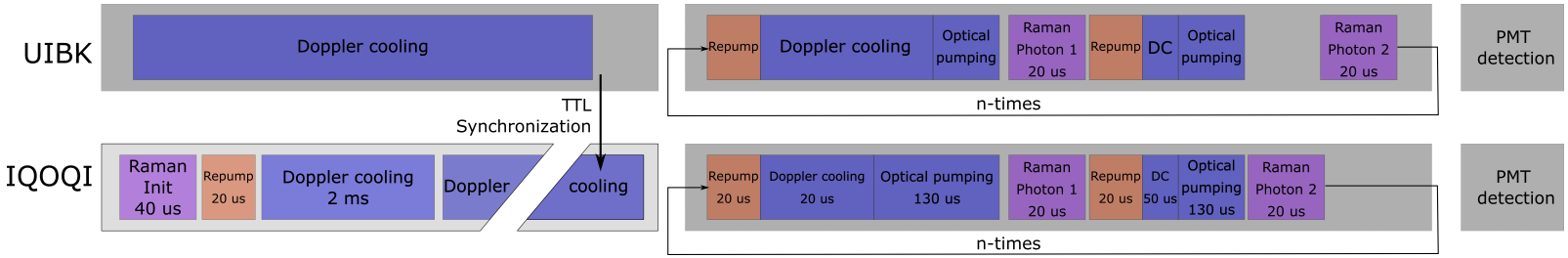

Figure 5.4: **A graphical interpretation of one cycle of the experimental laser pulse sequences used for the HOM experiment.** The IQOQI sequence scans over a dummy parameter, while the UIBK sequence is free running, continuously repeating itself. The break in the IQOQI sequence timeline symbolizes waiting until the synchronization trigger signal from UIBK arrives. Details on the pulse sequence are given in the main text.

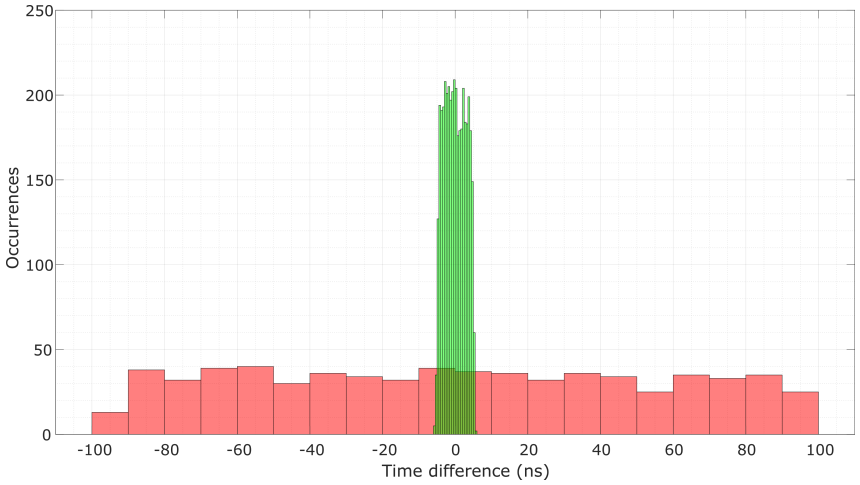

Figure 5.5: **A comparison of jittering of sequence start in a triggered regime.** Histogram of time differences between arrival time of the trigger pulse and a TTL pulse marking IQOQI synchronous photon generation. The red distribution shows the "old" trigger function of the IQOQI Pulsebox with 200 ns jitter (10 ns bins). The green distribution was achieved with the new trigger function and has a range of 12 ns (0.5 ns bins).

5.3 PRE-REQUISITIES AND KEY CALIBRATIONS

Temporal synchronization of the remote wavepackets

The purpose of the beamsplitter on the interference board is to erase the which-path information for the two photons and thus requires both temporal and spectral synchronization of the photon wavepackets. Temporal synchronization of the wavepackets on the beamsplitter is achieved in two steps. First the experimental sequence is run and various sequence events and markers are recorded on the Time Tagger (Table 5.3). The time difference between the TTL pulse marking the start of the IQOQI sequence (Channel 0) and the first of a train of IQOQI Raman pulse markers (Channel 3) was evaluated. At first, the analysis showed a 200 ns jitter, as can be seen in green in Figure 5.5. The origin of the jitter was traced to the Pulsebox at IQOQI and its implementation of triggering. A new triggering method was subsequently activated in the Pulsebox that reduced the jitter to 12 ns, small enough to be neglected in our experiments, as can be seen in red in Figure 5.5.

The second step was to match the arrival times of the single photon wavepackets at the beamsplitter. This was achieved by carefully adjusting the length of sequences executed in each node until the start of the wavepackets in the data were overlapped. Wavepacket synchronization was verified by running the experimental sequences, bypassing the beamsplitter and sending the photons from each node to a separate detector. Figure 5.6 shows a histogram of detection events (wavepack-

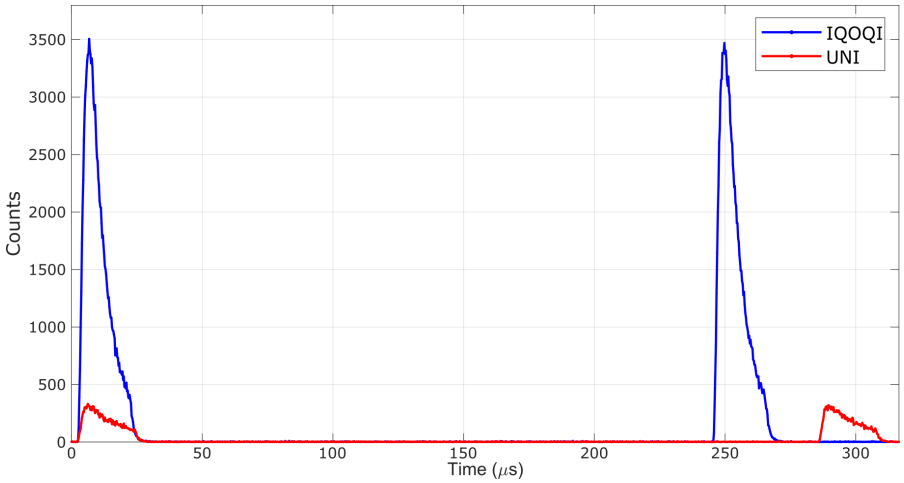

Figure 5.6: **Single photon wavepackets from each node detected in the IQOQI lab, using separate detectors.** Histogram of detection events (wavepackets) collected during the experiment with the beamsplitter in the HOM board (Figure 5.3) effectively removed, bringing photons from each node directly to a different detector. The detection events are plotted with respect to the IQOQI Raman marker TTL pulse, marking generation of the "synchronous" photon. The first, "synchronous" pair is overlapped in time, while the second, "asynchronous" pair is intentionally displaced in time by 40 μs.

ets) collected during a sequence execution with bypassed beamsplitter. The first photon from the IQOQI node is seen to be time-synchronized with photon arriving from UIBK node (synchronous pair), while the subsequent photons are intentionally displaced in time (asynchronous pair). The lower efficiency of the UIBK photons is caused by the propagation through the fiber link between the buildings as well as the higher losses in the UIBK cavity mirrors.

Frequency matching of the remote cavities

Frequency matching of the remote photons requires matching the resonant frequencies of the remote cavities. This is achieved via a calibration procedure described further in this paragraph in which a frequency reference is shared between the two buildings. Specifically, an 854 nm laser that is set to be resonant with the UIBK ion cavity is distributed over the optical fiber link to IQOQI prior to performing an experimental run. That distributed 854 nm laser light is injected into the IQOQI ion cavity and its length is changed by adjusting the frequency of the 806 nm locking laser until a maximum transmission signal is observed on a photodiode placed at the output of the IQOQI ion cavity.

The locking laser at 785 nm at UIBK is hidden from drifts of its reference cavity using a feedback setup described later in this subsection.

Nevertheless, a drift of the UIBK ion cavity at 854 nm of 200 kHz/hr was observed by measuring the frequency of the 393 nm Raman laser that maximizes photon generation rate. This drift is significant compared to the cavity linewidth of (140 ± 3) kHz and thus has to be compensated for before each experimental attempt.

Frequency beat between the Raman lasers

A frequency beat between the UIBK and IQOQI Raman lasers at 786 nm (the fundamental wavelengths, before doubling to 393 nm) was established. This measurement served to determine the linewidths and to characterize drifts of the transfer cavities[3]. Later the beat was used to compensate for drifts of the UIBK transfer lock cavity. The IQOQI Raman laser at 786 nm has previously been proven to have a linewidth $87(1)$ Hz at a drift rate of 200 mHz/s [114], which are both much smaller that corresponding values of the UIBK Raman laser. This beat was not required for the experiment in Chapter 6 as the local cavity stabilization had been improved.

The two 786 nm lasers, one from the UIBK node and one from the IQOQI node, were overlapped on a beamsplitter placed in the UIBK node laboratory. The signal is sent onto an amplified photodiode. The central frequency of the detected beat signal was analyzed by a spectrum analyzer, or its central frequency was determined by a frequency counter[4]. Observations of the beat revealed a drift of 40 Hz/s. This is attributed entirely to the drifts of the UIBK transfer cavity. To compensate for this and stabilize the beat signal, a digital feedback to an AOM in the UIBK Raman laser path at 786 nm based on constant monitoring of the frequency beat was established.

When initializing the feedback, we first set a target frequency by reading the initial frequency of the beat. When the frequency of the beat differs from the target value, the digital feedback loop changes the frequency of the frequency generator driving the AOM in the UIBK 786 nm laser path such that the beat frequency is kept constant. Additionally, we use the drift to provide feedback for the ion-cavity locking laser at UIBK that is stabilized to the same transfer lock cavity. A scheme of the beat and feedback setup is shown in Figure 5.7.

Transmission efficiency of the fiber bundle at 854 nm

Single photons used in our quantum network have a wavelength of 854 nm. Besides the long optical fiber bundles between the buildings, the total fiber path includes additional shorter optical fibers. One 1.5 m long fiber is placed on each input port of the HOM board, enabling classical light to be easily sent into the board for alignment, or to use

3 The fundamental of each Raman laser is locked to a "transfer lock" cavity, alongside the laser used to lock the ion-cavity length at each node.

4 TTi TF930

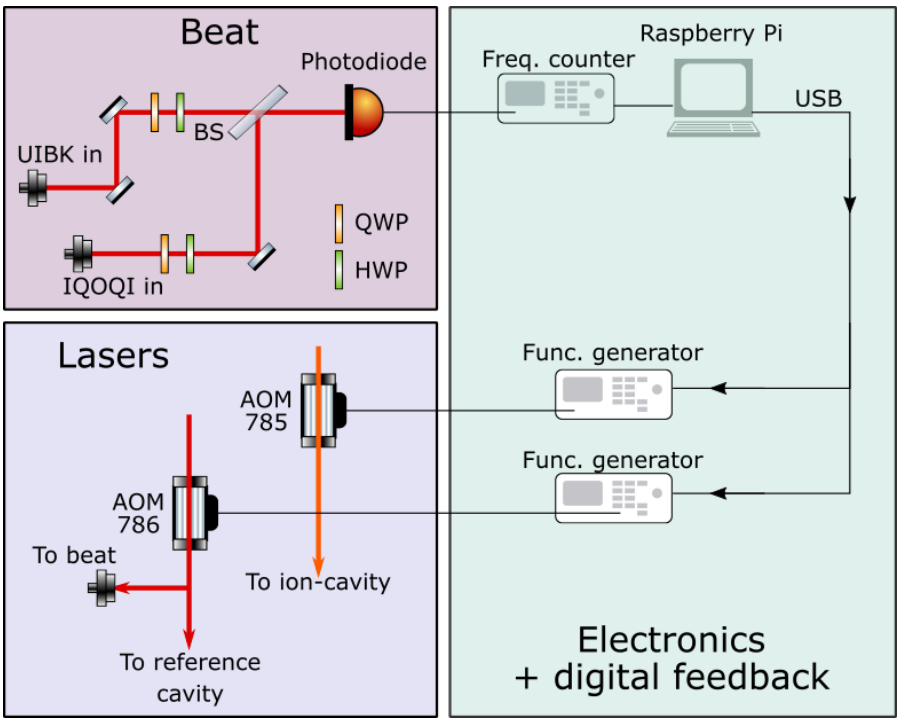

Figure 5.7: **Experimental setup for frequency beat between two Raman lasers at 786 nm with feedback to UIBK lasers.** The two lasers are overlapped on a beamsplitter (BS). Polarization of each of the lasers is optimized using a quarter waveplate (QWP) and a half waveplate (HWP). The overlapped light is then detected on a photodiode and a center of frequency beat signal is registered by a frequency counter connected to a computer (Raspberry Pi). Based on the drift of the center line of the beat, a program adjusts the frequency of function generators driving AOMs in laser paths of the UIBK 786 nm and 785 nm lasers. For a determination of laser linewidth (paragraph "Raman laser linewidth (γ_{laser})" in Section 5.4.1) the detected beat signal is analyzed with a spectrum analyzer instead of a frequency counter.

Position	Power μW	STD μW	Percent of input %
UIBK input	404.8	1	100
IQOQI basement	207.7	0.5	51.2
IQOQI lab	172.8	0.9	42.7
IQOQI HOM board	164.6	0.5	40.7

Table 5.4: Measured powers of an 854 nm laser through the single mode fiber link between the UIBK node and the HOM board at IQOQI. The entire path consists of 510(2) m single mode fiber (Bundle 2, Orange), a 20 m fiber between ICT basement and IQOQI node, and 1.5 m fiber at the input of HOM board. All fibers are joined using mating sleeves (ThorLabs ADAFCPM1).

the board for other experiments. One 5 m fiber is present in the UIBK lab, connecting the setup with the fiber link. One 20 m long fiber connects the basement of the ICT building, where the bundles end at IQOQI node, with the HOM board. Fibers are joined together using mating sleeves (ThorLabs ADAFCPM1) that introduce additional loss of < 0.5 dB per unit in the distribution channel. There are 3 such connectors in the fiber path taken by the UIBK photon. We measured the total transmission of the fiber path traveled by the UIBK photon by injecting laser light at 854 nm provided by a fiber-coupled Toptica DL Pro laser diode placed in the UIBK laboratory. The power was measured at different points along the fiber link using an optical powermeter[5]. The measurement shows total transmission of the entire fiber link to be 40.7%. The input power was measured as a power at the end of fiber that brings the light from the laser source, before the first mating sleeve connecting the fiber to the fiber bundle at UIBK node. Powers measured at different points of the link are presented in Table 5.4.

5.4 EXPERIMENTAL PARAMETERS

Both participating nodes use a cavity mediated Raman transition (CMRT) introduced in Section 3.2 to generate single photons. This process couples the initial electron state $|s\rangle = |4^2S_{1/2}, m_j = -1/2\rangle$ to the metastable final state $|d\rangle = |3^2D_{5/2}, m_j = -5/2\rangle$ via the intermediate excited state $|p\rangle = |4^2P_{3/2}, m_j = -3/2\rangle$, as can be seen in Figure 3.2. The $|s\rangle$ to $|p\rangle$ transition is driven by the *Raman* laser at 393 nm and with Rabi frequency Ω. The $|p\rangle$ to $|d\rangle$ transition is driven with the vacuum cavity field at 854 nm with maximum ion-cavity cou-

5 Thorlabs PM100D with sensor S130VC; SN 16022905

pling strength g_0. Both these drives are detuned from their respective transitions by Δ. More details on these parameters are now given.

5.4.1 *Parameters calibration*

Calibrated values of experimental parameters for the HOM experiments presented in this chapter are shown in Table 5.5. By calibration, it is meant that the values have been determined based on additional measurements as described in the subsequent paragraphs.

	$\Omega/(2\pi)$ MHz	$g_0/(2\pi)$ MHz	$\Delta/(2\pi)$ MHz	$\kappa/(2\pi)$ MHz	$\gamma_{laser}/(2\pi)$ kHz
UIBK	40 ± 1.2	1.53 ± 0.01	403 ± 5	68.4 ± 0.6	27.06 ± 0.44
IQOQI	40 ± 0.5	1.53 ± 0.30	403 ± 5	70 ± 2	0.087 ± 0.001

Table 5.5: Independently calibrated parameters for the remote HOM experiment.

Raman laser Rabi frequency (Ω)

The Rabi frequency Ω of the 393 nm laser is determined by measuring the AC Stark shift, δ_{AC}, of the Raman transition caused by the laser field. The Rabi frequency is then given by [83]

$$\Omega = \sqrt{4\delta_{AC}\Delta}, \tag{5.1}$$

where Δ is the detuning of the Raman laser from the $|s\rangle$ to $|p\rangle$ transition. This formula is a first order approximation of the full expression [83] for the AC Stark shift induced on an energy level of an atomic dipole transition and is valid in case $\Delta \gg \Omega$, as it is in our case. The measurement of δ_{AC} proceeds as follows. First, the frequency of the CMRT at the target laser power is determined by measuring the center of the spectroscopic line. In this measurement we scan the frequency of the Raman laser while monitoring the cavity-photon count rate and then determine the position of maximum count rate. Second, the center of the line is measured again but this time for a vanishingly small laser power, which reveals the unshifted line frequency. The difference between the two center line frequencies give δ_{AC}.

The measurements yielded $\Omega_{IQOQI}/(2\pi) = 40 \pm 0.5$ MHz for the transition driven at the IQOQI node, and $\Omega_{UIBK}/(2\pi) = 40 \pm 1.2$ MHz at the UIBK node.

Maximum ion-cavity coupling strength (g_0)

The calibration of the maximum ion-cavity coupling strength g_0 is described now. The coupling strength was defined earlier in Section 3.2, Equation 3.1. At IQOQI, a value of $g_0/(2\pi) = 1.53 \pm 0.01\,\text{MHz}$ was determined by measurement of the frequency spacing between various modes of the cavity to kHz precision, together with knowledge of atomic state lifetimes and branching ratios, as described in detail in Chapter 4 of [83]. At UIBK, a value of $g_0/(2\pi) = 1.53 \pm 0.30\,\text{MHz}$ was estimated in Chapter 4 of [82] using properties of the cavity and of the atomic transitions.

Cavity decay rates (κ)

The cavity decay rate of the mode used for the single photon generation at 854 nm, κ, was determined at both nodes via a ring-down measurement, as described in [41]. Laser light at 854 nm is coupled into the cavity and its frequency is swept across the resonance of the chosen TEM_{00} mode. Triggered on a predetermined cavity output level measured on a photodiode in transmission, the laser is rapidly switched off and the light stored in the cavity decays exponentially in time and is recorded by the photodiode. The cavity decay rate is obtained from the cavity decay time $\tau = 1/(2\kappa)$.

These measurements were performed several months prior to the HOM measurements, however the decay rates are not expected to change within statistical precision over these timescales. The IQOQI cavity decay rate of $\kappa = 2\pi \times 70 \pm 2\,\text{kHz}$ was obtained and is presented in Chapter 4.1.1 of [83]. The decay rate of the UIBK cavity of $\kappa = 2\pi \times 68.4 \pm 0.6\,\text{kHz}$ was obtained and is presented in Chapter 4.4.1 of [82].

Raman detunings (Δ)

The detuning of the Raman laser from the $|s\rangle$ to $|p\rangle$ transition was measured at the IQOQI node using a wavemeter (HighFinesse WSU10). Specifically, the CMRT process is set up to continuously generate cavity photons in the presence of 866 nm and 854 nm repumping lasers. The electronic state of the ion is measured, by the electron shelving technique, as the Raman laser frequency is scanned over the Raman resonance all the way to direct resonance with the $|s\rangle$ to $|p\rangle$ transition. The frequency difference between these two spectroscopic features, measured with the wavemeter, yields the detuning $\Delta = 2\pi \times (-403 \pm 5)\,\text{MHz}$. The uncertainty is set largely by the lifetime of the $|p\rangle$ state.

At UIBK, the same value of Δ is assumed. This can be justified with the following arguments. First, as the results of the two photon

interference experiment will show, the UIBK and IQOQI cavities had the same frequency to within less than a few hundred kHz. Second, the magnetic field difference between the two nodes causes shifts in the $|s\rangle$ to $|p\rangle$ transition on the order of a few hundred kHz at most. Both of these differences are well within the uncertainty of the value $\Delta/(2\pi) = -403 \pm 5\,\text{MHz}$.

Raman laser linewidth (γ_{laser})

The linewidth of the Raman laser at IQOQI was determined by performing a beat measurement between its fundamental wavelength of 786 nm and a frequency comb. The measurement was performed by Helene Hainzer and is reported in her Master thesis [114]. The result of the measurement revealed a full-width at half-maximum (FWHM) beat linewidth of 87 ± 1 Hz over a 12 s integration time. The linewidth of the Raman laser at 393 nm is then taken as twice this value. This linewidth plays a negligible role in the CMRT given its timescale of a few ten microseconds and is not considered in any modeling.

The linewidth of the Raman laser at UIBK was determined via beat measurements between the fundamental (786 nm) of that laser and the fundamental of the IQOQI Raman laser at the same wavelength sent over the optical fiber link. The setup is shown in Figure 5.7, except that instead of a frequency counter we used a spectrum analyzer to collect the data. The result of this measurement is shown in Figure 5.8. A beat note with FWHM of 13.53 ± 0.22 kHz over 10 s acquisition time at 786 nm was measured, corresponding to $2\gamma_{laser} = 27.06 \pm 0.44$ kHz at 393 nm.

5.4.2 *Parameters used in simulation*

Simulations of the remote HOM experiment were performed using the theoretical model presented in Section 3.3.4. Here, model parameters and specific values used are presented below.

Spontaneous decay from the $|p\rangle = 4^2P_{1/2,mj=-3/2}$ state competes with the CMRT process. The decay rate $\gamma_{ps} = 2\pi \times 10.7\,\text{MHz}$ is from the state $|p\rangle$ to ground state $|s\rangle$. The decay rate $\gamma_{pd} = 2\pi \times 0.75\,\text{MHz}$ describes the total decay from the state $|p\rangle$ to the states $|3^2D_{5/2,-5/2}\rangle$, $|3^2D_{5/2,-2/2}\rangle$ and $|3^2D_{5/2,-1/2}\rangle$, as well as to the $|3^2D_{3/2,-3/2}\rangle$ state and the $|3^2D_{3/2,-1/2}\rangle$ state.

Table 5.6 presents an overview of other key parameter values used in the HOM simulations to generate the models presented later in Figure 5.9, Figure 5.10, and Figure 5.11. The Raman Rabi frequency (Ω), detunings (Δ), and cavity linewidths (κ) used for simulations are all the ones found by independent calibrations, as described earlier and shown in Table 5.5. The simulations use a jitter of the UIBK Raman laser frequency of $\gamma_{laser} = 2\pi \times 15\,\text{kHz}$, approximately consistent with

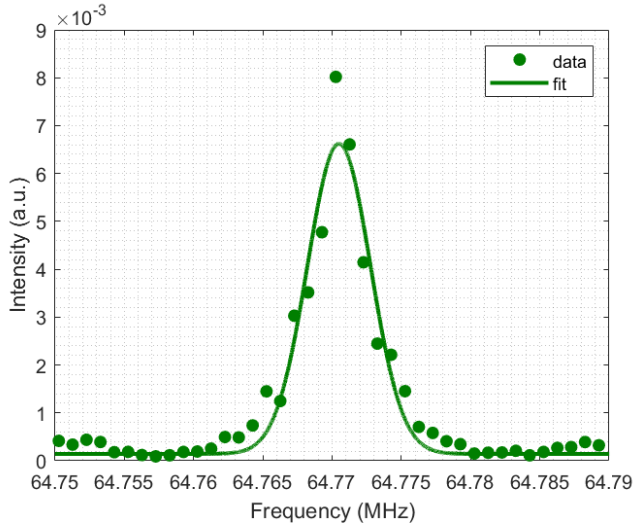

Figure 5.8: **Frequency beat between two Raman lasers at** 786 nm**, each at different node of the network.** Experimental data (green points) are fitted with a Gaussian function (solid line), revealing a FWHM $= 13.53 \pm 0.22$ kHz.

the independently calibrated value of $\gamma_{laser} = (13.53 \pm 0.22)$kHz, taken 3 months prior to the HOM experiment.

	$\Omega/(2\pi)$ MHz	$g_{eff}/(2\pi)$ MHz	$\Delta/(2\pi)$ MHz	$\kappa/(2\pi)$ kHz	$\gamma_{laser}/(2\pi)$ kHz	ϵ
UIBK	40	0.52	403	67.8	15	0.01
IQOQI	40	0.69	403	70	0	0.08

Table 5.6: **Parameters of the remote HOM experiment used in the simulations based on model presented in Chapter 3**

The theoretical model of Section 3.3 uses the symbol g for the ion-cavity coupling strength parameter. When simulating the HOM experiment we use the parameter g_{eff}, that is $g = g_{eff}$. In the following paragraphs the definition of g_{eff} and its value used for the simulation will be presented. As described in Chapter 3, the cavity mediated Raman transition (CMRT) can be described as driving an effective two-level atomic transition with the Hamiltonian parameterized by an effective Rabi frequency

$$\Omega_{eff} = \frac{\Omega g_{eff}}{\Delta}, \tag{5.2}$$

where Ω is the Raman laser Rabi frequency on the $|s\rangle$ to $|p\rangle$ transition and Δ is the overall CMRT detuning from the $|p\rangle$ state. The parameter g_{eff} is the effective ion-cavity coupling strength, defined as

$$g_{eff} = \alpha \cdot \mathcal{G}_m \cdot \zeta \cdot g_0. \tag{5.3}$$

Here α is a factor between 0 and 1, which has been introduced in addition to Equation 3.1 to account for experimental imperfections, $\mathcal{G}_m$ is the Clebsh-Gordan factor for the $|s\rangle$ to $|p\rangle$ transition and ζ is a geometrical factor due to the projection of the cavity polarization onto the atomic dipole moment and g_0 is the maximum ion-cavity coupling strength that could be achieved in the experiment, set by atomic and cavity properties (Section 5.4). As described in Section 5.1.2, the Raman laser in both nodes points along the quantization axis and has circular polarization set to maximally drive the $|s\rangle = |4^2S_{1/2}, m_j = -1/2\rangle$ to $|p\rangle = |4^2P_{3/2}, m_j = -3/2\rangle$ transition. The relevant Clebsh-Gordan coefficient is $\mathcal{G}_m = \sqrt{10/15}$. At both nodes, photon polarization along the quantization axis is denoted as being horizontal. At both nodes, the cavity axis is modelled as being perpendicular to the quantization axis, which is accurate up to a few degrees tilt. The polarization of the photon generated in the cavity during the HOM experiment is vertical (V), as determined by the projection of the $|p\rangle = |4^2P_{3/2}, m_j = 3/2\rangle$ to $|d\rangle = |3^2D_{5/2}, m_j = -5/2\rangle$ dipole moment onto the plane perpendicular to the cavity axis, corresponding to a cavity-projection parameter of $\zeta = \sqrt{0.5}$.

Lastly, the factor α has to be defined for each node. This factor captures any effects that reduce the achieved ion-cavity coupling strength in the experiment other than the Clebsch-Gordan and cavity projection factors. At IQOQI we use $\alpha = 0.78$, at UIBK we use $\alpha = 0.59$. The values of α were determined for both nodes by comparing simulations with measured single photon wavepackets for each node separately. Here, the simulations are done using a master-equation model of an 18-level atom and cavity system with all the aforementioned parameters. More information on the 18-level model can be found in Chapter 5.4 of [83] and Chapter 3 of [115]. The α parameters found provide a match between the simulated and measured single photon wavepackets at each node. The wavepackets are taken from the asynchronous photons generated in the HOM experiments. These parameters are therefore not independently calibrated from the data.

The α parameter at IQOQI is consistent with what we would expect due to the finite temperature of the ion after Doppler cooling. The dominant effect of being outside the ground state on cavity-photon generation is due to a change in the coupling of the Raman laser to the ion. Specifically, for a motional mode with phonon number n, the Raman laser Rabi frequency can be approximated by $\Omega_n \approx \Omega(1 - \eta^2 n)$, where η is the Lamb-Dicke parameter. The approximation holds for $\eta^2(2n + 1) \ll 1$ (the Lamb-Dicke regime). For the full expression without approximation see e.g., Ref. [116]. Outside of the ground state, the coupling of the 393 nm Raman laser to the axial motional mode ($\eta = 0.13$) causes the most significant reduction of the Rabi frequency. Taking the full expression [116], and using 10 and 5 as the average phonon numbers in our axial and radial modes after

Doppler cooling, respectively, yields $\alpha = 0.78$. Those average phonon values are consistent with direct measurements made via sideband and carrier Rabi flops (taken days before the HOM experiment) which yielded 11(2) and 8(2) for the axial and radial mode, respectively [102].

In contrast, the α parameter used in simulations of the UIBK wavepacket (0.59) is lower than one that can be expected due to the ion temperature measurements after Doppler cooling, which yield similar estimates for the phonon occupation numbers as for the IQOQI node. The cause of the lower-than-expected ion-cavity coupling strength at UIBK is not clear.

5.5 RESULTS

The Hong-Ou-Mandel experiment with remotely generated photons was performed on February 12th and 13th 2020. Results from the experimental run at 00:46:41 on February 13th 2020 are described first in this section. This experimental run is further called "004641" in the coming text. The 004641 run lasted 1428 seconds ($\approx$ 24 minutes). During the run, the total number of sequential photon generation attempts (synchronous and asynchronous) was $AT_I = 1101648$ by the IQOQI node and $AT_U = 1191326$ for the UIBK node. We attribute the difference to cases in which either the trigger communication failed, or the IQOQI Pulsebox was not ready to be triggered.

The temporal profile of photon detection events collected during the "004641" run, conditional on both nodes attempting to generate photons, is depicted in Figure 5.9(a). The first peak, seen between $t = 0\,\mu$s and $t = 30\,\mu$s, corresponds to the time window when the synchronous photons are expected to be detected. Photon counts from both nodes contribute to that peak. Two distinct peaks, one around 240 μs and one around 290 μs correspond to the asynchronously-generated photons from each node separately: first from the IQOQI node and then from the UIBK node. Since these asynchronous peaks do not contain photons from both nodes, we henceforth refer to them as single photon wavepackets.

The background count rate summed over the two detectors is 2.8 ± 0.2 cts/s and was estimated by counting the number of detection events in the 50 μs time window between 100 μs and 150 μs, outside of photon generation processes. This background is negligible compared to the signal generated by photons created during the sequence.

Figure 5.9(b) presents the detected asynchronous single photon wavepacket from the IQOQI node and compares it with the simulation produced by the model of Section 3.3. The simulation shows the modeled single photon wavepacket using Equation 3.20 and the parameters presented in Section 5.4 and Table 5.6 for the IQOQI node. The theoretical model and experimental data show a close qualitative agreement. An estimate for the probability of detecting an asyn-

chronous photon from IQOQI, P_I, is calculated by integrating the number of detected counts in the IQOQI single photon wavepacket (Figure 5.9(b)), and dividing by the number of generation attempts, AT_I, yielding $P_I = (670 \pm 2) \times 10^{-4}$, or 6.70(2)%.

Figure 5.9(c) shows the detected asynchronous single photon wavepacket from the UIBK node and compares it to the same theoretical model of Section 3.3, using Equation 3.20 with parameters specific for the UIBK node that are presented in Section 5.4 and Table 5.6. There is qualitative agreement between the theoretical model and the measured data for the first part of the wavepacket. However, there is a clear mismatch in the later part of the wavepacket. A possible explanation is that a cavity length jitter at the UIBK node is responsible for this effect. A detailed analysis and model of the effect of cavity jitter at the UIBK node on two-photon interference was not done until later, during the remote ion entanglement presented in Chapter 6. An estimate for the probability of detecting an asynchronous photon from UIBK, P_U, is calculated by integrating the number of detected counts in the UIBK single photon wavepacket (Figure 5.9c), and dividing by the number of generation attempts, AT_U, yielding $P_U = (800 \pm 9) \times 10^{-5}$, or 0.800(9)%, where the uncertainties derive from attributing Poissonian photon counting statistics to the number of photons detected.

To evaluate the distribution of coincident detection events between the two detectors we first choose a time window (gate) in which the corresponding photons are expected to arrive based on the sequence timing and the histogram of all recorded events. For the synchronous pair we consider a time window between 0 and 30 μs. For the asynchronous photons we consider a time window between 240 and 312 μs (see Figure 5.9(a)). Then we calculate the probability density $\rho_c(\tau)$ for observing a two-photon detection event in a given trial as a function of the detection time difference $\tau = t_2 - t_1$. The plotted values, presented in Figure 5.10 (a), are calculated as

$$\rho_c(\tau) = \frac{1}{\Delta_t k} \int_{gate} \mathrm{d}t_1 \int_{t_1+\tau}^{t_1+\tau+\Delta_t} \mathrm{d}t_2 N(t_1, t_2), \tag{5.4}$$

where $N(t_1, t_2)$ is the number of two-photon clicks that occurred between times t_2 and t_1, Δ_t is the bin size, and k is number of attempts. We label the coincidence probability density of synchronous photons with a superscript $\parallel$ and coincidence probability density of asynchronous photons with $\perp$. Clear suppression of the coincidence detection events for the synchronous photon pair is seen in Figure 5.10(a) for arrival time differences below 5 μs. In contrast, the asynchronous coincidences are seen to peak at a value consistent with the arrival time difference between the asynchronous photon wavepackets.

In order to quantify the visibility of the HOM dip, the coincidence distribution of the asynchronous photons in Figure 5.10(a), peaking at $\tau = \pm 42\,\mu$s, is shifted to $\tau = 0$ and summed over positive

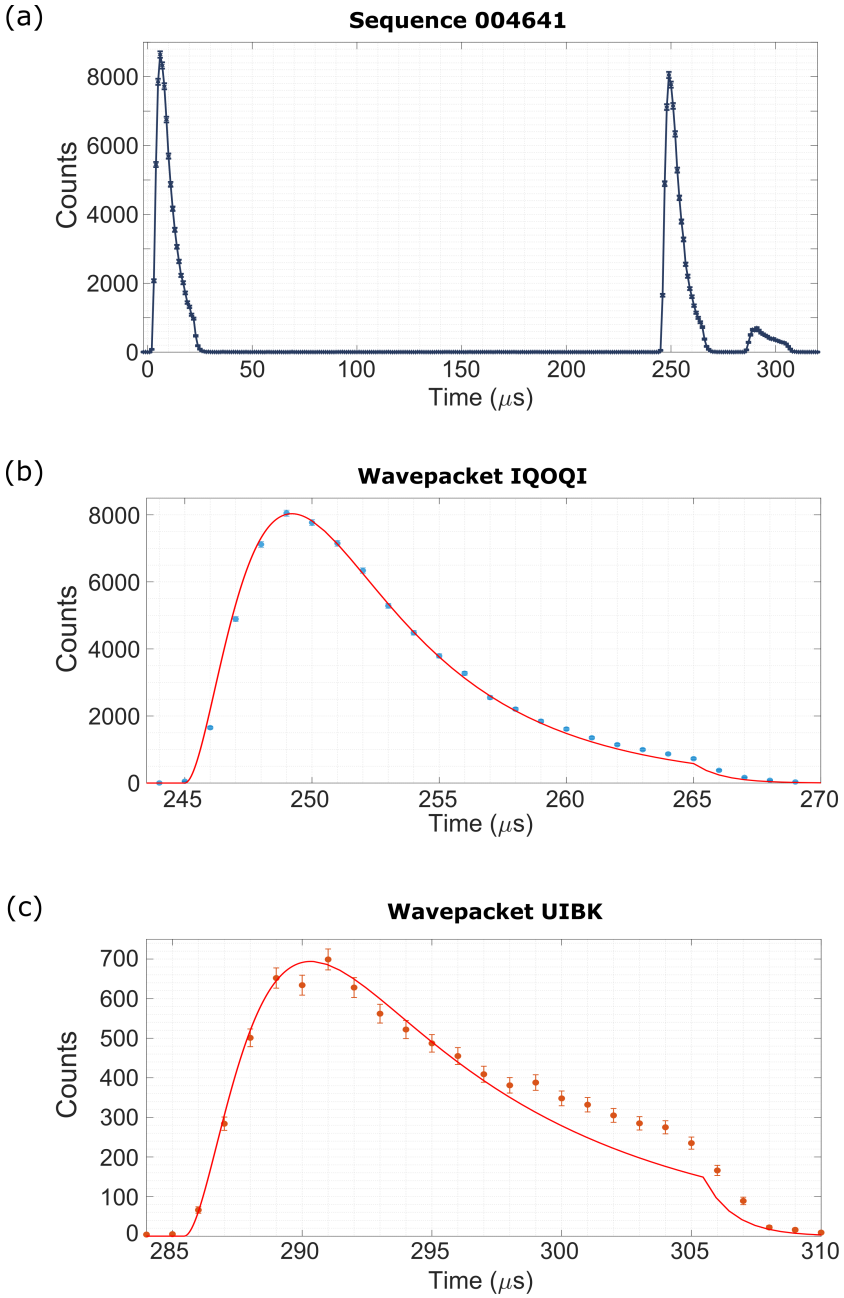

Figure 5.9: **Histogram of photon detection events during the remote HOM experimental run 004641.** (a) Temporal profile of photon detection events (crosses with joined lines, errorbars of the size of data points) recorded during the execution of the experimental sequence. The used time bin is 1 μs, referenced to the first Raman pulse of the UIBK node. The first peak between 0 and 25 μs represents the temporal profile of detector clicks (wavepacket) of the synchronous photons. The peaks between $t = 240\,\mu$s and $t = 310\mu$s represent wavepackets of asynchronous photons. (b) Blue data points: zoom in of the panel (a) showing the asynchronous single photon wavepacket from IQOQI. Red line: theoretical simulations based on 3-level model as described in the main text. (c) Orange data points: zoom-in of the asynchronous single photon wavepacket from the UIBK node. Red line: theoretical simulations based on 3-level model as described in the main text. The counts are the sum of the two detectors on the HOM board.

and negative branches. These time-shifted asynchronous coincidence counts represent the expected coincidence distribution for fully distinguishable photons arriving synchronized at the beamsplitter. The time-shifted asynchronous coincidence counts and synchronous coincidence counts are presented in Figure 5.10(b). The experimental data are compared to a theoretical model presented in Section 3.3.4. The model for distinguishable (temporally displaced) photons was presented in Equation 3.21 and the model for indistinguishable (temporally synchronous) photons was presented in Equation 3.23. Parameters used for the model are given in Table 5.6. Qualitative agreement is seen between the experimental data and the theoretical model.

To determine the visibility of two-photon interference, we first define the integrated coincidence probability for synchronous ($C^{\parallel}$) and time-shifted asynchronous ($C^{\perp}$) photons as

$$C^{\parallel,\perp}(T) = \int_{-T}^{T} (\rho_c^{\parallel,\perp}(\tau))\mathrm{d}\tau, \tag{5.5}$$

where T is total coincidence window of interest. The visibility is then defined as

$$V(T) = 1 - \frac{C^{\parallel}(T)}{C^{\perp}(T)}. \tag{5.6}$$

A comparison between visibility $V(T)$ extracted from the data and the one from the model, given by the Equation 3.27, is presented in Figure 5.10(c). The measured visibility for the smallest coincidence window of $1\,\mu$s is $V(1\,\mu\mathrm{s}) = 0.95 \pm 0.02$. To identify the limits to this value, more data would be required to reduce the statistical uncertainty. A decline in visibility with increasing coincidence window is evident in both the data and the model. One phenomenon that we consider and can lead to the drop of visibility is the laser phase noise in the UIBK node of $\gamma_{laser} = 27\,\mathrm{kHz}$ (see paragraph "Raman laser linewidth (γ_{laser})" in Section 5.4.1). The green dashed line in the visibility plot in Figure 5.10(c) shows the predicted drop of visibility when the laser phase noise at UIBK is set to 0. The model clearly predicts that eliminating the laser phase noise should have no significant effect on the visibility. The remaining modeled imperfections that compromise visibility are spontaneous scattering from each ion during the Raman processes and mismatches between the single photon wavepackets produced by different nodes.

We take the following approach to distinguish between the two aforementioned imperfections. Firstly, the theoretical model can predict the single photon states generated in the cases in which no spontaneous scattering event occurs during photon generation. The predicted interference visibility of two such "temporally-pure" photon wavepackets, in addition to no laser phase noise, is shown as a solid red line in Figure 5.10(c). The model clearly predicts that spontaneous scattering is the dominant factor that limits the interference visibility in the HOM

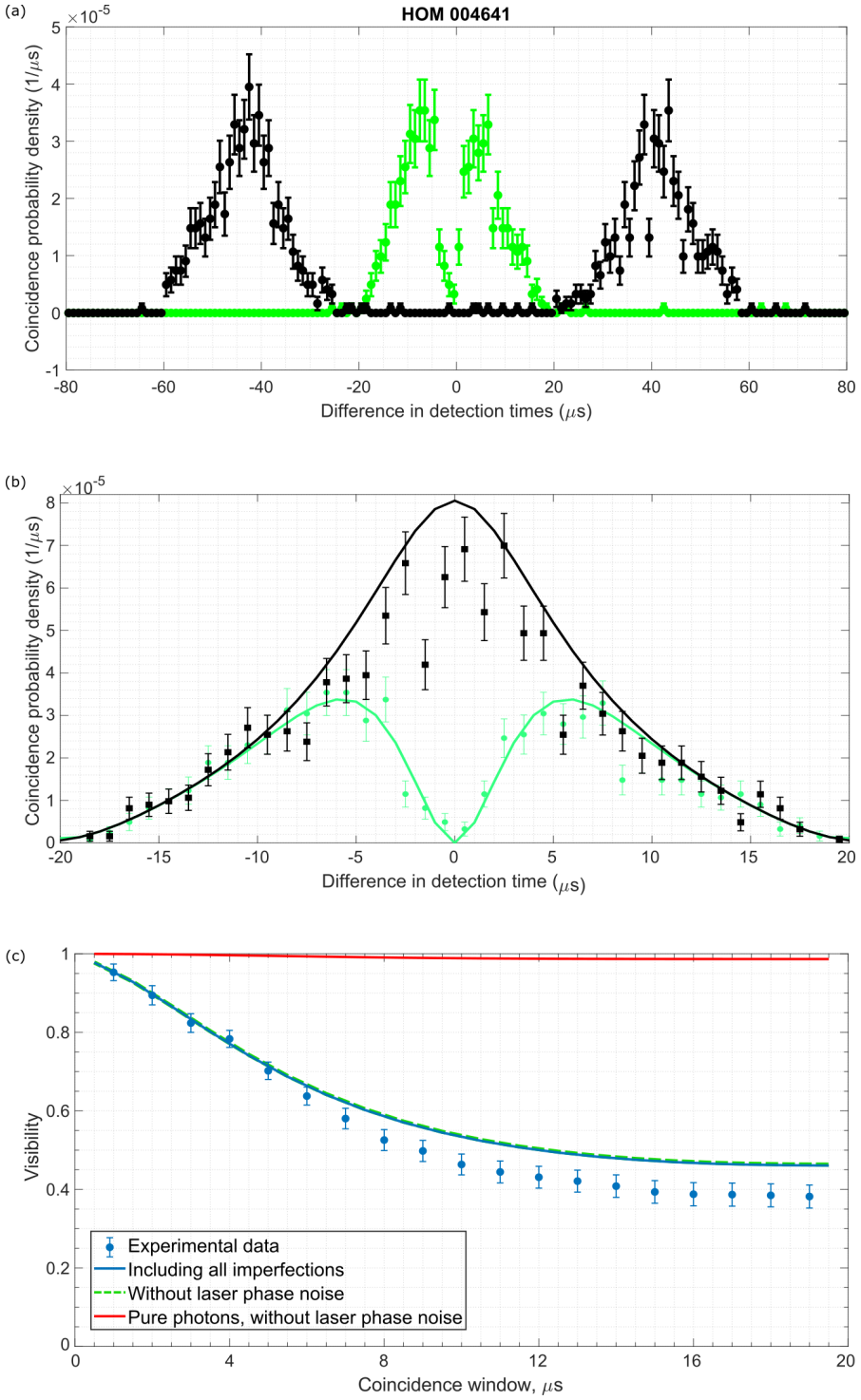

Figure 5.10: **Results of Hong-Ou-Mandel experiment run 004641.** (a) Coincidence probability density of temporally synchronous ($\rho^{\parallel}$, green dots) and asynchronous ($\rho^{\perp}$, black dots) photons. Time bin 1 μs. (b) The same plot as in the top panel after $\rho^{\perp}$ corrected for 42 μs shift. Solid lines represent theoretical model described in Section 3.3. (c) Visibility of the HOM interference calculated using Equation 5.6 compared to theoretical model of Section 3.3.4.3 with all considered imperfections (blue solid line), without laser jitter (green dashed line, largely hidden behind the blue line), and without both laser jitter and spontaneous scattering (solid red line). The biggest difference between the model including all imperfection and model without laser jitter is 0.0023 reached for 19.5 μs coincidence window.

experiment. The remaining predicted slight drop in the red line with increasing coincidence window can be assigned to temporal shape mismatch of the two "temporally-pure" photons.

The rate of spontaneous scattering events can be reduced in either node by increasing the effective coupling rate g_{eff} of the photon generation process. The methods to increase that rate are discussed and modeled in our paper [102] and would require e.g., a change in quantization axis direction or employing entangled superradient states of multiple ions, as demonstrated in the UIBK node cavity [113]. The reduction of g_{eff} due to ion temperature has been discussed earlier in Section 5.4.2. Ground state cooling of the ion's motional states offers a possibility to increase the α parameter to 1, as demonstrated in the IQOQI node [102] and thus increasing g_{eff}.

5.5.1 *Two-photon interference in the case of a cavity frequency mismatch*

Another experimental run was performed approximately 1 hour prior to the "004641" run presented in the previous section. The data set is called "233201". The process of matching frequency of the optical cavities, as described in Section 5.3, paragraph "Frequency matching of the remote cavities" is performed before each experimental run to bring the two photons from the participating nodes into resonance with each other. For the experimental run "233201" this happened at 22:40, about 50 minutes before we started the execution of the run. The procedure was repeated also directly after the experimental run. The second calibration measurement revealed a relative frequency difference of the two cavities of 0.2 MHz, where the precision is set by the combination of the linewidths of the cavities and the lasers used to lock them.

Since the two cavities were found to be off-resonant, we wanted to know whether the Raman processes at either node were also run off-resonantly. The answer to this question will determine how to correctly simulate the interference data from this experiment. To determine whether the Raman processes were run resonantly during this experimental run, we compare single photon wavepackets collected in the run "233201" with those collected during the experimental run "004641". A Raman process that is 0.2 MHz off-resonant would result in a notable difference between the wavepackets.

Figure 5.11(a) compares the measured IQOQI node's wavepackets collected during the "004641" and "233201" runs[6]. The comparison of the two wavepackets with theoretical model reveals no change in experimental parameters other than the total efficiency which increased

6 The simulations presented in Figure 5.11 do not include the smallest spontaneous decay rate to the $D_{3/2}$ state. However, we found that this shifts the amplitudes in modeled wavepackets by an amount on the same order as the error bar amplitudes in individual data points and does not affect the comparison between wavepackets.

by 1.8% in the "004641" run. The results in Figure 5.11(a) show no evidence for an off-resonant Raman process at IQOQI during either experimental run.

Wavepackets from the UIBK node taken in the "004641" and "233201" runs are compared in Figure 5.11(b). A change consistent with an overall efficiency increase of 13% in the "004641" run can be observed. In the Figure 5.11(c) we re-scaled the data collected during the "233201" experimental run by this amount to overlap with the data set "004641" and compared it to a common theoretical prediction, yielding a good qualitative match for both sets. There is then also no evidence for a change in the UIBK Raman resonance process between the two runs and thus the only additional imperfection in the "233201" run, compared to the "004641" was the two cavities being off resonant.

The two-photon coincidence data from the 233201 run, plotted in Figure 5.12, show a strong peak in the detected synchronous coincidences at approximately $\pm 3.5\,\mu$s time difference. This is a signature of photon anti-bunching. Figure 5.12 also presents the theoretical model as before, but now extended to include a DC offset between the two cavity frequencies as described in Section 3.3.5. A value of the DC offset of 160 kHz is used, which was found to match the position of the bunching peaks in the data. The model predicts oscillations in coincidences of the synchronous photon pair with a period given by $1/(2\delta_f)$, where δ_f is the frequency offset. For 160 kHz one expects the first peak at 3.13 μs.

This frequency offset compromises the interference visibility and should be avoided in future experiments. One approach would be to perform the resonance check and recalibration more often. Further learning about the origin of the relative cavity drift would enable designing strategies for reducing it.

While further investigation of the origin of the relative cavity drift is required and beyond the scope of this thesis, the following possible explanation of the phenomenon is offered. Recall that a beat between Raman lasers at 786 nm is used to stabilize drifts of the UIBK Raman laser, described in Section 5.3. The underlying cause is expected to be drifts in the cavity used to lock the UIBK Raman laser and the UIBK ion-cavity locking laser at 786 nm. To correct for these effects a feedback, described in Section 5.3, is implemented to two AOMs in the laser paths. We know that the beat lock was at least partially engaged since the frequency of the beat was recorded and constant within 3 kHz during the "233201" measurement. However, if feedback wasn't engaged to the AOM controlling the 785 nm cavity locking laser then the UIBK ion-cavity frequency drift at 785 nm would be 40 Hz/s, which over 60 mins yields 144 kHz. Although we have no reason to otherwise think that feedback to that AOM was not applied, the predicted effect is consistent with the results.

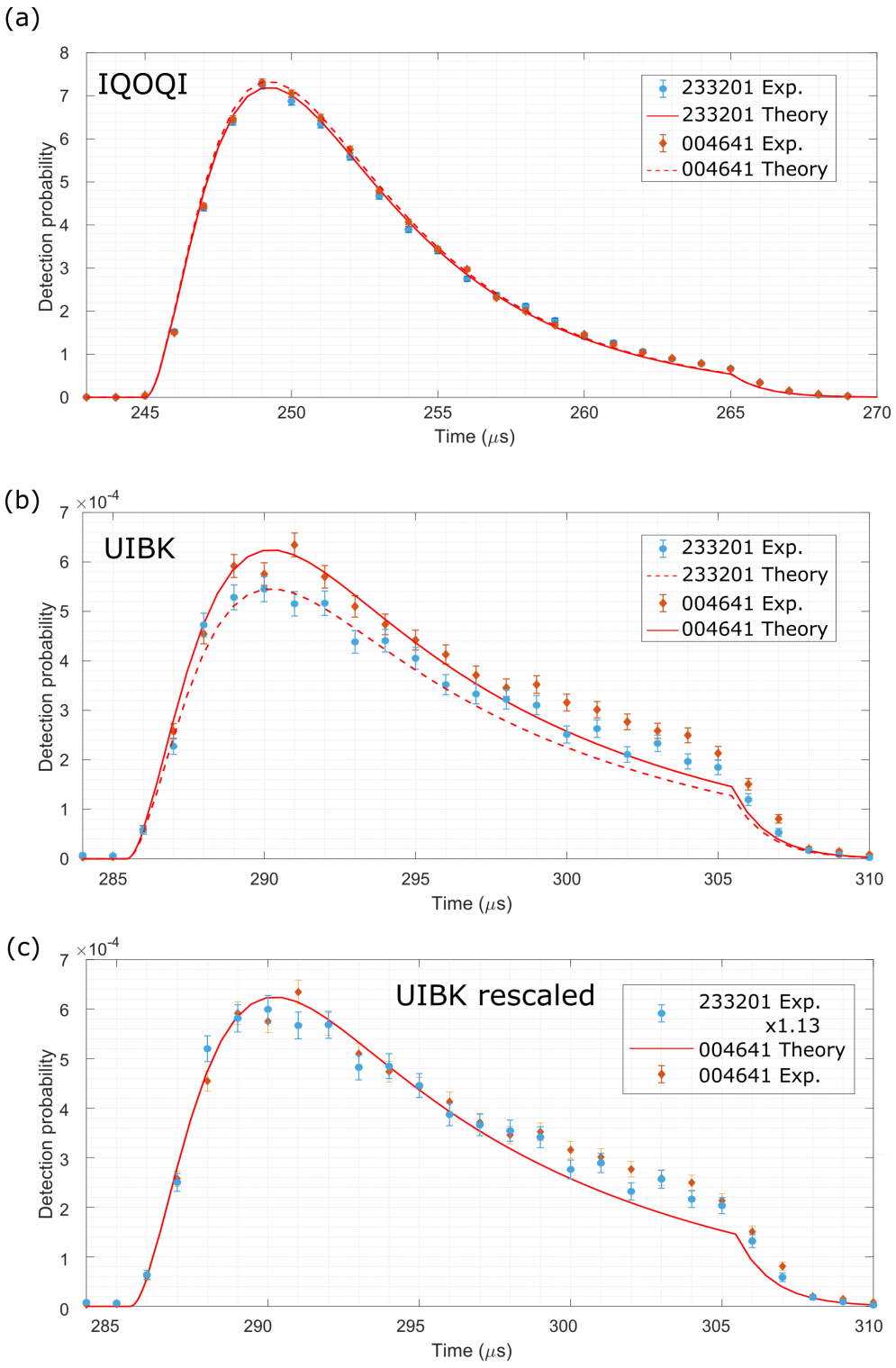

Figure 5.11: **Photon wavepacket comparison between two experimental runs.** (a) IQOQI wavepackets compared with the same theoretical predictions using the same parameters up to an overall efficiency factor. Specifically, the simulated wavepackets differ only by a 1.8% lower overall efficiency for the "233201" run. (b) UIBK wavepackets compared with the same theoretical predictions using the same parameters up to an overall efficiency. The simulated wavepackets differ only by a 13% lower overall efficiency for the "233201" run. (c) UIBK wavepacket of experimental run "233201" rescaled by a factor 1.13 and UIBK wavepacket of experimental run "004641" are both plotted alongside a common theoretical model. The theoretical model used to produce the simulations is described in Section 3.3.4.

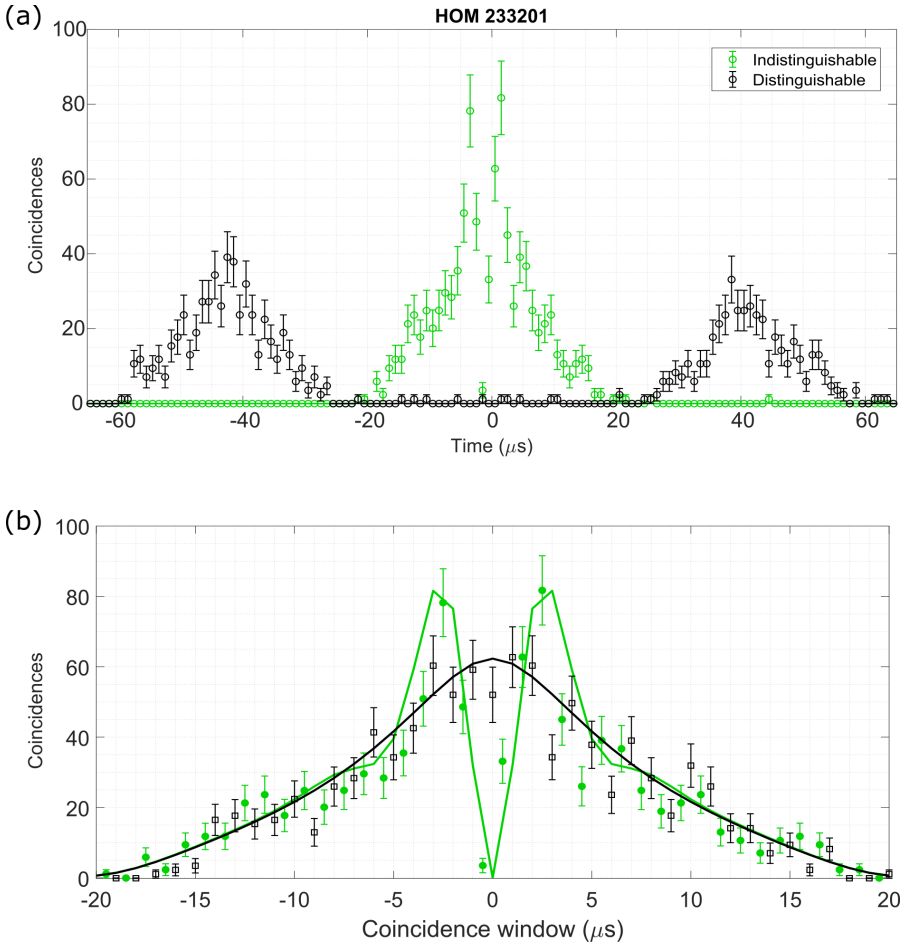

Figure 5.12: **Two-photon interference with frequency mismatched photons in experimental run "233201".** (a) Coincidence probability density of temporally synchronous ($\rho^{\parallel}$, green dots) and asynchronous ($\rho^{\perp}$, black dots) photons. Time bin 1 μs. (b) The same plot as in the top panel after $\rho^{\perp}$ corrected for 42 μs shift. Solid lines represent theoretical model described in Section 3.3 with 160 kHz DC offset of photon frequency.

Second, at each node, the Raman resonance condition at 854 nm is sometimes seen to drift away by many tens of kHz, even though the cavity remains locked to its laser who's center frequency is stable to less than a kHz over the same timescale. The Raman resonance drift is strongest after loading ions from the atomic oven and reduces the longer time that passes since loading. The problem is therefore likely to be temperature related. It seems as though the cavity length at 854 nm changes differently with temperature than at the locking wavelength (806 nm at IQOQI and 785 nm at UIBK). How long one should wait to obtain a satisfactorily stable Raman resonance condition after loading is different for each node. At UIBK one waits typically an hour after loading. A good practice at IQOQI is to wait 30 minutes after loading.

5.5.2 *Predicting the fidelity of remote ion-ion entanglement*

The two-photon interference data presented so far in this thesis can be used to predict the quality and rate at which entanglement between two remote ions could be established using the two-photon entanglement swapping method presented in Section 2.3. For the detector arrangement shown in Figure 2.1, the only input state that can lead to coincidences is the singlet state of photons $|\phi^-\rangle$. This, however is only true in case of perfectly indistinguishable photons (visibility $V = 1$). In the case of imperfect visibility one can show that the maximum Bell state fidelity $F(T)$ with which ion-ion entanglement can be achieved given a two-photon interference visibility $V(T)$ is given by

$$F(T) = \frac{1 + V(T)}{2}, \tag{5.7}$$

where T is the coincidence detection window [70]. This model does not include infidelity due to other imperfections, such as detector dark counts or infidelities in the generation of ion-photon entangled states. Nevertheless, it still provides a useful upper limit on performance as limited by the interference visibility. In the following calculations, the results of experimental run "004641" presented in Figure 5.10 (during which no cavity mismatch was evident) will be considered.

The heralding rate for remote entanglement R_{swap} is given by

$$R_{swap}(T) = 0.5 R_{gen} C^{\perp}(T), \tag{5.8}$$

where R_{gen} is the photon generation attempt rate at which each ion-trap network node attempts to generate a photon and $C^{\perp}$ is the coincidence probability at which fully distinguishable (asynchronous) photon pairs are detected. The factor 0.5 in Equation 5.8 arises from the fact that in the photonic Bell state measurement we are able to detect two out of four possible Bell states. Practically, achieving that rate requires modifying the scheme described in Section 3.3.4 to include four detectors at the output ports of the beamsplitter (each pair following a PBS, as shown in Chapter 6).

The predicted ion-ion entanglement fidelity $F(T)$ and $C^{\perp}(T)$, calculated from the interference data of experimental run "004641" presented in Figure 5.10 is shown in Figure 5.13. One can see that ion-ion entanglement is predicted for all lengths of the coincidence window, but that there is a trade off between entanglement fidelity and remote heralding rate, which is according to Equation 5.8 directly proportional to the plotted coincidence probability $C^{\perp}$.

In total 1,101,648 attempts to synchronously generate photons were performed in the experimental run "004641" over a total duration of 1428 s. This yields an overall attempt rate $R_{gen} = 771/\text{s}$. This attempt rate includes ion preparation and all wait times. It gives a conservative

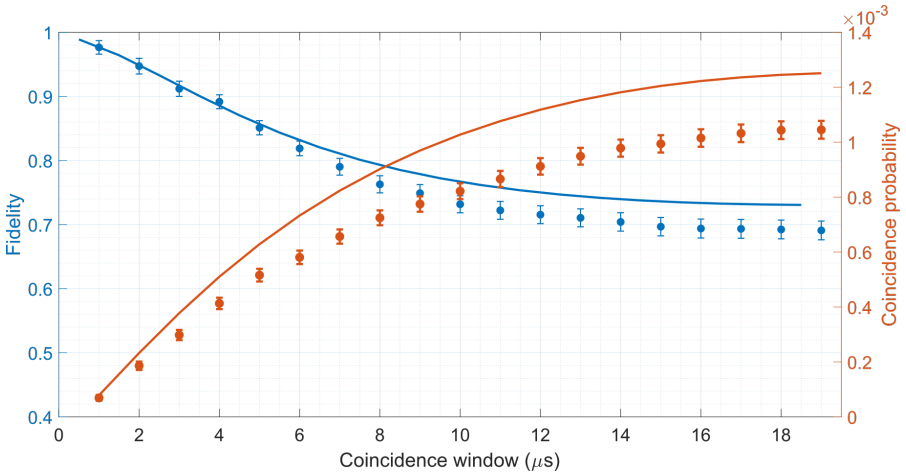

Figure 5.13: **Predicted Bell state fidelity of our remote ion entangled state and coincidence heralding rate.** Left axis: Predicted fidelity of remote ion-ion entanglement using formula $F(T) = (1 + V(T))/2$. Blue circles and solid lines show data and model, respectively, from the experimental run "004641" shown in Figure 5.10(c). Right axis: Coincidence probability for different coincidence window length. Orange solid line shows the theory, orange circles show data.

estimate for R_{gen} since e.g., the generation of the asynchronous pair can be omitted or replaced with the generation of another synchronous pair and thus doubling the R_{gen}. Moreover, the time necessary for photon generation can be further reduced by optimizing the sequence parameters and wait times. A 100 μs average time for photon generation should be achievable, yielding $R_{gen} \approx 10000/\text{s}$, however, limitations in our current experimental control hardware will reduce the average attempt rate to $R_{gen} \approx 6000/\text{s}$. Figure 5.14 presents how the predicted heralding rate of remote ion entanglement R_{swap} changes with the photon pair generation rate R_{gen}. Different target ion-ion fidelities are shown with different lines, as labeled. For example, if we choose $R_{gen} = 6000/\text{s}$, we expect to achieve remote ion-ion entanglement with a fidelity of $F(1\,\mu\text{s}) = 0.98$ at a heralding rate $R_{swap}(1\,\mu\text{s}) = 0.2/\text{s}$. If the entire wavepacket is used and $R_{gen} = 6000/\text{s}$, then the fidelity of the swapped state drops to $F(20\mu\text{s}) = 0.70$, but the maximum heralding rate increases to $R_{gen}(20\mu\text{s}) = 3.1/\text{s}$.

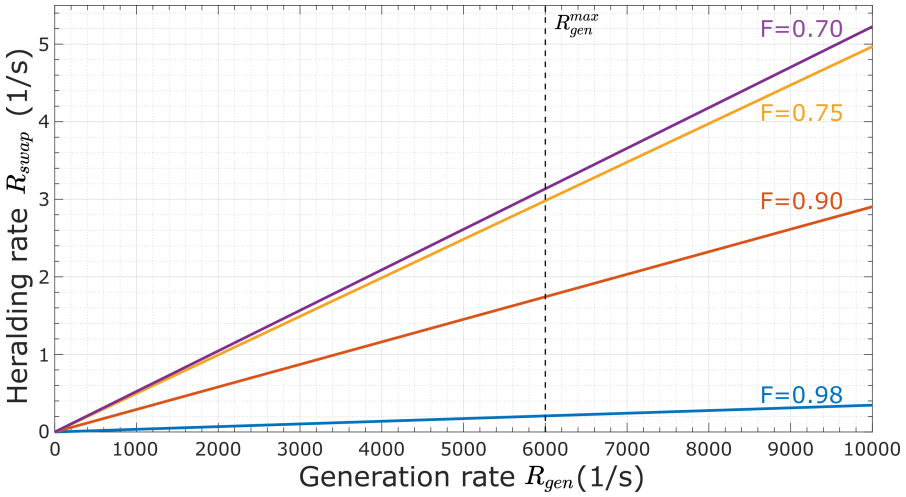

Figure 5.14: **Predicted rate of achieving remote ion entanglement states as a function of photon pair generation rate.** For each target remote ion entanglement fidelity F the corresponding coincidence probability $C^{\perp}$ was obtained from Figure 5.13. The Equation 5.8 was then used to obtain the heralding rate as a function of R_{gen}. Dashed vertical line R_{gen}^{max} marks our estimated limit for the attempt rate, given our current experimental control hardware.

6

ENTANGLEMENT OF IONS 230 M APART

In this chapter our paper "Entanglement of trapped-ion qubits separated by 230 meters" is presented in the form that was published in Physical Review Letters on February 2nd 2023 [112]. The paper reports on successful entanglement of two remote ions in our quantum network. One ion is at Node A (the UIBK node of this thesis) and one ion is at Node B (the IQOQI node of this thesis). The data were taken on July 21st 2021.

Before performing the experiment, several changes were made to the experimental configuration used for the Hong-Ou-Mandel interference measurements presented in the previous chapter of this thesis. The major changes are now briefly summarized.

First, the 'HOM board' setup of Figure 5.3 in previous chapter was modified. Specifically, the PBSs in each input path of beamsplitter were moved to the output paths and two additional single photon detectors were added to allow for monitoring both transmitted and reflected ports of those PBSs. In this configuration, the upgraded HOM board can now distinguish two out of four photonic Bell states, as discussed in Section 2.3. In the following paper, the HOM board is referred to as the PBSM, which stands for photonic Bell state measurement.

Second, a system to compensate for time-varying polarization dynamics observed in the optical fiber between the buildings was implemented using half-wave plate (HWP) and quarter-wave plates (QWP). Specifically, three motorized waveplates, in configuration QWP - HWP - QWP, were introduced into the PBSM input path of the photon from UIBK. The compensation system operates by periodically performing process tomography of the fiber channel. Specifically, we characterize the process implemented by the fiber on a single photon polarization qubit. We use the output to set the wave plate angles that together act to, as far as possible, undo the process implemented by the channel. This process tomography is repeated periodically to correct for any changes in the process implemented by the channel over time.

Third, the Raman process at both nodes, described in Section 3.2 was extended to a "bichromatic Raman process" (or "bichromatic CMRT") as first demonstrated in [39]. In this scheme, two Raman processes are driven simultaneously, ideally taking an electron prepared in the same ground state to different sub-levels of the $D_{5/2}$ manifold. Cavity photons generated in these two processes are orthogonally polarized and, if both processes occur with equal probability, ideally generate a maximally entangled final ion-photon state.

Fourth, the synchronization of remote sequence execution was upgraded. The synchronization introduced for the HOM experiment of previous chapter was extended to a two-sided hand shake to ensure that both nodes are executing the sequence simultaneously and that the ion qubits are measured in a known basis if a photon heralding signal occurs.

Fifth, after obtaining the heralding signal for potential remote-ion entanglement, quantum state tomography is performed to determine the final state of the two remote ion-qubits. For that, the measurement basis of the ions is changed using 729 nm laser operations, as mentioned at the end of Section 3.1. Finally, the three-level model, used for simulating the HOM experiment of the previous section was extended to a four level model to describe the bichromatic CMRT process.

An overview of each author's contribution to this paper is written at the end of the main paper. In the following paragraphs an expanded overview of my contribution is presented.

I constructed and aligned the PBSM board and established and first tested the classical remote connections for sequence synchronization. Together with members of the UIBK node team (Simon Baier, Maria Galli, Markus Teller), I participated in developing the final form of the remote sequence synchronization: the two-way handshake described in the Section IV. of the Supplementary material to the paper.

I developed and implemented the scheme for compensating the polarization drifts in the fibers between the buildings. The script automatically performs full quantum process tomography measurement by preparing six input polarization (single photons prepared by Node A) and measuring the transformed polarization state by projecting it into three bases at Node B. The script uses the measurement outcomes to estimate the completely positive map of the transformation [117, 118] implemented by the fiber on the traveling photons by means of maximum likelihood estimation [119]. The script then searches for the nearest unitary transformation. This transformation is then inverted and decomposed into the settings of three waveplates in the path to undo the polarization transformation induced by traveling through the optical fiber. Prior to implementing this compensation scheme, I analyzed the polarization dynamics of light sent through the deployed optical fiber.

Martin Meraner and I developed what is referred to as the "Coincident Logic Board", which is responsible for triggering ion state detection in the case of various detection patterns. The board has two operational modes. The first mode raises a TTL trigger in the case where two, and only two, detectors fire. The second mode generates a TTL signal when one detector fires, which is used to characterize ion-photon entangled states and is also used during the fiber polarization compensation. Switching between the two modes can be performed remotely for fluent transition between the two types of experiment.

In the following section, the paper is presented as it was published and consists of 7 pages of the main text with references followed by 17 pages of supplementary material.

Editors' Suggestion | Featured in Physics

Entanglement of Trapped-Ion Qubits Separated by 230 Meters

V. Krutyanskiy,[1,2] M. Galli,[2] V. Krcmarsky,[1,2] S. Baier,[2] D. A. Fioretto,[2] Y. Pu,[2] A. Mazloom,[3] P. Sekatski,[4] M. Canteri,[1,2] M. Teller,[2] J. Schupp,[1,2] J. Bate,[2] M. Meraner,[1,2] N. Sangouard,[5] B. P. Lanyon,[1,2,*] and T. E. Northup[2]

[1]*Institut für Quantenoptik und Quanteninformation, Österreichische Akademie der Wissenschaften, Technikerstraße 21a, 6020 Innsbruck, Austria*

[2]*Institut für Experimentalphysik, Universität Innsbruck, Technikerstraße 25, 6020 Innsbruck, Austria*

[3]*Department of Physics, Georgetown University, 37th and O Streets NW, Washington, D.C. 20057, USA*

[4]*Department of Applied Physics, University of Geneva, 1211 Geneva, Switzerland*

[5]*Institut de Physique Théorique, Université Paris-Saclay, CEA, CNRS, 91191 Gif-sur-Yvette, France*

(Received 3 September 2022; accepted 20 December 2022; published 2 February 2023)

We report on an elementary quantum network of two atomic ions separated by 230 m. The ions are trapped in different buildings and connected with 520(2) m of optical fiber. At each network node, the electronic state of an ion is entangled with the polarization state of a single cavity photon; subsequent to interference of the photons at a beam splitter, photon detection heralds entanglement between the two ions. Fidelities of up to $(88.0 + 2.2 - 4.7)\%$ are achieved with respect to a maximally entangled Bell state, with a success probability of 4×10^{-5}. We analyze the routes to improve these metrics, paving the way for long-distance networks of entangled quantum processors.

DOI: 10.1103/PhysRevLett.130.050803

The realization of quantum networks [1,2] that link cities and countries would open up powerful new applications in information security [3], distributed computing [4,5], precision sensing [6,7], and timekeeping [8]. These applications require distributed quantum network nodes that, first, can be entangled via the exchange of photons over long distances and, second, can store and process quantum information encoded in registers of qubits. A handful of experiments have demonstrated remote entanglement of 2 quantum-logic-capable qubits, including ions in linear Paul traps [9,10], optically trapped neutral atoms [11,12], color centers in diamond [13], quantum dots [14,15], and superconducting qubits [16]; furthermore, three-node entanglement of color centers was recently achieved [17]. These elementary networks have been extended to entangle quantum systems in separate buildings: two diamond color centers 1.3 km apart [18] and two neutral atoms 400 m apart [19,20].

Quantum network nodes based on trapped ions [21] promise high-fidelity quantum-gate operations on registers of tens of qubits [22,23], coherence times exceeding one hour [24], efficient interfacing with telecom-wavelength photons [25,26], and precision sensing and metrology [27–29]. Building on the first demonstration of remote-ion entanglement [9], significant improvements in both rate and fidelity [10,30] have recently enabled device-independent quantum key distribution [31] and enhanced timekeeping [32], and a multispecies node has been demonstrated [33]. Remote entanglement of trapped ions more than a few meters apart has not previously been reported.

In this Letter, we report on the entanglement of two trapped ions separated by 230 m. The two ions are in separate buildings, connected via 520(2) m of optical fiber, and controlled by independent lasers and electronics. Their entanglement is heralded by the coincident detection of two infrared photons that travel through the fiber. In contrast to implementations based on spontaneous emission [9,10,12–15,17,19,20,30,33], our photon generation method is based on a cavity-mediated Raman process providing tunable entangled states [34] and high efficiency [35], which are advantageous for establishing long-distance entanglement [36]. Remote ion-ion entanglement is characterized by quantum state tomography and analyzed for a range of time windows for coincident detection. A detailed model is developed that captures the observed trade-off between the fidelity of remote entanglement and the heralding efficiency and shows how significant improvements can be made in the future.

Each node in our quantum network [Figs. 1(a) and 1(b)] consists of a single $^{40}Ca^{+}$ atom confined in a linear Paul trap and coupled to a 20 mm cavity for photon collection at 854 nm. A photon is generated at each node via a bichromatic cavity-mediated Raman transition [Fig. 1(c)] [34]. Here, a Raman laser pulse applied to the ion ideally generates the maximally entangled ion-photon state $|\psi_k\rangle = 1/\sqrt{2}(|DV\rangle + e^{i\theta_k}|D'H\rangle)$, where $|D\rangle$ and $|D'\rangle$ are the respective Zeeman states $|3^2D_{5/2}, m_j = -5/2\rangle$ and $|3^2D_{5/2}, m_j = -3/2\rangle$, $|V\rangle$ and $|H\rangle$ are the vertical and horizontal polarization components of a photon emitted into the cavity vacuum mode, and θ_k is a phase set at node

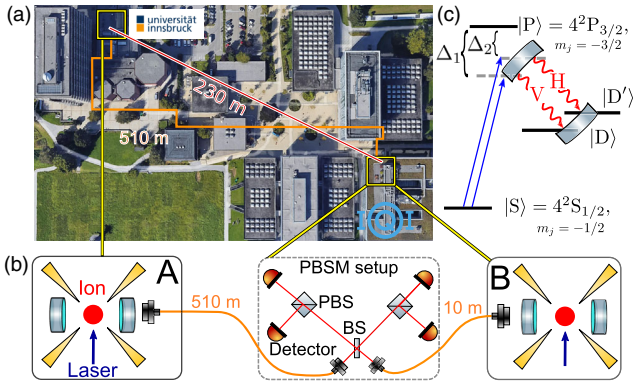

FIG. 1. The two-node quantum network. (a) Satellite image (Google Earth, image: Landsat/Copernicus). Nodes A and B are located in separate buildings, connected via a 520(2) m optical-fiber link and have a 230 m line of sight separation. (b) Nodes consist of an ion, a linear Paul trap (four yellow electrodes), and a cavity comprised of two mirrors. The PBSM setup contains a beam splitter (BS), polarizing beam splitters (PBSs), and photon detectors. (c) Energy-level diagram for $^{40}Ca^+$. When an ion is in state $|S\rangle$ and no photons are in the cavity, a laser pulse containing two tones generates the ion-photon entangled state $1/\sqrt{2}(|DV\rangle + e^{i\theta}|D'H\rangle)$, where $|V\rangle$ and $|H\rangle$ are the polarization components of a cavity photon and θ is a phase [34]. The frequency difference $\Delta_2 - \Delta_1$ is equal to the one between $|D'\rangle = 3^2D_{5/2}$, $m_j = -3/2$ and $|D\rangle = 3^2D_{5/2}$, $m_j = -5/2$.

$k \in \{A, B\}$. The photon exits the cavity and is coupled into a single-mode optical fiber. Two photons, one from each node, arrive at a photonic Bell-state measurement (PBSM) setup, where their spatial modes are overlapped on a balanced beam splitter [37–39]. Coincident detection of orthogonally polarized photons ideally heralds the maximally entangled ion-ion states

$$|\Psi^{\pm}\rangle = 1/\sqrt{2}(|D_A D'_B\rangle \pm e^{i\phi}|D'_A D_B\rangle), \tag{1}$$

with phase $\phi = \theta_A - \theta_B$, where subscripts indicate the ion node. The state $|\Psi^+\rangle$ is obtained if the two coincident detection events occur in the same output mode of the beam splitter, while $|\Psi^-\rangle$ is obtained if coincident detection occurs in opposite output modes.

Which-path information for the two photons can be erased in the PBSM, which requires both temporal and spectral indistinguishability of the photon wave packets. Each node has control software and hardware that executes a finite-length and node-specific remote entanglement sequence: a list of operations to perform. Each control system is referenced to its own 10 MHz global positioning system clock source. Temporal synchronization of the two sequences to within a 30 ns jitter is achieved via a handshake between the control systems at the start of each sequence. The handshake signal is sent over a dedicated optical fiber in a fiber bundle connecting the two labs, which also contains the fiber for single-photon distribution. Offsets in the arrival times of temporal photon wave packets at the PBSM, e.g., due to optical path differences, are compensated for by introducing sequence delays.

Spectral indistinguishability of the photons requires matching the resonant frequencies of the remote cavities. This is achieved via periodic calibration at 20 min intervals: 854 nm laser light that is resonant with the cavity at Node A is sent to Node B over a third fiber in the bundle, and the length of the Node B cavity is adjusted until it is resonant with this light. Also at 20 min intervals, the polarization rotation of the fiber that carries single photons is characterized and corrected for (see the Supplemental Material [40]).

The remote entanglement sequences at each node contain a loop in which up to 20 attempts are made to establish ion-ion entanglement. Each attempt contains 0.3 ms of state initialization, via Doppler cooling and optical pumping, followed by a Raman laser pulse of 50 μs to generate a photon. In the case of coincident detection of orthogonally polarized photons within a 50 μs window that encompasses the single-photon wave packets, the sequence exits the loop, and the ion qubits are measured. Ion-qubit measurement consists of laser-driven single-qubit rotations to set the measurement basis, followed by state detection via electron shelving for 1.5 ms, at which point the sequence is concluded.

The remote ion-ion state is characterized via quantum state tomography, for which the sequence is repeated for all nine combinations of the Pauli measurement bases for 2 ion qubits [52]. Tomographic reconstruction, via the maximum likelihood technique, yields the density matrices $\rho^{\pm}(T)$, where ρ^+ and ρ^- are reconstructed for the coincidences corresponding to ideally $|\Psi^+\rangle$ and $|\Psi^-\rangle$, respectively, and T is the maximum time difference for which entanglement is heralded between coincident photons. A fidelity $F^{\pm}(T) \equiv \langle\Psi^{\pm}|\rho^{\pm}(T)|\Psi^{\pm}\rangle > 0.5$ proves entanglement of the remote ions. Uncertainties for $F^{\pm}(T)$ and for all quantities derived from the density matrices are obtained via Monte Carlo resampling (see the Supplemental Material [40]). Data were acquired over seven hours, including interspersed calibrations. For each basis measurement setting, 17 min of data were acquired on average. In total, 13 656 928 attempts were made to generate remote entanglement, resulting in 4470 coincidence events within the interval $[t = 5.5\ \mu s, t = 23\ \mu s]$ [Fig. 2(a)], corresponding to a 0.033% probability of two-photon coincidence per attempt, which we define as the success probability. Here $t = 0$ indicates the start of the 50 μs detection window, and the narrower interval has been chosen to improve signal to noise. The remote entanglement rate during the data acquisition time is thus 0.49 s^{-1}. The fidelities of the reconstructed states are $F^+(17.5\,\mu s) = (58.7 + 1.7 - 2.1)\%$ and $F^-(17.5\,\mu s) = (58.0 + 2.0 - 2.9)\%$, where $T = 17.5$ μs corresponds to all possible coincidences within the 17.5 μs window.

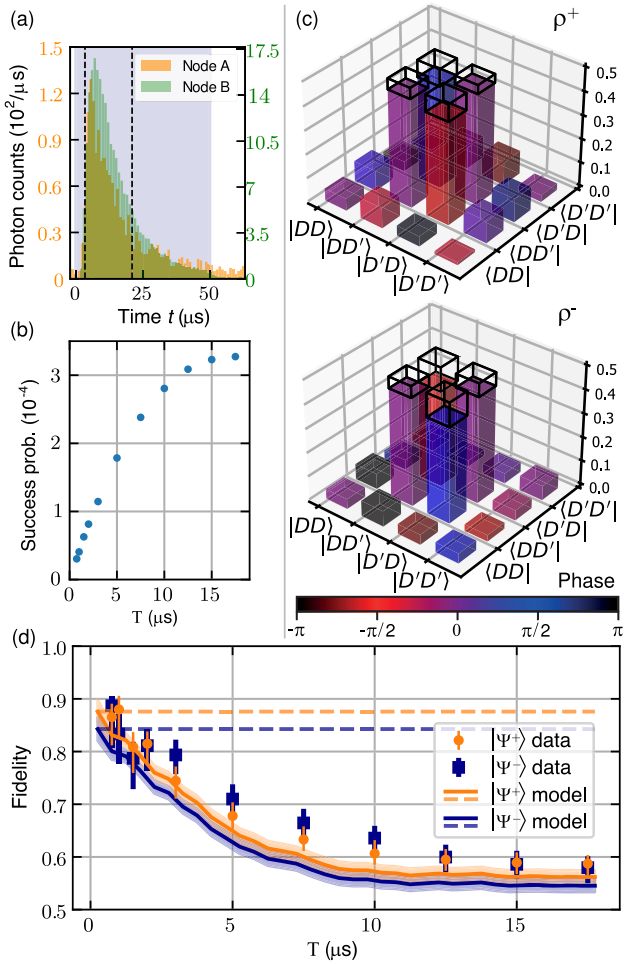

FIG. 2. Entanglement between ion qubits. (a) Single-photon wave packets measured at each node in a separate calibration experiment. Shown are histograms of photon counts per 1 μs time bin for ion-entangled photons from Node A only (orange) and Node B only (green). The gray region indicates when the Raman laser pulse is on. The dashed black lines indicate the window within which coincidence events are evaluated during entanglement experiments. (b) Success probability for a coincidence event heralding either $|\psi^+\rangle$ or $|\psi^-\rangle$ to occur as a function of T. (c) Experimentally reconstructed density matrices $\rho^+(T)$ and $\rho^-(T)$, for $T = 1$ μs. Bar heights indicate amplitudes of matrix entries; colors indicate phases. Amplitudes of the entries for $|\Psi^\pm\rangle\langle\Psi^\pm|$ are outlined for comparison. (d) Fidelity $F^\pm$ as a function of T. Markers indicate measured values; error bars correspond to 1 standard deviation. Solid lines show an empirical model discussed in the main text, with shaded regions indicating uncertainties. Dashed lines show a partial model omitting photon distinguishability.

When we take a subset of the data corresponding to coincidences separated by smaller values of T, entangled ion-ion states are generated with higher fidelity, at the cost of a lower success probability [Fig. 2(b)]. The density matrices shown in Fig. 2(c) correspond to $T = 1$ μs, for which we recorded 555 coincidence events, that is, a remote entanglement rate of 3.5 min^{-1}. The fidelities of the reconstructed states are $F^+(1\,\mu\text{s}) = (88.0 + 2.2 - 4.7)\%$ and $F^-(1\,\mu\text{s}) = (83.3 + 3.3 - 6.4)\%$. We optimize $F^\pm$ over the phase ϕ in Eq. (1) because we did not determine θ_A and θ_B independently; this optimization yields $\phi = 82.2°$. We then fix this value of ϕ for all subsequent data points. In Fig. 2(d), we plot the measured fidelities for values of T between 0.75 μs and 17.5 μs.

A decrease in fidelity as T increases is to be expected: For example, spontaneous emission during the Raman process provides information on which ion generated which cavity photon [53–55], that is, scattering introduces which-path information. To predict our experimentally determined fidelities, we have developed an empirical model for the ion-ion density matrix heralded by two-photon detection. The model contains photon distinguishability [56] along with two other sources of infidelity: detector background counts and imperfect ion-photon entanglement. The values of $F^\pm(T)$ calculated using this density-matrix model are plotted in Fig. 2(d) along with the measured values. We will first explain the contributions of photon distinguishability to this model and will afterward discuss the other sources of infidelity (see the Supplemental Material [40]).

To account for photon distinguishability, we employ a 2-qubit dephasing channel, which reduces the off diagonal elements of the ideal density matrices $|\Psi^\pm\rangle\langle\Psi^\pm|$ (see the Supplemental Material [40]). The probability for dephasing in the channel is parametrized by the Hong-Ou-Mandel (HOM) interference visibility, which provides direct information about photon indistinguishability [58]. For unit visibility, no dephasing occurs, while for a visibility of zero, all off diagonal matrix elements are zero.

The HOM visibility is extracted from the photon coincidence data by sorting all events in which photons are detected at opposite ports of the balanced beam splitter into two sets: coincidences with identical polarization and with orthogonal polarization. Photons with identical polarization will exit the balanced beam splitter at the same output port if they are otherwise indistinguishable, generating a HOM dip in coincidence counts at the two output ports [59]. Orthogonally polarized photons are distinguishable and thus exhibit no HOM effect; their cross-correlation function allows us to normalize the HOM dip and thereby to calculate the interference visibility. In Fig. 3(a), the number of coincidence events is plotted for both sets of data as a function of the time difference τ between photon detection events, for a time bin $\delta = 0.5$ μs. The HOM dip at $\tau = 0$ can be clearly observed. The interference visibility is then obtained from the data of Fig. 3(a) via the following procedure: First, the number of expected coincidences between photons and detector background counts is subtracted from the number of measured coincidences for each time bin. Next, the datasets are corrected for the detector efficiencies, which have been independently measured

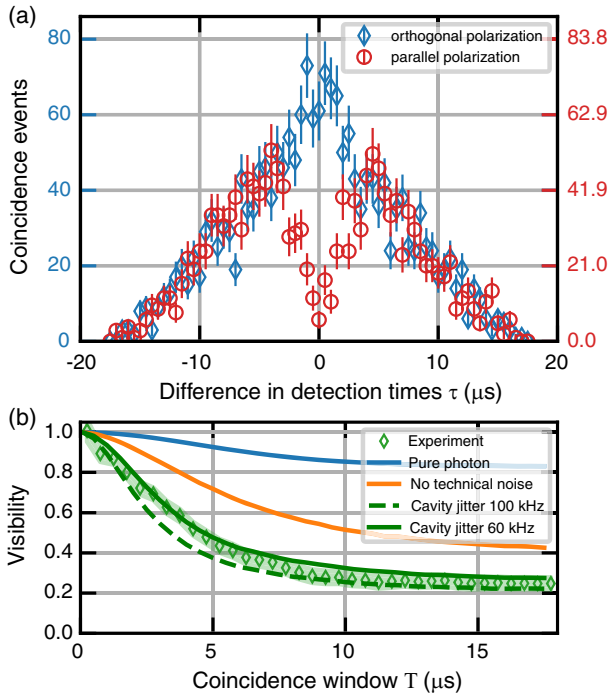

FIG. 3. (a) Number of coincidences recorded for orthogonal (blue) and parallel (red) polarization projections of photons from Nodes A and B, for the same dataset as in Fig. 2, where the axes are scaled by the ratio of detector efficiencies. Data are plotted as a function of the time difference τ between photon detection events, binned in 0.5 μs intervals. Error bars indicate Poissonian statistics. (b) Diamonds show the two-photon interference visibility calculated from the coincidence data after correction for background counts and detector efficiencies, using Eq. (2). The shaded region indicates the propagation of Poissonian uncertainties. Lines show a master-equation model discussed in the main text.

(see the Supplemental Material [40]). We define $N_{\parallel,k\delta}$ and $N_{\perp,k\delta}$ as the corrected numbers of coincidences for the time bin centered at $\tau = k\delta$ for $k \in \mathbb{Z}$, where the symbols $\parallel$ and $\perp$ indicate identical and orthogonal photon polarization, respectively. Finally, the interference visibility is calculated as a function of the coincidence window T:

$$V(T) = 1 - \frac{\sum_{(-T+\delta/2)\le k\delta\le(T-\delta/2)} N_{\parallel,k\delta}}{\sum_{(-T+\delta/2)\le k\delta\le(T-\delta/2)} N_{\perp,k\delta}}. \qquad (2)$$

In Fig. 3(b), $V(T)$ is plotted for coincidence windows up to 17.5 μs, as in Fig. 2(d), and for 0.5 μs time bins. The maximum visibility corresponds to 101(6)% for $T = 0.25$ μs; this value is above 100% because the background-corrected value for $N_{\parallel,k\delta}$ is negative, while consistent with zero within 1 standard deviation.

Our empirical model also includes detector background counts and imperfect ion-photon entanglement. For background counts, we use a white-noise channel based on the independently measured count rates of the four detectors. For ion-photon entanglement, we assume that imperfections translate as a 2-qubit depolarizing channel on the ion-ion state (see the Supplemental Material [40]). Ion-photon entanglement was characterized in a calibration measurement at each node via quantum state tomography immediately prior to ion-ion entanglement, and fidelities of $(92.9 + 0.4 - 0.5)\%$ and $(95.5 + 0.6 - 0.9)\%$ with respect to a maximally entangled state were obtained at Nodes A and B, respectively.

The empirical model is used to calculate the theoretical fidelities of Fig. 2(d): The solid lines are calculated from the full model, taking into account all three sources of infidelity, while the dashed lines are calculated when photon distinguishability is excluded from the model. Different values are predicted for F^+ and F^- due to the use of superconducting nanowire detectors at two of the four beam splitter outputs, which have lower dark-count rates than the single-photon-counting modules at the other two outputs. Based on the agreement between measured and modeled fidelities in Fig. 2(d), we conclude that the model captures the relevant properties of our setup and that the observed decline in fidelity as a function of T is due to the corresponding decline in visibility.

For insight into how, in the future, visibility could be maintained for larger coincidence windows—thereby increasing the probability to establish remote entanglement with a given fidelity—we have developed a master-equation model based on that of Ref. [55]. This model considers three independently estimated noise processes that result in non-transform-limited (and therefore distinguishable) photons at each node: frequency jitter of the Node A cavity by 60–100 kHz, Raman-laser phase noise, and spontaneous emission. We refer to the first two of these processes as technical noise. All parameter values used in the model are statistically consistent with independent estimates and determined via comparison of the model to measured single-photon wave packets (see the Supplemental Material [40]). The predicted visibility is plotted in Fig. 3(b): Green lines indicate the full model, including upper and lower estimates of the frequency jitter. It can be seen that the model is consistent with the visibility data.

We now look to the master-equation model to understand the impact of future improvements. Setting the technical noise contributions of cavity jitter and laser phase noise to zero, as shown in orange in Fig. 3(b), improves the model visibility. In addition, selecting only those ion-photon entanglement events for which no spontaneous emission occurs, corresponding to transform-limited or "pure" photons, leads to the most significant improvement in the model visibility (blue line). The remaining visibility imperfections are due to mismatch between the temporal wave packets of the transform-limited photons produced at each node (see the Supplemental Material [40]).

With regard to the technical noise contributions, we expect to suppress both cavity jitter and laser phase noise to

negligible levels by improving the lock electronics and the passive cavity used as a laser reference at Node A. Meanwhile, temporal wave packet mismatch can be addressed through amplitude shaping of the Raman laser pulse [60]. It is spontaneous emission that poses the most significant challenge. Using our existing setup, multi-ion superradiant states can be harnessed to boost the fraction of photons generated without prior spontaneous decay [53]; in future ion-cavity nodes, further gains can be obtained through judicious choice of the mirror properties and cavity geometry [35]. All these steps will increase the probability to generate transform-limited photons in each entanglement attempt. Additional steps can be taken to increase the attempt rate, namely, in the short term, implementing more efficient cooling and state detection protocols, and in the long term, coupling ions to fiber-based cavities with stronger coherent coupling and faster decay rates [61]. It is notable that the success probabilities shown in Fig. 2(b) are comparable to those achieved over a few meters in Ref. [10], and that in future long-distance networks limited by photon travel time, it will be success probabilities that determine entanglement rates [36].

In conclusion, we have verified entanglement over the longest trapped-ion network to date, with fidelities up to $(88.0 + 2.2 - 4.7)\%$ with respect to a maximally entangled state. A trade-off between fidelity and coincidence-window length was explained with the help of two models: an empirical model for the two-ion density matrix and a master-equation model to predict the interference visibility. Based on these models, we anticipate that we will be able to obtain significantly higher rates across this cavity-mediated network while maintaining high fidelities. Furthermore, efficient, low-noise and entanglement-preserving telecom wavelength conversion of the 854 nm photons used in the present Letter has been achieved [25,26], opening the possibility to extend the quantum channel to hundreds of kilometers. While the experiments presented here relied on just one ion at each node, a particular strength of the trapped-ion platform is the capability for quantum-information processing with dozens of addressed qubits in a single trap [22,23] and fidelities sufficient for fault-tolerant gate operations and error correction [62,63]. This capability provides a route to robust logical qubit encodings at network nodes [64], separate communication and information processing functionalities within each node [5,21], and quantum repeaters requiring Bell state measurements and either purification or error correction [65].

The data available in Ref. [66] includes raw tomographic data, calibration data, experimental parameters and sequences.

This work was supported by the European Union's Horizon 2020 research and innovation program under Grant Agreement No. 820445 and project name "Quantum Internet Alliance," by Projects No. F 7109 and No. Y 849 of the Austrian Science Fund (FWF), and by the U.S. Army Research Laboratory's Center for Distributed Quantum Information under Cooperative Agreement No. W911NF-15-2-0060. We acknowledge funding for S. B. by an FWF Erwin Schrödinger fellowship (No. J 4229), for V. Krutyanskiy by the Erwin Schrödinger Center for Quantum Science & Technology (ESQ) Discovery Programme, for B. P. L. by the CIFAR Quantum Information Science Program of Canada, for A. M. by the U.S. National Science Foundation under Grant No. PHY-1915130, for N. S. by the Commissariat à l'Energie Atomique et aux Energies Alternatives (CEA), and for M. T. by the Early Stage Funding Program of the Vice-Rectorate for Research of the University of Innsbruck.

M. G. and V. Krutyanskiy contributed equally to this work. S. B., D. F., M. G., V. Krcmarsky, V. Krutyanskiy, M. M., Y. P., and J. S. contributed to the experimental setup. S. B., J. B., M. C., D. F., M. G., V. Krcmarsky, V. Krutyanskiy, Y. P., and M. T. took data. S. B., M. C., M. G., and V. Krutyanskiy analyzed data. S. B., J. B., D. F., V. Krcmarsky, V. Krutyanskiy, A. M., Y. P., N. S., J. S., and P. S. performed theoretical modeling. B. P. L. and T. E. N. wrote the main text, with contributions from all authors. The project was conceived and supervised by B. P. L. and T. E. N.

*Corresponding author.
ben.lanyon@uibk.ac.at

[1] H. J. Kimble, The quantum internet, Nature (London) **453**, 1023 (2008).
[2] S. Wehner, D. Elkouss, and R. Hanson, Quantum internet: A vision for the road ahead, Science **362** (2018).
[3] S. Pirandola, U. L. Andersen, L. Banchi, M. Berta, D. Bunandar, R. Colbeck, D. Englund, T. Gehring, C. Lupo, C. Ottaviani, J. L. Pereira, M. Razavi, J. S. Shaari, M. Tomamichel, V. C. Usenko, G. Vallone, P. Villoresi, and P. Wallden, Advances in quantum cryptography, Adv. Opt. Photonics **12**, 1012 (2020).
[4] L. Jiang, J. M. Taylor, A. S. Sørensen, and M. D. Lukin, Distributed quantum computation based on small quantum registers, Phys. Rev. A **76**, 062323 (2007).
[5] C. Monroe, R. Raussendorf, A. Ruthven, K. R. Brown, P. Maunz, L.-M. Duan, and J. Kim, Large-scale modular quantum-computer architecture with atomic memory and photonic interconnects, Phys. Rev. A **89**, 022317 (2014).
[6] T. J. Proctor, P. A. Knott, and J. A. Dunningham, Multiparameter Estimation in Networked Quantum Sensors, Phys. Rev. Lett. **120**, 080501 (2018).
[7] P. Sekatski, S. Wölk, and W. Dür, Optimal distributed sensing in noisy environments, Phys. Rev. Res. **2**, 023052 (2020).
[8] P. Kómár, E. M. Kessler, M. Bishof, L. Jiang, A. S. Sørensen, J. Ye, and M. D. Lukin, A quantum network of clocks, Nat. Phys. **10**, 582 (2014).
[9] D. L. Moehring, P. Maunz, S. Olmschenk, K. C. Younge, D. N. Matsukevich, L. M. Duan, and C. Monroe,

Entanglement of single-atom quantum bits at a distance, Nature (London) **449**, 68 (2007).
[10] L. J. Stephenson, D. P. Nadlinger, B. C. Nichol, S. An, P. Drmota, T. G. Ballance, K. Thirumalai, J. F. Goodwin, D. M. Lucas, and C. J. Ballance, High-Rate, High-Fidelity Entanglement of Qubits Across an Elementary Quantum Network, Phys. Rev. Lett. **124**, 110501 (2020).
[11] S. Ritter, C. Nölleke, C. Hahn, A. Reiserer, A. Neuzner, M. Uphoff, M. Mücke, E. Figueroa, J. Bochmann, and G. Rempe, An elementary quantum network of single atoms in optical cavities, Nature (London) **484**, 195 (2012).
[12] J. Hofmann, M. Krug, N. Ortegel, L. Gérard, M. Weber, W. Rosenfeld, and H. Weinfurter, Heralded entanglement between widely separated atoms, Science **337**, 72 (2012).
[13] H. Bernien, B. Hensen, W. Pfaff, G. Koolstra, M. Blok, L. Robledo, T. Taminiau, M. Markham, D. Twitchen, L. Childress, and R. Hanson, Heralded entanglement between solid-state qubits separated by three metres, Nature (London) **497**, 86 (2013).
[14] A. Delteil, Z. Sun, W.-b. Gao, E. Togan, S. Faelt, and A. Imamoğlu, Generation of heralded entanglement between distant hole spins, Nat. Phys. **12**, 218 (2016).
[15] R. Stockill, M. J. Stanley, L. Huthmacher, E. Clarke, M. Hugues, A. J. Miller, C. Matthiesen, C. Le Gall, and M. Atatüre, Phase-Tuned Entangled State Generation Between Distant Spin Qubits, Phys. Rev. Lett. **119**, 010503 (2017).
[16] P. Magnard, S. Storz, P. Kurpiers, J. Schär, F. Marxer, J. Lütolf, T. Walter, J.-C. Besse, M. Gabureac, K. Reuer, A. Akin, B. Royer, A. Blais, and A. Wallraff, Microwave Quantum Link Between Superconducting Circuits Housed in Spatially Separated Cryogenic Systems, Phys. Rev. Lett. **125**, 260502 (2020).
[17] M. Pompili, S. L. N. Hermans, S. Baier, H. K. C. Beukers, P. C. Humphreys, R. N. Schouten, R. F. L. Vermeulen, M. J. Tiggelman, L. dos Santos Martins, B. Dirkse, S. Wehner, and R. Hanson, Realization of a multinode quantum network of remote solid-state qubits, Science **372**, 259 (2021).
[18] B. Hensen, H. Bernien, A. E. Dréau, A. Reiserer, N. Kalb, M. S. Blok, J. Ruitenberg, R. F. Vermeulen, R. N. Schouten, C. Abellán *et al.*, Loophole-free Bell inequality violation using electron spins separated by 1.3 kilometres, Nature (London) **526**, 682 (2015).
[19] W. Zhang, T. van Leent, K. Redeker, R. Garthoff, R. Schwonnek, F. Fertig, S. Eppelt, W. Rosenfeld, V. Scarani, C. C.-W. Lim, and H. Weinfurter, A device-independent quantum key distribution system for distant users, Nature (London) **607**, 687 (2022).
[20] T. van Leent, M. Bock, F. Fertig, R. Garthoff, S. Eppelt, Y. Zhou, P. Malik, M. Seubert, T. Bauer, W. Rosenfeld, W. Zhang, C. Becher, and H. Weinfurter, Entangling single atoms over 33 km telecom fibre, Nature (London) **607**, 69 (2022).
[21] L.-M. Duan and C. Monroe, Colloquium: Quantum networks with trapped ions, Rev. Mod. Phys. **82**, 1209 (2010).
[22] C. D. Bruzewicz, J. Chiaverini, R. McConnell, and J. M. Sage, Trapped-ion quantum computing: Progress and challenges, Appl. Phys. Rev. **6**, 021314 (2019).
[23] N. Friis, O. Marty, C. Maier, C. Hempel, M. Holzäpfel, P. Jurcevic, M. B. Plenio, M. Huber, C. Roos, R. Blatt, and B. Lanyon, Observation of Entangled States of a Fully Controlled 20-Qubit System, Phys. Rev. X **8**, 021012 (2018).
[24] Y. Wang, M. Um, J. Zhang, S. An, M. Lyu, J.-N. Zhang, L.-M. Duan, D. Yum, and K. Kim, Single-qubit quantum memory exceeding ten-minute coherence time, Nat. Photonics **11**, 646 (2017).
[25] M. Bock, P. Eich, S. Kucera, M. Kreis, A. Lenhard, C. Becher, and J. Eschner, High-fidelity entanglement between a trapped ion and a telecom photon via quantum frequency conversion, Nat. Commun. **9**, 1998 (2018).
[26] V. Krutyanskiy, M. Meraner, J. Schupp, V. Krcmarsky, H. Hainzer, and B. P. Lanyon, Light-matter entanglement over 50 km of optical fibre, npj Quantum Inf. **5**, 72 (2019).
[27] S. M. Brewer, J.-S. Chen, A. M. Hankin, E. R. Clements, C. W. Chou, D. J. Wineland, D. B. Hume, and D. R. Leibrandt, $^{27}Al^{+}$ Quantum-Logic Clock with a Systematic Uncertainty Below 10^{-18}, Phys. Rev. Lett. **123**, 033201 (2019).
[28] K. A. Gilmore, M. Affolter, R. J. Lewis-Swan, D. Barberena, E. Jordan, A. M. Rey, and J. J. Bollinger, Quantum-enhanced sensing of displacements and electric fields with two-dimensional trapped-ion crystals, Science **373**, 673 (2021).
[29] C. D. Marciniak, T. Feldker, I. Pogorelov, R. Kaubruegger, D. V. Vasilyev, R. van Bijnen, P. Schindler, P. Zoller, R. Blatt, and T. Monz, Optimal metrology with programmable quantum sensors, Nature (London) **603**, 604 (2022).
[30] D. Hucul, I. V. Inlek, G. Vittorini, C. Crocker, S. Debnath, S. M. Clark, and C. Monroe, Modular entanglement of atomic qubits using photons and phonons, Nat. Phys. **11**, 37 (2015).
[31] D. P. Nadlinger, P. Drmota, B. C. Nichol, G. Araneda, D. Main, R. Srinivas, D. M. Lucas, C. J. Ballance, K. Ivanov, E. Y.-Z. Tan, P. Sekatski, R. L. Urbanke, R. Renner, N. Sangouard, and J.-D. Bancal, Experimental quantum key distribution certified by Bell's theorem, Nature (London) **607**, 682 (2022).
[32] B. C. Nichol, R. Srinivas, D. P. Nadlinger, P. Drmota, D. Main, G. Araneda, C. J. Ballance, and D. M. Lucas, An elementary quantum network of entangled optical atomic clocks, Nature (London) **609**, 689 (2022).
[33] I. V. Inlek, C. Crocker, M. Lichtman, K. Sosnova, and C. Monroe, Multispecies Trapped-Ion Node for Quantum Networking, Phys. Rev. Lett. **118**, 250502 (2017).
[34] A. Stute, B. Casabone, P. Schindler, T. Monz, P. O. Schmidt, B. Brandstätter, T. E. Northup, and R. Blatt, Tunable ion-photon entanglement in an optical cavity, Nature (London) **485**, 482 (2012).
[35] J. Schupp, V. Krcmarsky, V. Krutyanskiy, M. Meraner, T. Northup, and B. Lanyon, Interface between trapped-ion qubits and traveling photons with close-to-optimal efficiency, PRX Quantum **2**, 020331 (2021).
[36] N. Sangouard, R. Dubessy, and C. Simon, Quantum repeaters based on single trapped ions, Phys. Rev. A **79**, 042340 (2009).
[37] L.-M. Duan and H. J. Kimble, Efficient Engineering of Multiatom Entanglement Through Single-Photon Detections, Phys. Rev. Lett. **90**, 253601 (2003).
[38] X.-L. Feng, Z.-M. Zhang, X.-D. Li, S.-Q. Gong, and Z.-Z. Xu, Entangling Distant Atoms by Interference of Polarized Photons, Phys. Rev. Lett. **90**, 217902 (2003).

[39] C. Simon and W. T. M. Irvine, Robust Long-Distance Entanglement and a Loophole-Free BEll Test with Ions and Photons, Phys. Rev. Lett. **91**, 110405 (2003).
[40] See Supplemental Material at http://link.aps.org/supplemental/10.1103/PhysRevLett.130.050803 for details on the synchronization and stabilization procedures between the two nodes, a full description of our density-matrix model, an independent characterization of the noise sources, and the calculation of interference visibility, including Refs. [41–51].
[41] C. Russo, H. G. Barros, A. Stute, F. Dubin, E. S. Phillips, T. Monz, T. E. Northup, C. Becher, T. Salzburger, H. Ritsch, P. O. Schmidt, and R. Blatt, Raman spectroscopy of a single ion coupled to a high-finesse cavity, Appl. Phys. B **95**, 205 (2009).
[42] A. Stute, B. Casabone, B. Brandstätter, D. Habicher, P. O. Schmidt, T. E. Northup, and R. Blatt, Toward an ion-photon quantum interface in an optical cavity, Appl. Phys. B **107**, 1145 (2012).
[43] K. Friebe, On dispersive interactions between a trapped ion and a cavity field, Ph.D. thesis, Leopold-Franzens-Universität Innsbruck, 2019.
[44] J. Schupp, Interface between trapped-ion qubits and travelling photons with close-to-optimal efficiency, Ph.D. thesis, Leopold-Franzens-Universität Innsbruck, 2021.
[45] B. Casabone, Two ions coupled to a cavity: From an enhanced quantum computer interface towards distributed quantum computing, Ph.D. thesis, Leopold-Franzens-Universität Innsbruck, 2015.
[46] B. Casabone, A. Stute, K. Friebe, B. Brandstätter, K. Schüppert, R. Blatt, and T. E. Northup, Heralded Entanglement of Two Ions in an Optical Cavity, Phys. Rev. Lett. **111**, 100505 (2013).
[47] H. Häffner, C. F. Roos, and R. Blatt, Quantum computing with trapped ions, Phys. Rep. **469**, 155 (2008).
[48] B. Efron and R. Tibshirani, *An Introduction to the Bootstrap* (Chapman & Hall, New York, 1993).
[49] A. N. Craddock, J. Hannegan, D. P. Ornelas-Huerta, J. D. Siverns, A. J. Hachtel, E. A. Goldschmidt, J. V. Porto, Q. Quraishi, and S. L. Rolston, Quantum Interference Between Photons from an Atomic Ensemble and a Remote Atomic Ion, Phys. Rev. Lett. **123**, 213601 (2019).
[50] H.-J. Briegel, B. Huttner, N. Gisin, C. Macchiavello, M. Murao, M. B. Plenio, S. Popescu, V. Vedral, P. L. Knight, W. Dür, S. J. van Enk, J. I. Cirac, and P. Zoller, Entanglement purification, in *The Physics of Quantum Information: Quantum Cryptography, Quantum Teleportation, Quantum Computation*, edited by D. Bouwmeester, A. Ekert, and A. Zeilinger (Springer Berlin Heidelberg, Berlin, Heidelberg, 2000), pp. 261–293.
[51] M. Horodecki, P. Horodecki, and R. Horodecki, General teleportation channel, singlet fraction, and quasidistillation, Phys. Rev. A **60**, 1888 (1999).
[52] D. F. V. James, P. G. Kwiat, W. J. Munro, and A. G. White, Measurement of qubits, Phys. Rev. A **64**, 052312 (2001).
[53] B. Casabone, K. Friebe, B. Brandstätter, K. Schüppert, R. Blatt, and T. E. Northup, Enhanced Quantum Interface with Collective Ion-Cavity Coupling, Phys. Rev. Lett. **114**, 023602 (2015).
[54] T. Walker, S. V. Kashanian, T. Ward, and M. Keller, Improving the indistinguishability of single photons from an ion-cavity system, Phys. Rev. A **102**, 032616 (2020).
[55] M. Meraner, A. Mazloom, V. Krutyanskiy, V. Krcmarsky, J. Schupp, D. A. Fioretto, P. Sekatski, T. E. Northup, N. Sangouard, and B. P. Lanyon, Indistinguishable photons from a trapped-ion quantum network node, Phys. Rev. A **102**, 052614 (2020).
[56] If photon distinguishability is due to a known frequency difference, it does not have to reduce entanglement fidelity [57]. Here, we consider distinguishability that cannot be attributed to such a frequency difference.
[57] G. Vittorini, D. Hucul, I. V. Inlek, C. Crocker, and C. Monroe, Entanglement of distinguishable quantum memories, Phys. Rev. A **90**, 040302(R) (2014).
[58] R. Trivedi, K. A. Fischer, J. Vučković, and K. Müller, Generation of non-classical light using semiconductor quantum dots, Adv. Quantum Technol. **3**, 1900007 (2020).
[59] C. K. Hong, Z. Y. Ou, and L. Mandel, Measurement of Subpicosecond Time Intervals Between Two Photons by Interference, Phys. Rev. Lett. **59**, 2044 (1987).
[60] D. A. Fioretto, Towards a flexible source for indistinguishable photons based on trapped ions and cavities, Ph.D. thesis, Leopold-Franzens-Universität Innsbruck, 2020.
[61] P. Kobel, M. Breyer, and M. Köhl, Deterministic spin-photon entanglement from a trapped ion in a fiber Fabry–Perot cavity, npj Quantum Inf. **7**, 6 (2021).
[62] C. Ryan-Anderson, J. G. Bohnet, K. Lee, D. Gresh, A. Hankin, J. P. Gaebler, D. Francois, A. Chernoguzov, D. Lucchetti, N. C. Brown, T. M. Gatterman, S. K. Halit, K. Gilmore, J. A. Gerber, B. Neyenhuis, D. Hayes, and R. P. Stutz, Realization of Real-Time Fault-Tolerant Quantum Error Correction, Phys. Rev. X **11**, 041058 (2021).
[63] L. Postler, S. Heußen, I. Pogorelov, M. Rispler, T. Feldker, M. Meth, C. D. Marciniak, R. Stricker, M. Ringbauer, R. Blatt, P. Schindler, M. Müller, and T. Monz, Demonstration of fault-tolerant universal quantum gate operations, Nature (London) **605**, 675 (2022).
[64] M. Zwerger, B. P. Lanyon, T. E. Northup, C. A. Muschik, W. Dür, and N. Sangouard, Quantum repeaters based on trapped ions with decoherence-free subspace encoding, Quantum Sci. Technol. **2**, 044001 (2017).
[65] W. J. Munro, K. Azuma, K. Tamaki, and K. Nemoto, Inside quantum repeaters, IEEE J. Sel. Top. Quantum Electron. **21**, 78 (2015).
[66] K. Viktor, G. Maria, K. Vojtech, S. Fioretto, D. Alessandro, P. Yunfei, M. Azadeh, S. Pavel, C. Marco, T. Markus *et al.*, Entanglement of trapped-ion qubits separated by 230 meters (2022), 10.5281/zenodo.7031042.

Entanglement of trapped-ion qubits separated by 230 meters: Supplemental material

V. Krutyanskiy,[1,2] M. Galli,[2] V. Krcmarsky,[1,2] S. Baier,[2] D. A. Fioretto,[2]
Y. Pu,[2] A. Mazloom,[3] P. Sekatski,[4] M. Canteri,[1,2] M. Teller,[2] J. Schupp,[1,2]
J. Bate,[2] M. Meraner,[1,2] N. Sangouard,[5] B. P. Lanyon,[1,2,*] and T. E. Northup[2]

[1] *Institut für Quantenoptik und Quanteninformation, Osterreichische Akademie der Wissenschaften, Technikerstr. 21a, 6020 Innsbruck, Austria*
[2] *Institut für Experimentalphysik, Universität Innsbruck, Technikerstr. 25, 6020 Innsbruck, Austria*
[3] *Department of Physics, Georgetown University, 37th and O Sts. NW, Washington, DC 20057, USA*
[4] *Department of Applied Physics, University of Geneva, 1211 Geneva, Switzerland*
[5] *Institut de Physique Théorique, Université Paris-Saclay, CEA, CNRS, 91191 Gif-sur-Yvette, France*

(Dated: December 20, 2022)

I. ION-TRAP NETWORK NODES

Overview. The ion-trap network nodes are both in room-temperature vacuum chambers and employ the same basic design. Specifically, a macroscopic linear Paul trap is rigidly suspended from the top flange of each vacuum chamber; thus, the ion's motional mode along the trap's axis of symmetry (the axial mode) is vertical, and the two other modes (radial modes) lie in the horizontal plane. An in-vacuum optical cavity around the ion trap is mounted via nanopositioning stages on the bottom flange of each chamber; the cavity axis is a few degrees off horizontal. Both cavities are 20 mm long and in the near-concentric regime, corresponding to microscopic waists at the ion location. Ions are loaded into each trap using a resistively heated oven of atomic calcium and a two-photon ionization process driven by lasers at 422 nm and 375 nm. Details on Node A can be found in [1–3]. Details on Node B can be found in [4–6].

Cavity parameters. At Node A, the transmission of the cavity mirrors at 854 nm was measured to be 13(1) ppm for the output mirror and 1.3(3) ppm for the second mirror [2], with a probability of 20(2) % that a photon in the cavity mode leaves the cavity through the output mirror [7]. At Node B, the measured transmission values at 854 nm are 90(4) ppm for the output mirror and 2.9(4) ppm for the second mirror, and the probability that a photon leaves through the output mode is 78(3) % [5]. The decay rates of the cavity fields, measured via cavity ringdown, are $\kappa_A = 2\pi \times 68.4(6)$ kHz [3] and $\kappa_B = 2\pi \times 70(2)$ kHz [5].

Trap frequencies. At Node A, the frequencies of the axial and radial modes are $(\omega_{\mathrm{ax}}, \omega_{\mathrm{r1}}, \omega_{\mathrm{r2}}) = 2\pi \times (1.13, 1.70, 1.76)$ MHz. At Node B, they are $2\pi \times (0.92, 2.40, 2.44)$ MHz [5].

Ion-cavity geometry. For the remaining discussions in this section, we use a Cartesian coordinate system with three orthogonal axes: x, y and z. At each node, the z axis is the ion trap's axis of symmetry, defined by the line connecting the trap's DC endcap electrodes, which is the axis of the ion's motion at frequency ω_{ax}. The xz plane is defined as the plane containing both the z axis and the cavity axis. The cavity axis subtends an angle with respect to the x axis of 4° at both Node A and Node B [2, 6, 8].

Quantization axis. At each node, the atomic quantization axis is chosen to be parallel to the axis of an applied static magnetic field. This magnetic-field axis is set to subtend an angle of 45° with respect to the z axis and to be perpendicular to the cavity axis; at Node B, it is likely that it is a few degrees off from perpendicular. At Node A, a magnetic field of 4.2303(2) G is set by DC currents in coils attached to the outside of the vacuum chamber. At Node B, a magnetic field of 4.1713(4) G is set by permanent magnets attached to the outside of the vacuum chamber. Both field strengths are measured via Ramsey spectroscopy of a single ion.

Laser beam geometry. A bichromatic laser field at 393 nm drives the cavity-mediated Raman transition. At each node, the propagation direction of the Raman laser field is parallel to the magnetic-field axis. The field is circularly polarized in order to maximize the coupling strength on the $|S\rangle \equiv |4^2S_{1/2}, m_j = -1/2\rangle$ to $|P\rangle \equiv |4^2P_{3/2}, m_j = -3/2\rangle$ transition. This coupling is depicted in Fig. 1c of the main text.

At Node A, Doppler cooling and state detection are implemented using 397 nm laser fields along two axes and a 866 nm field along a third axis. Optical pumping and ion-qubit rotations are implemented using a 729 nm field that lies in the xz plane at an angle of 45° with respect to the z axis.

At Node B, Doppler cooling is implemented using a single beam path that lies in the xz plane at an angle of 45° with respect to the z axis, along which both 397 nm and 866 nm laser fields are sent. Optical pumping is implemented using a second, circularly polarised, 397 nm laser field in a direction parallel to the magnetic-field axis. Ion-qubit rotations are implemented using a 729 nm field at an angle of 45° with respect to the z axis.

* Correspondence should be send to ben.lanyon@uibk.ac.at

II. FIBER-OPTIC CHANNELS

Fiber bundles. The laboratories in which Nodes A and B are located are connected with two optical fiber bundles, each of which contains eight single-mode optical fibers. The bundles are installed along the same path between the laboratories, which follows underground corridors but includes a section several tens of meters in length that is exposed to outdoor air. Three optical signals are sent between the laboratories using the fiber bundles, each in a different fiber:

1. 854 nm single photons,
2. 1550 nm laser light carrying digital trigger signals,
3. 854 nm laser light that is used to match the resonance frequencies of the cavities.

Signal 1 is sent through one of the bundles. Signals 2 and 3 are sent through different fibers in the other bundle. None of the fibers are polarization maintaining.

Stabilization of fiber polarization dynamics. Signal 1 consists of single photons that travel from Node A over one fiber bundle and through local fiber extensions to reach the photonic Bell-state measurement (PBSM) setup introduced in the main text. Every 20 minutes during attempts to generate remote ion entanglement, the polarization rotation of this fiber channel is characterized and corrected for, a process that takes a few minutes.

The polarization rotation is characterized via quantum process tomography, for which six input states are injected sequentially into the channel: single photons with horizontal, vertical, diagonal, antidiagonal, right-circular, and left-circular polarizations. The single photons are produced at Node A via a monochromatic cavity-mediated Raman process that is repumped continuously at 854 nm; this process generates linearly polarized photons with a measured contrast ratio of 10.5:1. After exiting the vacuum chamber, the photons pass through motorized waveplates, which we use to prepare the six input states.

For each input state, the output state is analyzed using existing components at the PBSM setup (a polarizing beam splitter and photon detectors) along with additional waveplates. We perform measurements in sufficiently many bases to reconstruct each output state via quantum state tomography. A numerical search is then carried out over the data from all six states to find the nearest unitary polarization rotation, which we identify as the transformation of the fiber channel. Finally, at the input to the PBSM setup, the angles of three waveplates—a half-waveplate sandwiched by two quarter-waveplates—are set so that collectively, the waveplates implement the inverse of the unitary operation, thereby correcting for the transformation of the channel.

III. PHOTONIC BELL-STATE MEASUREMENT (PBSM) SETUP

A simplified schematic of the PBSM setup is shown in Fig. 1b of the main text. The three waveplates described in the previous paragraph are not depicted in the figure. They are located between the output fiber coupler from Node A and the nonpolarizing beamsplitter. Two additional waveplates—also not depicted—are located between the output fiber coupler from Node B and the nonpolarizing beamsplitter. They consist of a quarter-waveplate and a half-waveplate and are used for calibration and analysis of the ion–photon state from Node A.

As shown in Fig. 1b, the PBSM setup has four single-photon detectors: two for each output mode of the nonpolarizing beamsplitter. In one of the beamsplitter output paths, the two detectors are single-photon counting modules (SPCMs); in the other output path, they are superconducting nanowire single-photon detectors (SNSPDs).

To determine the background counts and efficiency for each detector, we execute the same sequence as used for ion–ion entanglement (described in detail in Sec. IV) with one difference: photon detection does not terminate the photon-generation loop. In order to evaluate the values from each node separately, we block the beam path from the other node. First, we define the background window as the interval $[t = 70\,\mu\text{s}, t = 100\,\mu\text{s}]$, where, as in the main text, $t = 0$ indicates the start of the 50 µs detection window. No photons generated by an ion are expected in this window as the Raman laser pulse has been off for at least 20 µs. We determine the mean value of background counts per second as well as the probability of a background count during the detection window $p_{\text{bg}-\text{det}_r}$, where the detection window is defined as $[t = 5.5\,\mu\text{s}, t = 23\,\mu\text{s}]$.

Next, we determine the mean photon number within the detection window and subtract p_{bg}, yielding the probability $p^k_{\text{det}_r}$ of detecting a photon at detector r due to the Raman process at node $k \in \{\text{A}, \text{B}\}$ within this window. All values are summarized in Tab. I. These values are used in the empirical model of Sec. VIII in order to evaluate the influence of background counts on the ion-ion density matrices.

IV. EXPERIMENTAL SEQUENCES

Initialization and handshake. At each node, we implement a finite-length and node-specific sequence. The sequences at both Nodes A and B begin with Doppler cooling a single ion for at least 1.52 ms. Subsequently,

1. Node A sets $\text{TTL}^{A\to B}$ high on a 1550 nm communication channel to Node B (Signal 2 in Sec. II).
2. Upon receipt of the high $\text{TTL}^{A\to B}$, Node B sets $\text{TTL}^{B\to A}$ high on another communication channel

detector r	background (1/s)	$p_{\mathrm{bg-det}_r}(\%)$	$p^{\mathrm{A}}_{\mathrm{det}_r}(\%)$	$p^{\mathrm{B}}_{\mathrm{det}_r}(\%)$
SPCM_1	9.69	0.017	0.08	1.30
SPCM_2	9.37	0.016	0.12	1.96
SNSPD_1	0.25	0.0004	0.19	2.82
SNSPD_2	2.00	0.0035	0.24	3.62

TABLE I. Background counts, background-count probability within each detection window, and background-subtracted detection probability for each node, for each of the four detectors. In Sec. III, we describe how these values were determined.

on the same optical fiber to Node A. (The optical multiplexer supports four communication channels on one fiber.)

3. Upon receipt of the high $\mathrm{TTL}^{B\to A}$, Node A sets $\mathrm{TTL}^{A\to B}$ to low.

4. Upon receipt of the low $\mathrm{TTL}^{A\to B}$, Node B sets $\mathrm{TTL}^{B\to A}$ to low, completing the handshake.

Appropriate wait times are added between the operations to allow for processing and signal travel time at both nodes. The shortest time for a handshake is about 10 µs. We estimate remote clock-frequency mismatch of at most 50 mHz, which has a negligible effect on sequence synchronization given the maximum sequence length of 11.9 ms.

Following the handshake, the sequences at both nodes enter a photon generation loop.

Photon generation loop. Each iteration of the loop consists of the following operations:

1. Doppler cooling,
   - Node A: 63 µs
   - Node B: 60 µs + wait time
2. optical pumping,
   - Node A: 280 µs
   - Node B: 60 µs + wait time
3. a bichromatic Raman laser pulse,
   - Node A: 50 µs
   - Node B: 50 µs
4. a wait time for a signal that heralds coincident photon detection to be received at both nodes.

Each iteration lasts 420 µs. The loop is iterated up to 20 times. In the absence of coincident photon detection within any of the 20 iterations, the intialization and handshake are repeated. In the case of coincident detection of two photons produced within the same iteration, the loop is terminated, and the sequences proceed to ion-qubit measurement.

Ion-qubit measurement. Measurement of the ion's electronic state at each node proceeds in three steps:

1. A 729 nm π-pulse maps the state $|D\rangle \equiv \left|3^2D_{5/2}, m_j = -5/2\right\rangle$ to $|S\rangle$ at Node A. As a result, information that was encoded in a superposition of $|D\rangle$ and $|D'\rangle \equiv \left|3^2D_{5/2}, m_j = -3/2\right\rangle$ at each node is now encoded in a superposition of $|S\rangle$ and $|D'\rangle$. At the same time, at Node B, a 729 nm π-pulse maps the state $|D\rangle \equiv \left|3^2D_{5/2}, m_j = -3/2\right\rangle$ to $|S\rangle$, so that the encoding is in a superposition of $|S\rangle$ and $|D\rangle$. It is irrelevant whether $|D'\rangle$ or $|D\rangle$ is used for the measurement encoding; the experimenters at the two nodes just happened to make different choices.
   - Node A: 5.2 µs
   - Node B: 11.1 µs
2. An optional 729 nm $\pi/2$-pulse is implemented on the $|S\rangle$ to $|D'\rangle$ transition at Node A and on the $|S\rangle$ to $|D\rangle$ transition at Node B [9]. The pulse is implemented when the ion-qubit is to be measured in the Pauli σ_x or σ_y basis; we set the optical phase of the pulse to determine in which of the two bases the measurement is made. The pulse is not implemented when the ion-qubit is to be measured in the σ_z basis.
   - Node A: 4.3 µs
   - Node B: 7.81 µs
3. A projective fluorescence measurement on the 397 nm $4^2S_{1/2} \leftrightarrow 4^2P_{1/2}$ transition determines whether the ion is in $|S\rangle$ or $|D'\rangle$ at Node A, and whether it is in $|S\rangle$ or $|D\rangle$ at Node B. A photomultiplier tube is used to collect fluorescence.
   - Node A: 1.5 ms
   - Node B: 1.5 ms

V. SUCCESS PROBABILITY FOR REMOTE ENTANGLEMENT

The entanglement between ion qubits reported in the main text is heralded by the coincident detection of photons at two of the four detectors. Specifically, for the target Bell state $|\Psi^+\rangle$, we evaluate coincident events at the detector pair $\{\mathrm{SPCM}_1, \mathrm{SPCM}_2\}$ and at the detector pair $\{\mathrm{SNSPD}_1, \mathrm{SNSPD}_2\}$. For the target Bell state $|\Psi^-\rangle$, we evaluate coincident events at the detector pairs $\{\mathrm{SPCM}_1, \mathrm{SNSPD}_2\}$ and $\{\mathrm{SPCM}_2, \mathrm{SNSPD}_1\}$. We can use the probabilities $p^k_{\mathrm{det}_r}$ and $p_{\mathrm{bg-det}_r}$ defined in Sec. III to calculate the expected success probability P_{s}, that is, the

probability to herald ion–ion entanglement per entanglement generation attempt:

$$P_{\mathrm{s}} = P_{\mathrm{s},|\Psi^+\rangle} + P_{\mathrm{s},|\Psi^-\rangle},$$

where

$$\begin{aligned}
P_{\mathrm{s},|\Psi^+\rangle} = &(p^{\mathrm{A}}_{\mathrm{det}_{\mathrm{SPCM1}}} + p_{\mathrm{bg-det}_{\mathrm{SPCM1}}})(p^{\mathrm{B}}_{\mathrm{det}_{\mathrm{SPCM2}}} + p_{\mathrm{bg-det}_{\mathrm{SPCM2}}}) \\
&+(p^{\mathrm{B}}_{\mathrm{det}_{\mathrm{SPCM1}}} + p_{\mathrm{bg-det}_{\mathrm{SPCM1}}})(p^{\mathrm{A}}_{\mathrm{det}_{\mathrm{SPCM2}}} + p_{\mathrm{bg-det}_{\mathrm{SPCM2}}}) \\
&+(p^{\mathrm{A}}_{\mathrm{det}_{\mathrm{SNSPD1}}} + p_{\mathrm{bg-det}_{\mathrm{SNSPD1}}})(p^{\mathrm{B}}_{\mathrm{det}_{\mathrm{SNSPD2}}} + p_{\mathrm{bg-det}_{\mathrm{SNSPD2}}}) \\
&+(p^{\mathrm{B}}_{\mathrm{det}_{\mathrm{SNSPD1}}} + p_{\mathrm{bg-det}_{\mathrm{SNSPD1}}})(p^{\mathrm{A}}_{\mathrm{det}_{\mathrm{SNSPD2}}} + p_{\mathrm{bg-det}_{\mathrm{SNSPD2}}})
\end{aligned}$$

and

$$\begin{aligned}
P_{\mathrm{s},|\Psi^-\rangle} = &(p^{\mathrm{A}}_{\mathrm{det}_{\mathrm{SPCM1}}} + p_{\mathrm{bg-det}_{\mathrm{SPCM1}}})(p^{\mathrm{B}}_{\mathrm{det}_{\mathrm{SNSPD2}}} + p_{\mathrm{bg-det}_{\mathrm{SNSPD2}}}) \\
&+(p^{\mathrm{B}}_{\mathrm{det}_{\mathrm{SPCM1}}} + p_{\mathrm{bg-det}_{\mathrm{SPCM1}}})(p^{\mathrm{A}}_{\mathrm{det}_{\mathrm{SNSPD2}}} + p_{\mathrm{bg-det}_{\mathrm{SNSPD2}}}) \\
&+(p^{\mathrm{A}}_{\mathrm{det}_{\mathrm{SPCM2}}} + p_{\mathrm{bg-det}_{\mathrm{SPCM2}}})(p^{\mathrm{B}}_{\mathrm{det}_{\mathrm{SNSPD1}}} + p_{\mathrm{bg-det}_{\mathrm{SNSPD1}}}) \\
&+(p^{\mathrm{B}}_{\mathrm{det}_{\mathrm{SPCM2}}} + p_{\mathrm{bg-det}_{\mathrm{SPCM2}}})(p^{\mathrm{A}}_{\mathrm{det}_{\mathrm{SNSPD1}}} + p_{\mathrm{bg-det}_{\mathrm{SNSPD1}}})
\end{aligned}$$

are the expected success probabilities for the target states $|\Psi^+\rangle$ and $|\Psi^-\rangle$. This calculation yields 0.032 % for the values in Tab. I. As this value is consistent with the measured success probability of 0.033 % for ion–ion entanglement reported in the main text, we have confidence that the parameters in Tab. I accurately capture the conditions during our entanglement experiments.

Next, we break down the probabilities $p^k_{\mathrm{det}_r}$ in Tab. I into their individual components. For each component, we provide our best estimate of the probability on the day that the ion–ion entanglement data were acquired.

At Node A, the following probabilities are associated with individual steps of the experimental sequence, beginning with photon generation and ending in photon detection:

- $P_{1\mathrm{A}} = 0.75(27)$: probability for a photon to be generated in the cavity within the relevant 17.5 µs window, for each attempt.
- $P_{2\mathrm{A}} = 0.11(2)$: probability that a cavity photon is transmitted through the designated output mirror, rather than being scattered, absorbed, or transmitted through the less transmissive mirror [3].
- $P_{3\mathrm{A}} = 0.79(2)$: probability that a photon at the cavity output is coupled into single-mode fiber.
- $P_{4\mathrm{A}} = 0.399(7)$: probability that a photon is transmitted along the fiber channel between Node A and the PBSM setup.
- $P_{5\mathrm{A}} = \{0.255(3); 0.215(3); 0.157(3); 0.207(3)\}$: probabilities that a photon arriving at the PBSM setup will be transmitted to each of the four fiber-coupled detectors, including fiber-coupling efficiencies. The four values correspond to the four detectors in the order they appear in Tab. I, with the polarization optimized in each case.
- $P_{6\mathrm{A}} = 0.5$: theoretical probability for a photon that is maximally entangled with an ion to be directed to a specific output of a polarizing beamsplitter.
- $P_{7\mathrm{A}} = \{0.45(5); 0.45(5); 0.87(2); 0.87(2)\}$: probabilities that a photon will be detected at each of the four detectors (that is, detector efficiencies). The four values correspond to the four detectors in the order they appear in Tab. I.

The product

$$\begin{aligned}
&P_{1A}P_{2A}P_{3A}P_{4A}P_{5A}P_{6A}P_{7A} = \\
&\quad \{0.0015(7); 0.0013(6); 0.0018(8); 0.0024(10)\} \quad \text{(S1)}
\end{aligned}$$

gives the total probabilities within each entanglement attempt to detect a photon from Node A at the four detectors. We can now compare these four values with the four values in the column $p^{\mathrm{A}}_{\mathrm{det}_r}$ of Tab. I; we find that the two sets of probabilities agree within uncertainties. Note that the large uncertainty for $P_{1\mathrm{A}}$ and thus the large uncertainties in Eq. S1 are due to slow drifts in the relative position of the ion and the cavity mode during data acquisition over several hours.

At Node B, the corresponding probabilities are

- $P_{1\mathrm{B}} = 0.67(1)$,
- $P_{2\mathrm{B}} = 0.78(2)$ [5],
- $P_{3\mathrm{B}} = 0.76(3)$,
- $P_{4\mathrm{B}}P_{5\mathrm{B}} = \{0.235(3); 0.256(3); 0.135(3); 0.225(3)\}$,

- $P_{6\mathrm{B}} = P_{6\mathrm{A}}$,
- $P_{7\mathrm{B}} = P_{7\mathrm{A}}$.

Here, we obtain

$$P_{1B}P_{2B}P_{3B}P_{4B}P_{5B}P_{6B}P_{7B} = \{0.022(3); 0.024(3); 0.024(2); 0.040(2)\}. \quad \text{(S2)}$$

The values in Eq. S2 agree with the values in the column $p^{\mathrm{B}}_{\mathrm{det}_r}$ in Tab. I within uncertainties, with the exception of the value for SPCM_1.

We estimate that the following improved values can be achieved within our current setup, where the $*$ symbol indicates an estimated improvement:

- $P_{1\mathrm{A}*} = P_{1\mathrm{B}*} = 0.940(2)$, a value that was achieved at Node B following ground state cooling of the ion's axial mode of motion [5].
- $P_{2\mathrm{A}*} = 0.15(3), P_{2\mathrm{B}*} = P_{2\mathrm{B}}$, where the new value at Node A corresponds to the transmission probability when the cavity is locked to a different longitudinal mode [3]. Although here we are considering improvements to the current setup, we note that replacing the cavity at Node A would lead to more dramatic improvements, such that $P_{2\mathrm{A}*}$ and $P_{2\mathrm{B}*}$ would be roughly equal.
- $P_{3\mathrm{A}*} = P_{3\mathrm{B}*} = 0.9$, due to improved fiber-coupling optics.
- $P_{4\mathrm{A}*} = 0.65$, corresponding to the transmission of 854 nm light over 520 nm, as specified by the fiber manufacturer.
- $P_{5\mathrm{A}*} = P_{4\mathrm{B}*}P_{5\mathrm{B}*} = \{0.45; 0.45; 0.45; 0.45\}$, due to improved mode-matching within the PBSM.
- $P_{6\mathrm{A}*} = P_{6\mathrm{B}*} = P_{6\mathrm{A}} = P_{6\mathrm{B}}$,
- $P_{7\mathrm{A}*} = P_{7\mathrm{A}*} = \{0.87 \pm 0.02; 0.87 \pm 0.02; 0.87 \pm 0.02; 0.87 \pm 0.02\}$, corresponding to replacing the two SPCM detectors with SNSPD detectors.

These target values would lead to an improvement in P_{s} by a factor of 34(6), to 1.1(2) %.

VI. ION–ION STATE FIDELITIES

In this section, we explain how uncertainties are calculated for the ion–ion state fidelities presented in the main text.

As described in the main text, the joint state of two remote ions is characterized via quantum state tomography, yielding the density matrices $\rho^{\pm}(T)$, where ρ^{+} and ρ^{-} are reconstructed for the coincidences that should herald the Bell states $|\Psi^{+}\rangle$ and $|\Psi^{-}\rangle$, respectively, and T is the maximum time difference between coincident photons for which entanglement is heralded. The state ρ^{+} is obtained if coincident detection occurs either in the output path of the beamsplitter in which the SNSPDs are placed or in the output path in which the SPCMs are placed, while ρ^{-} is obtained if coincident detection occurs in opposite beamsplitter outputs, i.e., for the two combinations of a coincidence at one SPCM and one SNSPD. The fidelity is determined according to the expression $F^{\pm}(T) \equiv \langle\Psi^{\pm}|\rho^{\pm}(T)|\Psi^{\pm}\rangle$.

We use Monte Carlo resampling [10] to obtain the uncertainties in $F^{\pm}(T)$: Recall that $\rho^{\pm}(T)$ is determined from a set of measurement outcomes, which we can express as a vector. It is assumed that noise on these measurement outcomes is due to projection noise. We numerically generate $M = 200$ vectors of "noisy" observations based on a multinomial distribution around the experimentally recorded values. For each of these vectors, we reconstruct a density matrix just as for the experimental data, via the maximum likelihood technique. As a result, for each state $\rho^{\pm}(T)$ reconstructed directly from the raw data, we have M states reconstructed from simulated data. We calculate the value of some quantity of interest, e.g., the fidelity $F^{\pm}(T)$, not only for $\rho^{\pm}(T)$ but also for the associated M states, yielding a distribution D of values with mean F_m and standard deviation δ. The uncertainties are then given by $F^{\pm}(T)^{+(F_m+\delta-F)}_{-(F-Fm+\delta)}$.

If $F^{\pm}(T)$ is optimized over the phase ϕ of the Bell state, then this calculation is carried out for each value of ϕ.

VII. ION–PHOTON STATE FIDELITIES

Here, we provide more details on the calibration measurement of ion–photon entanglement that was carried out at each node immediately prior to ion–ion entanglement.

For the ion–photon state generated at Node B, photons were analyzed using the PBSM setup, details of which are given in Sec. III. Specifically, photon counts were recorded on the two SNSPDs. For the ion–photon state generated at Node A, photons were analyzed using a separate setup in the Node A laboratory.

For each ion–photon state, measurements are made in all nine combinations of the Pauli measurement bases for two qubits [11]. The measurement basis of the photon is changed using waveplates in the photon analysis path. Tomographic reconstruction via the maximum likelihood technique yields the ion–photon density matrices $\rho_k^{\mathrm{ion-photon}}$ for $k \in \{\mathrm{A}, \mathrm{B}\}$. The fidelities given in the main text are calculated as $\langle\Psi_k^{\theta}|\rho_k^{\mathrm{ion-photon}}|\Psi_k^{\theta}\rangle$, where $\left|\Psi_k^{\theta}\right\rangle = 1/\sqrt{2}\left(|\mathrm{DV}\rangle + e^{\mathrm{i}\theta}|\mathrm{D'H}\rangle\right)$ is the maximally entangled two-qubit state nearest to the state $\rho_k^{\mathrm{ion-photon}}$, found by numerical optimization over θ.

The method used to determine uncertainties in these fidelities is described in Sec. VI, where we replace the vector of ion–ion measurement outcomes by a vector of ion–photon measurement outcomes.

VIII. EMPIRICAL MODEL FOR THE ION–ION DENSITY MATRIX

The target states for ion–ion entanglement are the two Bell states in Eq. 1 of the main text:

$$|\Psi^{\pm}\rangle = 1/\sqrt{2}\left(|\mathrm{D_A D'_B}\rangle \pm e^{\mathrm{i}\phi}\,|\mathrm{D'_A D_B}\rangle\right). \tag{S3}$$

The corresponding density matrices are $\rho^{\pm} = |\Psi^{\pm}\rangle\langle\Psi^{\pm}|$. Here we describe an empirical model for the density matrix ρ heralded by two-photon detection in our experiments. For this model, we adapt $\rho^{\pm}$ to account for three sources of infidelity: detector background counts, photon distinguishability due to spontaneous emission, and imperfect ion–photon entanglement.

We first account for detector background counts. We define p_{mn} as the probability to detect the ion at Node A in state m and the ion at Node B in state n in a single experimental trial, where $m, n \in \{\mathrm{D}, \mathrm{D}'\}$. In the absence of detector background counts and all other imperfections, $p_{\mathrm{DD}} = p_{\mathrm{D'D'}} = 0$. We write

$$\begin{aligned} p_{\mathrm{DD}} &= p_{\mathrm{ph-bg}}/4 + p_{\mathrm{bg-bg}}/4, \\ p_{\mathrm{D'D'}} &= p_{\mathrm{DD}}, \\ p_{\mathrm{DD'}} &= p_{\mathrm{ph-ph}}/2 + p_{\mathrm{ph-bg}}/4 + p_{\mathrm{bg-bg}}/4, \\ p_{\mathrm{D'D}} &= p_{\mathrm{DD'}}, \end{aligned} \tag{S4}$$

where $p_{\mathrm{ph-bg}}$, $p_{\mathrm{bg-bg}}$, and $p_{\mathrm{ph-ph}}$ are the probabilities to detect a coincidence in a single experimental trial between a photon and a background count, between two background counts, and between two photons. The scaling factors account for the chance to measure a certain ion-ion correlator given a coincidence. An underlying assumption of Eqs. (S4) is that when a coincidence due to one or two background counts occurs, it is equally likely to find the two ions in each of their four possible states. This assumption is valid for the Bell states considered here, and it will still be valid when we introduce a depolarizing channel to model imperfect ion-photon entanglement later in this section.

The ion–ion density matrix that accounts for background counts is given by

$$\rho^{\pm}_{\mathrm{bg}} = \frac{1}{\sum_{m,n} p_{mn}} \begin{pmatrix} |\mathrm{D'_A D'_B}\rangle & |\mathrm{D'_A, D_B}\rangle & |\mathrm{D_A, D'_B}\rangle & |\mathrm{D_A, D_B}\rangle & \\ p_{\mathrm{D'D'}} & 0 & 0 & 0 & \langle \mathrm{D'_A, D'_B}| \\ 0 & p_{\mathrm{D'D}} & \pm e^{-\mathrm{i}\phi} p_{\mathrm{ph-ph}}/2 & 0 & \langle \mathrm{D'_A, D_B}| \\ 0 & \pm e^{\mathrm{i}\phi} p_{\mathrm{ph-ph}}/2 & p_{\mathrm{DD'}} & 0 & \langle \mathrm{D_A, D'_B}| \\ 0 & 0 & 0 & p_{\mathrm{DD}} & \langle \mathrm{D_A, D_B}| \end{pmatrix} \tag{S5}$$

The matrix ρ_{bg} can also be expressed as

$$\rho^{\pm}_{\mathrm{bg}} = \frac{1}{\sum_{m,n} p_{mn}} \left(\frac{p_{\mathrm{ph-ph}}}{2} \rho^{\pm} + \frac{p_{\mathrm{tot-bg}}}{4} \mathbb{1} \right), \tag{S6}$$

where $p_{\mathrm{tot-bg}} = p_{\mathrm{ph-bg}} + p_{\mathrm{bg-bg}}$ and $\mathbb{1}$ is the two-qubit identity matrix. Here one sees more clearly that the background-count model acts to add white noise to the ion-ion state.

In general, for a given detector combination det_1 and det_2, one can write the coincidence probabilities as:

$$\begin{aligned} p_{\mathrm{ph-ph}} &= p^{\mathrm{A}}_{\mathrm{det}_1} \times p^{\mathrm{B}}_{\mathrm{det}_2} + p^{\mathrm{B}}_{\mathrm{det}_1} \times p^{\mathrm{A}}_{\mathrm{det}_2} \\ p_{\mathrm{ph-bg}} &= (p^{\mathrm{A}}_{\mathrm{det}_1} + p^{\mathrm{B}}_{\mathrm{det}_1}) \times p_{\mathrm{bg-det}_2} \\ &\quad + (p^{\mathrm{A}}_{\mathrm{det}_2} + p^{\mathrm{B}}_{\mathrm{det}_2}) \times p_{\mathrm{bg-det}_1} \\ p_{\mathrm{bg-bg}} &= p_{\mathrm{bg-det}_1} \times p_{\mathrm{bg-det}_2} \end{aligned} \tag{S7}$$

where $p^{k}_{\mathrm{det}_r}$ is the probability of detecting a photon at detector r emitted by node $k \in \{\mathrm{A}, \mathrm{B}\}$ and $p_{\mathrm{bg-det}_r}$ is the probability to get a background count within the detection window at detector r. Note that we use four detectors, two of which are SNSPDs and two of which are SPCMs. Background counts and efficiencies have been measured independently for each detector (Sec. III), from which we calculate the probabilities in Eq˙ (S7).

Second, we account for photon distinguishability using a two-qubit dephasing channel. We define a completely dephased density matrix, for which we set the off-diagonal elements of ρ_{bg} to zero:

$$\rho_{\mathrm{bg,dephase}} = \frac{1}{\sum_{m,n} p_{mn}} \begin{pmatrix} p_{\mathrm{D'D'}} & 0 & 0 & 0 \\ 0 & p_{\mathrm{D'D}} & 0 & 0 \\ 0 & 0 & p_{\mathrm{DD'}} & 0 \\ 0 & 0 & 0 & p_{\mathrm{DD}} \end{pmatrix} \tag{S8}$$

The probability for dephasing in the channel is parameterized by the Hong-Ou-Mandel interference visibility V. The density matrix $\rho^{\pm}_{\mathrm{dist}}$ accounts for both background

counts and photon distinguishability:

$$\rho^{\pm}_{\rm dist} = V \times \rho^{\pm}_{\rm bg} + (1-V) \times \rho_{\rm bg,dephase}. \quad \text{(S9)}$$

As discussed in the main text, the value of V is experimentally determined as a function of the coincidence window for photon detection. In the absence of background counts or other imperfections, Eq. (S9) predicts an ion–ion state of the form $\rho^{\pm}(1+V)/2 + \rho^{\mp}(1-V)/2$. An equivalent model of the effect of photon distinguishability on entanglement swapping is derived in the Supplemental Material of Ref. [12]; see in particular Eq. (S29).

Finally, we account for imperfect ion–photon entanglement at Nodes A and B, for which we introduce a two-qubit depolarizing channel. We define $F'_{\rm ip,k}$ to be the fidelity of ion–photon entanglement with respect to a maximally entangled state at node k, where $F'_{\rm ip,k}$ has been corrected for background counts, and we define $\rho_{\rm depol}$ to be a completely depolarized density matrix:

$$\rho_{\rm depol} = \frac{1}{4}\mathbb{1}. \quad \text{(S10)}$$

If we assume that the infidelity $1-F'_{\rm ip,k}$ is due to depolarizing noise, and that the entanglement-swapping process that creates ion–ion entanglement between Nodes A and B is perfect, then the fidelity of ion–ion entanglement with respect to a maximally entangled state is given by [13]

$$F'_{\rm ii} = \frac{1}{4}\left(1 + 3\left(\frac{4F'_{\rm ip,A}-1}{3}\right)\left(\frac{4F'_{\rm ip,B}-1}{3}\right)\right). \quad \text{(S11)}$$

We can then describe the depolarizing channel that generates the state with fidelity $F'_{\rm ii}$ with a parameter λ [14]:

$$\rho^{\pm} = \lambda \times \rho^{\pm}_{\rm dist} + (1-\lambda) \times \rho_{\rm depol}, \quad \text{(S12)}$$

where

$$\lambda = \frac{4F'_{\rm ii}-1}{3}. \quad \text{(S13)}$$

We thus arrive at the density matrix ρ from which the fidelities plotted in Fig. 2d of the main text are calculated:

$$F^{\pm}_{\rm model} = \left\langle \Psi^{\pm} \right| \rho^{\pm} \left| \Psi^{\pm} \right\rangle. \quad \text{(S14)}$$

In Fig. 2d, the fidelities are plotted as a function of coincidence window. To calculate ρ for a given coincidence window T, we take into account the visibility $V(T)$ and the background counts that (on average) occur within the detection window. The depolarizing correction is treated as independent of T. The uncertainties given in the fidelity values predicted by the empirical model in Fig. 2d only consider the uncertainty in $V(T)$. To calculate the dashed lines in Fig. 2d, we omit the second step in this model—the dephasing channel parameterized by the visibility— and determine ρ only taking into account detector background counts and imperfect ion–photon entanglement.

The ion–photon entanglement fidelities at Nodes A and B without background-count subtraction are given in the main text. After background-count subtraction, these values are $F'_{\rm ip,A} = (93.8 + 0.4 - 0.5)\%$ and $F'_{\rm ip,B} = (95.6 + 0.7 - 0.8)\%$.

IX. MASTER-EQUATION MODEL FOR TWO-PHOTON INTERFERENCE VISIBILITY

A. The master equation

We present in this section the master-equation model of the ion–cavity system. We start with the Hamiltonian, then review the noise terms, and conclude the section with the master equation that is relevant for the description of the experiment.

Ultimately the model is used to predict the visibility of the interference obtained by combining on a beamsplitter two photons emitted from the two nodes of the ion-trap quantum network (Fig. 3b of the main text). As a first step, we calculate the joint ion–photon states produced at each node. Then the ions are traced out and the interference visibility is computed from the marginal states of the two photons.

1. Hamiltonian of the bichromatic cavity-mediated Raman transition

We start by presenting our model for a single $^{40}Ca^{+}$ ion trapped inside a cavity and driven by laser light. We restrict the atom model to a simple four-level system that includes the sublevels of direct importance for the experiment: $|S\rangle, |P\rangle, |D\rangle$, and $|D'\rangle$ (see Fig. 1). The ion is initially prepared in $|S\rangle$. The $|S\rangle - |P\rangle$ transition is driven off-resonantly with a bichromatic laser field with frequencies ω_1 and ω_2 and Rabi frequencies Ω_1 and Ω_2. The bichromatic field is detuned from the $|S\rangle - |P\rangle$ transition frequency ω_{PS} by $\Delta_1 = \omega_1 - \omega_{PS}$ and $\Delta_2 = \omega_2 - \omega_{PS}$. In addition, an exchange interaction between the ion and the cavity couples the $|P\rangle - |D\rangle$ transition to the emission and absorption of a photon with vertical polarization into the cavity and the $|P\rangle - |D'\rangle$ transition to the emission and absorption of a photon with horizontal polarization. The cavity has frequency $\omega_{\rm c}$. The vertically and horizontally polarized cavity modes are described with bosonic operators $\hat{a}^{\dagger}_{\rm v}$ or $\hat{a}^{\dagger}_{\rm h}$, and the corresponding coupling constants are denoted g_1 and g_2.

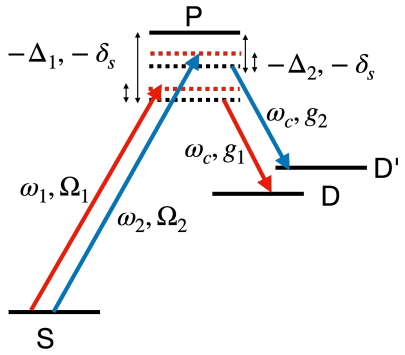

FIG. 1. Representation of the energy levels $|S\rangle, |P\rangle, |D\rangle$, and $|D'\rangle$ relevant for the experiment. The frequencies of the bichromatic laser field are denoted ω_1 and ω_2, with corresponding Rabi frequencies Ω_1 and Ω_2 and detunings Δ_1 and Δ_2 from $|P\rangle$. The cavity frequency is ω_c, and g_1 and g_2 are the cavity coupling constants. The Stark shift due to the bichromatic field is δ_s. (Note that in Fig. 1 of the main text, δ_s is set to zero for simplicity.)

The Hamiltonian H of the ion-cavity system is given by

$$\begin{aligned} H/\hbar = {} & \omega_c(\hat{a}_h^\dagger \hat{a}_h + \hat{a}_v^\dagger \hat{a}_v) + \omega_{PS}\,|P\rangle\langle P| + \omega_{DS}\,|D\rangle\langle D| + \omega_{D'S}\,|D'\rangle\langle D'| \\ & + \frac{1}{2}\left(\Omega_1 e^{i\omega_1 t} + \Omega_1 e^{-i\omega_1 t}\right)\left(|S\rangle\langle P| + |P\rangle\langle S|\right) + \frac{1}{2}\left(\Omega_2 e^{i\omega_2 t} + \Omega_2 e^{-i\omega_2 t}\right)\left(|S\rangle\langle P| + |P\rangle\langle S|\right) \\ & + g_1\left(|D\rangle\langle P| + |P\rangle\langle D|\right)\left(\hat{a}_v^\dagger + \hat{a}_v\right) + g_2\left(|D'\rangle\langle P| + |P\rangle\langle D'|\right)\left(\hat{a}_h^\dagger + \hat{a}_h\right). \end{aligned} \tag{S15}$$

Note that the energies of the ion levels are defined with respect to $|S\rangle$. An effective Hamiltonian with a simpler form can be obtained by noting that the cavity is initially empty and consequently, the atom-cavity system remains in the four level manifold $\{|S,0\rangle, |P,0\rangle, |D,1_v\rangle, |D',1_h\rangle\}$, where 0 and 1 are cavity photon numbers and subscripts indicate polarization. The corresponding Hilbert space is labelled $\mathcal{H}^C$. Below, we shorten the notation to $|D,1_v\rangle = |D,1\rangle$ and $|D',1_h\rangle = |D',1\rangle$ as there is no ambiguity with the polarization of the cavity photon. Under the rotating wave approximation, the effective Hamiltonian H_t^C is given by

$$\begin{aligned} H_t^C/\hbar = {} & -\Delta_1\,|P,0\rangle\langle P,0| + (\Delta_{c_1} - \Delta_1)\,|D,1\rangle\langle D,1| + (\Delta_{c_2} - \Delta_1)\,|D',1\rangle\langle D',1| \\ & + \frac{1}{2}\left(\Omega_1 + \Omega_2 e^{i(\omega_2-\omega_1)t}\right)|S,0\rangle\langle P,0| + \frac{1}{2}\left(\Omega_1 + \Omega_2 e^{-i(\omega_2-\omega_1)t}\right)|P,0\rangle\langle S,0| \\ & + g_1\left(|D,1\rangle\langle P,0| + |P,0\rangle\langle D,1|\right) + g_2\left(|D',1\rangle\langle P,0| + |P,0\rangle\langle D',1|\right). \end{aligned} \tag{S16}$$

In the rotating frame $|P\rangle_{L.F.} \to e^{i\omega_1 t}|P\rangle_{R.F.}$, $|1\rangle_{L.F.} \to e^{i\omega_c t}|1\rangle_{R.F.}$, $|D\rangle_{L.F.} \to e^{i(\omega_1-\omega_c)t}|D\rangle_{R.F.}$, and $|D'\rangle_{L.F.} \to e^{i(\omega_1-\omega_c)t}|D'\rangle_{R.F.}$, where $L.F.$ and $R.F.$ stand for lab frame and rotating frame. Here, we have introduced the cavity detunings $\Delta_{c_1} = \omega_c - \omega_{PD}$ and $\Delta_{c_2} = \omega_c - \omega_{PD'}$, with $\omega_{PD} = \omega_{PS} - \omega_{DS}$ and $\omega_{PD'} = \omega_{PS} - \omega_{D'S}$. In the subspace $\mathcal{H}_E$ spanned by $\{|D,0\rangle, |D',0\rangle\}$, the Hamiltonian is simply

$$H_E/\hbar = (\Delta_{c_1} - \Delta_1)\,|D,0\rangle\langle D,0| + (\Delta_{c_2} - \Delta_1)\,|D',0\rangle\langle D',0|. \tag{S17}$$

In the experiment, the detunings are calibrated with respect to the observed resonance frequency. It is thus natural to define the detunings $\Delta_1' = \Delta_1 - |\delta_S|$ and $\Delta_2' = \Delta_2 - |\delta_S|$ that incorporate the AC Stark shift $\delta_s = \Omega_1^2/(4\Delta_1) + \Omega_2^2/(4\Delta_2)$ calculated for the $|S\rangle - |P\rangle$ transition. In terms of the new detunings, the Hamiltonian is recast to

$$\begin{aligned} H_t^C/\hbar = {} & -(\Delta_1' + |\delta_s|)\,|P,0\rangle\langle P,0| + (\Delta_{c_1} - \Delta_1' - |\delta_s|)\,|D,1\rangle\langle D,1| + (\Delta_{c_2} - \Delta_1' - |\delta_s|)\,|D',1\rangle\langle D',1| \\ & + \frac{1}{2}\left(\Omega_1 + \Omega_2 e^{i(\omega_2-\omega_1)t}\right)|S,0\rangle\langle P,0| + \frac{1}{2}\left(\Omega_1 + \Omega_2 e^{-i(\omega_2-\omega_1)t}\right)|P,0\rangle\langle S,0| \\ & + g_1\left(|D,1\rangle\langle P,0| + |P,0\rangle\langle D,1|\right) + g_2\left(|D',1\rangle\langle P,0| + |P,0\rangle\langle D',1|\right), \\ H_E/\hbar = {} & (\Delta_{c_1} - \Delta_1' - |\delta_s|)\,|D,0\rangle\langle D,0| + (\Delta_{c_2} - \Delta_1' - |\delta_s|)\,|D',0\rangle\langle D',0|. \end{aligned} \tag{S18}$$

The total Hamiltonian is denoted $H_t = H_t^C + H_E$.

2. Noise terms

In addition to the Hamiltonian evolution, there are noise terms that affect the dynamics of the system. We review them below.

Spontaneous decay of the ion. To account for spontaneous decay of the P level to S, D or D' (outside of the cavity mode), we introduce the noise operators

$$\begin{aligned} L_{sp} &= \sqrt{2\gamma_{sp}}\,|S,0\rangle\langle P,0|\,, \\ L_{dp} &= \sqrt{2\gamma_{dp}}\,|D,0\rangle\langle P,0|\,, \\ L_{d'p} &= \sqrt{2\gamma_{d'p}}\,|D',0\rangle\langle P,0|\,, \end{aligned} \tag{S19}$$

where γ_{sp}, γ_{dp}, and $\gamma_{d'p}$ are atomic polarization decay rates. These operators pick a phase in the rotating frame. However, these phases do not influence the master equation (see Eq. (S23)) and can thus be ignored.

Laser noise. A finite coherence time of the Raman drive laser can be modelled by a process in which each of the Rabi frequencies Ω_1 and Ω_2 (which originate from the same laser field) has a small chance to acquire a random phase $e^{\mathrm{i}\varphi_t}$ at each moment of time. Since the level $|S,0\rangle$ only couples to other levels by absorbing a laser photon, the laser phase noise can be accounted for in the master equation by introducing a dephasing channel that reduces the coherences $|S,0\rangle\langle P,0|$, $|S,0\rangle\langle D,1|$, and $|S,0\rangle\langle D',1|$. This is done by introducing the noise operator

$$L_{ss} = \sqrt{2\gamma_{ss}}\,|S,0\rangle\langle S,0|\,. \tag{S20}$$

Cavity jitter. The cavity jitter stems from slow drifts of the cavity frequency away from the reference frequency between recalibration steps, which we attribute to imperfect active stabilization of the cavity length. The resonator is a massive system, so that the cavity length drifts on timescales much slower than the duration of the Raman pulse. Therefore, we assume the cavity frequency ω_c to be fixed during a single iteration of the experiment (i.e., an attempt to generate a single photon). On the other hand, ω_c can change from one iteration to the next. We thus assume that for each iteration, the cavity frequency is a Gaussian random variable with standard deviation γ_{clj}, which is well justified because the data analysis of the run sequence is unordered. That is, at each iteration, $\hat{\omega}_\mathrm{c}$ is sampled from the Gaussian distribution

$$\mathrm{p}(\hat{\omega}_\mathrm{c}) = \frac{1}{\sqrt{2\pi}} \exp\left(-\frac{(\hat{\omega}_\mathrm{c}-\omega_\mathrm{c})^2}{2\gamma_{clj}^2}\right). \tag{S21}$$

Concretely, this means that we solve the dynamics of the two ion–cavity systems for fixed values of $\hat{\omega}_\mathrm{c}$ that are sampled from $\mathrm{p}(\hat{\omega}_\mathrm{c})$. The final state is a mixture of these solutions. In practice, to compute the model for $\hat{\omega}_\mathrm{c}$, we take a discrete ensemble of $2k_{\max}+1$ equally spaced values $\omega_k = w_\mathrm{c} + \Delta k$ for $|k| \le k_{\max}$, then renormalize the distribution by a constant such that it sums to one: $\sum_k \mathrm{p}(\omega_k) = 1$, that is, the contribution of each frequency in the ensemble is weighted by the distribution. For the numerical analysis below, we take $k_{\max} = 6$ for Node A (yielding 13 possible values for $\hat{\omega}_\mathrm{c}$), and we neglect the effect of the cavity lock jitter for Node B (fixing $\hat{\omega}_c = \omega_c$) as it is estimated to be an order of magnitude smaller.

Photon emission The possibility for the photon to leave the cavity gives rise to two noise operators

$$\begin{aligned} L_4 &= \sqrt{2\kappa}\,|D,0\rangle\langle D,1| \\ L_5 &= \sqrt{2\kappa}\,|D',0\rangle\langle D',1| \end{aligned} \tag{S22}$$

with κ the cavity field decay rate. In our rotating frame, the noise operators are time dependent: $L_4 = \sqrt{2\kappa}\,|D,0\rangle\langle D,1|\,e^{-\mathrm{i}\omega_c t}$, $L_5 = \sqrt{2\kappa}\,|D',0\rangle\langle D',1|\,e^{-\mathrm{i}\omega_c t}$. For the master equation, however (see Eq. (S23)), the phase of the noise operators plays no role. Note that the noise channels L_4 and L_5 encompass all cavity decay processes, including transmission, scattering, and absorption at both mirrors. Only a fraction of these photons are transmitted through the output mirror and sent to the PBSM.

3. The master equation for the full dynamics

To capture not only the unitary dynamics of the ion-cavity system but also decoherence and photon emission from the cavity, we use the master equation

$$\dot{\varrho}_t = -\mathrm{i}\,[H_t, \varrho_t]/\hbar + \sum_i \left(L_i \varrho_t L_i^\dagger - \frac{1}{2}\{L_i^\dagger L_i, \varrho_t\}\right), \tag{S23}$$

where the density matrix ϱ_t is defined on the six-level subspace $\mathcal{H}$ spanned by $\{|S,0\rangle, |P,0\rangle, |D,1\rangle, |D',1\rangle, |D,0\rangle, |D',0\rangle\}$. The index i includes all the terms described above, that is, $i = sp, ss, dp, d'p, 4, 5$. The probability density (rate) for a noise event L_i to occur at time t is denoted by $P_i(t) = \mathrm{tr}\, L_i \varrho_t L_i^\dagger$. The event leaves the system in the state

$$\varrho_{t|i} = \frac{L_i \varrho_t L_i^\dagger}{\mathrm{tr}\, L_i \varrho_t L_i^\dagger}. \tag{S24}$$

B. Photon envelope and scattering rates

In this section, we solve the dynamics of the master-equation model developed in Sec. IX A for the ion–cavity system. As we will see, it is enough to model the system's

state inside the four-dimensional subspace $\mathcal{H}^C$ for this purpose. Below, the density matrix is thus restricted to this subspace.

Knowledge of the ion–cavity state is sufficient to predict the scattering rates and the temporal envelopes of photons leaving the cavity. Through a comparison between the prediction of our theoretical model and the experimental data for the photon temporal envelopes, we are able to fix free parameters in the model, including the cavity loss, cavity jitter and the overall detection efficiency.

1. *Ion-cavity dynamics*

In the master equation given in Eq. (S23), different noises play different roles. The terms L_{sp} and L_{ss} leave the system in a state in the $\mathcal{H}^C$ subspace where it can still emit a photon. However, if the noise events L_{dp}, $L_{d'p}$, L_4, or L_5 occur, no photon can be emitted afterwards as the system is projected into $\mathcal{H}_E$. Since we are only interested in the evolution branch that can lead to the emission of a photon, we solve the master equation with the system remaining inside $\mathcal{H}^C$, that is,

$$\dot{\varrho}_t = -\,\mathrm{i}\,[H_t^C, \varrho_t]/\hbar + \sum_{i=sp,ss}\left(L_i \varrho_t L_i^\dagger - \frac{1}{2}\{L_i^\dagger L_i, \varrho_t\}\right) - \sum_{i=dp,d'p,4,5}\frac{1}{2}\{L_i^\dagger L_i, \varrho_t\}. \tag{S25}$$

Note that the solution of this equation is not trace preserving, as it ignores the branches where L_{dp}, $L_{d'p}$, L_4, or L_5 happen. In fact, the trace of ϱ_t gives the probability that none of these noises have happened before time t.

2. *Photon envelope*

We are primarily interested in the emission of a photon from each cavity to the PBSM setup when the ion-cavity system is initially in state $\varrho_0 = |S,0\rangle\langle S,0|$. If a photon is generated in the cavity mode, it leaves the cavity with rate 2κ. To compute the probability that a photon of a given polarization (horizontal or vertical) is emitted at time t, it is thus sufficient to solve the master equation (S25) for the initial state $\varrho_0 = |S,0\rangle\langle S,0|$ and compute

$$\begin{aligned} p_{\mathrm{v}}(t) &= 2\kappa\,\langle D,1|\,\varrho_t\,|D,1\rangle \\ p_{\mathrm{h}}(t) &= 2\kappa\,\langle D',1|\,\varrho_t\,|D',1\rangle\,. \end{aligned} \tag{S26}$$

The envelope of this photon is thus defined by the functions $p_{\mathrm{v}}(t)$ and $p_{\mathrm{h}}(t)$. In the presence of cavity jitter, the photon envelopes are the weighted averages over the different cavity frequency values

$$\begin{aligned} \bar{p}_{\mathrm{v}}(t) &= \sum_k \mathrm{p}(\omega_k)\, p_{\mathrm{v}}(t|\omega_k), \\ \bar{p}_{\mathrm{h}}(t) &= \sum_k \mathrm{p}(\omega_k)\, p_{\mathrm{h}}(t|\omega_k), \end{aligned} \tag{S27}$$

where $p_{\mathrm{v}}(t|\omega_k)$ and $p_{\mathrm{h}}(t|\omega_k)$ give the probabilities that a photon of a given polarization leaves the cavity at time t for a fixed cavity frequency ω_k. The photon envelopes of Eq. (S26) and Eq. (S27) can be compared with the time histograms of click events obtained at the PBSM setup. For these measurements, data are taken when only one node is sending photons, while the other is blocked.

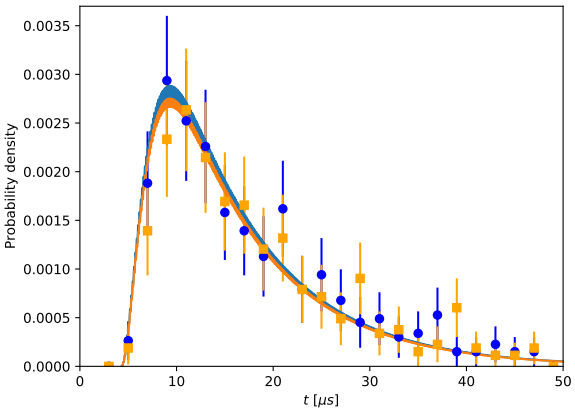

FIG. 2. Single-photon temporal wavepacket emitted from Node B and detected on the PBSM setup. Orange squares and blue circles correspond to vertical and horizontal polarizations. Squares and circles represent experimental data; error bars are calculated from Poissonian statistics. Lines are the envelopes found theoretically, which have been multiplied by $\eta = 1/10.5 \approx 0.095$.

In Fig. 2, we compare our model with data obtained from Node B. To obtain agreement between the observed detection rates and the model, we have multiplied the predicted emission rate $\bar{p}_{\mathrm{h(v)}}(t)$ by a factor $1/10.5 \approx 0.095$, which corresponds to the overall detection efficiency η, including detector efficiencies, photon loss in the channel, and scattering and absorption losses contained in the noise channels L_4 and L_5.

In Fig. 3, we compare our model with data obtained from Node A. Here as well, the predicted emission rates at time t are multiplied by a prefactor that accounts for the detection efficiency. In contrast to the comparison in Fig. 2, here we include cavity jitter, that is, we use Eq. (S27) instead of Eq. (S26). All parameters used for the numerical simulation are reported in Tab. II.

Node	Ω_1	Ω_2	g	Δ_1	Δ_2	κ	γ_{sp}	$\gamma_{dp}+\gamma_{d'p}$	γ_{ss}	γ_{clj}	η
A	43.8	30.9	0.77	412.8206	419.8574	0.0684	10.74	0.75	0.01	0.06 – 0.1	0.069– 0.08
B	24.76	21.05	1.2	414.0917	421.2091	0.07	10.74	0.75	0	0	0.095

TABLE II. The parameters that are used in the theoretical model to simulate the experimental data. All parameters have units of MHz and must be multiplied by 2π. In order to obtain the coupling strengths g_1 and g_2 shown in Fig. 1, we multiply g with the relevant atomic transition strength and with the projection of the transition polarization onto the photon polarization [2].

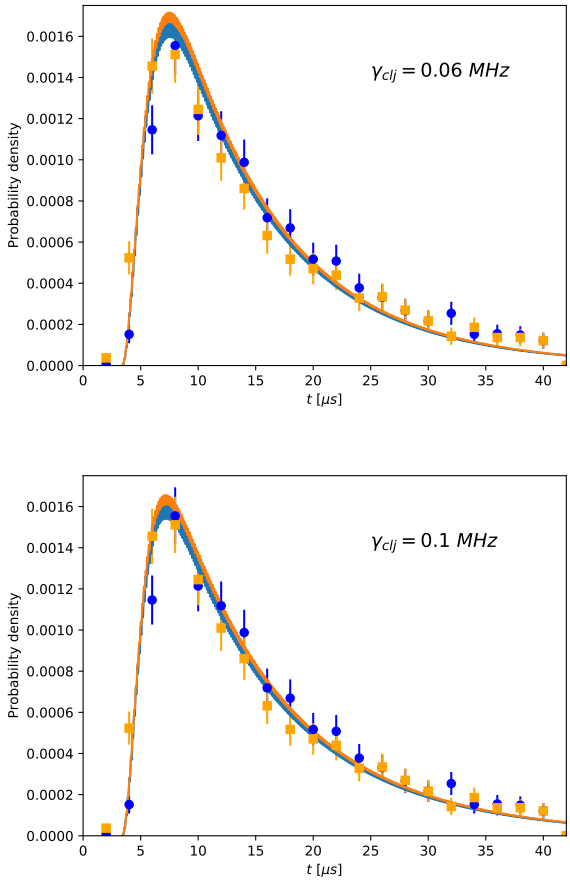

FIG. 3. Single-photon temporal wavepacket emitted from Node A and detected a few meters away. Orange squares and blue circles correspond to vertical and horizontal polarizations. Squares and circles represent experimental data; error bars are calculated from Poissonian statistics. Lines are the envelopes found theoretically, which have been multiplied by $\eta = 1/14.47 \approx 0.069$ (above) and $\eta = 1/12.46 \approx 0.08$ (below). Cavity jitter has been added with $\gamma_{clj} = 0.06$ (above) and $\gamma_{clj} = 0.1$ (below). Both parameter regimes are consistent with the data, that is, are within the uncertainties of experimentally determined values for η and γ_{clj}.

3. *Scattering rates*

To compute the interference visibility in the next section, we need to predict the scattering rates of the ion-cavity system back to its initial state. Once Eq. (S25) has been solved and the state ϱ_t has been computed, the rate of scattering back to to $|S,0\rangle$ can be obtained as

$$\mathrm{P}_s(t) = \mathrm{tr}\left((L_{sp}^\dagger L_{sp} + L_{ss}^\dagger L_{ss})\varrho_t\right). \tag{S28}$$

Note that whenever such a scattering event occurs, the system is projected onto the state $|S,0\rangle$ at the corresponding time.

C. The full state of the photon

The photon envelopes $p_\mathrm{v}(t)$ and $p_\mathrm{h}(t)$ defined in Eq. (S26) give the probabilities for photon emission at different times, but they do not tell us how coherent the emission process is. In particular, they do not tell us about the purity of the state of the emitted photon (for a fixed polarization) and are not sufficient to predict the interference visibility between two photons coming from different nodes. A more detailed analysis is thus required.

Such an analysis is reported below in three steps. First, we compute the ion–cavity state conditional on no noise events occurring during the evolution. Combining this pure state with the scattering rate computed in the previous section, we compute the actual ion–photon state. Finally, tracing out the ion, we obtain the full state of the photon emitted from each cavity and use it to predict the interference visibility.

1. *No-noise branch*

To compute the final ion–photon state, our first step is to extract from the master equation the branch that corresponds to the evolution branch on which no noise events occur. This is given by the equation

$$\dot\rho = -\mathrm{i}[H_t^C,\rho]/\hbar - \frac{1}{2}\{\sum_i L_i^\dagger L_i,\rho\}, \tag{S29}$$

where we have simply removed all post-noise terms $L_i\rho_t L_i^\dagger$. This equation can be cast in the form

$$\begin{aligned}&\dot\rho_t = -D_t\rho_t - \rho_t D_t^\dagger,\\ &\text{with}\quad D_t = \mathrm{i}H_t^C/\hbar + \frac{1}{2}\sum_i L_i^\dagger L_i.\end{aligned} \tag{S30}$$

One sees that if the state is initially pure, $\rho_{t_0} = |\Psi_{t_0}\rangle\langle\Psi_{t_0}|$, it will remain pure in the no-noise-branch evolution, that is, the evolution given by the Schrödinger

equation

$$\left|\dot{\Psi}_t\right\rangle = -D_t \left|\Psi_t\right\rangle, \tag{S31}$$

with a non-Hermitian Hamiltonian D_t. The norm of the state decreases in general as $\frac{d}{dt}\| \left|\Psi_t\right\rangle \| = -\left\langle\Psi_t\right| \sum_i L_i^\dagger L_i \left|\Psi_t\right\rangle$, reflecting the fact that the system leaves the no-noise branch whenever a noise event occurs. The solution of Eq. (S31) can be expressed formally by defining the time-ordered propagator

$$\begin{aligned} \left|\Psi_t\right\rangle &= V_{t_0}(t-t_0)\left|\Psi_{t_0}\right\rangle, \\ V_{t_0}(\tau) &= \mathcal{T}\left[e^{-\int_{t_0}^{t_0+\tau} D_s \mathrm{d}s}\right], \end{aligned} \tag{S32}$$

where $\mathcal{T}[\bullet]$ is the time-ordering operator.

For our noise model, the initial state for the no-noise evolution is always pure and given by $\left|\Psi_{t_0}\right\rangle = \left|S,0\right\rangle$ for some time t_0 where t_0 is determined by a noise event projecting the system onto $\left|S\right\rangle$, as discussed below. Let us denote $\left|\Psi_{t|t_0}\right\rangle$ the state of the system at time t, given that it was prepared in $\left|S,0\right\rangle$ at time $t_0 \leq t$ and no scattering events occurred in between, that is, given that the system has evolved between t_0 and t following the no-noise branch. This state is the solution of $\left|\dot{\Psi}_{t|t_0}\right\rangle = -D_t \left|\Psi_{t|t_0}\right\rangle$ and can also be expressed as

$$\left|\Psi_{t|t_0}\right\rangle = V_{t_0}(t-t_0)\left|S,0\right\rangle. \tag{S33}$$

It is worth noting that the Hamiltonian has a time dependence, meaning that time-translation symmetry is broken: $V_{t_1}(\tau) \neq V_{t_0}(\tau)$, that is, the evolution for a duration τ depends on the start time. Nevertheless, in our numerical computations we ignore this asymmetry and use the approximation $\left|\Psi_{t|t_0}\right\rangle \approx \left|\Psi_{(t-t_0)|0}\right\rangle$. This approximation results in a substantial computational speedup. We have established the validity of this approximation by comparing its results with the results of a time-dependent model for several values of t_0.

2. Ion–cavity state revisited

At this point, we know how to compute the scattering rate $\mathrm{P}_s(t)$ and the state $\left|\Psi_{t|t_0}\right\rangle$. It is then convenient to express the total state of the system in the form

$$\begin{aligned} \varrho_t &= \left|\Psi_{t|0}\right\rangle\!\left\langle\Psi_{t|0}\right| + \int_0^t \mathrm{d}s\, \mathrm{P}_s(s)\, \left|\Psi_{t|s}\right\rangle\!\left\langle\Psi_{t|s}\right| \\ &\approx \left|\Psi_{t|0}\right\rangle\!\left\langle\Psi_{t|0}\right| + \int_0^t \mathrm{d}s\, \mathrm{P}_s(s)\, \left|\Psi_{t-s|0}\right\rangle\!\left\langle\Psi_{t-s|0}\right|, \end{aligned} \tag{S34}$$

where in the second step, we use the approximation $\left|\Psi_{t|t_0}\right\rangle \approx \left|\Psi_{(t-t_0)|0}\right\rangle$ discussed above. This expression captures the fact that given a state at a certain time, the system will either evolve without noise until t (no-noise branch), trigger a noise event L_{ss} or L_{ps} at a later time t' ($s \leq t' \leq t$) that keeps it within the four-dimensional manifold $\mathcal{H}^C$, or trigger one of the other four noise events that causes it to leave $\mathcal{H}^C$ (and never emit a photon that is sent to the PBSM setup). Note that the probability that at time t, the most recent scattering event happened at time $s \leq t$ is $\mathrm{d}s\, \mathrm{P}_s(s) \| \left|\Psi_{t|s}\right\rangle \|$, which explains the term in the integral of Eq. (S34).

3. Ion–photon state

We now show that the decomposition of the state ϱ_t in the form proposed in Eq. (S34) results in a natural description of the entangled state of the ion and the cavity photon. First, note that the states entering in the decomposition ($\Psi_{t|s}$) are pure, i.e., Eq. (S34) gives an explicit decomposition of ϱ_t into pure states. For a pure ion–cavity state $\left|\Psi_t\right\rangle$, the probability amplitude that a photon leaves the cavity after a time duration $\mathrm{d}t$ (corresponding to the L_4 and L_5 decay channels when the photon is traced out) is obtained from

$$\begin{aligned} &\mathrm{d}t\, E_t \left|\Psi_t\right\rangle \equiv \\ &\mathrm{d}t\sqrt{2\kappa}\left(\left|D,0\right\rangle\!\left\langle D,1\right| a_{\mathrm{v}}^\dagger(t) + \left|D',0\right\rangle\!\left\langle D',1\right| a_{\mathrm{h}}^\dagger(t)\right)\left|\Psi_t\right\rangle, \end{aligned} \tag{S35}$$

where the ion–cavity state is projected into the $\mathcal{H}_E$ subspace. Here we have introduced the creation and annihilation operators for the continuous temporal (and polarization) modes outside the cavity directed to the PBSM setup, which satisfy $[a_{\mathrm{v}}(t), a_{\mathrm{v}}^\dagger(t')] = [a_{\mathrm{h}}(t), a_{\mathrm{h}}^\dagger(t')] = \delta(t-t')$. Thus, for the ion–cavity system evolving in the no-noise branch, with the system in state $\left|S,0\right\rangle$ at time s and in $\left|\Psi_{t|s}\right\rangle$ at time t, we can associate a probability amplitude that a photon is emitted from the cavity towards the PBSM setup in an infinitesimal time window $[t', t'+dt']$ with $s \leq t'$ and $t' + \mathrm{d}t' \leq t$. These events are coherent and described by the states $E'_t\, \mathrm{d}t' \left|\Psi_{t'|s}\right\rangle \left|0\right\rangle_{t'}$, where $\left|0\right\rangle_{t'}$ is the vacuum state of all the temporal modes in the interval $[t', t'+dt']$. It follows that the no-noise evolution branch corresponds to a branch where a single photon has been coherently emitted, which is described by the state

$$\begin{aligned} &\left(\int_s^t \mathrm{d}t'\, e^{-\mathrm{i}(t-t')H_E} E_{t'} \left|\Psi_{t'|s}\right\rangle\right)\left|0\right\rangle = \sqrt{2\kappa}\int_s^t \mathrm{d}t' \times \\ &\Big(\left|D,0\right\rangle e^{-\mathrm{i}(t-t')(\Delta_{\mathrm{c}_1} - \Delta'_1 - |\delta_s|)} \left\langle D,1\right|\Psi_{t'|s}\rangle\, a_{\mathrm{v}}^\dagger(t') \\ &+ \left|D',0\right\rangle e^{-\mathrm{i}(t-t')(\Delta_{\mathrm{c}_2} - \Delta'_1 - |\delta_s|)} \left\langle D',1\right|\Psi_{t'|s}\rangle\, a_{\mathrm{h}}^\dagger(t')\Big)\left|0\right\rangle. \end{aligned} \tag{S36}$$

Here, $\left|0\right\rangle$ denotes all the temporal modes of the photons traveling to the PBSM setup. In Eq. (S36), the term $e^{-\mathrm{i}(t-t')H_E}$ describes the evolution of the ion–cavity system following the emission of a photon at time t'. Recall from Eq. (S18) that the states $\left|D,0\right\rangle$ and $\left|D',0\right\rangle$ acquire phases $\left|D,0\right\rangle \mapsto e^{-\mathrm{i}(t-t')(\Delta_{\mathrm{c}_1} - \Delta'_1 - |\delta_s|)}\left|D,0\right\rangle$ and $\left|D',0\right\rangle \mapsto e^{-\mathrm{i}(t-t')(\Delta_{\mathrm{c}_2} - \Delta'_1 - |\delta_s|)}\left|D',0\right\rangle$ between the times

t' and t, as given by the energies of the Hamiltonian H_E. To shorten the notation, it is convenient to introduce the complex amplitudes

$$\begin{aligned}\alpha(t'|s) &= e^{\mathrm{i}t'(\Delta_{\mathrm{c}_1}-\Delta_1'-|\delta_s|)}\left\langle D,1\middle|\Psi_{t'|s}\right\rangle,\\ \beta(t'|s) &= e^{\mathrm{i}t'(\Delta_{\mathrm{c}_2}-\Delta_1'-|\delta_s|)}\left\langle D',1\middle|\Psi_{t'|s}\right\rangle.\end{aligned} \tag{S37}$$

Then in the photon-emitted branch of the evolution, with the ion–cavity system prepared in $|S,0\rangle$ at time s, the ion–photon state at time t is given by

$$\begin{aligned}\left|\Phi_{t|s}\right\rangle =&\sqrt{2\kappa}\Big(|D,0\rangle\int_s^t \mathrm{d}t'\alpha(t'|s)a_{\mathrm{v}}^\dagger(t')\\ &+e^{\mathrm{i}t(\Delta_{\mathrm{c}_1}-\Delta_{\mathrm{c}_2})}|D',0\rangle\int_s^t \mathrm{d}t'\beta(t'|s)a_{\mathrm{h}}^\dagger(t')\Big)|0\rangle.\end{aligned} \tag{S38}$$

This state can be rewritten as

$$\left|\Phi_{t|s}\right\rangle = |D,0\rangle\left|V_{t|s}\right\rangle + e^{\mathrm{i}t(\Delta_{\mathrm{c}_1}-\Delta_{\mathrm{c}_2})}|D',0\rangle\left|H_{t|s}\right\rangle \tag{S39}$$

with the unnormalized single-photon states

$$\begin{aligned}\left|V_{t|s}\right\rangle &= \sqrt{2\kappa}\int_s^t \mathrm{d}t'\alpha(t'|s)a_{\mathrm{v}}^\dagger(t')|0\rangle,\\ \left|H_{t|s}\right\rangle &= \sqrt{2\kappa}\int_s^t \mathrm{d}t'\beta(t'|s)a_{\mathrm{h}}^\dagger(t')|0\rangle.\end{aligned} \tag{S40}$$

From this point on, we will write $|D\rangle$ and $|D'\rangle$ instead of $|D,0\rangle$ and $|D',0\rangle$ since there is no ambiguity concerning the absence of cavity photons.

From the decomposition in pure states of the ion–cavity state given in Eq. (S34), we can now deduce the full (unnormalized) ion–photon state associated with the evolution branch in which a single cavity photon has been emitted towards the PBSM setup:

$$\rho_t^E = \left|\Phi_{t|0}\middle\rangle\middle\langle\Phi_{t|0}\right| + \int_0^t \mathrm{d}s\,\mathrm{P}_s(s)\,\left|\Phi_{t|s}\middle\rangle\middle\langle\Phi_{t|s}\right|, \tag{S41}$$

with the pure states $\left|\Phi_{t|s}\right\rangle$ given in Eqs. (S38) and (S39).

4. The marginal state of the photon

From the ion–photon state ρ_t^E (Eq. (S41)) (with an empty cavity), it is straightforward to compute the marginal state σ_t of the emitted photon by tracing out the ion–cavity system. We obtain

$$\sigma_t = \mathrm{tr}_{\mathrm{ion-cavity}}\,\rho_t^E = \mathbf{V}_t + \mathbf{H}_t, \tag{S42}$$

with

$$\begin{aligned}\mathbf{V}_t &= \left|V_{t|0}\middle\rangle\middle\langle V_{t|0}\right| + \int_0^t \mathrm{d}s\,\mathrm{P}_s(s)\,\left|V_{t|s}\middle\rangle\middle\langle V_{t|s}\right|,\\ \mathbf{H}_t &= \left|H_{t|0}\middle\rangle\middle\langle H_{t|0}\right| + \int_0^t \mathrm{d}s\,\mathrm{P}_s(s)\,\left|H_{t|s}\middle\rangle\middle\langle H_{t|s}\right|.\end{aligned} \tag{S43}$$

Here the density matrices $\mathbf{V}_t$ and $\mathbf{H}_t$ are not normalized. Their traces corresponds to the probabilities that a vertically or horizontally polarized photon has been emitted outside of the cavity in the mode of interest before time t.

Note that the components of the states in Eq. (S43) can be conveniently written as

$$\begin{aligned}\mathbf{V}_t &= \int_0^t \widetilde{\mathrm{P}}_s(s)\left|V_{t|s}\middle\rangle\middle\langle V_{t|s}\right|\\ &\text{with } \widetilde{\mathrm{P}}_s(s) = \mathrm{P}_s(s) + \delta(s)\end{aligned} \tag{S44}$$

such that $\int_0^t \mathrm{d}s\,\delta(s)\left|V_{t|s}\middle\rangle\middle\langle V_{t|s}\right| = \left|V_{t|0}\middle\rangle\middle\langle V_{t|0}\right|$, with an equivalent expression for $\mathbf{H}_t$. It is then straightforward to include the effects of cavity jitter, as we now show.

5. Effects of cavity jitter

We first remark that the above derivation of the ion–photon state assumes that the cavity frequency ω_{c} is constant, which is not the case in the presence of cavity jitter, where $\hat{\omega}_c$ is a random variable distributed according to $\mathrm{p}(\delta w)$, as discussed earlier in the context of Eq. (S21). Nevertheless, the effects of cavity jitter on the final state can be straightforwardly included, as we now discuss.

In our model, we take a discrete set of possible values: $\hat{\omega}_c \in \{\omega_k\}_{k=1}^{13}$. The final ion-cavity state is then a mixture

$$\bar{\rho}_t^E = \sum_k \mathrm{p}(\omega_k)\rho_t^{E,(\delta\omega_k)} \qquad \text{for} \qquad \delta\omega_k = \omega_k - \omega_c, \tag{S45}$$

where each state $\rho_t^{E,(\delta w)}$ takes the form

$$\begin{aligned}\rho_t^{E,(\delta w)} &= \left|\Phi_{t|0}^{(\delta w)}\middle\rangle\middle\langle\Phi_{t|0}^{(\delta w)}\right|\\ &\quad+\int_0^t \mathrm{d}s\,\mathrm{P}_s^{(\delta w)}(s)\,\left|\Phi_{t|s}^{(\delta w)}\middle\rangle\middle\langle\Phi_{t|s}^{(\delta w)}\right|,\\ \alpha^{(\delta w)}(t'|s) &= e^{\mathrm{i}t'(\widehat{\Delta}_{\mathrm{c}_1}-\Delta_1'-|\delta_s|)}\left\langle D,1\middle|\Psi_{t'|s}^{(\delta w)}\right\rangle\\ &= e^{\mathrm{i}t'(\Delta_{\mathrm{c}_1}+\delta w-\Delta_1'-|\delta_s|)}\left\langle D,1\middle|\Psi_{t'|s}^{(\delta w)}\right\rangle\\ \beta^{(\delta w)}(t'|s) &= e^{\mathrm{i}t'(\widehat{\Delta}_{\mathrm{c}_2}-\Delta_1'-|\delta_s|)}\left\langle D',1\middle|\Psi_{t'|s}^{(\delta w)}\right\rangle\\ &= e^{\mathrm{i}t'(\Delta_{\mathrm{c}_2}+\delta w-\Delta_1'-|\delta_s|)}\left\langle D',1\middle|\Psi_{t'|s}^{(\delta w)}\right\rangle;\end{aligned} \tag{S46}$$

see Eqs. (S39) and (S40). Here $\mathrm{P}_s^{(\delta w)}(s)$ and $\left|\Psi_{t|s}^{(\delta w)}\right\rangle$ are obtained similarly to $\mathrm{P}_s(s)$ in Eq. (S28) and $\left|\Psi_{t|s}\right\rangle$ in Eq. (S33) for a shifted cavity frequency $\omega_c + \delta w$.

The final state of the emitted photon also becomes a statistical mixture over the possible values of the cavity frequency $\omega_c + \delta\omega_k$:

$$\bar{\mathbf{V}}_t = \sum_k \mathrm{p}(\omega_k)\mathbf{V}_t^{(\delta\omega_k)}, \qquad \bar{\mathbf{H}}_t = \sum_k \mathrm{p}(\omega_k)\mathbf{H}_t^{(\delta\omega_k)}, \tag{S47}$$

with

$$\begin{aligned}
\mathbf{V}_t^{(\delta\omega)} &= \int_0^t \widetilde{\mathrm{P}}_s^{(\delta\omega)}(s) \left|V_{t|s}^{(\delta\omega)}\right\rangle\!\left\langle V_{t|s}^{(\delta\omega)}\right|, \\
\mathbf{H}_t^{(\delta\omega)} &= \int_0^t \widetilde{\mathrm{P}}_s^{(\delta\omega)}(s) \left|H_{t|s}^{(\delta\omega)}\right\rangle\!\left\langle H_{t|s}^{(\delta\omega)}\right|, \\
\left|V_{t|s}^{(\delta\omega)}\right\rangle &= \sqrt{2\kappa}\int_s^t \mathrm{d}t' \alpha^{(\delta\omega)}(t'|s) a_{\mathrm{v}}^\dagger(t')\left|0\right\rangle, \\
\left|H_{t|s}^{(\delta\omega)}\right\rangle &= \sqrt{2\kappa}\int_s^t \mathrm{d}t' \beta^{(\delta\omega)}(t'|s) a_{\mathrm{h}}^\dagger(t')\left|0\right\rangle.
\end{aligned} \tag{S48}$$

D. Visibility of a Hong-Ou-Mandel-type interference

At this point, we know how to compute the state of the photon emitted by a single node, and we are ready to analyze the interference between photons coming from two nodes. First, note that we are only interested in events where two photons are detected at the PBSM setup. For such an event to occur (neglecting background counts), a single photon has to be emitted from both Nodes A and B, as fully captured by the non-normalized state $\mathbf{H}_t + \mathbf{V}_t$ given in Eq. (S42). We first model the two-photon interference by considering the cavity frequency to be fixed. We then come back to the effect of cavity jitter towards the end of this section.

1. Two-photon state

To fix our notation, we denote the single-photon states of Eq. (S43) as $\mathbf{V}_t^{\mathrm{A}}$, $\mathbf{V}_t^{\mathrm{B}}$, $\mathbf{H}_t^{\mathrm{A}}$ and $\mathbf{V}_t^{\mathrm{B}}$ for Nodes A and B. The underlying pure states will be denoted

$$\begin{aligned}
\left|V_{t|s}^{\mathrm{A}}\right\rangle &= \sqrt{2\kappa}\int_s^t \mathrm{d}t' \alpha^{\mathrm{A}}(t'|s) a_{\mathrm{v}}^\dagger(t')\left|0\right\rangle \\
\left|H_{t|s}^{\mathrm{A}}\right\rangle &= \sqrt{2\kappa}\int_s^t \mathrm{d}t' \beta^{\mathrm{A}}(t'|s) a_{\mathrm{h}}^\dagger(t')\left|0\right\rangle \\
\left|V_{t|s}^{\mathrm{B}}\right\rangle &= \sqrt{2\kappa}\int_s^t \mathrm{d}t' \alpha^{\mathrm{B}}(t'|s) b_{\mathrm{v}}^\dagger(t')\left|0\right\rangle \\
\left|H_{t|s}^{\mathrm{B}}\right\rangle &= \sqrt{2\kappa}\int_s^t \mathrm{d}t' \beta^{\mathrm{B}}(t'|s) b_{\mathrm{h}}^\dagger(t')\left|0\right\rangle
\end{aligned} \tag{S49}$$

with the natural notation for the bosonic operators $a_{\mathrm{v}}(t), a_{\mathrm{h}}(t)$ and $b_{\mathrm{v}}(t), b_{\mathrm{h}}(t)$ for Nodes A and B respectively. The scattering rates are $\mathrm{P}_s^{\mathrm{A}}(s)$ and $\mathrm{P}_s^{\mathrm{B}}(s)$. The overall density matrix Σ_t describing the two photons (one emitted from each node) at time t is thus the tensor product of the (unnormalized) states emitted from each node:

$$\Sigma_t = (\mathbf{V}_t^{\mathrm{A}} + \mathbf{H}_t^{\mathrm{A}}) \otimes (\mathbf{V}_t^{\mathrm{B}} + \mathbf{H}_t^{\mathrm{B}}). \tag{S50}$$

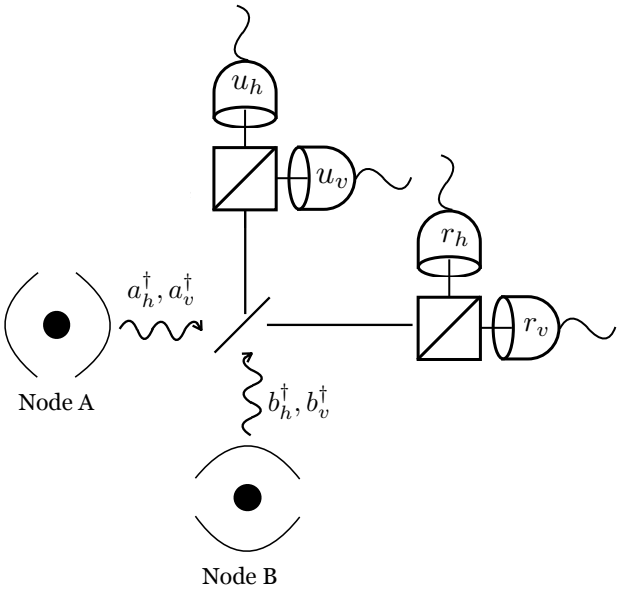

FIG. 4. Representation of the detection scheme for interfering two photons from two distant nodes in a photonic Bell-state measurement (PBSM). The bosonic operators associated to the fields leaving the cavity at Node A (B) are labeled a_h and a_v (b_h and b_v). The fields are combined on a nonpolarizing beamsplitter at a central station. Two detectors preceded by a polarizing beamsplitter are placed at each output of the nonpolarizing beamsplitter. The detected fields are called u_h, u_v, r_h and r_v.

2. Model of the PBSM

Given the two photon states, we now consider the PBSM; see Fig. 4. The beamsplitter output modes u and r are linked to the input modes a and b via

$$\begin{pmatrix} u \\ r \end{pmatrix} = \frac{1}{\sqrt{2}}\begin{pmatrix} 1 & \mathrm{i} \\ \mathrm{i} & 1 \end{pmatrix}\begin{pmatrix} a \\ b \end{pmatrix} \Leftrightarrow \begin{pmatrix} a \\ b \end{pmatrix} = \frac{1}{\sqrt{2}}\begin{pmatrix} 1 & -\mathrm{i} \\ -\mathrm{i} & 1 \end{pmatrix}\begin{pmatrix} u \\ r \end{pmatrix}. \tag{S51}$$

Each output mode of the (nonpolarizing) beamsplitter consists of a polarizing beamsplitter followed by two detectors; each detector detects one of the four modes u_h, u_v, r_h and r_v.

Let us consider the coincidence events where two clicks occur at detectors on opposite outputs of the beamsplitter, that is, clicks at detector pairs $\{u_h, r_h\}$, $\{u_h, r_v\}$, $\{u_v, v_h\}$ or $\{u_v, r_v\}$. We denote the rate of such coincidences for detector $u_{h(v)}$ at time t_1 and detector $r_{h'(v')}$ at time t_2 as $\det_{h(v),h'(v')}(t_1, t_2)$, that is, $\det_{v,h}(t_1, t_2)\mathrm{d}t^2$ corresponds to the probability to get a click at u_v in the time interval $[t_1, t_1 + \mathrm{d}t]$ and a click at r_h in the time interval $[t_2, t_2 + \mathrm{d}t]$, for example. The rate $\det_{v,h}(t_1, t_2)$ corresponds to a POVM density

$$E_{v,h}(t_1, t_2) = \eta_{u_v}\eta_{r_h}\left|v(t_1), h(t_2)\right\rangle\!\left\langle v(t_1), h(t_2)\right| \tag{S52}$$

with $\left|v(t_1), h(t_2)\right\rangle = u_v^\dagger(t_1) r_h^\dagger(t_2)\left|0\right\rangle$, where η_{u_v} is the overall detection efficiency of detector u_v and η_{r_h} is

the overall detection efficiency of detector r_h. Analogously, one defines POVM densities related to the other relevant coincidence rates $E_{h,v}(t_1,t_2)$, $E_{h,h}(t_1,t_2)$ and $E_{v,v}(t_1,t_2)$, with

$$E_{\pi_1,\pi_2}(t_1,t_2) = \eta_{u_{\pi_1}}\eta_{v_{\pi_2}}\, u^\dagger_{\pi_1}(t_1) r^\dagger_{\pi_2}(t_2)\,|0\rangle\langle 0|\, u_{\pi_1}(t_1) r_{\pi_2}(t_2), \tag{S53}$$

which describes the event where the upper detector for polarization π_1 clicks at time t_1 and the right detector for polarization π_2 clicks at time t_2. In principle, one can also compute the probability of events where both upper detectors or both right detectors click at different times, but here we are not interested in those events.

3. Coincidence rates for orthogonally polarized photons

Let us now compute the coincidence rates for two clicks from orthogonally polarized photons. We will explicitly compute the rate $\det_{v,h}(t_1,t_2)$. By the Born rule, one has

$$\begin{aligned}
\det_{v,h}(t_1,t_2) &= \operatorname{tr}\Sigma_t E_{v,h}(t_1,t_2)\\
&= \operatorname{tr}\left(\mathbf{H}^{\mathrm{A}}_t\otimes\mathbf{H}^{\mathrm{B}}_t + \mathbf{H}^{\mathrm{A}}_t\otimes\mathbf{V}^{\mathrm{B}}_t + \mathbf{V}^{\mathrm{A}}_t\otimes\mathbf{H}^{\mathrm{B}}_t + \mathbf{V}^{\mathrm{A}}_t\otimes\mathbf{V}^{\mathrm{B}}_t\right) E_{v,h}(t_1,t_2)\\
&= \operatorname{tr}\big(\mathbf{H}^{\mathrm{A}}_t\otimes\mathbf{V}^{\mathrm{B}}_t + \mathbf{V}^{\mathrm{A}}_t\otimes\mathbf{H}^{\mathrm{B}}_t\big) E_{v,h}(t_1,t_2)\\
&= \frac{\eta_{u_v}\eta_{r_h}}{4}\big(\operatorname{tr}\mathbf{H}^{\mathrm{A}}_t a^\dagger_{\mathrm{h}}(t_2)\,|0\rangle\langle 0|\,a_{\mathrm{h}}(t_2)\big)\big(\operatorname{tr}\mathbf{V}^{\mathrm{B}}_t b^\dagger_{\mathrm{v}}(t_1)\,|0\rangle\langle 0|\,b_{\mathrm{v}}(t_1)\big)\\
&+ \frac{\eta_{u_v}\eta_{r_h}}{4}\big(\operatorname{tr}\mathbf{H}^{A}_t a^\dagger_{\mathrm{v}}(t_1)\,|0\rangle\langle 0|\,a_{\mathrm{v}}(t_2)\big)\big(\operatorname{tr}\mathbf{V}^{B}_t b^\dagger_{\mathrm{h}}(t_1)\,|0\rangle\langle 0|\,b_{\mathrm{h}}(t_2)\big),
\end{aligned} \tag{S54}$$

or simply

$$\det_{v,h}(t_1,t_2) = \frac{\eta_{u_v}\eta_{r_h}}{4}\big(p^{\mathrm{A}}_{\mathrm{h}}(t_2)p^{\mathrm{B}}_{\mathrm{v}}(t_1) + p^{\mathrm{A}}_{\mathrm{v}}(t_1)p^{\mathrm{B}}_{\mathrm{h}}(t_2)\big). \tag{S55}$$

where $p^{\mathrm{A}}_{\mathrm{h}}(t_2) = \operatorname{tr}\mathbf{H}^{\mathrm{A}}_t a^\dagger_{\mathrm{h}}(t_2)\,|0\rangle\langle 0|\,a_{\mathrm{h}}(t_2)$ is the probability density that Node A emits a horizontally polarized photon at time t_2, and the probability densities for a vertically polarized photon and for Node B are defined equivalently. This coincidence rate can already be computed from the ion-cavity state according to Eq. (S26) because photons of orthogonal polarization do not interfere.

Similarly, one finds

$$\det_{h,v}(t_2,t_1) = \frac{\eta_{u_h}\eta_{r_v}}{4}\big(p^{\mathrm{A}}_{\mathrm{h}}(t_2)p^{\mathrm{B}}_{\mathrm{v}}(t_1) + p^{\mathrm{A}}_{\mathrm{v}}(t_1)p^{\mathrm{B}}_{\mathrm{h}}(t_2)\big). \tag{S56}$$

4. Coincidence rates for photons with identical polarization

It is more interesting to analyze the detection rates for two detectors sensitive to the same polarization. For example, consider $\det_{h,h}(t_1,t_2)$, which is related to the projector on

$$\begin{aligned}
|h(t_1),h(t_2)\rangle &= u^\dagger_h(t_1) r^\dagger_h(t_2)\,|0\rangle\\
&= \frac{1}{2}(a^\dagger_{\mathrm{h}}(t_1) + \mathrm{i}b^\dagger_{\mathrm{h}}(t_1))(\mathrm{i}a^\dagger_{\mathrm{h}}(t_2) + b^\dagger_{\mathrm{h}}(t_2))\,|0\rangle\\
&= \frac{1}{2}(a^\dagger_{\mathrm{h}}(t_1)b^\dagger_{\mathrm{h}}(t_2) - a^\dagger_{\mathrm{h}}(t_2)b^\dagger_{\mathrm{h}}(t_1))\,|0\rangle + \dots
\end{aligned} \tag{S57}$$

The dots here indicate terms with two photons emitted by a single node; these terms can be ignored as Σ_t has no support on such states. For $t_1,t_2\le t$, the rate is thus given by

$$\begin{aligned}
\det_{h,h}(t_1,t_2) &= \eta_{u_h}\eta_{r_h}\operatorname{tr}\Sigma_t\,|h(t_1),h(t_2)\rangle\langle h(t_1),h(t_2)|\\
&= \eta_{u_h}\eta_{r_h}\operatorname{tr}\left(\mathbf{H}^{\mathrm{A}}_t\otimes\mathbf{H}^{\mathrm{B}}_t + \mathbf{H}^{\mathrm{A}}_t\otimes\mathbf{V}^{\mathrm{B}}_t + \mathbf{V}^{\mathrm{A}}_t\otimes\mathbf{H}^{\mathrm{B}}_t + \mathbf{V}^{\mathrm{A}}_t\otimes\mathbf{V}^{\mathrm{B}}_t\right)|h(t_1),h(t_2)\rangle\langle h(t_1),h(t_2)|\\
&= \eta_{u_h}\eta_{r_h}\operatorname{tr}\mathbf{H}^{\mathrm{A}}_t\otimes\mathbf{H}^{\mathrm{B}}_t\,|h(t_1),h(t_2)\rangle\langle h(t_1),h(t_2)|\\
&= \frac{\eta_{u_h}\eta_{r_h}}{4}\int_0^t \mathrm{d}s\,\mathrm{d}s'\,\tilde{\mathrm{P}}^{\mathrm{A}}_s(s)\tilde{\mathrm{P}}^{\mathrm{B}}_s(s')\left|\left\langle H^{\mathrm{A}}_{t|s}, H^{\mathrm{B}}_{t|s'}\right|\left(a^\dagger_{\mathrm{h}}(t_1)b^\dagger_{\mathrm{h}}(t_2) - a^\dagger_{\mathrm{h}}(t_2)b^\dagger_{\mathrm{h}}(t_1)\right)|0\rangle\right|^2\\
&= \frac{\eta_{u_h}\eta_{r_h}}{4}\int_0^t \mathrm{d}s\,\mathrm{d}s'\,\tilde{\mathrm{P}}^{\mathrm{A}}_s(s)\tilde{\mathrm{P}}^{\mathrm{B}}_s(s')\left|\beta^{\mathrm{A}}(t_1|s)\beta^{\mathrm{B}}(t_2|s') - \beta^{\mathrm{A}}(t_2|s)\beta^{\mathrm{B}}(t_1|s')\right|^2.
\end{aligned} \tag{S58}$$

Similarly,

$$\mathrm{det}_{v,v}(t_1,t_2)=\frac{\eta_{u_v}\eta_{r_v}}{4}\int_0^t \mathrm{d}s\,\mathrm{d}s'\,\tilde{\mathrm{P}}_s^{\mathrm{A}}(s)\tilde{\mathrm{P}}_s^{\mathrm{B}}(s')\Big|\alpha^{\mathrm{A}}(t_1|s)\alpha^{\mathrm{B}}(t_2|s')-\alpha^{\mathrm{A}}(t_2|s)\alpha^{\mathrm{B}}(t_1|s')\Big|^2. \tag{S59}$$

In the integrals above, in order to use a more compact notation, we formally extend the function $\alpha(t|s)=\beta(t|s)$ to times $t<s$ by setting $\alpha(t|s)=\beta(t|s)=0$ for $t<s$, as it is impossible for the photon to be emitted from the cavity before a scattering event to the $|S,0\rangle$ level. One can easily see from Eqs. (S58) and (S59) that for indistinguishable pure photons, that is, $\alpha^{\mathrm{A}}(t|s)=\alpha^{\mathrm{B}}(t|s)$ and $\beta^{\mathrm{A}}(t|s)=\beta^{\mathrm{B}}(t|s)$, and no scattering, that is, $\tilde{\mathrm{P}}_s^{\mathrm{A}}(s)=\tilde{\mathrm{P}}_s^{\mathrm{B}}(s)=\delta(s)$, the photons bunch perfectly as expected at the outputs of the nonpolarizing beamsplitter, that is, $\mathrm{det}_{h,h}(t_1,t_2)=\mathrm{det}_{v,v}(t_1,t_2)=0$.

5. *Interference visibility*

Since we can now compute the coincidence rates at all pairs of detection times (t_1,t_2) (Eqs. (S58) and (S59)), we are also able to calculate the two-photon interference visibility. To do so, let us first define probabilities to detect two clicks delayed by at most T:

$$\mathrm{Det}_{\pi_1,\pi_2}(T)\equiv\int_{|t_1-t_2|\le T}\mathrm{d}t_1\mathrm{d}t_2\,\mathrm{det}_{\pi_1,\pi_2}(t_1,t_2). \tag{S60}$$

Then the two-photon interference visibility is by definition given by

$$V(T)=1-\frac{\mathrm{Det}_{h,h}(T)+\mathrm{Det}_{v,v}(T)}{\mathrm{Det}_{v,h}(T)+\mathrm{Det}_{h,v}(T)}, \tag{S61}$$

which one computes with the help of Eqs. (S55), (S56), (S58), (S59), and (S60).

To account for the effects of the cavity jitter at Node A, we simply replace the detection probabilities above with average quantities

$$\mathrm{Det}_{\pi_1,\pi_2}(T)=\sum_k \mathrm{p}(\omega_k)\mathrm{Det}^{(\delta\omega_k)}_{\pi_1,\pi_2}(T), \tag{S62}$$

which are obtained by averaging the detection probabilities over the possible values of ω_k, as discussed previously in Sec. IX C 5.

6. *Comparison with the experimental data*

In this section, we focus on Fig. 3b of the main text, in which the interference visibility computed with the theoretical model presented above is compared with the experimentally determined values. The figure has already been explained and discussed in the main text; our goal here is to make the connection clear between the notation used in the previous sections and the values in the plot.

The green solid line and green dashed line in Fig. 3b, which have the lowest values for visibility as a function of coincidence window, are computed with the model discussed above. The only difference between the two is the value of the cavity jitter parameter γ_{clj} for Node A, which is given by $\gamma_{clj}=2\pi\times 0.1\,\mathrm{MHz}$ for the dashed line and $\gamma_{clj}=2\pi\times 0.06\,\mathrm{MHz}$ for the solid line. Both values are consistent with independently characterized experimental parameters within uncertainties.

Next, we compute the visibility expected in the absence of both laser noise ($\gamma_{ss}=0$) and cavity jitter ($\gamma_{clj}=0$), which is plotted in orange. These are "technical" noises that could be reduced to negligible values by realistic improvements to the setup at Node A.

Finally, the top (blue) line provides information about the role of the mismatch between pure photon wavepackets. Concretely, we consider the case $\gamma_{ss}=\gamma_{clj}=0$ and compute the interference visibility between pure photons with the wavepackets $\left|H_{t|0}^{\mathrm{A(B)}}\right\rangle$ and $\left|V_{t|0}^{\mathrm{A(B)}}\right\rangle$ given in Eq. (S49), which describe the photonic states with no scattering on the $|S\rangle-|P\rangle$ transition during their evolution. The difference between the orange line and the blue line is thus solely due to the photon purity, that is, to the fact that the orange line takes into account emitted photons that are not pure due to spontaneous emission from $|P\rangle$ to $|S\rangle$. This effect can be in principle reduced by improving the coherent coupling strengths g_1 and g_2 between the ion and the cavity modes. Note that the computation of the average number of scattering events from $|P\rangle$ to $|S\rangle$ per experimental run gives 2.1 for Node B and 5.3 for Node A.

7. *Independent measurements of experimental parameters*

Cavity jitter. An independent estimate for the cavity jitter of Node A was obtained on a separate day than the one on which the ion–ion entanglement data was taken. That estimate was made by analysis of the error signal produced via the Pound-Drever-Hall system used to lock the cavity length to an injected 785 nm laser. A value of $\gamma_{clj}=2\pi\times 60\,\mathrm{kHz}$ was obtained, which was traced back to improper frequency stabilization of the 785 nm laser, the linewidth of which was found to be an order of magnitude larger than its usual value. We estimate that, on the day when the ion–ion entanglement data was taken, the value of γ_{clj} was most likely between $2\pi\times 60\,\mathrm{kHz}$ and $2\pi\times 100\,\mathrm{kHz}$ (that is, we believe that the laser frequency was also not properly stabilized on that day). At Node B, the same estimation technique yielded an upper bound on the cavity jitter of $2\pi\times 10(2)\,\mathrm{kHz}$. As this value is an order of magnitude smaller than the jitter at Node A, it was not included in the master-equation model (in

particular, via the methods described in Sec. IX C 5).

Laser noise. The phase noise of the Raman lasers was estimated independently in the following way. First, a beat between the Raman laser at Node B and a frequency comb yielded a FWHM Lorentzian linewidth of $2 \times \gamma_{ss} = 2\pi \times 88(1)$ Hz. Second, a beat between the Node A and Node B Raman lasers yielded a FWHM linewidth of $2 \times \gamma_{ss} = 2\pi \times 20(10)$ kHz. We thus assign a phase noise of $\gamma_{ss} = 2\pi \times 10(5)$ kHz to the Raman laser at Node A and assume that the phase noise of the Raman laser at Node B is negligible. We attribute the larger phase noise at Node A to the lower finesse and larger temperature drifts of that laser's external reference cavity. Those beat measurements were carried out many months before the measurements of ion–ion entanglement.

Rabi frequencies of the Raman laser fields. At each node, the total Rabi frequency $\Omega = \sqrt{\Omega_1^2 + \Omega_2^2}$ of the bichromatic 393 nm laser field is calibrated via measurement of the AC Stark shift it induces on the $|S\rangle - |D\rangle$ and $|S\rangle - |D'\rangle$ Raman transitions. At Node A, the value $\Omega = 2\pi \times 55(3)$ MHz was obtained. At Node B, the value $2\pi \times 32(2)$ MHz was obtained. More details on the calibration processes are given in Sec. 7.3.1 of Ref. [15] and Sec. 5.2 of Ref. [6].

Raman detunings. At each node, the detuning $\Delta_2 = 2\pi \times 420(5)$ MHz is determined via spectroscopy of the $|S\rangle - |P\rangle$ transition using a single-frequency (monochromatic) 393 nm field. Here, the laser power is set far below saturation, and the laser frequency is measured with a wavemeter. The laser frequency is scanned over the atomic resonance whilst the probability is measured for pumping to the $3^2D_{5/2}$ manifolds via electron shelving; the transition frequency is then extracted from a fit. The detuning Δ_2 corresponds to the difference between this transition frequency and the frequency of the monochromatic laser when it satisfies the $|S\rangle - |D'\rangle$ Raman resonance condition for a vanishing AC Stark shift. The difference frequency $\Delta_2 - \Delta_1$ is set by a radio frequency applied to an acousto-optic modulator at each node. At Node A, that frequency is $2\pi \times 7.107\,059$ MHz, and at Node B, it is $2\pi \times 7.005\,82$ MHz.

Ion-cavity coupling strengths. The strength of the coherent coupling between a single photon and a single $^{40}Ca^+$ ion is calculated to be $g_0 = 2\pi \times 1.53$ MHz at both Nodes A and B, based on the cavity geometries and the properties of the atomic transition. Here we consider the $|P\rangle - |D\rangle$ and $|P\rangle - |D'\rangle$ transitions but do not take into account the different Clebsch-Gordon coefficients for the two transitions or the projection of the transition polarizations onto the cavity-photon polarizations, both of which are accounted for separately in simulations [2]. The coupling strength of the bichromatic cavity-mediated Raman transition is reduced by the ion's motion in the trap. We model that effect using a reduced ion-cavity coupling strength $g = \alpha g_0$, where $0 \leq \alpha \leq 1$. For each node, we determine α by comparing measured single-photon temporal wavepackets with simulated wavepackets based on numerical integration of the master equation for a range of values of the coupling strength [6]. At Node A, we find $\alpha = 0.64$ and $g = 0.77$; at Node B, $\alpha = 0.78$ and $g = 1.2$.

[1] C. Russo, H. G. Barros, A. Stute, F. Dubin, E. S. Phillips, T. Monz, T. E. Northup, C. Becher, T. Salzburger, H. Ritsch, P. O. Schmidt, and R. Blatt, Raman spectroscopy of a single ion coupled to a high-finesse cavity, Appl. Phys. B **95**, 205 (2009).

[2] A. Stute, B. Casabone, B. Brandstätter, D. Habicher, P. O. Schmidt, T. E. Northup, and R. Blatt, Toward an ion-photon quantum interface in an optical cavity, Appl. Phys. B **107**, 1145 (2012).

[3] K. Friebe, *On dispersive interactions between a trapped ion and a cavity field*, Ph.D. thesis, Leopold-Franzens-Universität Innsbruck (2019).

[4] V. Krutyanskiy, M. Meraner, J. Schupp, V. Krcmarsky, H. Hainzer, and B. P. Lanyon, Light-matter entanglement over 50 km of optical fibre, npj Quantum Inf. **5**, 72 (2019).

[5] J. Schupp, V. Krcmarsky, V. Krutyanskiy, M. Meraner, T. Northup, and B. Lanyon, Interface between trapped-ion qubits and traveling photons with close-to-optimal efficiency, PRX Quantum **2**, 020331 (2021).

[6] J. Schupp, *Interface between trapped-ion qubits and travelling photons with close-to-optimal efficiency*, Ph.D. thesis, Leopold-Franzens-Universität Innsbruck (2021).

[7] B. Casabone, *Two ions coupled to a cavity: From an enhanced quantum computer interface towards distributed quantum computing*, Ph.D. thesis, Leopold-Franzens-Universität Innsbruck (2015).

[8] B. Casabone, A. Stute, K. Friebe, B. Brandstätter, K. Schüppert, R. Blatt, and T. E. Northup, Heralded entanglement of two ions in an optical cavity, Phys. Rev. Lett. **111**, 100505 (2013).

[9] H. Häffner, C. F. Roos, and R. Blatt, Quantum computing with trapped ions, Phys. Rep. **469**, 155 (2008).

[10] B. Efron and R. Tibshirani, *An Introduction to the Bootstrap* (Chapman & Hall, New York, 1993).

[11] D. F. V. James, P. G. Kwiat, W. J. Munro, and A. G. White, Measurement of qubits, Phys. Rev. A **64**, 052312 (2001).

[12] A. N. Craddock, J. Hannegan, D. P. Ornelas-Huerta, J. D. Siverns, A. J. Hachtel, E. A. Goldschmidt, J. V. Porto, Q. Quraishi, and S. L. Rolston, Quantum interference between photons from an atomic ensemble and a remote atomic ion, Phys. Rev. Lett. **123**, 213601 (2019).

[13] H.-J. Briegel, B. Huttner, N. Gisin, C. Macchiavello, M. Murao, M. B. Plenio, S. Popescu, V. Vedral, P. L. Knight, W. Dür, S. J. van Enk, J. I. Cirac, and P. Zoller, Entanglement purification, in *The Physics of Quantum Information: Quantum Cryptography, Quantum Teleportation, Quantum Computation*, edited by D. Bouwmeester, A. Ekert, and A. Zeilinger (Springer Berlin Heidelberg, Berlin, Heidelberg, 2000) pp. 261–293.

[14] M. Horodecki, P. Horodecki, and R. Horodecki, General teleportation channel, singlet fraction, and quasidistillation, Phys. Rev. A **60**, 1888 (1999).

[15] D. A. Fioretto, *Towards a flexible source for indistinguishable photons based on trapped ions and cavities*, Ph.D. thesis, Leopold-Franzens-Universität Innsbruck (2020).

7 SUMMARY AND OUTLOOK

7.1 SUMMARY

The presented thesis reports on the realization of a two-node quantum network consisting of two cavity-integrated ion-trap nodes separated by 230 m. In the thesis, three main results were obtained: (1) the construction of one of the two network nodes - the IQOQI node, (2) the observation of two-photon (Hong-Ou-Mandel) interference between photons produced by the remote nodes, and (3) the observation of entanglement between two ions, one in each node.

Chapter 4 presented the construction of a second cavity-integrated ion trap network node called the "IQOQI node". The heart of the node is a radio-frequency linear Paul trap surrounded by an optical cavity. This network node has achieved maximal ion-photon entanglement with fidelity of 96.6(5)% [102], which matches the 97.4(2%) fidelity achieved in the UIBK node [39]. The IQOQI node achieves a significantly improved single photon efficiency. Specifically, the IQOQI node has achieved a 72(3)% probability for obtaining a single photon out of the cavity in free space [102], while the UIBK node has reported values of 14(4)%[1]. A discussion on the remaining limits in the IQOQI system are detailed in [102].

Chapter 5 presented the observation of Hong-Ou-Mandel interference of two photons originating from the two independent network nodes. In these experiments two photons, each originating from different network node interact on a beamsplitter. A suppression of coincidence detection events between detectors in each output port of the beamsplitter is observed, depending on the arrival time window between the detection events. Interference visibilities from 0.95(2) to 0.38(3) were obtained as the arrival time window is varied from 1 μs to 20 μs, respectively. The longer time window corresponds to the entire length of the single photon wavepackets. These results are well described by a theoretical model introduced in Chapter 3 which considers imperfections induced by spontaneous scattering by the ions during the photon generation process and finite linewidth of the Raman laser driving the photon generation process at UIBK. Of these two, spontaneous scattering is found to play the dominant role in limiting the visibility of the Hong-Ou-Mandel interference. In the last part of Chapter 5, the achieved two-photon interference visibility

1 The value has been calculated using the photon creation efficiency of $\eta_c = 88(17)\%$ presented in [120] and known values of cavity mirror transmissions $T_1 = 1.3(3)$, $T_2 = 13(1)$, and total unwanted losses $L = 68(2)$, as measured in [41], using the formula $p_{out} = \eta_c T_1/(T_1 + T_2 + L)$

was used to predict the fidelity and rate at which remote ion-ion entanglement could be observed in our network, via two-photon swap technique. A trade off was identified between the achievable fidelity and rate of remote entanglement. Nevertheless, fidelities over 50% were predicted at heralding rates of a Hz.

Chapter 6 presented the observation of entanglement between ions in the two remote nodes. That is the first instance of entanglement of ions in traps more than a few meters apart. Moreover, the two nodes are fully independent, with their own separate laser systems and control. Bell state fidelities of the ion-ion state of up to $(88 + 2.2 - 4.7)\%$ were achieved for the smallest $1\,\mu$s coincidence window. That fidelity was achieved for a heralding rate of $3.5\,\mathrm{min}^{-1}$. For a larger coincidence window of $17.5\,\mu$s, a Bell state fidelity of $(58 + 1.7 - 2.1)\%$ was achieved at rate $0.49\,\mathrm{s}^{-1}$. A numerical and an analytical model of the experiment were developed. The analytical model was used to predict two-photon interference quality extracted from the data and applied to independent calibrated experimental parameters. The numerical model was used to predict the ion-ion entanglement fidelities, using e.g., the two-photon interference quality extracted form the data. The models predict that spontaneous scattering is one of the dominating imperfections in that experiment. However, technical noise (jitter of laser and cavity frequencies), as well as a mismatch in the "pure photon wavepacket" also play significant role in the drop in fidelity with increasing coincidence window.

Spontaneous scattering during the cavity-mediated Raman photon generation process introduces indistinguishability into the emitted single photons. Filtering on the arrival time allows for the highest fidelities for remote ion entanglement but comes at the cost of a reduced heralding rate. Reducing spontaneous scattering would allow us to keep high fidelity of remote ion entanglement without filtering on the arrival time, yielding a rate improvement. A possible way to reduce the spontaneous scattering rate is to increase the ion-cavity coupling strength g (the g-factor of Equation 3.1). This could be achieved by reducing the cavity waist, as seen in Equation 3.1 and thus designing a new ion-cavity system. Ion-cavity systems with smaller cavity waists than those considered here exist. We can name fiber cavities, that achieve waist size of micrometers [121–123].

The heralding rate for remote ion entanglement can be increased in our experiments by making more attempts per second. This can be achieved via sequence optimization. Achieving the 6000/s attempt rate discussed at the end of Chapter 5, could increase the heralding rate already by a factor of four over the presented experiment. Reducing photon losses throughout the detection path offer another path for significantly improving the heralding rate. An investigation into the possibilities for optimizing those two parameters (sequence and path) is planned in future work carried out beyond this thesis.

7.2 OUTLOOK

Our simple quantum network of two remote entangled ions demonstrates a building block for creating larger quantum networks which connect multiple nodes over long distances.

Our results show a trade-off between heralding rate of remote ion entanglement generation and the fidelity of the final swapped state. This drop of fidelity could, in future, be compensated by techniques such as entanglement purification [124]. This has been shown with trapped beryllium ions [125] but has not been demonstrated with remote trapped-ion network nodes yet. If such an experiment should be performed in our two-node network, at least two pairs of entangled ions should be created. Afterwards quantum gates need to be done in each node. The entanglement of one remote ion pair thus must persist while entanglement of the other pair is being created. Considering the results of the ion-ion entanglement experiment of Chapter 6, a remote entangled pair was established at rates of up to $\approx 0.5/\mathrm{s}$. This puts a requirement on the storage (coherence) time for the remote ion-ion entanglement on the order of seconds which has not been observed in either node and remains an open challenge. Since both nodes of our network are capable of trapping multiple ions that could be used to access decoherence free subspaces with lifetimes of tens of seconds [126] and performing quantum logic operations, it is reasonable that entanglement purification could be demonstrated in the existing systems in the future.

Building a quantum network over distances on the order of tens of kilometers is another step towards a world-wide quantum network. A photon at 854 nm, such as the ones generated by the calcium ion used in our experiments, suffers from 3dB/km loss when propagating through optical fiber. This fact itself limits the maximum practical distance between two nodes to a few kilometers. The distance between two nodes can be increased if photons of telecom wavelength are used. Such photons suffer propagation losses of typically 0.2dB/km and thus can travel over many tens of kilometers with similar losses. Ion-photon entanglement preservation after photon conversion from the natural wavelengths of trapped ions to telecom wavelengths have been shown by us [127] and other groups [128]. Achieving entanglement between our two network nodes over tens of kilometers of optical fibers is an ongoing project in our groups. A key requirement is that the telecom conversion process preserves the initial degree of photon indistinguishability, as we have recently investigated using sequentially generated photons from our IQOQI node [69]. For connecting quantum network nodes even further apart — hundreds, or even thousands of kilometers — a system of *quantum repeaters* could be established [129]. A theoretical proposal for a trapped-ion quantum repeater was made [130] and, using the single IQOQI node, we have

recently demonstrated this [131]. The future work here is to extend our quantum network with a third node. In this three-node network, the central node plays the quantum repeater node and establishes entanglement between the outer two nodes.

Building a world-wide quantum network will require placing many repeater nodes across the globe. It will require storing e.g., many ions for distributing entanglement and also error correction. Our current system does not allow for straightforward practical scaling of the quantum network. The ion-trap system is bulky and requires frequent maintenance. Novel methods of fabrication of miniature traps on chip [132–134] and high-finesse optical cavities [135] are showing the path towards scalable quantum computing with trapped-ion quantum networks. Complete ion-trap systems are already available in the size of a standard rack, including not only the trap, but also the entire laser system necessary for manipulating the ion [93]. When combined together, intercity scale quantum networks can soon become a reality.

A

ANTIREFLECTION COATINGS OF VIEWPORTS

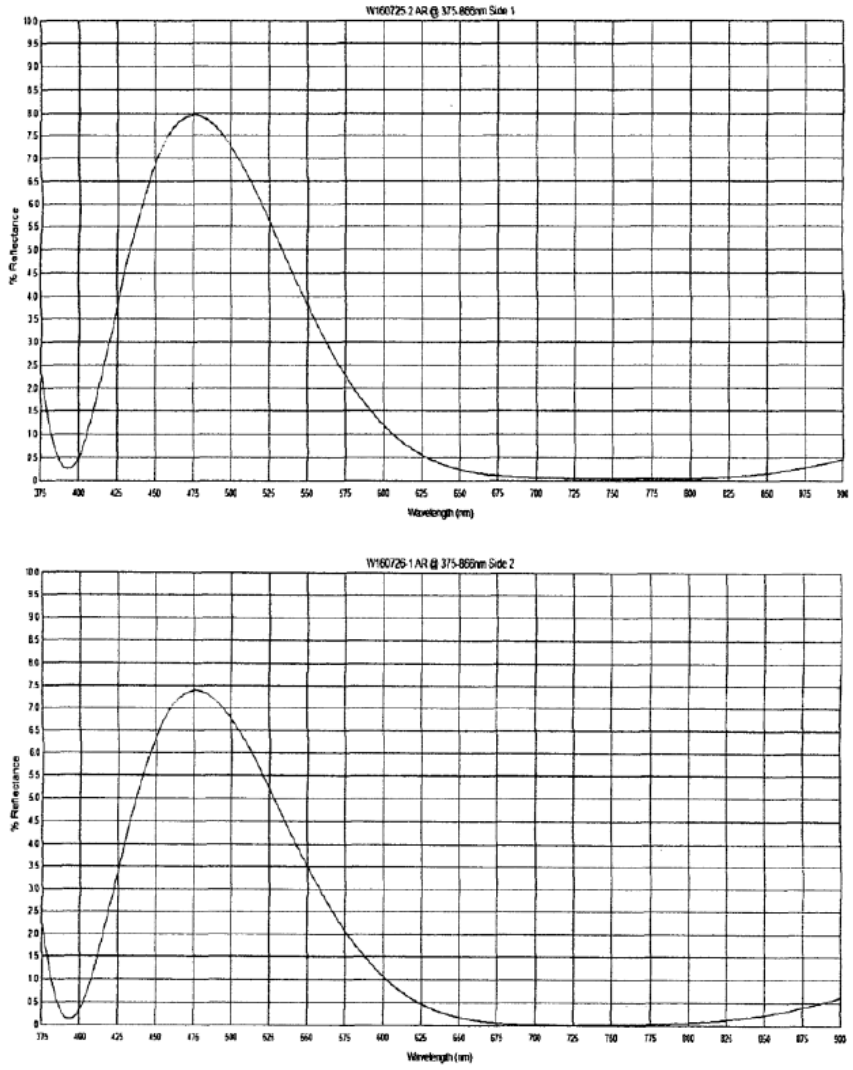

Figure A.1: Result of antireflection coating of viewports provided by VACOM company (result provided by the company).

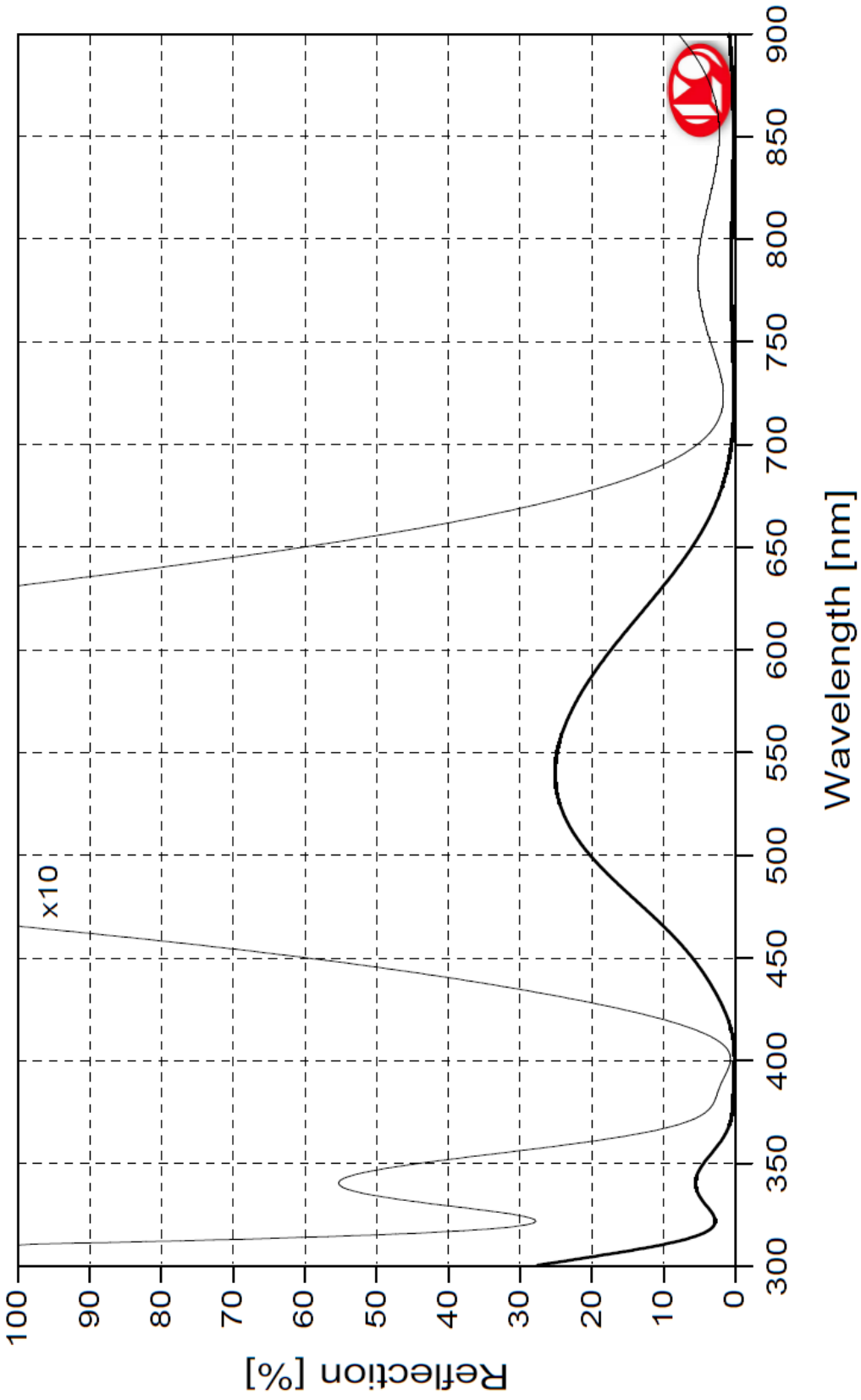

Figure A.2: Antireflection coating of the inverted viewport and two standard viewports in the cavity axis direction provided by the UKAEA company.

B

CLEANING OF IN-VACUUM COMPONENTS

To safeguard against contamination of in-vacuum components, the strict use of protective gear is essential. Common sources of contamination include body-related elements such as fingerprints, skin particles, and hair. In our preparations for Ultra-High Vacuum (UHV) conditions, we implemented stringent measures, wearing a protective coat, hair net, mouth cover, and gloves. The choice of gloves is crucial, and we selected powder-free latex gloves; however, alternative recommendations, such as the use of nitrile gloves, have been proposed by others [108].

The dominant gas in a properly-cleaned and out-gassed setup is hydrogen. This gas diffuses out from the bulk material of the vacuum chamber. To reduce this effect, a diffusion barrier was created on the surface of our stainless steel vacuum chamber by air-baking at 300°C for around 24 hours. The chamber itself was not cleaned prior to air baking as it was specified as vacuum-clean upon delivery. The cavity setup limited the maximum bake-out temperature of the whole system below 100°C. Therefore, it was necessary to properly clean each and every part which was placed into vacuum, from big flanges to the tiniest screw. All parts that allowed it were also air-baked prior placing the cavity setup to the chamber. The typical sequence for cleaning parts made of stainless steel, titanium, sapphire, or Macor was:

1. Hand wash in warm water with soap; use soft brush to wipe the surface
2. Rinse with warm water
3. Ultrasonic bath (20 min) with SimpleGreen (diluted 1:9)
4. Rinse with tap water
5. Rinse with distilled water
6. Ultrasonic bath in acetone (20 min)
7. Rinse with distilled water
8. Ultrasonic bath with methanol/isopropanol (20 min)

The choice of methanol or isopropanol depended on availability of the chemicals. Parts made of copper were cleaned differently, avoiding the use of acetone due to its chemical reactions with water vapor in the presence of ambient light [136]. The modified sequence for cleaning copper parts was:

1. Hand wash in warm water with soap; use soft brush to wipe the surface
2. Rinse with warm water
3. Ultrasonic bath (20 min) with SimpleGreen (diluted 1:9)
4. Rinse with tap water
5. Rinse with distilled water
6. Ultrasonic bath in isopropanol (2×20 min)[1]
7. Rinse with distilled water
8. Ultrasonic bath with methanol (if available) (20 min)

After each part was cleaned, it was wrapped in a vacuum-compatible aluminum foil and stored inside the clean area until it was assembled into the vacuum chamber. When cleaning parts made of Macor, the power of the ultrasonic bath was reduced from maximum to minimize the risk of pieces cracking.

1 the isopropanol was changed after 20 minutes

SPECIFICATIONS OF OPTICAL FIBER CONNECTING TWO BUILDINGS

LASER 2000
THE FUTURE OF PHOTONICS

Kabeldatenblatt "Laser 2000 - IQOQI LWL Special"

Aufbau :

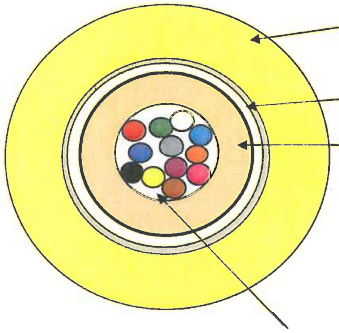

Halogenfreier Mantel für Außen und Innenverlegung

Nagetierschutz bestehend aus Glasrovings

Zentrale Bündelader Gel-gefüllt

Kabelaufdruck :

"LASER 2000 - IQOQI - LWL - Special"

Faserdaten :

Artikelnummer	Farbe	Typ
SMF 28	Weiss	Standard Singelmode Faser
SMF 28	Gelb	Standard Singelmode Faser
S&Y-SCSM-780-HP1	Orange	Singelmode Faser 780-970 nm
S&Y-SCSM-780-HP1	Grün	Singelmode Faser 780-970 nm
S&Y-SCSM-633-HP1	Blau	Singelmode Faser 600-760 nm
S&Y-PMF-820-B1	Schwarz	PM Faser 800-980 nm
S&Y-PMF-633-B1	Rot	PM Faser 630-780 nm

Die einzelnen Faserdaten finden Sie auf den angefügten Spulen Datenblättern.

Erstellt : Heiko Pierchalla
Datum : 25.09.2005
Kabelübergabe : 22.09.2005
Anhänge :
Faserdatenblätter

LASER 2000
THE FUTURE OF PHOTONICS

Laser 2000 GmbH
Argelsrieder Feld 14
D-82234 Wessling

Tel. +49 (0)8153/405-0
Fax +49 (0)8153/405-33
contact@laser2000.de

www.laser2000.de

OPTICAL COMPONENTS

StockerYale Spool Data Sheet

Select Cut-Off Single-Mode Fiber

Product Code	SCSM-633-HP1
Fiber ID	SCSM102-R3S1-D1-S2.1
Product Description	Select Cut-Off Single-Mode Fiber
Numerical Aperture (nominal)	0.13
Attenuation @ 633 nm	8.71 dB/km
Cut-Off Wavelength	582 nm
Mode Field Diameter @ 633 nm	4.10 µm
Core-Cladding Offset (concentricity)	< 0.5 µm
Cladding Diameter	125 ± 1 µm
Coating Diameter	245 ± 10 µm
Coating	UV-curable dual-coat acrylate
Coating Color	Blue
Proof Test	100 kpsi

For more information contact us at opticalsales@stockeryale.com or call a sales representative at **(603) 870-8286**.

StockerYale
Simply brilliant ideas™

Corporate Headquarters
32 Hampshire Road
Salem, New Hampshire 03079 USA
603-893-8778
Fax: 603-893-5604
opticalsales@stockeryale.com
www.stockeryale.com

StockerYale Spool Datasheet

Polarization Maintaining Fiber

Product Number	PMF-633-B1
Fiber ID Number	FU0112VI1088S1-D1-S1.1
Product Description	Bow-Tie Type Polarization Maintaining Fiber
Operating Wavelength	633 nm
Mode Field Diameter	3.4 μm @ 633 nm
Cut-Off Wavelength	586 nm
Beat Length	1.1 mm @ 633 nm
Attenuation	10.5 dB/km
Core-Cladding Offset (concentricity)	< 1.0 μm
Cladding Diameter	125 ± 1.0 μm
Coating Diameter	245 ± 10.0 μm
Coating	UV-cured Dual Acrylate
Coating Color	Red
Proof Test	100 kpsi

For more information contact us at opticalsales@stockeryale.com or call a sales representative at **(603) 870-8286**.

StockerYale
Simply brilliant ideas™

Corporate Headquarters
32 Hampshire Road
Salem, New Hampshire 03079 USA
Tel: 603-893-8778
Fax: 603-893-5604
opticalsales@stockeryale.com
www.stockeryale.com

StockerYale Spool Datasheet

Polarization Maintaining Fiber

Product Number	PMF-820-B1
Fiber ID Number	PMF173-R1S2-D2-S3.1
Product Description	Bow-Tie Polarization Maintaining Fiber
Operating Wavelength	820 nm
Attenuation	2.72 dB/km @ 820 nm
Cut-Off Wavelength	788 nm
Mode Field Diameter	4.31 µm @ 820 nm (*Petermann II*)
Beat Length	1.34 mm @ 820 nm
Core-Cladding Offset (concentricity)	< 1.0 µm
Cladding Diameter	125 ± 1.0 µm
Coating Diameter	245 ± 10.0 µm
Coating	UV-cured Dual Acrylate
Coating Color	Black
Proof Test	100 kpsi

For more information contact us at opticalsales@stockeryale.com or call a sales representative at **(603) 870-8286**.

Corporate Headquarters
32 Hampshire Road
Salem, New Hampshire 03079 USA
Tel: 603-893-8778
Fax: 603-893-5604
opticalsales@stockeryale.com
www.stockeryale.com

OPTICAL COMPONENTS

StockerYale Spool Data Sheet

Select Cut-Off Single-Mode Fiber

Product Code	SCSM-780-HP1
Fiber ID	SCSM102-R1S1-D1-S1.3
Product Description	Select Cut-Off Single-Mode Fiber
Numerical Aperture (nominal)	0.13
Attenuation @ 780 nm	2.90 dB/km
Cut-Off Wavelength	683 nm
Mode Field Diameter @ 780 nm	5.11 µm
Core-Cladding Offset (concentricity)	< 1.0 µm
Cladding Diameter	125 ± 1 µm
Coating Diameter	245 ± 10 µm
Coating	UV-curable dual-coat acrylate
Coating Color	Green
Proof Test	100 kpsi

For more information contact us at opticalsales@stockeryale.com or call a sales representative at **(603) 870-8286**.

StockerYale
Simply brilliant ideas™

Corporate Headquarters
32 Hampshire Road
Salem, New Hampshire 03079 USA
603-893-8778
Fax: 603-893-5604
opticalsales@stockeryale.com
www.stockeryale.com

OPTICAL COMPONENTS

StockerYale Spool Data Sheet

Select Cut-Off Single-Mode Fiber

Product Code	SCSM-780-HP1
Fiber ID	SCSM102-R1S1-D1-S1.2
Product Description	Select Cut-Off Single-Mode Fiber
Numerical Aperture (nominal)	0.13
Attenuation @ 780 nm	2.90 dB/km
Cut-Off Wavelength	683 nm
Mode Field Diameter @ 780 nm	5.11 µm
Core-Cladding Offset (concentricity)	< 1.0 µm
Cladding Diameter	125 ± 1 µm
Coating Diameter	245 ± 10 µm
Coating	UV-curable dual-coat acrylate
Coating Color	Orange
Proof Test	100 kpsi

For more information contact us at opticalsales@stockeryale.com or call a sales representative at (603) 870-8286.

StockerYale
Simply brilliant ideas™

Corporate Headquarters
32 Hampshire Road
Salem, New Hampshire 03079 USA
603-893-8778
Fax: 603-893-5604
opticalsales@stockeryale.com
www.stockeryale.com

BIBLIOGRAPHY

[1] ICAO. *Annex 14 to the Convention on International Civil Aviation — Aerodromes, Volume I Aerodrome Design and Operations*. 2020.

[2] United States National Institute of Standards and Technology (NIST). *Federal Information Processing Standards Publication 197 November 26, 2001 Announcing the ADVANCED ENCRYPTION STANDARD (AES*. 2021. URL: https://nvlpubs.nist.gov/nistpubs/FIPS/NIST.FIPS.197.pdf.

[3] J. Bardeen and W.H. Brattain. "The Transistor, A Semiconductor Triode." In: *Proceedings of the IEEE* 86.1 (1998), pp. 29–30. DOI: 10.1109/JPROC.1998.658753.

[4] T. H. Maiman. "Stimulated Optical Radiation in Ruby." In: *Nature* 187.4736 (1960), pp. 493–494. ISSN: 1476-4687. DOI: 10.1038/187493a0.

[5] Andrew Steane. "Quantum computing." In: *Reports on Progress in Physics* 61.2 (1998), p. 117. DOI: 10.1088/0034-4885/61/2/002.

[6] I. M. Georgescu, S. Ashhab, and Franco Nori. "Quantum simulation." In: *Rev. Mod. Phys.* 86 (2014), pp. 153–185. DOI: 10.1103/RevModPhys.86.153. URL: https://link.aps.org/doi/10.1103/RevModPhys.86.153.

[7] S. A. Diddams, J. C. Bergquist, S. R. Jefferts, and C. W. Oates. "Standards of Time and Frequency at the Outset of the 21st Century." In: *Science* 306.5700 (2004), pp. 1318–1324. DOI: 10.1126/science.1102330.

[8] C. L. Degen, F. Reinhard, and P. Cappellaro. "Quantum sensing." In: *Rev. Mod. Phys.* 89 (2017), p. 035002. DOI: 10.1103/RevModPhys.89.035002.

[9] Nicolas Gisin, Grégoire Ribordy, Wolfgang Tittel, and Hugo Zbinden. "Quantum cryptography." In: *Rev. Mod. Phys.* 74 (2002), pp. 145–195. DOI: 10.1103/RevModPhys.74.145.

[10] Hans Dehmelt. "Experiments with an isolated subatomic particle at rest." In: *Rev. Mod. Phys.* 62 (1990), pp. 525–530. DOI: 10.1103/RevModPhys.62.525.

[11] Wolfgang Paul. "Electromagnetic traps for charged and neutral particles." In: *Rev. Mod. Phys.* 62 (1990), pp. 531–540. DOI: 10.1103/RevModPhys.62.531.

[12] H. Häffner, C.F. Roos, and R. Blatt. "Quantum computing with trapped ions." In: *Physics Reports* 469.4 (2008), pp. 155–203. ISSN: 0370-1573. DOI: https://doi.org/10.1016/j.physrep.2008.09.003.

[13] D.J. Wineland and D. Leibfried. "Quantum information processing and metrology with trapped ions." In: *Laser Physics Letters* 8.3 (2011), pp. 175–188. DOI: https://doi.org/10.1002/lapl.201010125.

[14] M Saffman. "Quantum computing with atomic qubits and Rydberg interactions: progress and challenges." In: *Journal of Physics B: Atomic, Molecular and Optical Physics* 49.20 (2016), p. 202001. DOI: 10.1088/0953-4075/49/20/202001.

[15] Jörg Wrachtrup and Fedor Jelezko. "Processing quantum information in diamond." In: *Journal of Physics: Condensed Matter* 18.21 (2006), S807. DOI: 10.1088/0953-8984/18/21/S08.

[16] R. Hanson, L. P. Kouwenhoven, J. R. Petta, S. Tarucha, and L. M. K. Vandersypen. "Spins in few-electron quantum dots." In: *Rev. Mod. Phys.* 79 (2007), pp. 1217–1265. DOI: 10.1103/RevModPhys.79.1217.

[17] John Clarke and Frank K. Wilhelm. "Superconducting quantum bits." In: *Nature* 453.7198 (2008), pp. 1031–1042. ISSN: 1476-4687. DOI: 10.1038/nature07128.

[18] id Quantique. *ID Quantique Celebrates 10-Year Anniversary of the World's First Real-Life Quantum Cryptography installation*. 2017. URL: https://marketing.idquantique.com/acton/attachment/11868/f-0303/1/-/-/-/-/-/2017-11-20-IDQ-celebrates-10-year-anniversary-1.pdf (visited on 03/06/2023).

[19] *IBM Quantum systems*. https://www.ibm.com/quantum/systems. Accessed: 2023-04-02.

[20] *XEED*. https://xeedq.com/. Accessed: 2023-04-02.

[21] *Alpine Quantum Technologies GmbH*. https://www.aqt.eu/. Accessed: 2023-04-02.

[22] *IonQ*. https://ionq.com/. Accessed: 2023-04-02.

[23] H J Kimble. "The quantum internet." In: *Nature* 453.7198 (2008), pp. 1023–1030. ISSN: 0028-0836. DOI: 10.1038/nature07127.

[24] Stephanie Wehner, David Elkouss, and Ronald Hanson. "Quantum internet: A vision for the road ahead." In: *Science* 362.6412 (2018), eaam9288. ISSN: 0036-8075. DOI: 10.1126/science.aam9288.

[25] D L Moehring, P Maunz, S Olmschenk, K C Younge, D N Matsukevich, L-M Duan, and C Monroe. "Entanglement of single-atom quantum bits at a distance." In: *Nature* 449.7158 (2007), pp. 68–71. ISSN: 0028-0836. DOI: 10.1038/nature06118.

[26] D. N. Matsukevich, P. Maunz, D. L. Moehring, S. Olmschenk, and C. Monroe. "Bell Inequality Violation with Two Remote Atomic Qubits." In: *Phys. Rev. Lett.* 100 (2008), p. 150404. DOI: 10.1103/PhysRevLett.100.150404.

[27] S. Olmschenk, D. N. Matsukevich, P. Maunz, D. Hayes, L.-M. Duan, and C. Monroe. "Quantum Teleportation Between Distant Matter Qubits." In: *Science* 323.5913 (2009), pp. 486–489. DOI: 10.1126/science.1167209.

[28] P. Maunz, S. Olmschenk, D. Hayes, D. N. Matsukevich, L.-M. Duan, and C. Monroe. "Heralded Quantum Gate between Remote Quantum Memories." In: *Phys. Rev. Lett.* 102 (2009), p. 250502. DOI: 10.1103/PhysRevLett.102.250502.

[29] Tim van Leent et al. "Entangling single atoms over 33 km telecom fibre." In: *Nature* 607.7917 (2022), pp. 69–73. ISSN: 1476-4687. DOI: 10.1038/s41586-022-04764-4.

[30] B. Hensen et al. "Loophole-free Bell inequality violation using electron spins separated by 1.3 kilometres." In: *Nature* 526.7575 (2015), pp. 682–686. ISSN: 0028-0836. DOI: 10.1038/nature15759.

[31] M. Pompili et al. "Realization of a multinode quantum network of remote solid-state qubits." In: *Science* 372.6539 (2021), pp. 259–264. DOI: 10.1126/science.abg1919.

[32] Colin D. Bruzewicz, John Chiaverini, Robert McConnell, and Jeremy M. Sage. "Trapped-ion quantum computing: Progress and challenges." In: *Applied Physics Reviews* 6.2 (2019), p. 021314. DOI: 10.1063/1.5088164.

[33] G Wendin. "Quantum information processing with superconducting circuits: a review." In: *Reports on Progress in Physics* 80.10 (2017), p. 106001. DOI: 10.1088/1361-6633/aa7e1a.

[34] Ye Wang, Mark Um, Junhua Zhang, Shuoming An, Ming Lyu, Jing-Ning Zhang, L.-M. Duan, Dahyun Yum, and Kihwan Kim. "Single-qubit quantum memory exceeding ten-minute coherence time." In: *Nature Photonics* 11.10 (2017), pp. 646–650. ISSN: 1749-4893. DOI: 10.1038/s41566-017-0007-1.

[35] C. Monroe et al. "Programmable quantum simulations of spin systems with trapped ions." In: *Rev. Mod. Phys.* 93 (2021), p. 025001. DOI: 10.1103/RevModPhys.93.025001.

[36] Thomas Monz, Daniel Nigg, Esteban A. Martinez, Matthias F. Brandl, Philipp Schindler, Richard Rines, Shannon X. Wang, Isaac L. Chuang, and Rainer Blatt. "Realization of a scalable Shor algorithm." In: *Science* 351.6277 (2016), pp. 1068–1070. DOI: 10.1126/science.aad9480.

[37] S. M. Brewer, J.-S. Chen, A. M. Hankin, E. R. Clements, C. W. Chou, D. J. Wineland, D. B. Hume, and D. R. Leibrandt. "$^{27}Al^{+}$ Quantum-Logic Clock with a Systematic Uncertainty below 10^{-18}." In: *Phys. Rev. Lett.* 123 (2019), p. 033201. DOI: 10.1103/PhysRevLett.123.033201.

[38] E. A. Burt, J. D. Prestage, R. L. Tjoelker, D. G. Enzer, D. Kuang, D. W. Murphy, D. E. Robison, J. M. Seubert, R. T. Wang, and T. A. Ely. "Demonstration of a trapped-ion atomic clock in space." In: *Nature* 595.7865 (2021), pp. 43–47. ISSN: 1476-4687. DOI: 10.1038/s41586-021-03571-7.

[39] A. Stute, B. Casabone, P. Schindler, T. Monz, P. O. Schmidt, B. Brandstätter, T. E. Northup, and R. Blatt. "Tunable ion–photon entanglement in an optical cavity." In: *Nature* 485.7399 (2012), pp. 482–485. ISSN: 0028-0836. DOI: 10.1038/nature11120.

[40] L. J. Stephenson, D. P. Nadlinger, B. C. Nichol, S. An, P. Drmota, T. G. Ballance, K. Thirumalai, J. F. Goodwin, D. M. Lucas, and C. J. Ballance. "High-Rate, High-Fidelity Entanglement of Qubits Across an Elementary Quantum Network." In: *Phys. Rev. Lett.* 124 (2020), p. 110501. DOI: 10.1103/PhysRevLett.124.110501.

[41] Carlos Russo. "Photon statistics of a single ion coupled to a high-finesse cavity." PhD thesis. University of Innsbruck, 2008.

[42] Jarryd J. Pla, Kuan Y. Tan, Juan P. Dehollain, Wee H. Lim, John J. L. Morton, Floris A. Zwanenburg, David N. Jamieson, Andrew S. Dzurak, and Andrea Morello. "High-fidelity readout and control of a nuclear spin qubit in silicon." In: *Nature* 496.7445 (2013), pp. 334–338. ISSN: 1476-4687. DOI: 10.1038/nature12011.

[43] B. E. Kane. "A silicon-based nuclear spin quantum computer." In: *Nature* 393.6681 (1998), pp. 133–137. ISSN: 1476-4687. DOI: 10.1038/30156.

[44] Shuai Chen, Yu-Ao Chen, Bo Zhao, Zhen-Sheng Yuan, Jörg Schmiedmayer, and Jian-Wei Pan. "Demonstration of a Stable Atom-Photon Entanglement Source for Quantum Repeaters." In: *Phys. Rev. Lett.* 99 (18 2007), p. 180505. DOI: 10.1103/PhysRevLett.99.180505.

[45] A. A. Houck et al. "Controlling the Spontaneous Emission of a Superconducting Transmon Qubit." In: *Phys. Rev. Lett.* 101 (8 2008), p. 080502. DOI: 10.1103/PhysRevLett.101.080502.

[46] Fulvio Flamini, Nicolò Spagnolo, and Fabio Sciarrino. "Photonic quantum information processing: a review." In: *Reports on Progress in Physics* 82.1 (2018), p. 016001. DOI: 10.1088/1361-6633/aad5b2.

[47] Cornelius Hempel. "Digital quantum simulation, Schr´odinger cat state spectroscopy and setting up a linear ion trap." PhD thesis. University of Innsbruck, 2014.

[48] Sam A. Hill and William K. Wootters. "Entanglement of a Pair of Quantum Bits." In: *Phys. Rev. Lett.* 78 (1997), pp. 5022–5025. DOI: 10.1103/PhysRevLett.78.5022.

[49] G. Vidal and R. F. Werner. "Computable measure of entanglement." In: *Phys. Rev. A* 65 (2002), p. 032314. DOI: 10.1103/PhysRevA.65.032314.

[50] Charles H. Bennett, David P. DiVincenzo, John A. Smolin, and William K. Wootters. "Mixed-state entanglement and quantum error correction." In: *Phys. Rev. A* 54 (1996), pp. 3824–3851. DOI: 10.1103/PhysRevA.54.3824.

[51] Shi-Hai Wei et al. "Towards Real-World Quantum Networks: A Review." In: *Laser & Photonics Reviews* 16.3 (2022), p. 2100219.

[52] C. K. Hong, Z. Y. Ou, and L. Mandel. "Measurement of subpicosecond time intervals between two photons by interference." In: *Physical Review Letters* 59.18 (1987), pp. 2044–2046. ISSN: 0031-9007. DOI: 10.1103/PhysRevLett.59.2044.

[53] Sudhakar Prasad, Marlan O. Scully, and Werner Martienssen. "A quantum description of the beam splitter." In: *Optics Communications* 62.3 (1987), pp. 139–145. ISSN: 0030-4018. DOI: https://doi.org/10.1016/0030-4018(87)90015-0.

[54] Z.Y. Ou, C.K. Hong, and L. Mandel. "Relation between input and output states for a beam splitter." In: *Optics Communications* 63.2 (1987), pp. 118–122. ISSN: 0030-4018. DOI: https://doi.org/10.1016/0030-4018(87)90271-9.

[55] H. Fearn and R. Loudon. "Quantum theory of the lossless beam splitter." In: *Optics Communications* 64.6 (1987), pp. 485–490. ISSN: 0030-4018. DOI: https://doi.org/10.1016/0030-4018(87)90275-6.

[56] Hannes Bernien, Lilian Childress, Lucio Robledo, Matthew Markham, Daniel Twitchen, and Ronald Hanson. "Two-Photon Quantum Interference from Separate Nitrogen Vacancy Centers in Diamond." In: *Phys. Rev. Lett.* 108 (2012), p. 043604. DOI: 10.1103/PhysRevLett.108.043604.

[57] A. Sipahigil, M. L. Goldman, E. Togan, Y. Chu, M. Markham, D. J. Twitchen, A. S. Zibrov, A. Kubanek, and M. D. Lukin. "Quantum Interference of Single Photons from Remote Nitrogen-Vacancy Centers in Diamond." In: *Phys. Rev. Lett.* 108 (2012), p. 143601. DOI: 10.1103/PhysRevLett.108.143601.

[58] H. Bernien et al. "Heralded entanglement between solid-state qubits separated by three metres." In: *Nature* 497.7447 (2013), pp. 86–90. ISSN: 1476-4687. DOI: 10.1038/nature12016.

[59] Victor Leong, Sandoko Kosen, Bharath Srivathsan, Gurpreet Kaur Gulati, Alessandro Cerè, and Christian Kurtsiefer. "Hong-Ou-Mandel interference between triggered and heralded single photons from separate atomic systems." In: *Phys. Rev. A* 91 (2015), p. 063829. DOI: 10.1103/PhysRevA.91.063829.

[60] N. Somaschi et al. "Near-optimal single-photon sources in the solid state." In: *Nature Photonics* 10.5 (2016), pp. 340–345. ISSN: 1749-4893. DOI: 10.1038/nphoton.2016.23.

[61] Xing Ding et al. "On-Demand Single Photons with High Extraction Efficiency and Near-Unity Indistinguishability from a Resonantly Driven Quantum Dot in a Micropillar." In: *Phys. Rev. Lett.* 116 (2016), p. 020401. DOI: 10.1103/PhysRevLett.116.020401.

[62] Sebastian Unsleber, Yu-Ming He, Stefan Gerhardt, Sebastian Maier, Chao-Yang Lu, Jian-Wei Pan, Niels Gregersen, Martin Kamp, Christian Schneider, and Sven Höfling. "Highly indistinguishable on-demand resonance fluorescence photons from a deterministic quantum dot micropillar device with 74% extraction efficiency." In: *Opt. Express* 24.8 (2016), pp. 8539–8546. DOI: 10.1364/OE.24.008539.

[63] Daniel Huber, Marcus Reindl, Yongheng Huo, Huiying Huang, Johannes S. Wildmann, Oliver G. Schmidt, Armando Rastelli, and Rinaldo Trotta. "Highly indistinguishable and strongly entangled photons from symmetric GaAs quantum dots." In: *Nature Communications* 8.1 (2017), p. 15506. ISSN: 2041-1723. DOI: 10.1038/ncomms15506.

[64] Taek Jeong, Yoon-Seok Lee, Jiho Park, Heonoh Kim, and Han Seb Moon. "Quantum interference between autonomous single-photon sources from Doppler-broadened atomic ensembles." In: *Optica* 4.10 (2017), pp. 1167–1170. DOI: 10.1364/OPTICA.4.001167.

[65] D. P. Ornelas-Huerta, A. N. Craddock, E. A. Goldschmidt, A. J. Hachtel, Y. Wang, P. Bienias, A. V. Gorshkov, S. L. Rolston, and J. V. Porto. "On-demand indistinguishable single photons from an efficient and pure source based on a Rydberg ensemble." In: *Optica* 7.7 (2020), pp. 813–819. DOI: 10.1364/OPTICA.391485.

[66] T. Legero, T. Wilk, A. Kuhn, and G. Rempe. "Time-resolved two-photon quantum interference." In: *Applied Physics B* 77.8 (2003), pp. 797–802. ISSN: 1432-0649. DOI: 10.1007/s00340-003-1337-x.

[67] F. Dubin, D. Rotter, M. Mukherjee, S. Gerber, and R. Blatt. "Single-Ion Two-Photon Source." In: *Phys. Rev. Lett.* 99 (18 2007), p. 183001. DOI: 10.1103/PhysRevLett.99.183001. URL: https://link.aps.org/doi/10.1103/PhysRevLett.99.183001.

[68] Thomas Walker, Samir Vartabi Kashanian, Travers Ward, and Matthias Keller. "Improving the indistinguishability of single photons from an ion-cavity system." In: *Phys. Rev. A* 102 (2020), p. 032616. DOI: 10.1103/PhysRevA.102.032616.

[69] M. Meraner, A. Mazloom, V. Krutyanskiy, V. Krcmarsky, J. Schupp, D. A. Fioretto, P. Sekatski, T. E. Northup, N. Sangouard, and B. P. Lanyon. "Indistinguishable photons from a trapped-ion quantum network node." In: *Phys. Rev. A* 102 (2020), p. 052614. DOI: 10.1103/PhysRevA.102.052614.

[70] A. N. Craddock, J. Hannegan, D. P. Ornelas-Huerta, J. D. Siverns, A. J. Hachtel, E. A. Goldschmidt, J. V. Porto, Q. Quraishi, and S. L. Rolston. "Quantum Interference between Photons from an Atomic Ensemble and a Remote Atomic Ion." In: *Phys. Rev. Lett.* 123 (2019), p. 213601. DOI: 10.1103/PhysRevLett.123.213601.

[71] L-M Duan, Mikhail D Lukin, J Ignacio Cirac, and Peter Zoller. "Long-distance quantum communication with atomic ensembles and linear optics." In: *Nature* 414.6862 (2001), pp. 413–418. DOI: 10.1038/35106500.

[72] A. Kuzmich, W. P. Bowen, A. D. Boozer, A. Boca, C. W. Chou, L.-M. Duan, and H. J. Kimble. "Generation of nonclassical photon pairs for scalable quantum communication with atomic ensembles." In: *Nature* 423.6941 (2003), pp. 731–734. ISSN: 1476-4687. DOI: 10.1038/nature01714.

[73] C. W. Chou, H. de Riedmatten, D. Felinto, S. V. Polyakov, S. J. van Enk, and H. J. Kimble. "Measurement-induced entanglement for excitation stored in remote atomic ensembles." In: *Nature* 438.7069 (2005), pp. 828–832. ISSN: 1476-4687. DOI: 10.1038/nature04353.

[74] Chin-Wen Chou, Julien Laurat, Hui Deng, Kyung Soo Choi, Hugues de Riedmatten, Daniel Felinto, and H. Jeff Kimble. "Functional Quantum Nodes for Entanglement Distribution over Scalable Quantum Networks." In: *Science* 316.5829 (2007), pp. 1316–1320. DOI: 10.1126/science.1140300.

[75] Stephan Ritter, Christian Nölleke, Carolin Hahn, Andreas Reiserer, Andreas Neuzner, Manuel Uphoff, Martin Mücke, Eden Figueroa, Joerg Bochmann, and Gerhard Rempe. "An elementary quantum network of single atoms in optical cavities." In: *Nature* 484.7393 (2012), pp. 195–200. ISSN: 0028-0836. DOI: 10.1038/nature11023.

[76] M. Zukowski, A. Zeilinger, M. A. Horne, and A. K. Ekert. ""Event-ready-detectors" Bell experiment via entanglement swapping." In: *Phys. Rev. Lett.* 71 (1993), pp. 4287–4290. DOI: 10.1103/PhysRevLett.71.4287.

[77] Bernard Yurke and David Stoler. "Bell's-inequality experiments using independent-particle sources." In: *Phys. Rev. A* 46 (1992), pp. 2229–2234. DOI: 10.1103/PhysRevA.46.2229.

[78] Juraj Farkaš. "Calcium Isotopes." In: *Encyclopedia of Geochemistry: A Comprehensive Reference Source on the Chemistry of the Earth*. Ed. by William M. White. Cham: Springer International Publishing, 2018, pp. 181–186. ISBN: 978-3-319-39312-4. DOI: 10.1007/978-3-319-39312-4_237.

[79] D. M. Lucas, A. Ramos, J. P. Home, M. J. McDonnell, S. Nakayama, J.-P. Stacey, S. C. Webster, D. N. Stacey, and A. M. Steane. "Isotope-selective photoionization for calcium ion trapping." In: *Phys. Rev. A* 69 (2004), p. 012711. DOI: 10.1103/PhysRevA.69.012711.

[80] S. Gulde, D. Rotter, P. Barton, F. Schmidt-Kaler, R. Blatt, and W. Hogervorst. "Simple and efficient photo-ionization loading of ions for precision ion-trapping experiments." In: *Applied Physics B* 73.8 (2001), pp. 861–863. ISSN: 1432-0649. DOI: 10.1007/s003400100749.

[81] Andreas Stute. "A light-matter quantum interface:ion-photon entanglementand state mapping." PhD thesis. University of Innsbruck, 2012.

[82] Konstantin Friebe. "On dispersive interactions between a trapped ion and a cavity field." PhD thesis. University of Innsbruck, 2019.

[83] Josef Schupp. "Towards a deterministic ion-photon interface for quantum networks." PhD thesis. University of Innsbruck, 2022.

[84] Regina Lechner, Christine Maier, Cornelius Hempel, Petar Jurcevic, Ben P. Lanyon, Thomas Monz, Michael Brownnutt, Rainer Blatt, and Christian F. Roos. "Electromagnetically-induced-transparency ground-state cooling of long ion strings." In: *Phys. Rev. A* 93 (2016), p. 053401. DOI: 10.1103/PhysRevA.93.053401.

[85] F. Diedrich, J. C. Bergquist, Wayne M. Itano, and D. J. Wineland. "Laser Cooling to the Zero-Point Energy of Motion." In: *Phys. Rev. Lett.* 62 (1989), pp. 403–406. DOI: 10.1103/PhysRevLett.62.403.

[86] C. Monroe, D. M. Meekhof, B. E. King, S. R. Jefferts, W. M. Itano, D. J. Wineland, and P. Gould. "Resolved-Sideband Raman Cooling of a Bound Atom to the 3D Zero-Point Energy." In: *Phys. Rev. Lett.* 75 (1995), pp. 4011–4014. DOI: 10.1103/PhysRevLett.75.4011.

[87] G. Birkl, J. A. Yeazell, R. Rückerl, and H. Walther. "Polarization Gradient Cooling of Trapped Ions." In: *Europhysics Letters* 27.3 (1994), p. 197. DOI: 10.1209/0295-5075/27/3/005.

[88] P. A. Barton, C. J. S. Donald, D. M. Lucas, D. A. Stevens, A. M. Steane, and D. N. Stacey. "Measurement of the lifetime of the $3d^2D_{5/2}$ state in $^{40}Ca^+$." In: *Phys. Rev. A* 62 (2000), p. 032503. DOI: 10.1103/PhysRevA.62.032503.

[89] R. Blatt, H. Häffner, C. F. Roos, C. Becher, and F. Schmidt-Kaler. "Ion Trap Quantum Computing with Ca+ Ions." In: *Quantum Information Processing* 3.1 (2004), pp. 61–73. ISSN: 1573-1332. DOI: 10.1007/s11128-004-3105-1.

[90] P. Jurcevic, H. Shen, P. Hauke, C. Maier, T. Brydges, C. Hempel, B. P. Lanyon, M. Heyl, R. Blatt, and C. F. Roos. "Direct Observation of Dynamical Quantum Phase Transitions in an Interacting Many-Body System." In: *Phys. Rev. Lett.* 119 (2017), p. 080501. DOI: 10.1103/PhysRevLett.119.080501.

[91] Tiff Brydges, Andreas Elben, Petar Jurcevic, Benoît Vermersch, Christine Maier, Ben P. Lanyon, Peter Zoller, Rainer Blatt, and Christian F. Roos. "Probing Rényi entanglement entropy via randomized measurements." In: *Science* 364.6437 (2019), pp. 260–263. DOI: 10.1126/science.aau4963.

[92] M. K. Joshi, F. Kranzl, A. Schuckert, I. Lovas, C. Maier, R. Blatt, M. Knap, and C. F. Roos. "Observing emergent hydrodynamics in a long-range quantum magnet." In: *Science* 376.6594 (2022), pp. 720–724. DOI: 10.1126/science.abk2400.

[93] I. Pogorelov et al. "Compact Ion-Trap Quantum Computing Demonstrator." In: *PRX Quantum* 2 (2021), p. 020343. DOI: 10.1103/PRXQuantum.2.020343.

[94] Lukas Postler et al. "Demonstration of fault-tolerant universal quantum gate operations." In: *Nature* 605.7911 (2022), pp. 675–680. ISSN: 1476-4687. DOI: 10.1038/s41586-022-04721-1.

[95] A. H. Myerson, D. J. Szwer, S. C. Webster, D. T. C. Allcock, M. J. Curtis, G. Imreh, J. A. Sherman, D. N. Stacey, A. M. Steane, and D. M. Lucas. "High-Fidelity Readout of Trapped-Ion Qubits." In: *Phys. Rev. Lett.* 100 (2008), p. 200502. DOI: 10.1103/PhysRevLett.100.200502.

[96] C. K. Law and H. J. Kimble. "Deterministic generation of a bit-stream of single-photon pulses." In: *Journal of Modern Optics* 44.11-12 (1997), pp. 2067–2074. DOI: 10.1080/09500349708231869.

[97] Matthias Keller, Birgit Lange, Kazuhiro Hayasaka, Wolfgang Lange, and Herbert Walther. "Continuous generation of single photons with controlled waveform in an ion-trap cavity system." In: *Nature* 431.7012 (2004), pp. 1075–1078. ISSN: 1476-4687. DOI: 10.1038/nature02961.

[98] Christopher C. Gerry and J. H. Eberly. "Dynamics of a Raman coupled model interacting with two quantized cavity fields." In: *Phys. Rev. A* 42 (1990), pp. 6805–6815. DOI: 10.1103/PhysRevA.42.6805.

[99] Moorad Alexanian and Subir K. Bose. "Unitary transformation and the dynamics of a three-level atom interacting with two quantized field modes." In: *Phys. Rev. A* 52 (1995), pp. 2218–2224. DOI: 10.1103/PhysRevA.52.2218.

[100] Ying Wu. "Effective Raman theory for a three-level atom in the Λ configuration." In: *Phys. Rev. A* 54 (1996), pp. 1586–1592. DOI: 10.1103/PhysRevA.54.1586.

[101] "Polarisation-preserving photon frequency conversion from a trapped-ion-compatible wavelength to the telecom C-band." In: *Applied Physics B* 123.9 (2017), p. 228. ISSN: 0946-2171. DOI: 10.1007/s00340-017-6806-8.

[102] J. Schupp, V. Krcmarsky, V. Krutyanskiy, M. Meraner, T.E. Northup, and B.P. Lanyon. "Interface between Trapped-Ion Qubits and Traveling Photons with Close-to-Optimal Efficiency." In: *PRX Quantum* 2 (2021), p. 020331. DOI: 10.1103/PRXQuantum.2.020331.

[103] Michael Chwalla. "Precision spectroscopy with 40Ca+ ions in a Paul trap." PhD thesis. University of Innsbruck, 2009.

[104] Michael Guggemos. "Precision spectroscopy with trapped $^{40}Ca^{+}$ and $^{27}Al^{+}$ ions." PhD thesis. University of Innsbruck, 2017.

[105] Milena Guevara-Bertsch. "Optical clocks with trapped ions." PhD thesis. University of Innsbruck, 2023.

[106] Daniel Heinrich. "Ultrafast Coherent Excitation of a $^{40}Ca^{+}$ Ion." PhD thesis. University of Innsbruck, 2020.

[107] Betsy Bland, Thomas Bocek, Dennis Coyne, and Jodi Fauver. *LIGO Vacuum Compatibility, Cleaning Methods and Qualification Procedures (LIGO-E960022-v24)*. Tech. rep. California Institute of Technology and Massachusetts Institute of Technology, 2012.

[108] P. Obšil, A. Lešundák, T. Pham, K. Lakhmanskiy, L. Podhora, M. Oral, O. Číp, and L. Slodička. "A room-temperature ion trapping apparatus with hydrogen partial pressure below 10^{11} mbar." In: *Review of Scientific Instruments* 90.8 (2019), p. 083201. DOI: 10.1063/1.5104346.

[109] W. W. Macalpine and R. O. Schildknecht. "Coaxial Resonators with Helical Inner Conductor." In: *Proceedings of the IRE* 47.12 (1959), pp. 2099–2105. DOI: 10.1109/JRPROC.1959.287128.

[110] J. D. Siverns, L. R. Simkins, S. Weidt, and W. K. Hensinger. "On the application of radio frequency voltages to ion traps via helical resonators." In: *Applied Physics B* 107.4 (2012), pp. 921–934. ISSN: 1432-0649. DOI: 10.1007/s00340-011-4837-0.

[111] Philipp Schindler. "Quantum computation and simulation with trapped ions using dissipation." PhD thesis. University of Innsbruck, 2013.

[112] V. Krutyanskiy et al. "Entanglement of Trapped-Ion Qubits Separated by 230 Meters." In: *Phys. Rev. Lett.* 130 (2023), p. 050803. DOI: 10.1103/PhysRevLett.130.050803.

[113] B. Casabone, K. Friebe, B. Brandstätter, K. Schüppert, R. Blatt, and T. E. Northup. "Enhanced Quantum Interface with Collective Ion-Cavity Coupling." In: *Phys. Rev. Lett.* 114 (2015), p. 023602. DOI: 10.1103/PhysRevLett.114.023602.

[114] Helene Hainzer. "Laser locking for trapped-ion quantum networks." MA thesis. University of Innsbruck, 2018.

[115] Birgit Brandstätter. "Integration of fiber mirrors and ion traps for a high-fidelity quantum interface." PhD thesis. University of Innsbruck, 2013.

[116] D J Wineland, C Monroe, W M Itano, D Leibfried, B E King, and D M Meekhof. "Experimental issues in coherent quantum-state manipulation of trapped atomic ions." In: *Journal of Research of the National Institute of Standards and Technology* 103.3 (1998). DOI: 10.6028/jres.103.019.

[117] Man-Duen Choi. "Completely positive linear maps on complex matrices." In: *Linear Algebra and its Applications* 10.3 (1975), pp. 285–290. ISSN: 0024-3795. DOI: https://doi.org/10.1016/0024-3795(75)90075-0.

[118] A. Jamiołkowski. "Linear transformations which preserve trace and positive semidefiniteness of operators." In: *Reports on Mathematical Physics* 3.4 (1972), pp. 275–278. ISSN: 0034-4877. DOI: https://doi.org/10.1016/0034-4877(72)90011-0.

[119] Jaromír Fiurášek and Zdeněk Hradil. "Maximum-likelihood estimation of quantum processes." In: *Phys. Rev. A* 63 (2001), p. 020101. DOI: 10.1103/PhysRevA.63.020101.

[120] H. G. Barros, A. Stute, T. E. Northup, C. Russo, P. O. Schmidt, and R. Blatt. "Deterministic single-photon source from a single ion." In: *New Journal of Physics* 11.10 (2009), p. 103004. ISSN: 1367-2630. DOI: 10.1088/1367-2630/11/10/103004.

[121] Matthias Steiner, Hendrik M. Meyer, Christian Deutsch, Jakob Reichel, and Michael Köhl. "Single Ion Coupled to an Optical Fiber Cavity." In: *Phys. Rev. Lett.* 110 (2013), p. 043003. DOI: 10.1103/PhysRevLett.110.043003.

[122] Chi Huan Nguyen, Adrian Nugraha Utama, Nick Lewty, and Christian Kurtsiefer. "Operating a near-concentric cavity at the last stable resonance." In: *Phys. Rev. A* 98 (2018), p. 063833. DOI: 10.1103/PhysRevA.98.063833.

[123] Hiroki Takahashi, Ezra Kassa, Costas Christoforou, and Matthias Keller. "Cavity-induced anticorrelated photon-emission rates of a single ion." In: *Phys. Rev. A* 96 (2017), p. 023824. DOI: 10.1103/PhysRevA.96.023824.

[124] Jian-Wei Pan, Christoph Simon, Časlav Brukner, and Anton Zeilinger. "Entanglement purification for quantum communication." In: *Nature* 410.6832 (2001), pp. 1067–1070. ISSN: 1476-4687. DOI: 10.1038/35074041.

[125] R. Reichle, D. Leibfried, E. Knill, J. Britton, R. B. Blakestad, J. D. Jost, C. Langer, R. Ozeri, S. Seidelin, and D. J. Wineland. "Experimental purification of two-atom entanglement." In: *Nature* 443.7113 (2006), pp. 838–841. ISSN: 1476-4687. DOI: 10.1038/nature05146.

[126] H. Häffner et al. "Robust entanglement." In: *Applied Physics B* 81.2 (2005), pp. 151–153. ISSN: 1432-0649. DOI: 10.1007/s00340-005-1917-z.

[127] V. Krutyanskiy, M. Meraner, J. Schupp, V. Krcmarsky, H. Hainzer, and B. P. Lanyon. "Light-matter entanglement over 50 km of optical fibre." In: *npj Quantum Information* 5.1 (2019), p. 72. ISSN: 2056-6387. DOI: 10.1038/s41534-019-0186-3.

[128] Matthias Bock, Pascal Eich, Stephan Kucera, Matthias Kreis, Andreas Lenhard, Christoph Becher, and Jürgen Eschner. "High-fidelity entanglement between a trapped ion and a telecom photon via quantum frequency conversion." In: *Nature Communications* 9.1 (2018), p. 1998. ISSN: 2041-1723. DOI: 10.1038/s41467-018-04341-2.

[129] H.-J. Briegel, W. Dür, J. I. Cirac, and P. Zoller. "Quantum Repeaters: The Role of Imperfect Local Operations in Quantum Communication." In: *Phys. Rev. Lett.* 81 (1998), pp. 5932–5935. DOI: 10.1103/PhysRevLett.81.5932.

[130] Nicolas Sangouard, Romain Dubessy, and Christoph Simon. "Quantum repeaters based on single trapped ions." In: *Phys. Rev. A* 79 (2009), p. 042340. DOI: 10.1103/PhysRevA.79.042340.

[131] Victor Krutyanskiy, Marco Canteri, Martin Meraner, James Bate, Vojtech Krcmarsky, Josef Schupp, Nicolas Sangouard, and Ben P. Lanyon. "A telecom-wavelength quantum repeater node based on a trapped-ion processor." In: (2022). DOI: 10.48550/ARXIV.2210.05418.

[132] D. Stick, W. K. Hensinger, S. Olmschenk, M. J. Madsen, K. Schwab, and C. Monroe. "Ion trap in a semiconductor chip." In: *Nature Physics* 2.1 (2006), pp. 36–39. ISSN: 1745-2481. DOI: 10.1038/nphys171.

[133] Chiara Decaroli, Roland Matt, Robin Oswald, Christopher Axline, Maryse Ernzer, Jeremy Flannery, Simon Ragg, and Jonathan P Home. "Design, fabrication and characterization of a micro-fabricated stacked-wafer segmented ion trap with two X-junctions." In: *Quantum Science and Technology* 6.4 (2021), p. 044001. DOI: 10.1088/2058-9565/ac07ee.

[134] S Auchter et al. "Industrially microfabricated ion trap with 1 eV trap depth." In: *Quantum Science and Technology* 7.3 (2022), p. 035015. DOI: 10.1088/2058-9565/ac7072.

[135] Naijun Jin, Charles A. McLemore, David Mason, James P. Hendrie, Yizhi Luo, Megan L. Kelleher, Prashanta Kharel, Franklyn Quinlan, Scott A. Diddams, and Peter T. Rakich. "Micro-fabricated mirrors with finesse exceeding one million." In: *Optica* 9.9 (2022), pp. 965–970. DOI: 10.1364/OPTICA.467440.

[136] Sanjay V Kagwade, Clive R Clayton, Devicharan Chidambaram, and Gary P Halada. "Photochemical breakdown of acetone on copper." In: *Electrochimica Acta* 46.15 (2001), pp. 2337–2342. ISSN: 0013-4686. DOI: https://doi.org/10.1016/S0013-4686(01)00359-0.